A Generic and Robust Numerical Framework for Multiphase Flows using Volume-of-Fluid/Immersed Boundary Methods

A thesis submitted in partial fulfilment of the requirements for the Degree of

DOCTOR OF PHILOSOPHY

in

Mechanical Engineering

by

JITENDRA KUMAR PATEL

Department of Mechanical Engineering

Indian Institute of Technology Guwahati

Guwahati - 781 039, India

FEBRUARY, 2018

☆ ☆ ☆ ☆ ☆ ☆ ☆

Dedicated to my parents, Shri Lochan Prasad Patel and Smt. Mongara Patel

☆ ☆ ☆ ☆ ☆ ☆ ☆

CERTIFICATE

This is to certify that the work presented in the thesis entitled "**A Generic and Robust Numerical Framework for Multiphase Flows using Volume-of-Fluid/Immersed Boundary Methods**" is carried out by **Jitendra Kumar Patel** for the award of **Doctor of Philosophy** in the Department of Mechanical Engineering from Indian Institute of Technology Guwahati. The thesis embodies result of original work and studies carried out by student himself under my supervision and has not been submitted elsewhere for the degree.

Dr. Ganesh Natarajan
Associate Professor
Department of Mechanical Engineering
Indian Institute of Technology Guwahati
Guwahati - 781039, Assam, India

Date:

Place: Guwahati

ACKNOWLEDGEMENTS

First of all, I would like to express my sincere gratitude towards my supervisor Dr. Ganesh Natarajan, for his invaluable guidance, caring and encouragement during the research work. It is a privilege to work under him who has motivated me at each and every step to carry out my thesis work successfully. I thank him for giving me an opportunity to work under him.

I would like to extend my gratitude to my doctoral committee members; Prof. Anoop K. Dass, Dr. Amaresh Dalal, Dr. Nanda Kishore and Dr. Hrishikesh Gadgil for all their crucial suggestions, precious time and support throughout my thesis work. I am highly indebted to the Indian Institute of Technology Guwahati for providing ideal environment to carry out my research work and its my honor to be a part of such prestigious institute.

I am also thankful to my dear colleagues and friends for their continuous support and jollity discussions that make the research work more enjoyable. I will cherish all the memories we have shared together throughout my life.

Above all, words are not enough to show my gratitude towards my family for the patience and sacrifices they have borne to ensure the fulfillment of my dreams.

ABSTRACT

This thesis is devoted to the development of a generic and robust framework for multi-phase/multi–fluid flows on arbitrary polygonal meshes and its application. Such a framework is a seamless conglomeration of several efficient numerical strategies that can handle different challenges encountered in multiphase flow simulations. In this context we first propose a generic methodology for the design of interface capturing schemes for immiscible multi-fluid flows using the VOF (Volume–Of–Fluid) approach. Interface capturing schemes are devised as a blend of high-resolution and compressive schemes and their efficiency and accuracy depend on the choice of the constituent schemes and the blending function. On the basis of a set of design principles proposed in this work, we show that existing interface capturing schemes may be encompassed into a single class of GPL (Generalised Piecewise Linear)–κ schemes allowing for a unified approach for development of such schemes. Following these set of design guidelines, we construct two new schemes for interface capture in an unstructured finite volume framework. The schemes are tested on challenging advection problems using both structured and unstructured grids to evaluate their performance. The new schemes perform as well as existing schemes and even outperform them on unstructured grids, while also exhibiting near Courant number independence for all test problems and grid topologies. The CUIBS (Cubic Upwind Interpolation based Blending Scheme) proposed in the study shows the best performance among all interface capturing schemes discussed herein and is chosen for further studies of immiscible multiphase flows. The VOF approach is combined with a novel hybrid staggered/non–staggered finite volume framework to devise an unstructured data–based multiphase flow solver. The multiphase solver is based on the segregated approach typical of single phase incompressible flow solvers, employing an incremental fractional step approach but with a variable coefficient Poisson equation to handle variable density flows. We further discuss the development and assessment of a robust numerical framework targeted at simulations of high density ratio flows with large interfacial and/or body

forces. The key principles that characterise this framework are the consistent treatment of discrete mass and momentum transport and the similar discretisation of dominant force terms appearing in the momentum equation. The former is achieved by invoking identical high–resolution schemes for convective transport of volume fraction and momentum in the respective discrete equations. The latter is realised by representing the gravity and surface tension (or interfacial tension) terms as gradients of suitable scalars which are then discretised in identical fashion resulting in a balanced formulation. The hybrid staggered/non–staggered framework is shown to naturally lead to similar terms for pressure and its correction in the momentum and pressure correction equations respectively, which are again treated discretely in a similar manner. We show that spurious currents that corrupt the solution may arise both from an unbalanced formulation and from an inconsistent approach, with the latter prominent in flows which are convection–dominant with high density ratios. We show that the inconsistent approach, which uses dissimilar convective schemes at the discrete level, might perform as well as the consistent approach even for high density ratio flows in some cases and that it exhibits anomalous behaviour for other scenarios even at low density ratios. Using a plethora of test problems of increasing complexity, we conclusively demonstrate that the consistent transport and balanced force treatment results in a numerically stable solution procedure and physically consistent results. We further the capability and versatility of the framework to solve fluid–structure interactions in multiphase flows by combining it with a diffuse interface immersed boundary method (DIIBM). The latter, which uses the solid fraction to identify the rigid solid(s) implements the effect of no-slip boundary condition by constructing and solving for a “hybridised" momentum equation. This modified momentum equation is solved everywhere in the computational domain including the solid region thereby eliminating cumbersome velocity and pressure interpolations. The methodology is extended to multi–fluid systems by considering a “virtual" fluid inside the solid which is tracked using a fully Eulerian approach. The immersed boundary–finite volume (IB–FV) flow solver which is temporally second-order accurate and exhibits nominal second-order accuracy in space is capable of simulating multiphase flows with moving rigid solid(s) in a cost–efficient and accurate manner. The IB–FV solver shows no spurious force oscillations in mov-

ing body problems and keeps the diffusion of fluid–fluid and solid–fluid interfaces to acceptable levels without compromising on solution accuracy. The numerical framework involving consistent and well–balanced methodologies in conjunction with DIIBM is extended to tackle binary miscible flows. We show that miscible flows are in general quasi–incompressible necessitating a non–zero divergence constraint and solution to a convective–diffusive transport equation for mass fractions. We investigate the implications of quasi–incompressibility and show that assuming a purely incompressible flow in miscible flow simulations is not prone to significant error and can be justified in practice. Challenging flow problems involving falling of half and neutrally buoyant cylinders on air–water interface, two–particle sedimentation in discretely stratified media and two–fluid mixing in micromixer configurations are investigated to demonstrate the efficacy and utility of the proposed framework. The numerical investigations on several problems of varying complexity in immiscible and miscible regimes categorically establish the proposed numerical framework as a robust, accurate and competitive approach for realistic multiphase flow simulations involving high density ratios in presence of large interfacial/body forces and multiple arbitrarily moving rigid bodies.

CONTENTS

LIST OF FIGURES

LIST OF TABLES

NOMENCLATURE

Symbols

Co	Courant number
C	Control volume for scalar variables
C_D	Coefficient of drag
C_L	Coefficient of lift
C_M	Coefficient of moment
Fr	Froude number
I	Mixing index
p	Piezometric pressure
$\acute{p}$	Hydrodynamic pressure
$\mathcal{P}$	Piezometric pressure correction
Re	Reynolds number
Sc	Schmidt number
Δs	Surface area
Δt	Time step
U_f	Normal velocity
u, v	Cartesian components of velocity vector
We	Weber number

Abbreviations

BD	Compressive/bounded downwind scheme
CUIBS	Cubic upwind interpolation based blending scheme
DIIBM	Diffuse interface immersed boundary method
HR	High resolution scheme
LiS	Library of iterative solvers for linear systems
PETSc	Portable, extensible toolkit for scientific computation
VOF	Volume–Of–Fluid

Subscripts and superscripts

f	Face value
m, n	Adjacent cells sharing the common face
D, U, FU	Downwind, upwind and far upwind cells
L	Lighter/less denser fluid
H	Heavier/denser fluid
n	Time level
$\star$	Intermediate time level
$*$	Non–dimensional value

Greek letters

ρ	Density
μ	Dynamic viscosity
ϕ	Volume fraction
φ	Solid fraction
ϕ'	Mass fraction
$\tilde{\phi}$	Normalised value of volume fraction
γ	Flux limiter
κ	Linear schemes

$\varkappa$	Curvature
σ	Surface tension coefficient
η_{mix}	Mixing efficiency
Ω	Control volume for normal momentum equation

CHAPTER 1

INTRODUCTION

Multiphase flows and their interactions with rigid solids are ubiquitous in several engineering applications that include chemical processing, spray atomisation and marine structures to name a few. As the name suggests, these flows normally describe the interaction of two or more phases and may be classified as gas–liquid (eg. slug flows, evaporating droplets), gas–solid (eg. particle laden flows, fluidised beds), solid–liquid (eg. blood flows) and gas–liquid–solid (eg. wave impact on marine structures) flows. In many applications, one would however encounter scenarios which involve two or more components of the same phase. For instance, while water–steam flow has two phases but a single component, a typical micromixer would have two components which are both in liquid phase. While the latter class of flow need to be strictly referred to as multi–component flows or multi–fluid flows, they have been also referred to as multiphase flows in literature. The multitude of applications involving multiphase flows necessitates a better fundamental understanding of flow phenomena. The use of theoretical approaches are restricted to simple geometries while experimental studies are mostly difficult or expensive for many applications. Owing to the rapid development in the field of computational fluid dynamics (CFD) and with the increasing computational power, numerical approaches are the only viable means to gain deeper insights into complex flow phenomena associated with multiphase flows. Nevertheless, numerical simulations are also fraught with difficulties when applied to multiphase flows

with researchers often finding it difficult to reproduce the true physical behaviour of the complex fluid flows. The abrupt jumps in fluid properties across interfaces in immiscible flows, the need to account for interfacial tension and phase changes and simulating fluid–structure interactions are representative of the challenges faced by researchers in making accurate predictions in multiphase flows.

Developing a numerical framework for multiphase flows (with arbitrary number of phases/components) which also incorporates multiphysics is undoubtedly a huge challenge. Rather than attempting this ambitious and arduous task, the efforts in this thesis are channelised to address the challenges in a specific subset of multiphase flows. Specifically, the broad aim of the work embodied in this thesis is the development of a numerical framework for simulations of liquid–liquid and liquid–gas flows, which could be miscible or immiscible, and their interactions with arbitrarily moving rigid objects. Towards achieving this overall objective, we first carry out a comprehensive survey of previous numerical efforts. This survey, which is however not exhaustive, presents prominent and seminal efforts in numerical advances for multiphase flows and the state–of–art algorithms for numerical simulations. This would help identify potential difficulties in numerical simulations of such flows and thus paves way for defining a set of concrete objectives for the thesis.

1.1 Interfaces in immiscible flows

The interaction of immiscible fluids with distinct interface(s) can be seen in several engineering and environmental phenomena. Understanding these multi–component flows and their underlying physics necessitate the use of high–resolution numerical algorithms for their simulations. The last few decades have witnessed the development of the numerical techniques for incompressible immiscible flows and an authoritative overview may be found in [1]. Numerical techniques for the interfacial flows can generally be classified into two basic categories: moving and fixed mesh methods. In moving mesh method also known as Lagrangian method [2], the mesh conforms to and moves with the interface. As the interface moves the mesh needs to be updated or regener-

ated locally or globally depending upon the extent of the deformation. This requires interpolations which incur computational effort, introduces error and is not always robust. In fixed mesh methods also known as Eulerian method, the interface is tracked throughout the computational domain on a fixed mesh at every time step. Eulerian methods, which are also adopted in this thesis, can be divided into surface methods and volume methods (schematically presented in Figures 1.1(a) and 1.1(b)).

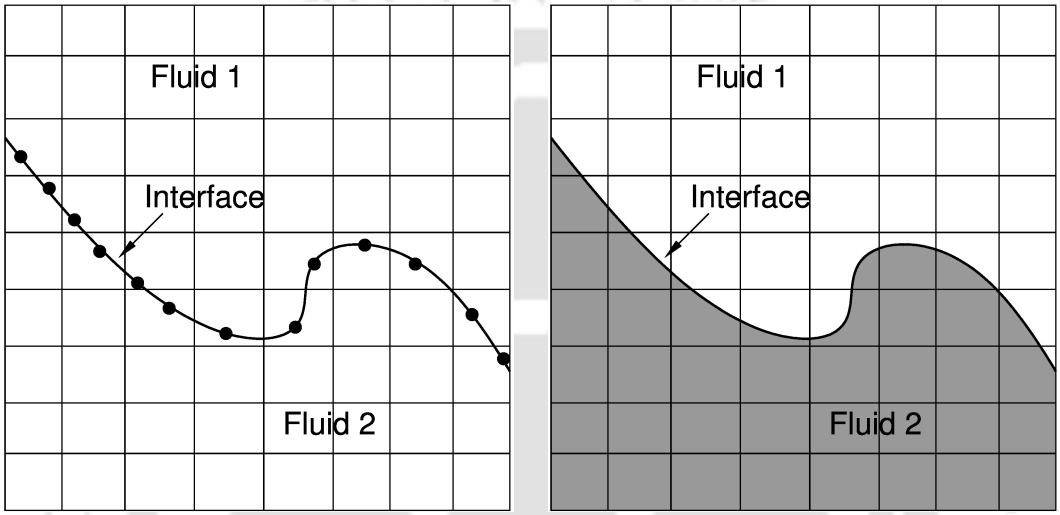

(a) Surface method (b) Volume method

Figure 1.1: Numerical techniques: (a) surface and (b) volume methods.

The surface methods, which include front tracking method [3] consist of connected marker particles that represent the interface as shown in Figure 1.1(a). A major drawback of this class of methods is that the particle connectivity is very sensitive and very difficult to maintain when subjected to high shear flows which involve significant topological changes. This has led to the emergence of volume methods with the level–set (LS) approach pioneered by Osher and Sethian [4] and volume–of–fluid (VOF) method [5] becoming very popular in the numerical community. The LS approach uses the concept of distance functions, with the interface being the zero–level set. On the other hand, VOF identifies the interface through the use of indicator functions known as volume fractions, which unlike distance functions are discontinuous. The interface in VOF methods may be reconstructed using simple line interface calculation [6] or piecewise linear interface calculations [7], with the latter having improved accuracy. In case

of moving interfaces, LS approaches necessitate re–initialisation of the distance function which impacts conservation. VOF methods are advantageous in such scenarios because they guarantee conservation, but the discontinuous nature of volume fractions hamper computations of interfacial tension. There have been attempts at developing variants such as the mass–conserving level set method (MCLS) [8] and also at hybridising these approaches such as the CLSVOF method [9] and the VOSET method [10], which have met with considerable success. There are other approaches as well, most notably the Lattice Boltzmann method (LBM) [11], which evolves from the kinetic theory and instead of the Navier–Stokes equation the density distribution function is solved to obtain the density and velocities. Owing to the simplicity and easily parallelisability its popularity is increasing in the multiphase community, however, special care is required when simulating the high density ratio flows. An interesting approach to solving immiscible flows that has also received significant attention is the diffuse interface technique [12], where the Navier–Stokes equations are solved in conjunction with the convective Cahn–Hilliard equation. The method needs special treatment for the mass conservation and to maintain the sharpness of the interface. Meshless approaches like smoothed particle hydrodynamics [13] have also been employed for the efficient simulation of multiphase/multi–fluid flows in recent studies. We do not delve further into discussing LS or VOF methods and their variants but it suffice to mention that each of these approaches have their own merits and de–merits.

From a perspective of devising a flow solver on unstructured meshes, we choose to adopt the VOF methodology for immiscible multiphase flows. Moreover, we propose to employ a reconstruction–free strategy, in order to avoid costs and difficulties associated with interface reconstruction on arbitrary polygonal meshes. This is possible if the convection schemes used in the VOF approach are of sufficient accuracy to capture the interface in a reasonably sharp manner. The need for advection schemes that preserve a sharp interface without compromising on solution accuracy and allows for easy implementation on arbitrary mesh topologies leads to the concepts of interface capturing schemes. Interface capturing schemes are constructed by combining high–resolution schemes with compressive schemes, using a suitable blending function, thereby obvi-

ating the need for any geometric reconstruction of the interfaces. Among the earliest works in this regard are the HRIC scheme of Muzafireja et al. [14] and the CICSAM scheme proposed by Ubbink and Issa [15]. A prominent drawback of both these methods is the deterioration of their performance with Courant number necessitating the use of smaller values of Courant number. Darwish and Moukalled [16] developed the STACS scheme to successfully overcome this drawback and subsequently proposed a family of transient interface capturing schemes referred to as TICS^m schemes [17], that combine bounded high–order transient scheme with a bounded high–order compressive scheme. Gopala and co–workers [18] proposed a scheme akin to the Inter–Gamma scheme of Jasak and Weller [19] and investigated its utility for free–surface flows. Walters et al. [20] proposed the Bounded Gradient Maximization scheme which involves a cell–based flux limiting with a suitable weighting factor while Xiao and co–workers [21] developed the THINC scheme based on the tangent function to compute volume fraction flux that ensures oscillation–free solution for fluid interface problems. A more recent work by Tsui et al. [22] discusses a novel scheme called FBICS (Flux Blending Interface Capture Scheme) which shows a superior performance compared to HRIC and CICSAM schemes on advection problems. Heyns and co–workers [23] added an artificial compressive term to the advection equation along with an improved blending function to develop the HiRAC scheme for interface capture on unstructured meshes.

1.2 Algorithmic challenges in multiphase flow simulations

Unlike incompressible approaches for single–phase flows, studies in multiphase flows are fraught with several challenges that include resolving the interface(s) sharply and simulating realistic and high density and viscosity contrasts successfully. In addition, the presence of interfacial forces due to surface tension and volumetric forces such as those due to gravity and electromagnetic effects need to be suitably accounted for in the numerical discretisation to ensure a stable solution procedure. The issues pertaining to interface sharpness have been dealt with in the previous section and algorithmic

difficulties arising from large density ratios and/or large interfacial forces are discussed in this section.

A very important issue that plagues multiphase flow simulations, particularly those involving interfacial tension, is the generation of spurious currents. Spurious currents in surface–tension dominated flows arise due to the errors in calculation of curvature and the discrete imbalance between surface tension and pressure forces [24]. Curvature errors can be minimised using improved approaches for calculating the interface curvature as detailed in [25–27] but can never be completely eliminated and represent a constant source of non–zero spurious currents. Abadie et al. [28] have shown that spurious currents are related to spurious vorticity production and have investigated the role of advection schemes in their evolution in conjunction with different curvature calculation approaches. It is also discussed in [29] that coupling between surface tension force, advection scheme and momentum transport is crucial. A recent study by Pan et al. [30] have shown that spurious currents in low Capillary number flows can be significantly reduced by employing a moving reference frame for simulations. However, one can totally eliminate errors due to force imbalances by carefully constructing a discretisation that enforces balance between competing forces, leading to a class of approaches referred to as “well–balanced" (or “balanced force") algorithms. The principle behind these class of methods is to use identical discretisation of the pressure gradient and surface tension term that appear in the momentum equation and with a reasonably accurate interface curvature calculation leads to acceptably low spurious currents. The earliest and significant contributions to well–balanced algorithms include the works of Renardy and Renardy [31] and Francois et al. [32]. While the former proposed the parabolic reconstruction of surface tension (PROST) for accurate and balanced implementation of interfacial tension, the latter discusses the need for and development of a balanced algorithm for multiphase flows on uniform structured meshes. Their algorithm however involved interpolations of centroidal quantities to faces and vice–versa and did not account for body forces. Montazeri and Ward [33] devised an improved pressure–velocity coupling based on Newton’s divided–differences for multiphase flows that is effective on non–uniform meshes and considers interfacial

and body forces. Denner and van Wachem [34] have proposed a pressure–velocity coupling for multiphase flows on unstructured meshes with modifications to the original momentum interpolation method for surface tension and gravity forces as well as grid non–orthogonality. Ghods and Herrmann [35] adopt a different approach to achieve the force balance by employing a least–squares based reconstruction for centroidal gradients, although despite its generic nature this approach has not been extensively investigated on unstructured grids for multiphase flows with large body forces. It must be remarked that while many researchers discuss and test balanced force algorithms for interfacial tension dominated flows, they are equally important in presence of other forces as well, such as body forces like gravity [36, 37].

A related pertinent challenge for simulating realistic flows that has received comparatively lesser attention is the ability of the solver to handle large density and viscosity ratios. This is critical because the density and viscosity ratios are $\mathrm{O}(100)$–$\mathrm{O}(1000)$ for most engineering applications. The key idea for a robust and stable numerical algorithm at high density ratios is to ensure a consistent transport of mass and momentum and the discrete level. This was first proposed by Rudman within a VOF framework on staggered grids [38] which is also adopted to level–set method by Desjardins and Moureau [39] and later extended to unstructured collocated meshes by Bussmann [40]. Raessi and Pitsch [41] proposed a density–based momentum flux correction in a level–set framework for tightly coupling mass and momentum, where the density fluxes computed from the level–set are used to define the momentum fluxes. More recently, Ghods and Herrmann [35] proposed a consistent rescaled mass–momentum transport (CRMT) algorithm in a level–set framework for multiphase flows. The fundamental philosophy was to convect mass and momentum using the same upwind scheme, then solve the level set equation using a higher–order accurate scheme and recompute the density using the level set information. This led to conservation errors in both mass and momentum, but in a consistent manner, which allowed a stable simulation of large density ratio flows.

1.3 Immersed boundary methods

Multiphase flows interacting with solid bodies are ubiquitous in several realms of engineering that include naval structures, chemical processing and gaseous combustion among others. The numerical modeling of such flows are challenging since different sets of governing equations must be satisfied in fluid and solid domains with their coupling at the interface pivotal for meaningful solutions. The simulations become even more difficult when the bodies are in motion, either imposed or induced by the flow around them. Traditional approaches to tackle such problems employ Arbitrary Lagrangian–Eulerian methods [42] which work with body conforming grids. However, these methods are computationally expensive owing to moving/deforming meshes and in cases of significant displacement/deformation necessitate continuous re-meshing. One could circumvent this problem, in a general scenario, using overset meshes [43] but these also incur significant cost, including those of identifying overlapping volumes and transferring solutions by interpolation. A simple and interesting alternative to ALE and overset approaches is to employ a fixed background mesh with the stationary/moving solid(s) “immersed" into it. This philosophy, pioneered in early seventies by the seminal work of Peskin [44] is now classified under the broad category of Immersed Boundary (IB) methods.

Different classifications of the IB methods are possible, but they are widely distinguished as continuous and discrete forcing based approaches [45]. Discrete forcing approaches can themselves be classified as being sharp interface IB and diffuse interface IB methods. The key difference between the sharp and diffuse interface approaches lie in the fact that the former retains the immersed geometry as a “sharp" interface while the latter would smear the interface over a few cell widths (typically two or three). The sharp interface IB methods are typically favoured over the entire range of Reynolds numbers, since the “spreading" effect in diffuse interface IB could become detrimental. For the same reasons, continuous forcing approaches are less desirable for turbulent simulations since they inherently do not preserve the sharpness of the interface. The notable efforts in the category of sharp interface IB include the ghost–cell finite difference approach in [46], the cut–cell finite volume approach in [47] and the

hybrid Cartesian IB (HCIB) of [48]. Interestingly, while all of these preserve a sharp interface, they enforce the boundary conditions within the IB framework in completely different ways. All three approaches however involve interpolations to determine the solution in the vicinity of the immersed boundary. The ghost–cell approach defines “ghost" cells inside the body while HCIB does not include cells inside the body. The cut–cell approach differs from the others in that it requires cell reshaping near the vicinity to ensure strict mass and momentum conservation, which could however become computationally expensive for three–dimensional geometries. Moreover, while the ghost–cell and cut–cell methods involve bilinear/trilinear interpolations, the HCIB employs an effectively uni–dimensional interpolation in any space dimensions [49]. Despite the similarities and differences in the sharp interface approaches, they have found widespread application in a range of problems including phonation [50], biofluid dynamics [51], dune morphodynamics [52] and not surprisingly, multiphase flows [53].

Diffuse interface IB, as the name suggests, comprises of all methods that necessarily smear the interface. It is therefore easy to see that all continuous forcing methods and a few discrete forcing methods fall into this class of IB methods. There also exist several variants of the classical IB approaches that can be encompassed within this category. A notable variant is the fictitious domain method [54], which employs the idea of Lagrangian multipliers with the rigidity constraint enforced for rigid solids [55]. This approach has been used by several researchers [56, 57] for fluid–structure interaction problems. Another interesting alternative is the Brinkman penalization or volume penalization [58–60], which considers the rigid solid as a porous medium of very low porosity and enforces the boundary condition through a masking function. Nakayama and Yamamoto [61] proposed a smooth profile method while Xiao [62] used a color function to distinguish and track solids in a domain consisting of fluids. Pan [63] proposed a diffuse interface methodology based on volume–of–solid approach, where the solid fraction is employed to construct a single momentum equation that is solved everywhere in the domain. This methodology, which is inspired by the volume–of–fluid approach in multiphase flows, has been applied to single–phase flows past stationary and moving bodies [63] and more recently investigated for flows with heat transfer

in [64].

It is pertinent to discuss the advantages and limitations of the methods in either category so that potential users can make a judicious choice of the IB approach for their applications. Sharp interface IB methods enforce the boundary conditions exactly since the sharpness of the geometry is preserved and the body tracked using Lagrangian markers. These methods can handle Dirichlet, Neumann and Robin BCs with equal ease, but lead to spurious oscillations in time histories of integrated quantities (such as lift and drag) for moving bodies. There have been limited but in–depth studies on the mechanisms behind these unphysical oscillations and means of suppressing/eliminating them. While these oscillations do reduce with increasing grid resolution and larger time steps, use of extremely fine meshes is not a computationally viable option and the choice of timestep is largely dictated by the flow physics and numerical stability. It is important to note that the spurious force oscillations is a critical issue for problems involving fluid–structure interactions and necessitates special treatments such as the use of hybrid stencils [65], field extension [66] or resorting a cut–cell conservative scheme [67]. Diffuse interface IB, while only “approximately" accounting for the boundary conditions result is significantly lower spurious force oscillations as compared to their sharp interface IB counterparts. Therefore, while the geometry is smeared as a consequence of the IB approach, this diffusion generates a “damping" effect to suppress the oscillations. Nevertheless, one could argue that the lack of sharp interface representation and non–exact imposition of the BCs in diffuse IB approaches could adversely affect the numerical solutions.

While the majority of the studies with IB approaches have been carried out for the single fluid–solid systems, there is a greater scope in investigating solid object(s) interacting with free–surface or multiphase flows due to its broad engineering applications. Combining IB methodologies with multiphase simulation approaches such as volume–of–fluid and level set can provide a powerful tool to analyse complex flow problems with multiple solids interacting with multiple fluids. Mirzaii and Fard [68] have used the fictitious domain method in conjunction with volume–of–fluid approach for mod-

elling free surface flows with moving rigid bodies. Calderer et al. [53] developed a curvilinear sharp interface immersed boundary method with a level–set framework for arbitrary complex geometries. Kocabiyik and Bozkaya [69] studied the effect of frequency ratio on oscillating cylinders below a free surface on fixed Cartesian grids with an improved volume–of–fluid approach. More recently, Pathak and Raessi [70] combined the fictitious domain method with the volume–of–fluid approach to develop an Eulerian–Eulerian framework for rigid body simulations in two–fluid flows. Their work which showed the applicability of the approach for multibody simulations employed the consistent mass and momentum transport algorithm to efficiently handle high density ratios between the fluids.

1.4 Miscible flow

In many multiphase flows, fluids have tendency to diffuse in other fluids at the molecular level. Miscibility of the fluids finds many engineering applications with enhanced oil recovery, drug delivery systems and lab–on–chip devices being a few examples. While numerical studies in miscible regimes were possibly motivated by their need in oil and gas industries, greater and growing emphasis on microchannels and their application to healthcare have led to a renewed interest in miscible flow simulations. Sahu et al. [71] have attempted to understand the role of viscosity contrasts on miscible displacement and studies of Ranganathan and Govindarajan [72] investigated the effects of Reynolds number and Schmidt number in three–layer Poiseuille flow. Fundamental studies on double diffusive systems were carried out by Mishra et al. [73] and numerical algorithms for miscible flows have found applications for realistic animations [74]. Studies on micromixers, with a view to understand mechanisms of mixing and means to improve their performance, have led to numerical investigations in passive [75] and active micromixers [76, 77]. Different configurations such as Y–mixer [78, 79] and T–mixer [80, 81] have also been studied and investigations have been conducted to assess the role of obstacles [82] and related unconventional configurations [83] on enhancement of mixing efficiency. The numerical studies in miscible flows and in particu-

lar, those involving micro–channel configurations, have been however carried out with standard commercial solvers and there have been no major efforts to uncover potential numerical challenges in miscible regimes and to address these issues in an extensive manner.

1.5 Objectives of the thesis

The comprehensive survey on the different aspects of multiphase flows and their simulations help to understand the myriad challenges that lie before anyone developing numerical methodologies for such applications. While there have been noteworthy contributions in different facets, there appears to be room for a generic solver that works with both structured and unstructured meshes, is robust for high density ratio flows with strong interfacial and body forces, can accurately resolve solid–fluid interactions at moderate computational effort that is simple to implement within legacy codes and easy to use. In light of our survey on liquid–liquid/gas–liquid multiphase flows and their simulations, we set the following objectives to be realised in the course of this thesis.

1. Analysis of existing convection schemes and devise novel schemes for interface capture in immiscible fluid flows. This would lead to an accurate scheme for convective transport of volume fractions, necessary for immiscible multiphase flows.

2. Devising a numerical framework based on the finite volume (FV) method and segregated approach for incompressible flows that can handle variable density flows with large, realistic density and viscosity ratios including surface tension and gravity dominated flows. This would result in a robust Navier–Stokes flow solver for multi–fluid applications.

3. Developing a diffuse interface immersed boundary (IB) method and an IB–FV solver to accurately compute fluid–structure interactions. This would enhance the versatility of the numerical framework to tackle problems involving multiple rigid solid(s) interacting with one or more fluids which are relevant in many practical applications.

4. Incorporating miscibility effects in the IB–FV framework to efficiently compute flows with mixing. This extension to the numerical framework would turn it into a promising tool for potentially interesting studies of current relevance such as those encountered in micromixers.

The numerical framework, emerging from the amalgamation of these objectives would constitute a valuable addition to simulation tools in multiphase flows. The development and validation of this framework through extensive numerical studies and its application to realistic and complex multiphase flows to demonstrate its accuracy, robustness and practical feasibility would be an apt description of this thesis, in a nutshell.

1.6 Outline of the thesis

The remainder of this thesis is organized as follows. Chapter 2 presents a generic framework for examination of existing interface capture schemes for VOF methods and development of novel alternatives. The chapter also contains thorough investigations of the performance of existing and new schemes for typical advection problems. The governing equations for the multiphase flow and their discretisation using the novel hybrid staggered/non–staggered framework are presented in Chapter 3 along with validation tests on the structured and unstructured meshes. Subsequently, in Chapter 4, a consistent and well balanced algorithm for multiphase flow simulations is discussed in great detail, underlining the importance of such a formulation for numerical simulations of gravity and surface tension dominated flows on arbitrary polygonal meshes. A novel diffuse interface immersed boundary method capable of handling multiple fluid–solid interactions is proposed in Chapter 5. This simple methodology is coupled with the multiphase flow solver to devise a powerful IB–FV solver which is applied to a spectrum of flow problems including particle sedimentation. Chapter 6 discusses the extension of the numerical framework comprising of the IB–FV solver to miscible flows. Finally, Chapter 7 gives a bird's eye view of the salient contributions of this thesis and suggests a few possible directions for future research.

CHAPTER 2

INTERFACE CAPTURING SCHEMES[†]

Immiscible multi–fluid flows have a distinct sharp interface that plays a significant role in the dynamics. The numerical techniques should therefore ensure that the representation of fluid–fluid interfaces remain as sharp as possible while also ensuring that the simulations do not become unstable. We use a volume–of–fluid approach for multiphase simulations which employs an advection equation for volume fractions. In this chapter, we discuss the convective schemes employed for volume fraction transport. In particular, such interface capturing schemes are analysed using design principles that allow a deconstruction of existing schemes and construction of new schemes. New schemes are proposed and their applicability on unstructured meshes are demonstrated through a series of canonical test cases.

2.1 Interface advection equation

While there are several approaches for simulating multi–fluid problems, we employ the volume–of–fluid (VOF) approach in the present studies. The VOF approach captures the interface by solving a transport equation for the scalar volume fraction (ϕ). The volume fraction, as the name suggests, represents the fraction of volume of a cell filled by a certain fluid. In case of immiscible binary fluid flows, cells which are completely

[†]The contents in this chapter have been published as J.K. Patel and G. Natarajan, "A generic framework for design of interface capturing schemes for multi-fluid flows", Computers & Fluids 106 (2015) [84].

filled with one fluid have ϕ values of either 0 or 1, while the volume fraction jumps across the fluid–fluid interface. In theory, the interface may be treated as a discontinuity which propagates passively with the fluid. The volume fraction is therefore convected as a passive scalar and therefore satisfies a hyperbolic equation,

$$\frac{D\phi}{Dt} = \frac{\partial \phi}{\partial t} + \mathbf{u} \cdot \nabla \phi = 0 \tag{2.1}$$

This equation is a mathematical representation of the fact that the material derivative of volume fraction $(\frac{D\phi}{Dt})$ is zero, if each fluid maintains its identity which means there is no phase change or mixing due to diffusion between the fluids. The immiscible incompressible fluid flows, which are largely studied in this thesis (except in Chapter 6) precisely satisfy this constraint. The divergence–free condition and $\sum_{k=1}^{2} \phi^k$ = 1 is then employed to recast the advection equation in its conservative form,

$$\frac{\partial \phi}{\partial t} + \nabla \cdot (\mathbf{u}\, \phi) = 0 \tag{2.2}$$

The advection equation for the volume fraction can be discretised on unstructured meshes using the finite volume approach, the semi–discrete form of Eq. (2.2) reads,

$$\Omega_c \frac{d\phi_c}{dt} + \sum_f \phi_f U_f \Delta s_f = 0 \tag{2.3}$$

where Ω_c is the volume (or area in two–dimensions) of the cell C, ϕ_c is the cell–averaged value of the volume fraction in that cell and ϕ_f denotes the value at the midpoint of faces constituting the cell. A fully discrete version of this equation can be realised by employing a suitable temporal discretisation. The second-order accurate backward differencing scheme is chosen to achieve time–accurate solutions for unsteady flows that are routinely encountered with immiscible binary fluids,

$$\Omega_c \frac{3\phi_c^{n+1} - 4\phi_c^n + \phi_c^{n-1}}{2\Delta t} + \sum_{f \in C} \phi_f^{n+1} U_f^n \Delta s_f = 0 \tag{2.4}$$

The face normal velocity U_f is obtained from the solution of the momentum equation and is the advecting velocity for the volume fractions. It must be however remarked that

for the tests carried out in Section 2.7, the velocity field is prescribed directly, rather than computed as the solution to the momentum equations. The advection equation is solved assuming a known value for the velocity field at a particular time-step and is known, in principle, from the solution to the momentum equations in the previous time-step. This approach of freezing the velocity field linearises the interface advection equation and the resulting system of linear algebraic equations (at a discrete level) can be written as,

$$\mathbb{A}\Phi + f(\Phi) = \mathbb{S} \tag{2.5}$$

where $\mathbb{A}$ is a geometric matrix, Φ is the vector of volume fraction (containing the volume fraction at all cells) and $\mathbb{S}$ is the known source vector. The function $f(\Phi)$ contains the gradients of volume fraction which are calculated using the Green–Gauss approach [85], that are lagged in order to construct the linear system. Introducing sub-iterations denoted by k we have,

$$\mathbb{A}\Phi^{k+1} = \mathbb{S} - f(\Phi^k) \tag{2.6}$$

At each sub–iteration, this represents a locally linear problem and is solved using a generalized minimal residual method (GMRES) that employs SAAMG preconditioning [86]. A suitable termination criterion for the sub-iterations is $|\Phi^{k+1} - \Phi^k| \leq 10^{-12}$. Typically, 6–8 sub–iterations are suffice to obtain the volume fractions at the new time level starting from the values at the old time level even on unstructured meshes. The value of the volume fraction obtained in each cell is limited to lie in the range [0,1]. We discuss the discretisation of the convective terms, which leads to the study of interface capturing schemes, in the following sections.

2.2 Non–linear schemes

The solution to the interface advection equation necessitates a robust convection scheme that ensures sharp resolution of the discontinuity. First order schemes are robust but they are overly diffusive and smear the interfaces. While higher–order (second–order or more) accurate schemes appear to be a natural solution, they suffer from loss in monotonicity as a consequence of the Godunov Barrier Theorem [87]. The devel-

opment of high–resolution schemes, which are at-least second–order accurate with solution boundedness, has been a subject of research over the years. These schemes overcome the barrier theorem by introducing non–linear “flux limiters" to achieve solution monotonicity. Thus, the face value ϕ_f of the volume fraction on the uni–dimensional grid shown in Figure 2.1(a) may be determined as,

$$\phi_f = \phi_U + \frac{\phi_U - \phi_{FU}}{2} \cdot \gamma(r)$$

where ϕ_U and ϕ_{FU} are values of volume fraction at cell centroid of the upwind and far upwind cell respectively. Here, $\gamma(r)$ represents the flux limiter (FL) which depends on the gradient ratio r, which may be defined as the ratio of centered to upwind gradient ($r = \frac{\phi_D - \phi_U}{\phi_U - \phi_{FU}}$, in structured mesh). It should be remarked that some authors have defined r as a reciprocal of that used in the present work.

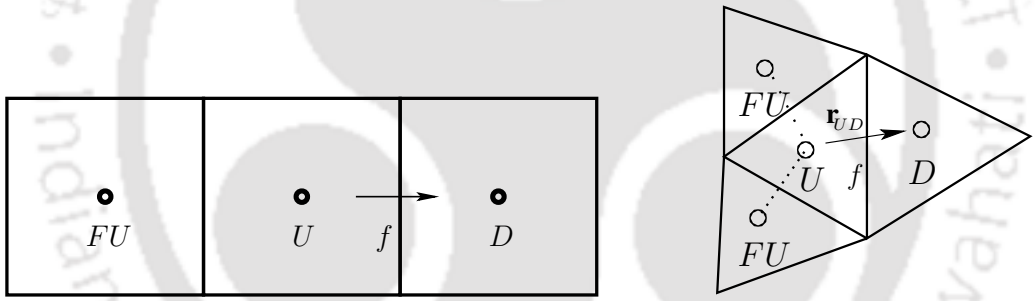

(a) Structured mesh (b) Unstructured mesh

Figure 2.1: Grid topology (a) structured and (b) unstructured mesh showing downwind (D), upwind (U) and far upwind (FU) cells.

2.3 The convection boundedness criterion on unstructured mesh

Schemes which are higher order accurate but remain stable must satisfy boundedness criterion. The principle of convection boundedness [88] requires that the scheme has convective stability and interpolative boundedness. The former necessitates an upwind bias while the latter ensures that the values computed face values are bounded between cell-averaged values in its neighbourhood. We employ the normalised vari-

able approach as also in [88]. This criterion is quite robust in practice and amenable for application on arbitrary polygonal meshes such as those encountered in this study. The normalised variable is defined as,

$$\tilde{\phi} = \frac{\phi - \phi_{FU}}{\phi_D - \phi_{FU}}$$

Recall that the gradient ratio r is defined by,

$$r = \frac{\phi_D - \phi_U}{\phi_U - \phi_{FU}}$$

It is therefore easy to show that the FL and NV approaches are related by,

$$\tilde{\phi}_U = \frac{1}{r+1} \tag{2.7}$$

$$\tilde{\phi}_f = \tilde{\phi}_U \left(1 + \frac{\gamma(r)}{2}\right) \tag{2.8}$$

The FL/NV transformations described above is particularly helpful to understand the construction of interface capturing schemes as discussed in the later sections. The CBC criterion is based on the idea that the normalised face values be bounded by the normalised values in cells sharing the face, which in turn implies that the boundedness region is a triangle enclosed by the lines $\tilde{\phi}_f$ = 1, $\tilde{\phi}_U$ = 0 and $\tilde{\phi}_f$ = $\tilde{\phi}_U$. Figure 2.2 shows TVD and CBC constraints in shaded region. It is clear that while all schemes that satisfy CBC are also TVD, the converse is not true. This reveals that CBC is a weaker stability criterion as compared to TVD, we believe that the CBC is capable to promise monotonic solutions as demonstrated in Section 2.7.

The CBC approach utilizes the value of far upwind node (FU) to determine the normalised value $\tilde{\phi}$. In arbitrarily unstructured meshes, determining a unique far upwind cell which represents the right choice is not a straightforward exercise. For example in Figure 2.1(b) there are two possible choices for far upwind cell. For generalization of the CBC approach on unstructured meshes, the value of ϕ_{FU} needs to be altered by the known values of ϕ_U and ϕ_D which is readily available on an unstructured mesh. This can be derived by using the gradient of volume fraction at the upwind cell U in the

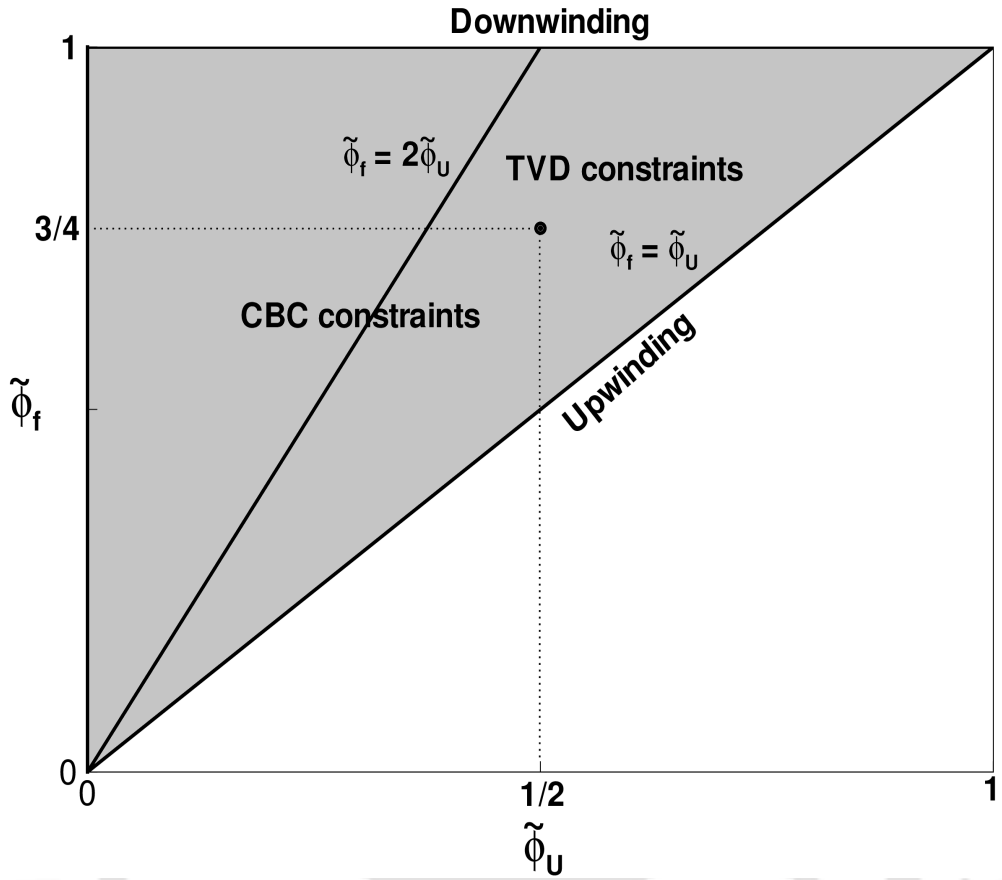

Figure 2.2: Convection boundedness criterion on normalised variable diagram.

unit normal direction to the upwind and downwind cell centers as,

$$(\nabla\phi_U)_{UD} = \nabla\phi_U \cdot \frac{\mathbf{r}_{UD}}{|\mathbf{r}_{UD}|} \tag{2.9}$$

This directional derivative can also be approximated with the central differencing scheme,

$$(\nabla\phi_U)_{UD} = \frac{\phi_D - \phi_{FU}}{2|\mathbf{r}_{UD}|} \tag{2.10}$$

Equating above equations, we get the co–relation for ϕ_{FU} as,

$$\phi_{FU} = \phi_D - 2\nabla\phi_U \cdot \mathbf{r}_{UD} \tag{2.11}$$

where $\mathbf{r}_{UD}$ is distance between node U and D normal to the face f.

2.4 Design principles for interface capturing schemes

Several flux limiters and high–resolution schemes have been proposed in literature and a comprehensive study of these schemes have been carried out by Waterson and Deconinck [89]. They showed that the best high–resolution schemes for advection problems could be encapsulated into a single class of generalized piecewise linear schemes, referred to as GPL-κ, whose flux limiter maybe defined as,

$$\gamma(r)^{HR} = max\Big[0, min\{(2+\alpha)r, \frac{1+\kappa}{2}r + \frac{1-\kappa}{2}, M\}\Big]$$

where κ defines the unbounded linear scheme (also called the base scheme) and M is the extent of downwinding. This flux limiter for the high–resolution scheme may now be converted to its equivalent NV form using Eq. (2.8) easily. While high–resolution schemes lead to reduced numerical diffusion as compared to their first–order counterparts, they still do not lead to sufficiently sharp resolution of discontinuities such as fluid–fluid interfaces that arise in multi–fluid flows. In order to maintain the interface sharp, it is therefore necessary to introduce further anti–diffusion in a controlled manner. The basic philosophy behind the design of robust schemes for interface capture is to *combine high–resolution (HR) and compressive (BD) schemes using a suitable blending function* [16]. There are however no guidelines provided on how these constituent schemes need to be chosen and their impact on the resulting interface capture scheme. In this section, we attempt to elaborate on this key philosophy, along the lines of the unified framework for higher–order schemes proposed in [89], to evolve a set of detailed guidelines for interface capturing schemes.

1. Blending function: The blending function must be a continuous function that allows for a smooth transition between the HR and BD schemes which is dictated by the orientation of the physical interface with the mesh. A sharp interface will result when the physical interface is aligned with the cell face if the fully compressive scheme is used, while a purely high–resolution scheme is desirable when the cell face is normal to the physical interface. Of the different blending functions proposed in previous works, the function $f(\theta_f) = \cos^4\theta_f$ is found to work well and is adopted in the present study. A computationally less expensive blend-

ing devoid of trigonometric functions as suggested in [23] may also be pursued. Therefore, the normalised face value for the volume fraction may be obtained as,

$$\tilde{\phi_f} = \tilde{\phi}_{f(BD)} f(\theta_f) + \tilde{\phi}_{f(HR)}(1 - f(\theta_f))$$

where

$$\theta_f = \arccos \| \frac{\nabla \phi_f \cdot \mathbf{r}_{UD}}{|\nabla \phi_f||\mathbf{r}_{UD}|} \|$$

2. Boundedness and linearity preservation: The interface capturing scheme must be bounded so that the values of volume fraction lie in [0,1]. This means that the constituent HR and BD schemes must respect the CBC to ensure no undershoots and overshoots. Furthermore, in order to ensure second–order accuracy in regions of smooth solutions (r=1), the HR scheme must be linearity preserving which implies that it must pass through (1/2, 3/4) in the NV diagram.

3. High–resolution scheme: The high–resolution scheme allows higher–order accuracy with monotonicity and is constructed using the following limiter, very similar to the GPL–κ limiter in [89], where ψ refers to a constant quantity that may depend on the Courant number.

$$\gamma(r)^{HR} = max\Big[0, min\Big\{(2+\alpha)r, \psi\Big(\frac{1+\kappa}{2}r + \frac{1-\kappa}{2}\Big), M\Big\}\Big]$$

4. Compressive scheme: The compressive scheme is responsible for sharpening the interface with its contribution being controlled by the blending function. There are no definitive strategies as yet to choose the BD scheme, and therefore we recommend that they be derived from the HR scheme itself by using the following limiter.

$$\gamma(r)^{BD} = max\Big[0, min\{(2+\alpha)r, M\}\Big]$$

It is quite easy to see that the limiter has been derived from that of GPL–κ scheme, by simply dropping the base unbounded linear scheme.

5. Influence and extent of downwinding: The concept of downwinding is related to anti–diffusion and determines the ability to sharpen the interface. The parameter

α denotes the proximity to full downwinding while the maximum bound M determines the extent of downwinding from the compressive (BD) scheme. We choose a value of α = 0 to ensure full downwinding, but its extent (value of M) will be determined based on numerical experiments. We remark that although different value of upper bounds for the HR and BD limiters maybe used, we recommend that the same value be used in both limiters.

We remark here that while the blending function and properties of boundedness and linearity preservation for convection schemes are well–established, the construction of the limiters for high–resolution and compressive schemes, with a view to unify interface capturing schemes, is a novel proposal of the present study. Along with the choice of a suitable downwind parameter, these set of guidelines provide a complete unified framework that can be used to analyse/develop new schemes for interface capture in multi–fluid flows.

2.5 Investigation of existing interface capturing schemes

The design guidelines discussed in the previous Section are now utilized to examine and de–construct existing schemes as well as to propose two new schemes for interfacial flows. In particular, we discuss the construction of the limiters for the HR and BD schemes and suggest possible reasons for success or failure of various schemes. We employ the FL/NV transformations for this analysis and the FL and NV form of the schemes discussed below are summarized in Table 2.1.

2.5.1 Compressive Interface Capturing Scheme for Arbitrary Meshes, CICSAM

The CICSAM scheme was proposed by Ubbink and Issa [15] for multi-fluid flows. The scheme switches (with a different blending function than discussed earlier) between the HYPER–C scheme and ULTIMATE QUICKEST scheme, the latter being the HR scheme and the former the BD scheme, and both satisfying CBC. The HR scheme preserves linearity as well, and employs for itself a blend of upwind and QUICK schemes

with a Courant number dependence, defined by ψ = (1-Co) where Co is the local Courant number. A simple analysis also shows that the unbounded linear scheme corresponds to the QUICK scheme so that κ = $\frac{1}{2}$. The HYPER–C is a very compressive scheme with the downwind extent parameter depending on Courant number. A close examination of the compressive limiter by using FL/NV transformations shows that M = 2($\frac{1}{Co} - 1$) and α = 0. The limiter for the BD scheme is clearly derived from that of the HR scheme. An important distinction of the CICSAM schemes from new schemes proposed in this work is the explicit dependence of the limiters on the Courant number.

Clearly, for lower values of Courant number, a greater extent of downwinding is achieved along with a higher–order accurate convection scheme which confirms the superior performance of the scheme for $Co < 0.3$. For higher values of Courant number, the HR scheme becomes heavily biased to first–order upwind and the downwind influence diminishes considerably, which explains the loss of resolution and diffusion of the interfaces for higher Courant numbers. The performance of CICSAM may also be influenced, albeit to a lesser extent, by the choice of the blending function. The M–CICSAM scheme proposed in [90] is a definite improvement over the CICSAM scheme not just because it chooses a different HR scheme but also because it avoids Courant number dependence in the limiters employed for the compressive and high–resolution schemes. We refrain from the analysis of the M–CICSAM scheme, but remark that it shares nearly all characteristics of the FBICS scheme [22] which is discussed in the following, except for a different choice of the downwind influence parameter M and the blending function.

2.5.2 High Resolution Interface Capturing scheme, HRIC

The HRIC scheme [14] attempts to avoid explicit Courant number dependence that plagues CICSAM scheme and simplifies the calculation of face values for the variables, which in the present study is the volume fraction. The overall scheme is characterized by a three–step method to enforce a switching in Courant–number domain. Unfortunately, this brings in dependence of the Courant number into the HRIC scheme, which in fact it sought to eliminate. Moreover, the use of FL/NV transformations to each of

the three steps indicates that the HR scheme for very low (less than 0.3) and very high (greater than 0.7) Courant numbers is merely the first–order upwind scheme, with a good amount of compression in the former case which deteriorates to zero in the latter case. It therefore follows that ψ = 0 and the value of M = 2 (for $Co <$ 0.3) and M = 0 (for $Co >$ 0.7). For intermediate values of Courant number 0.3$< Co <$0.7, the HR scheme remains first–order upwind with ψ = 0, while the compressive scheme involves downwinding whose extent and influence are dependent on Courant number, reducing as Courant number increases. Specifically, a closer examination using FL/NV formulations show that α = 2K-2 and M = 2K where $K = \frac{0.7-Co}{0.7-0.3}$ is a Courant–number dependent constant. For all three Courant number regimes, the lack of any genuinely high–order accurate scheme in the blending makes HRIC a more diffusive scheme than CICSAM, and the compressive scheme only serves to selectively diminish this over–diffusion. We remark that the scheme is fully first–order upwind for high Courant numbers and remains robust at the expense of severe loss of resolution of interface sharpness. The fact that the HR scheme for HRIC is infact a low–resolution scheme explains the superior performance of CICSAM in comparison to HRIC in the studies in [91]. The HRIC scheme in its original form would be advisable only on very fine meshes with a severe Courant number restriction if satisfactory results are to be obtained.

2.5.3 Inter–Gamma scheme

The Inter–Gamma [19] was proposed to specifically target sharp resolution of discontinuities by introducing significant downwinding within a single advection scheme. Consequently, it involves no blend of HR and BD schemes but rather behaves merely as a BD scheme. There is no control on amount and manner of downwinding that must be applied in response to the orientation of the interface and the NV formulation of the scheme (Table 2.1) shows a quadratic segment which violates linearity preservation. The poor performance of the Inter–Gamma scheme for simple advection problems in [18] may be attributed to these characteristics of the scheme, although it is shown to work well for some practical flow problems with a severe Courant number restriction. Any scheme that violates the requirements outlined in Section 2.4 does not qualify as a “good" interface capturing scheme and the excellent performance of the Inter–Gamma

scheme for some practical problems as rather fortuitous.

2.5.4 Flux Blending Interface Capturing Scheme, FBICS

Tsui and co–workers [22] have developed two novel schemes for interface captures based on flux blending, FBICS–A and FBICS–B and compared their performance with HRIC and CICSAM schemes for typical advection problems. The FBICS–A scheme (hereafter referred to simply as FBICS) was found to be most efficient in capturing the discontinuities with low errors that were not dependent on the Courant number. FBICS is built to satisfy CBC, and uses the Fromm scheme as the base linear scheme. The study in [22] however does not discuss the construction of the limiters employed for the HR and BD schemes.

It is easy to see that the HR scheme is linearity preserving and the FL/NV transformations show that the choice of κ = 0 and M = 4 would result in the flux limiter for the HR scheme. The limiter for BD scheme may then be easily derived by dropping the unbounded Fromm scheme. The specific choice of the value of M remains unexplained in the original work and we shall attempt an explanation of this choice in the subsequent sections. It may be remarked that if M = 2, the FBICS scheme would reduce to the M–CICSAM scheme, with the only difference then being the choice of blending function whose effect is less significant in the overall performance. While the schemes have been independently developed, the present analysis show that the two schemes are only minor variants of each other.

2.6 Development of new schemes for interface capture

We propose the development of robust and accurate interface capturing schemes devoid of complex geometric reconstruction based on the design principles in Section 2.4. Two different schemes are constructed, viz. the M-Gamma scheme and CUIBS, and the former may be considered as an improved version of the Inter–Gamma scheme presented earlier. These schemes are designed to work with arbitrary polygonal meshes and as demonstrated in later sections show a performance that is nearly

independent of the Courant number unlike HRIC and CICSAM schemes. The FL/NV description of the limiters used to construct the HR and BD schemes are summarized in Table 2.1.

2.6.1 Modified Gamma scheme (M-Gamma)

The failure of the Inter–Gamma scheme motivates the construction of a new interface capturing scheme within the class of blended GPL–κ schemes that respects the design guidelines. We begin by considering the original Gamma scheme [92], which is a HR scheme that in itself combines central differencing scheme with an ad-hoc quadratic variation, controlled by a parameter β. The quadratic variation which is applied in the range $\tilde{\phi}_U \in [0, \beta]$ is defined by,

$$\tilde{\phi}_f = -\frac{\tilde{\phi}_U^2}{2\beta} + (1 + \frac{1}{2\beta})\tilde{\phi}_U$$

Comparing this variation with the quadratic variation adopted in Inter–Gamma scheme (Table 2.1), it follows that β = 1/4. We construct the HR scheme for M-Gamma simply by considering a linear variation in the range $\tilde{\phi}_U \in [0, 1/4]$ followed by the central differencing scheme (which is the base linear scheme). The HR scheme may be considered as a special case of GPL-κ schemes where κ = 1 and M = 3 with the BD scheme obtained by discarding the base scheme, resulting in the limiters shown in Table 2.1. The value of M is fixed here by the choice of β as can be seen from a closer consideration of the NV diagram shown in Figure 2.3 which also indicates that the HR scheme is linearity preserving. A different choice for M in both HR and BD limiters may be employed (such as that of FBICS where M = 4) or the values of M in the limiters can be differentially selected but these ideas are not explored in this study.

2.6.2 Cubic upwind interpolation based blending Scheme (CUIBS)

The CUIBS scheme is inspired by the work of Waterson and Deconinck [89] which shows that the best convective schemes belong to the GPL–κ class of schemes. These schemes are MUSCL, SMART and Koren's limited CUI scheme and perform excellently

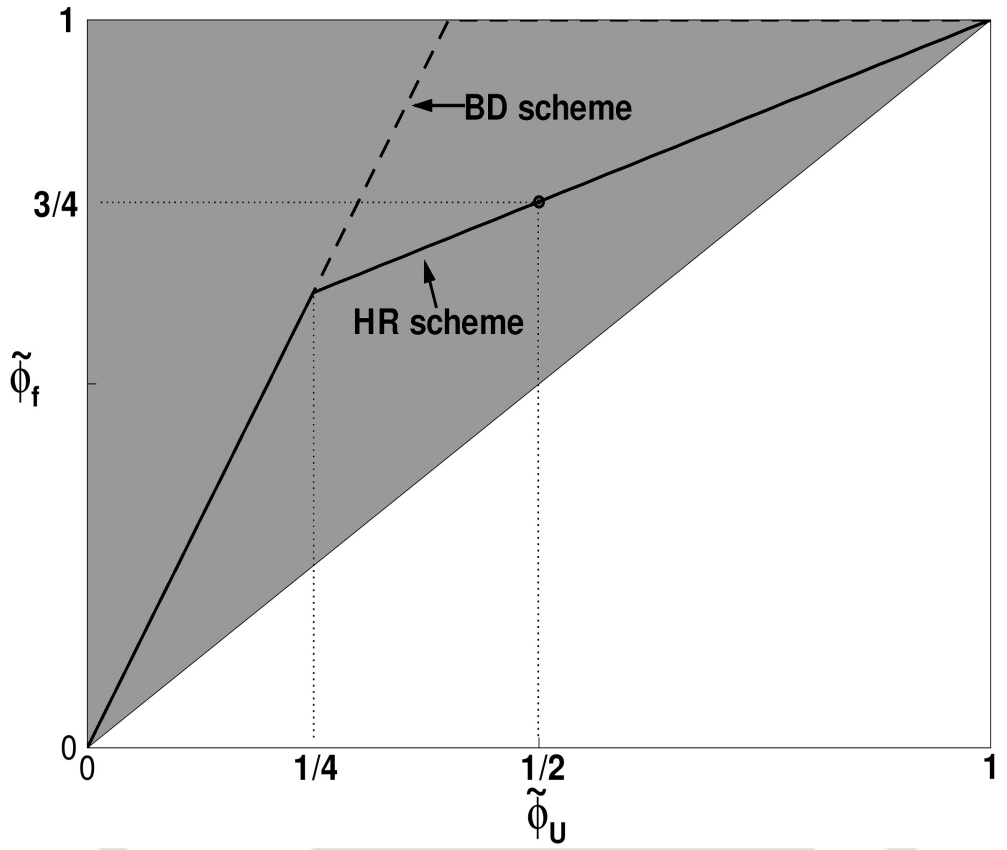

Figure 2.3: Normalised variable diagram for M-Gamma scheme.

on smooth and discontinuous advection problems. While the first two schemes have been employed as HR schemes for interface capture to varying extent in the past (in FBICS [22] and STACS [16] for instance), there have been no attempts to date to use the limited CUI scheme as a building block for interface capturing schemes. We merely use the Koren limited CUI scheme as the HR scheme, which corresponds to a HR limiter with κ = 1/3 and M = 4. We remark however that the M value is different from the original scheme and the choice of this value is justified through numerical experiments in the following section. The BD limiter for the compressive scheme may be obtained by dropping the base scheme and the resulting limiter is same as that used for FBICS scheme. The HR scheme is linearity preserving and the normalised variable diagram for this scheme is depicted in Figure 2.4. It is expected that the superior characteristics of this unique third–order upwind scheme in the HR limiter will result in CUIBS having improved interface capture performance in comparison to its counterparts. We emphasis that this work is the first instance of the CUI scheme being employed for sharp resolution of interfaces.

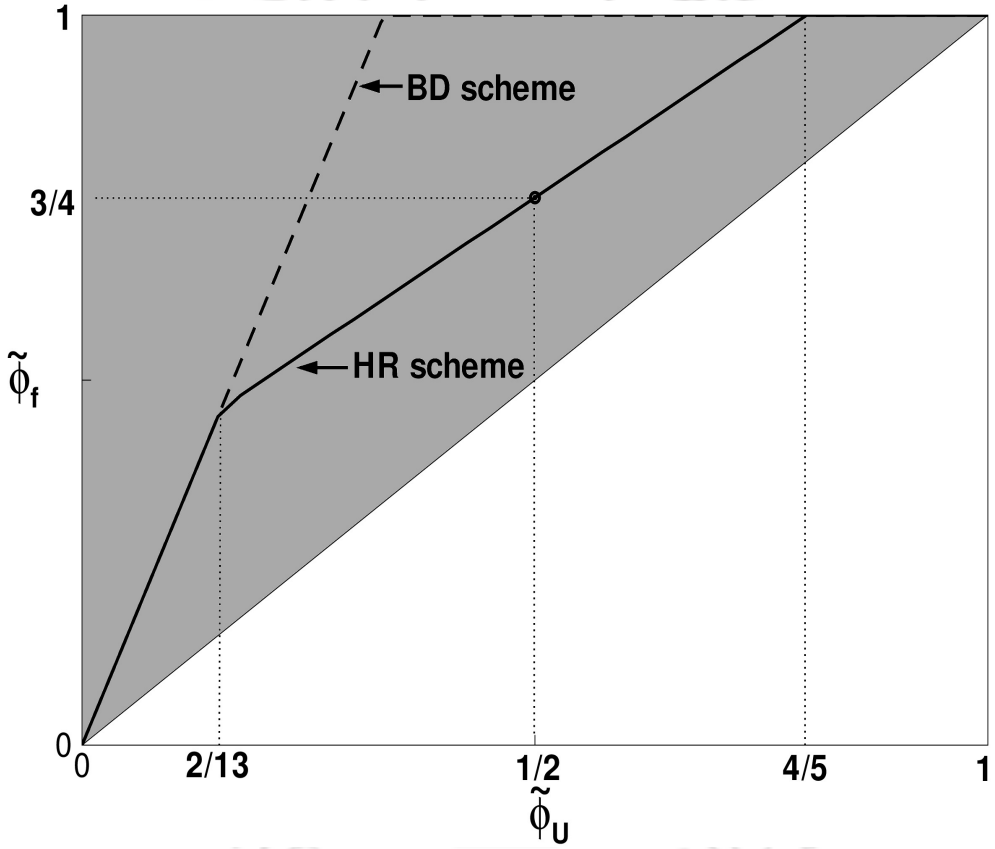

Figure 2.4: Normalised variable diagram for CUIBS scheme.

Table 2.1: Schemes in flux limiters and normalised form.

Schemes	Flux limiters	Values of M, ψ and κ	Normalised form
CICSAM [15]	$\gamma(r)^{HR} = max[0, min\{2r, \frac{3r}{4} + \frac{1}{4}, 2(Co^{-1} - 1)\}]$ $\gamma(r)^{BD} = max[0, min\{2r, 2(Co^{-1} - 1)\}]$	$M = 2(Co^{-1} - 1)$ $\psi = (1 - Co)$ $\kappa = 1/2$	$\tilde{\phi_f}^{HR} = \begin{cases} min\{\frac{8\ Co\ \tilde{\phi}_U + (1-Co)(6\tilde{\phi}_U+3)}{8}, \tilde{\phi}_f^{BD}\} & 0 \le \tilde{\phi}_U \le 1 \\ \tilde{\phi}_U & 0 \ge \tilde{\phi}_U \ge 1 \end{cases}$ $\tilde{\phi_f}^{BD} = \begin{cases} min\{1, \frac{\tilde{\phi}_U}{Co}\} & 0 < \tilde{\phi}_U \le 1 \\ \tilde{\phi}_U & 0 \ge \tilde{\phi}_U \ge 1 \end{cases}$
HRIC [14]	$\gamma(r)^{HR} = 0$ $\gamma(r)^{BD} = min\{2\frac{0.7-Co}{0.7-0.3}r, 2\frac{0.7-Co}{0.7-0.3}\}$	$M = 2\frac{\overbrace{0.7 - Co}^{K}}{0.7 - 0.3}$ $\psi = 0$ $\kappa = --$	$\tilde{\phi_f}^{HR} = \{\ \tilde{\phi}_U$ $\tilde{\phi_f}^{BD} = \begin{cases} 2\tilde{\phi}_U & 0 < \tilde{\phi}_U \le \frac{1}{2} \text{ and } Co < 0.3 \\ 1 & \frac{1}{2} \le \tilde{\phi}_U \le 1 \text{ and } Co < 0.3 \\ (1+K)\tilde{\phi}_U & 0 < \tilde{\phi}_U \le \frac{1}{2} \text{ and } 0.3 < Co < 0.7 \\ K + (1-K)\tilde{\phi}_U & \frac{1}{2} \le \tilde{\phi}_U \le 1 \text{ and } 0.3 < Co < 0.7 \\ \tilde{\phi}_U & 0 \ge \tilde{\phi}_U \ge 1 \text{ and } Co < 0.7 \\ \tilde{\phi}_U & \text{for all values of } \tilde{\phi}_U \text{ and } Co > 0.7 \end{cases}$
Inter–Gamma [19]	–	–	$\tilde{\phi_f}^{BD} = \begin{cases} -2\tilde{\phi}_U^2 + 3\tilde{\phi}_U & 0 < \tilde{\phi}_U \le \frac{1}{2} \\ 1 & \frac{1}{2} < \tilde{\phi}_U \le 1 \\ \tilde{\phi}_U & 0 \ge \tilde{\phi}_U \ge 1 \end{cases}$
FBICS [22]	$\gamma(r)^{HR} = max[0, min\{2r, \frac{r}{2} + \frac{1}{2}, 4\}]$ $\gamma(r)^{BD} = max[0, min\{2r, 4\}]$	$M = 4$ $\psi = 1$ $\kappa = 0$	$\tilde{\phi_f}^{HR} = \begin{cases} 3\tilde{\phi}_U & 0 < \tilde{\phi}_U \le \frac{1}{8} \\ \tilde{\phi}_U + \frac{1}{4} & \frac{1}{8} < \tilde{\phi}_U \le \frac{3}{4} \\ 1 & \frac{3}{4} < \tilde{\phi}_U \le 1 \\ \tilde{\phi}_U & 0 \ge \tilde{\phi}_U \ge 1 \end{cases}$ $\tilde{\phi_f}^{BD} = \begin{cases} 3\tilde{\phi}_U & 0 < \tilde{\phi}_U \le 1/3 \\ 1 & 1/3 < \tilde{\phi}_U \le 1 \\ \tilde{\phi}_U & 0 \ge \tilde{\phi}_U \ge 1 \end{cases}$
M–Gamma	$\gamma(r)^{HR} = max\left[0, min\left\{r, 3\right\}\right]$ $\gamma(r)^{BD} = max\left[0, min\left\{2r, 3\right\}\right]$	$M = 3$ $\psi = 1$ $\kappa = 1$	$\tilde{\phi_f}^{HR} = \begin{cases} \frac{5}{2}\tilde{\phi}_U & 0 < \tilde{\phi}_U \le \frac{1}{4} \\ \frac{1}{2}\tilde{\phi}_U + \frac{1}{2} & \frac{1}{4} < \tilde{\phi}_U \le 1 \\ \tilde{\phi}_U & 0 \ge \tilde{\phi}_U \ge 1 \end{cases}$ $\tilde{\phi_f}^{BD} = \begin{cases} \frac{5}{2}\tilde{\phi}_U & 0 < \tilde{\phi}_U \le \frac{2}{5} \\ 1 & \frac{2}{5} < \tilde{\phi}_U \le 1 \\ \tilde{\phi}_U & 0 \ge \tilde{\phi}_U \ge 1 \end{cases}$
CUIBS	$\gamma(r)^{HR} = max[0, min\{2r, \frac{2}{3}r + \frac{1}{3}, 4\}]$ $\gamma(r)^{BD} = max\left[0, min\left\{2r, 4\right\}\right]$	$M = 4$ $\psi = 1$ $\kappa = 1/3$	$\tilde{\phi_f}^{HR} = \begin{cases} 3\tilde{\phi}_U & 0 < \tilde{\phi}_U \le \frac{2}{13} \\ \frac{5}{6}\tilde{\phi}_U + \frac{1}{3} & \frac{2}{13} < \tilde{\phi}_U \le \frac{4}{5} \\ 1 & \frac{4}{5} < \tilde{\phi}_U \le 1 \\ \tilde{\phi}_U & 0 \ge \tilde{\phi}_U \ge 1 \end{cases}$ $\tilde{\phi_f}^{BD} = \begin{cases} 3\tilde{\phi}_U & 0 < \tilde{\phi}_U \le \frac{1}{3} \\ 1 & \frac{1}{3} < \tilde{\phi}_U \le 1 \\ \tilde{\phi}_U & 0 \ge \tilde{\phi}_U \ge 1 \end{cases}$

2.7 Investigation on advection tests

The new schemes proposed in this study are tested for the ability to capture interfaces and preserve their sharpness using three advection test cases. Tests are simulated by computing decoupled advection equation with prescribed velocity field. The M-Gamma and CUIBS schemes are also compared with the FBICS scheme, to understand the relative merits of different schemes. A computational domain of 4×4 is chosen The schemes are compared qualitatively in terms of contour plots of the volume fraction for two extreme values of the cell Courant (Co) number and quantitatively in terms of the global solution error since the exact solutions are known. The Courant number and error are defined as,

$$Co = \frac{\sum_{f \in C} max(\mathbf{u} \cdot \Delta \mathbf{s}_f, 0)\Delta t}{\Omega_c}$$

$$E = \frac{\sum_{c=1}^{nc} \|\phi_c^{\mathsf{N}}\Omega_c - \phi_c^{\mathsf{E}}\Omega_c\|}{\sum_{c=1}^{nc} \phi_c^{0}\Omega_c}$$

where nc is the number of volumes in the domain, c denotes the cell, f denotes the faces of the cell, $\Delta \mathbf{s}_f$ represents the vectorial area and superscripts N, E and 0 represent the numerical and exact solutions at the final time level and the exact solution at the initial time level respectively.

2.7.1 Test 1: Advection of hollow square in oblique flow

To validate the accuracy of interface capturing schemes, we first consider a hollow square of outer width equal to 0.8 and inner width of 0.4 centered at (0.8, 0.8) that is advected in an uniform oblique velocity field of (u, v) = (2, 1). The computational domain is discretised using both 100×100 structured mesh as well an unstructured mesh of 22584 triangular elements. The simulations are carried out till t = 1 so that it arrives at its final position of (1.8, 2.8).

The contour plots of volume fraction on the structured and unstructured meshes employing FBICS, M-Gamma and CUIBS schemes are shown in Table 2.2. The sim-

Table 2.2: ϕ-contours for Test 1. Contour levels are 0.05:0.05:0.95.

Schemes	Structured mesh		Unstructured mesh	
	Co = 0.15	Co = 0.8	Co = 0.15	Co = 0.8
FBICS [22]	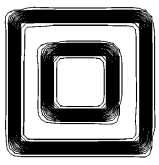	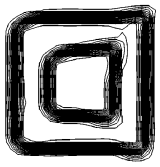	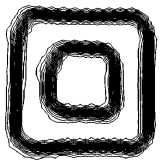	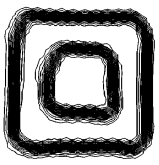
M-Gamma	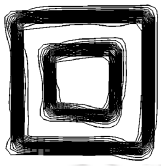	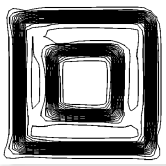	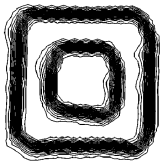	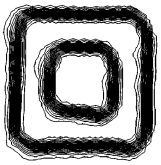
CUIBS	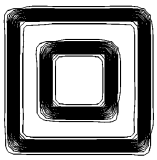	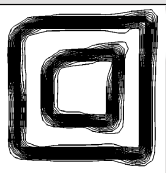	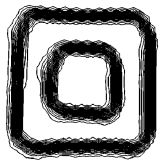	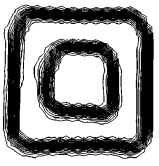

ulation has been performed for both low and high Courant numbers (Co) of 0.15 and 0.8 respectively on both the mesh topologies, which are intended to check the Courant number dependency of shape errors. The performance of FBICS is in line with the work of Tsui et al. [22] wherein similar results have been reported. The M-Gamma scheme leads to slightly diffusive results when compared to FBICS and CUIBS on the structured mesh. The results from CUIBS scheme are comparable, qualitatively, with those obtained using FBICS for the mesh topologies and Courant numbers studied herein. A quantitative analysis of the shape error with Courant number is shown in Figures 2.5(a) and 2.5(b) which confirms that the M-Gamma scheme leads to higher shape errors than both the CUIBS and FBICS schemes, both of which behave in a very similar manner for this case, and that the errors are larger on the unstructured meshes when compared with their structured counterparts.

2.7.2 Test 2: Advection of a circle in shear flow

The test consists of a circle of radius 0.2π units centered at (1.5, 0.8) and subjected to a velocity field (u, v) = (sin(x)cos(y), -cos(x)sin(y)). The circle is strained for N time units after which the velocity is reversed and the circle returns to its original configuration

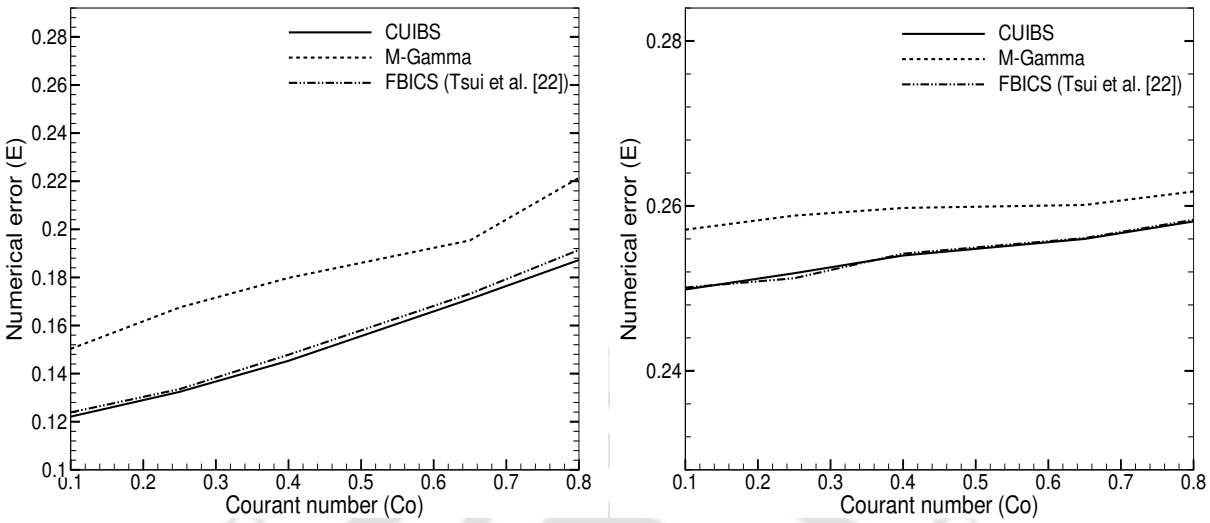

(a) Structured mesh (b) Unstructured mesh

Figure 2.5: Variation of numerical error with Courant number for Test 1 on (a) structured mesh (b) unstructured mesh.

after further N time units. Computations are done on 100×100 structured mesh and a triangular mesh consisting of 22584 cells. The contours of the volume fraction for N = 8 for the three schemes on both meshes for Co = 0.8 are shown in Table 2.3. The error variation with Courant number for these grids are depicted in Figures 2.6(a) and 2.6(b). While all three schemes show Courant number independent errors, the M-Gamma scheme is found to be inferior to the FBICS and CUIBS schemes. However, M–Gamma is no longer restricted by a Courant number restriction unlike the Inter–Gamma scheme. While the FBICS and CUIBS schemes are comparable on structured meshes, the latter outperforms on unstructured grid in terms of the error.

2.7.3 Test 3: Zalesak solid body rotation

This test consists of the advection of a slotted disk in a rotational flow field. The disk has unit diameter and is centered at (2, 2.75) and is cut by a slot of 0.12 unit width. The disk is rotated around center of rotation (x_0, y_0)=(2, 2) with a constant angular velocity of 0.5. The velocity field is therefore (u, v) = (-$\omega(y - y_0), \omega(x - x_0)$). Simulations are carried out for one rotation using structured mesh of 200×200 and unstructured mesh of 40532 triangles. Table 2.4 shows the contours of volume fraction for different Courant numbers and the error variation on both grids as a function of Courant number

Table 2.3: ϕ-contours for Test 2 at Co = 0.8. Contour levels are 0.05:0.05:0.95.

Schemes	Structured mesh		Unstructured mesh	
	Forward	Backward	Forward	Backward
FBICS [22]			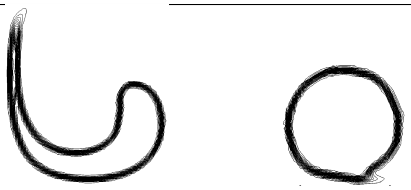	
M-Gamma			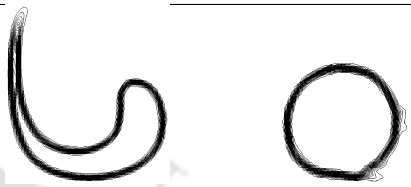	
CUIBS				

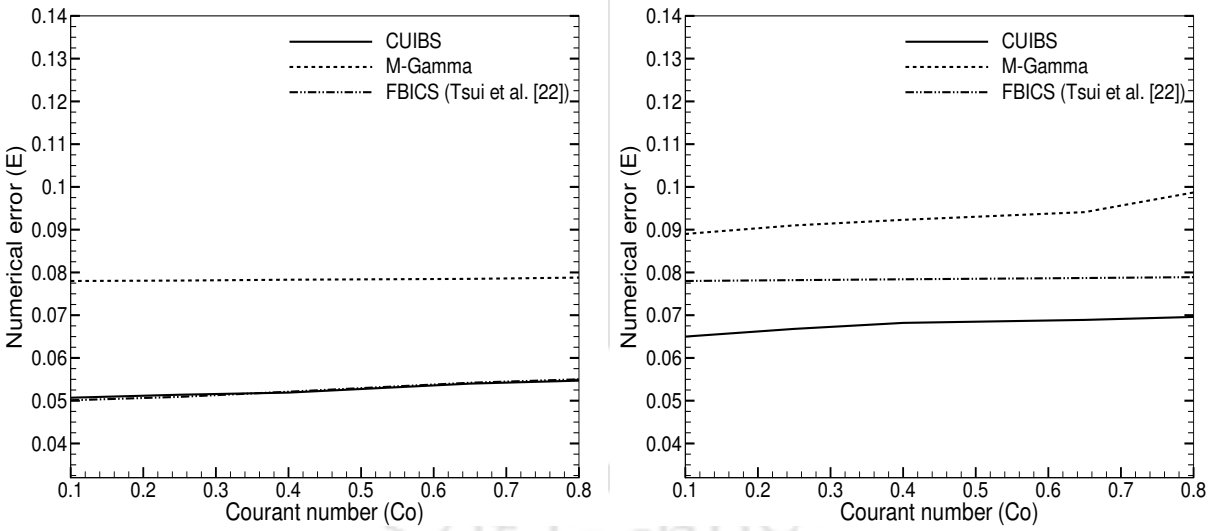

(a) Structured mesh (b) Unstructured mesh

Figure 2.6: Variation of numerical error with Courant number for Test 2 on (a) structured mesh (b) unstructured mesh.

are shown in Figures 2.7(a) and 2.7(b). While this case gives further evidence of performance not depending on Courant number, the M-Gamma and CUIBS schemes are found to have lower errors compared to the FBICS scheme on unstructured meshes. On structured meshes, all three schemes show very similar behaviour. The contour plots indicate that the FBICS scheme distorts the profiles on unstructured meshes as

compared to the new schemes proposed here. This test case was not investigated in [22] and this observation is surprising. The CUIBS scheme is atleast as competitive as FBICS, and the improved performance of the former for some cases maybe attributed to the third–order accurate base scheme and the marginally lesser extent of downwinding introduced in the constituent HR scheme. Nevertheless, the behaviour of M-Gamma scheme is somewhat perplexing, and it is conjectured that the downwinding extent plays a major role. In particular, the upper bound M may have an optimal value that depends on the test problem and/or grid employed which decides the superior interface capturing scheme for a particular problem and grid topology. We precisely investigate the role of the maximum bound, albeit in a limited sense, in the following numerical experiment.

Table 2.4: ϕ-contours for Test 3. Contour levels are 0.05:0.05:0.95.

Schemes	Structured mesh		Unstructured mesh	
	Co = 0.15	Co = 0.8	Co = 0.15	Co = 0.8
FBICS [22]				
M-Gamma				
CUIBS				

2.7.4 Effect of extent of downwinding

We study the effect of the maximum bound M in the flux limiters of the schemes to understand its role in interface capture and determine an optimal value, if possible. We consider the advection of a hollow square translated obliquely by a constant velocity field (u, v) = (2, 1) on unstructured grids using the CUIBS scheme. The error variation with Courant number plotted in Figure 2.8 for different values of M show that the errors

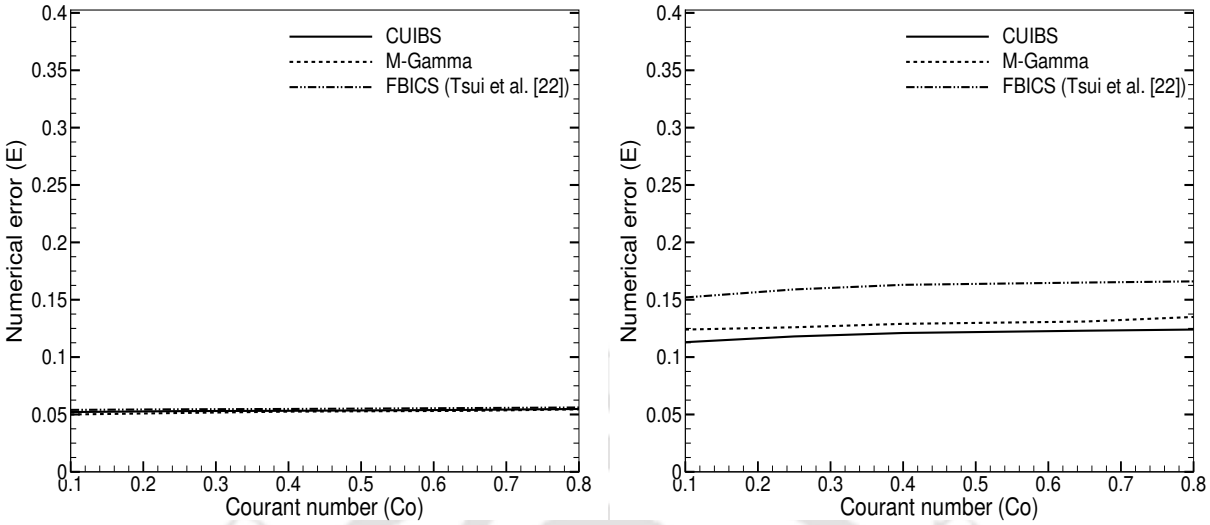

(a) Structured mesh (b) Unstructured mesh

Figure 2.7: Variation of numerical error with Courant number for Test 3 on (a) structured mesh (b) unstructured mesh.

are minimal for $M \in [2, 4]$. This suggests the existence of a possibly “optimal" range for M which may be understood from the fact that smaller M results in lesser downwinding from the compressive scheme and hence more diffusion while a higher value of M may result in over–compression. This study justifies $M = 4$ as a good choice in terms of error and explains its choice in CUIBS and FBICS schemes. We remark, as also discussed earlier, that a different value of M could become optimal for the schemes in certain interface problems and grid topologies and therefore the value of $M = 4$ is by no means a universal choice.

2.7.5 Volume conservation

An important and often overlooked issue in interface capturing schemes and VOF approaches, particularly on unstructured meshes, is the conservation of volume of the fluids. Despite solving the conservation laws in a conservative framework, the clipping of the volume fraction (to ensure it is bounded between 0 and 1 in each cell) may introduce errors that can violate *discrete* conservation. The fluids in the domain are immiscible and the incompressibility conditions means that volume of each of the fluids in a closed domain must be conserved over time. We therefore quantify the volume errors (or shape errors) as,

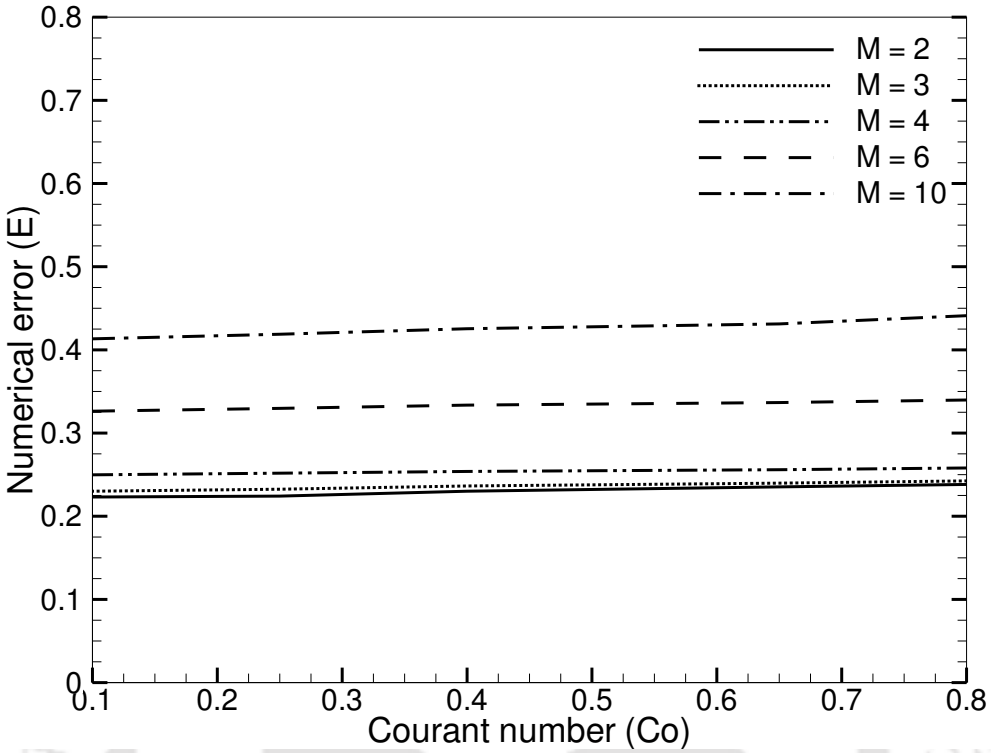

Figure 2.8: Error variation with Courant number for different values of the upper bound M on unstructured mesh using CUIBS scheme in shear flow.

$$E_{shape} = \frac{\sum_{c=1}^{nc} |\phi_c^n \Omega_c - \phi_c^0 \Omega_c|}{\sum_{c=1}^{nc} \phi_c^0 \Omega_c} \tag{2.12}$$

where the subscript and superscript denote the volume and time level where the volume fraction is computed.

To investigate the volume loss (or gain) due to limiting of the volume fraction, especially on non–orthogonal meshes with time, we consider the advection of circle in shear flow as discussed in Section 2.7.2 using the CUIBS scheme on unstructured meshes. The shape error E_{shape} is evaluated for this case and its temporal history is shown in Figure 2.9. We see that the average shape error is of the $\mathbf{O}(10^{-4})$ and remains bounded, ensuring that the present approaches leads to acceptably low shape errors even on unstructured grids. The loss/gain in volume (and hence mass, since each fluid has a constant density) is therefore negligible and is not expected to significantly affect the solutions to complex interfacial flows, as is demonstrated in the test

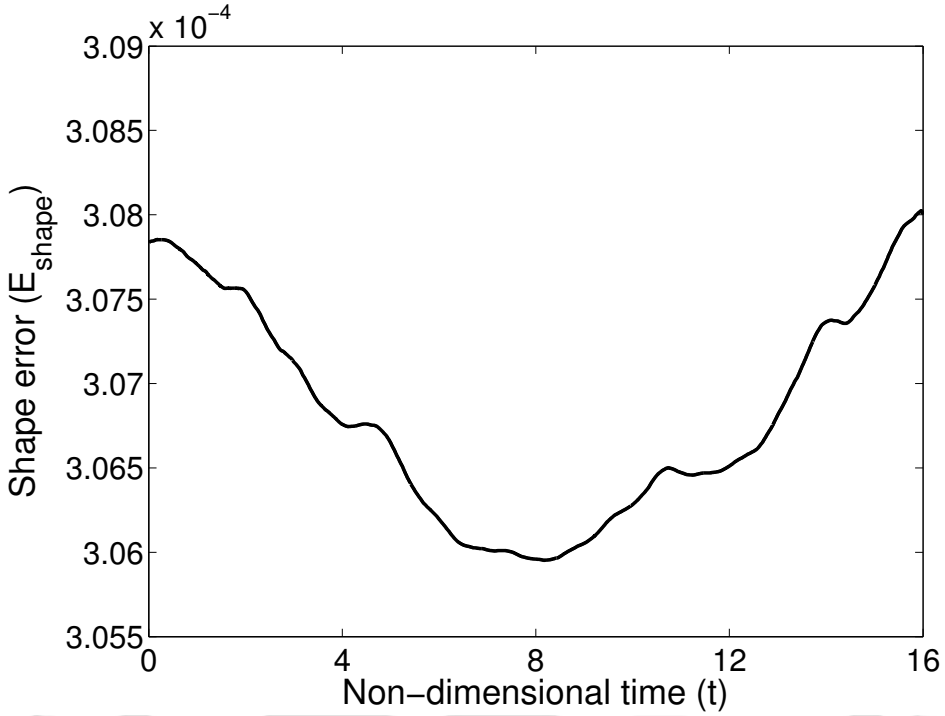

Figure 2.9: Relative change of the total volume/shape of the volume fraction in the shearing flow test using CUIBS scheme on unstructured mesh.

cases considered in Chapter 3.

CHAPTER 3

THE INCOMPRESSIBLE MULTIPHASE SOLVER

In this chapter, we discuss the salient features of the incompressible multiphase flow solver which forms the backbone of the numerical framework in this thesis. We employ a novel hybrid staggered/non–staggered framework for solution of the Navier–Stokes equations which is among the highlights of this thesis. A single continuum model is presented for multiple fluids with property jumps at the interface. The derivation and finite volume discretisation of the normal momentum equation, which is applicable for arbitrary topologies, is discussed in detail as is the complete solution methodology based on a fractional step method. The proposed solver, which is specifically discussed with reference to multiphase flows is validated for binary immiscible fluid flows on structured and unstructured meshes.

3.1 Governing Equations

We study the flow of one or more immiscible fluids which are governed by the two–dimensional, incompressible, laminar Navier–Stokes equations, which in conservative form read,

$$\nabla \cdot \mathbf{u} = 0 \tag{3.1}$$

$$\frac{\partial(\rho \mathbf{u})}{\partial t} + \nabla \cdot (\rho \mathbf{u}\mathbf{u}) = -\nabla \acute{p} + \nabla \cdot (\ \mu(\nabla \mathbf{u} + \nabla \mathbf{u}^T)) + \rho \mathbf{g} + \mathbf{F_{st}} \tag{3.2}$$

where $\mathbf{u}$ is the velocity vector $\begin{pmatrix} u \\ v \end{pmatrix}$, $\mathbf{g}$ is the gravitational acceleration $\begin{pmatrix} g_x \\ g_y \end{pmatrix}$, $\acute{p}$ is the pressure, μ is the dynamic viscosity and ρ denotes density. The term, $\mathbf{F_{st}}$, is the force due to surface tension, which is implemented using the continuum surface force (CSF) model [93],

$$\mathbf{F_{st}} = \sigma \varkappa \, \mathbf{n_I} \, \delta \tag{3.3}$$

Here σ, $\varkappa$, $\mathbf{n_I}$ and δ represent the surface tension coefficient, interface curvature, normal and the Dirac delta function, respectively. We adopt the curvature model proposed by Ubbink [94], on account of its simplicity. In order to minimise errors in curvature calculations, we employ smoothed volume fractions obtained using Laplacian smoothing (typically 3-4 smoothing iterations) to calculate interfacial curvature while the non-smoothed volume fractions are employed everywhere else when required. Expressing the interface normal in terms of the volume fraction, Eq. (3.3) can be simplified as,

$$\mathbf{F_{st}} = \sigma \varkappa \, \nabla \phi. \tag{3.4}$$

The curvature appearing in the computation of surface tension force is related to the interface normal as,

$$\varkappa = -\nabla \cdot \mathbf{n_I} \tag{3.5}$$

Following [94] we use the smoothed volume fraction to calculate the curvature and its cell–averaged value is computed as,

$$\varkappa = -\frac{1}{\Omega_c} \sum_f \left(\frac{\nabla \check{\phi}}{|\nabla \check{\phi}|} \right) \cdot \Delta \mathbf{s}_f \tag{3.6}$$

where Ω_c and $\Delta \mathbf{s}_f$ are the cell volume and surface area vector. In order to reduce errors in curvature calculations, we employ smoothed volume fractions $\check{\phi}$ obtained using Laplacian smoothing [94] given by,

$$\check{\phi} = \frac{\sum_f \phi_f |\Delta \mathbf{s}_f|}{\sum_f |\Delta \mathbf{s}_f|} \tag{3.7}$$

where the summation is over the faces of a cell. In this work we typically use 3-4

smoothing iterations for curvature calculations while the non-smoothed volume fractions are employed everywhere else when required.

Following [33], we rewrite equation by defining the piezometric pressure as,

$$p = \acute{p} - \rho \mathbf{g} \cdot \mathbf{x} \tag{3.8}$$

where $\mathbf{x}$ is the position vector. Consequently, we see that both pressure and gravity forces appear as gradients of scalar quantities, which allow for a balanced force formulation [33],

$$\frac{\partial(\rho \mathbf{u})}{\partial t} + \nabla \cdot (\rho \mathbf{u}\mathbf{u}) = -\nabla p + \nabla \cdot (\, \mu(\nabla \mathbf{u} + \nabla \mathbf{u}^T)) - \mathbf{g} \cdot \mathbf{x} \nabla \rho + \sigma \varkappa \, \nabla \phi \tag{3.9}$$

The readers are referred to Section A.1 for more details on the derivation of this equation. The multi–fluid flows involves more than one fluid with each having distinct densities and viscosities. A single fluid formalism is employed to calculate the mixture density and viscosity in above equation using volume fraction as,

$$\rho = \phi \rho_L + (1 - \phi) \rho_H \tag{3.10}$$

$$\mu = \phi \mu_L + (1 - \phi) \mu_H \tag{3.11}$$

These correlations for mixture density and viscosity are used in binary immiscible fluid systems (where subscripts L and H represent the properties of light and heavy fluids respectively), with the volume fraction ϕ obtained from the solution of the advection equation as discussed in Section 2.1. While a similar correlation can be employed even for multiple immiscible fluids, the expressions for density and viscosity may be different in case of miscible flows.

3.2 Hybrid staggered/non–staggered framework

The choice of variable arrangement on the grid is a key feature for the success of any solution algorithm. While the earliest efforts have employed a staggered grid [1], a majority of numerical approaches in the last three decades have favoured collocated grids. The use of collocated grids is advantageous, particularly on unstructured meshes, because the solution variables are located at the same point (typically, cell centroids). However, collocated mesh frameworks suffer from pressure–velocity decoupling (also called the “checker–board" problem) necessitating the use of Rhie–Chow interpolation or related techniques to overcome this problem. Staggered grid frameworks lead to smooth pressure and velocity fields but book–keeping and programming are a bit cumbersome owing to the solution variables stored at different locations. Furthermore, while a staggered arrangement of variables is relatively easy on Cartesian meshes, the associated flow solver becomes complicated on curvilinear and more so, in case of unstructured meshes. We propose to combine the staggered arrangement of variables with computational ease of a collocated grid, which results in the hybrid staggered/non–staggered framework for the present incompressible flow solver. One can therefore realise near machine–zero velocity divergence, as on a staggered grid, with the versatility of a non–staggered grid in this hybrid framework. This approach has been successfully implemented with Cartesian meshes in the past [49] and we now extend it to arbitrary polygonal meshes for the first time. This novel hybrid staggered/non–staggered framework is briefly described here since it forms the backbone of the multiphase flow solver but we remark that an extensive study on the specific details of its implementation for incompressible flows is part of another independent thesis.

The use of a staggered grid would mean that there are multiple variable arrangements possible. In order to have a better understanding and appreciation of the hybrid staggered/non–staggered approach, consider the Cartesian staggered mesh as shown in Figure 3.1(a), where the pressure ‘p’ stored at the cell center, velocities (u and v) are placed at the vertical and horizontal face centers. The momentum equations on

[1] We use the terms staggered(non–staggered) grid and staggered(non–staggered) framework interchangeably in this discussion and both refer to the variable arrangement on the underlying mesh.

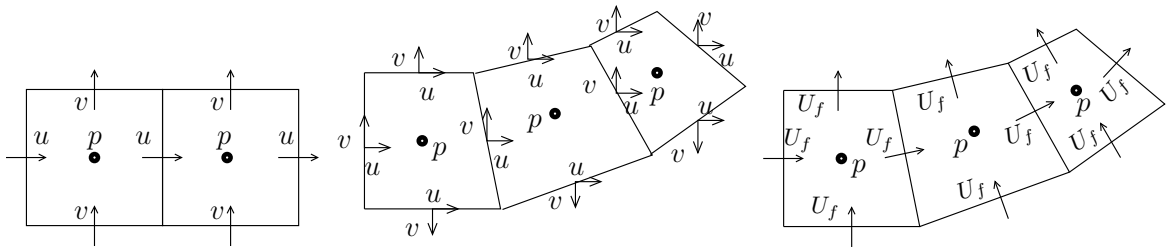

(a) Staggered (b) Staggered on unstructured (c) Hybrid staggered

Figure 3.1: Variable arrangement on (a) staggered (b) staggered on unstructured and (c) hybrid staggered mesh.

such a grid are therefore discretised on control volume that are staggered with respect to the cell, which is itself the control volume for discretisation of pressure. It must be realised that the convective and diffusive fluxes would be calculated at the cell faces themselves, if a finite volume framework were to be adopted with a Cartesian staggered grid. A staggered arrangement on unstructured meshes can be constructed in a similar manner (see Figure 3.1(b)), but leads to no clarity as to the choice of control volumes for the momentum equation(s). Unlike the Cartesian mesh where the grid alignment can be exploited, there are obvious difficulties in porting the staggered grid philosophy to non–Cartesian meshes. The viable alternative in this regard is the arrangement in Figure 3.1(c), which may be viewed as a “natural" extension of the staggered grid philosophy to arbitrary polygonal meshes. This is because, like in the case of Cartesian staggered grid, this arrangement stores the “normal" velocities at the face centers. The control volumes for and solution to the momentum equations is still unclear, but this concern can be overcome by borrowing ideas from non–staggered (collocated) grids. Stated specifically, we evaluate the convective and viscous fluxes at the cell centroids akin to the case of a non–staggered framework and then interpolate them to the cell interfaces. This is in sharp contrast to a fully staggered framework and this feature, which also adds to the novelty, completely explains why the framework is referred to as a hybrid staggered/non–staggered framework. It must be remarked that the proposed hybrid staggered/non–staggered framework is generic and is applicable to unstructured hybrid meshes as well as adaptive grids. We shall now discuss, albeit briefly, the salient details pertaining to the numerics of the proposed framework.

3.3 Normal momentum equation

The governing equations are discretised using the finite volume approach employing the hybrid staggered/non–staggered framework discussed earlier. As also described earlier, in this framework, the normal velocities are stored at the cell faces and all scalars (pressure, density and volume fraction) are stored at the cell centroids. In order to derive the normal momentum equation, which is solved for, we start with the non–dimensional linear momentum equations for incompressible flow. To non–dimensionalise the Eqs. (3.1) and (3.9) we consider following variables,

$$\nabla^* = L_\infty \nabla,\ \mathbf{u}^* = \frac{\mathbf{u}}{U_\infty},\ p^* = \frac{p}{\rho_L U_\infty^2},\ t^* = \frac{t}{L_\infty / U_\infty},\ \rho^* = \frac{\rho}{\rho_L},\ \mu^* = \frac{\mu}{\mu_L}$$

where L_∞ and U_∞ are suitably defined length and velocity scales, depending on the flow problem. We use properties of less denser fluid (defined with subscript L) for non–dimensionalisation. The resulting dimensionless momentum equation obtained as,

$$\frac{\partial(\rho^*\mathbf{u}^*)}{\partial t^*} + \nabla^* \cdot (\rho^* \mathbf{u}^* \mathbf{u}^*) = -\nabla^* p^* + \frac{1}{Re} \nabla \cdot (\ \mu^* (\nabla^* \mathbf{u}^* + \nabla^* \mathbf{u}^{\mathbf{T}^*})) - \frac{\nabla \rho^*}{Fr} \mathbf{e} \cdot \mathbf{x} + \frac{\varkappa^*\ \nabla \phi}{We} \quad (3.12)$$

where $Re = \frac{\rho_L U_\infty L_\infty}{\mu_L}$, $Fr = \frac{U_\infty^2}{g L_\infty}$ and $We = \frac{\rho_L L_\infty U_\infty^2}{\sigma}$ are the Reynolds number, Froude number and Weber number respectively. In the above equation $\mathbf{e}$ and g denote the unit vector in the direction of gravitational force and the magnitude of the gravitational acceleration. It must be remarked that all discussions in this study pertain to the dimensionless form of the equations and the superscript '$*$' representing the non–dimensional quantities in these equations is dropped for sake of convenience.

The novel hybrid staggered/non–staggered framework provides a "natural" extension of staggered philosophy to unstructured meshes and proves beneficial for multiphase simulations as demonstrated later in Chapter 4. The key component of the framework is the solution of a single momentum equation for the normal momentum at the cell faces, as opposed to individual velocity components at cell centers. The control volume for the solution of normal momentum equation a union of two cells which share

the same face. The normal momentum equation is derived for face 'f', by projecting the linear momentum equation Eq. (3.12), onto the direction of face unit normal $\mathbf{n}_f$. In the discussions to follow, integration is performed over the control volume $\Omega = \Omega_m \cup \Omega_n$, where subscript '$m$' and '$n$' depict cells sharing the face 'f' as shown in Figure 3.2.

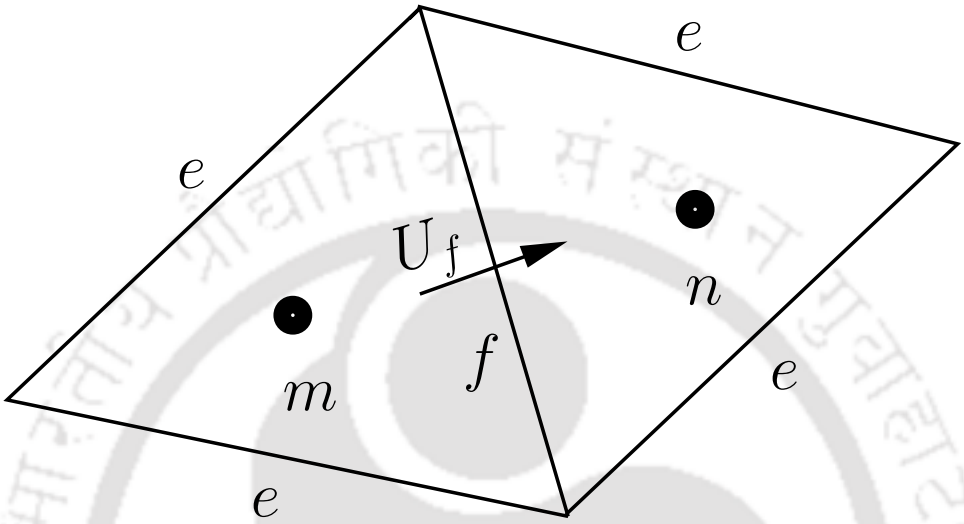

Figure 3.2: The control volume $\Omega = \Omega_m \cup \Omega_n$ for the normal momentum combines the two adjacent cells m and n shared by the face f. In the figure U_f represents the face normal velocity and arrow indicates the direction of the fluxes.

$$\int_\Omega \frac{\partial(\rho\mathbf{u})}{\partial t}\cdot\mathbf{n}_f d\Omega + \int_\Omega \nabla\cdot(\rho\mathbf{u}\mathbf{u})\cdot\mathbf{n}_f d\Omega = -\int_\Omega \nabla p\cdot\mathbf{n}_f d\Omega + \int_\Omega \frac{1}{Re}\nabla\cdot(\mu(\nabla\mathbf{u}+\nabla\mathbf{u}^T))\cdot\mathbf{n}_f d\Omega - \int_\Omega (\frac{\nabla\rho}{Fr}\mathbf{e}\cdot\mathbf{x})\cdot\mathbf{n}_f d\Omega + \int_\Omega \frac{\varkappa\,\nabla\phi}{We}\cdot\mathbf{n}_f d\Omega \tag{3.13}$$

We approximate the first term by assuming that U_f is an averaged value for the normal velocity (over the control volume Ω) lumped at the face center and that volumetric averaging of centroidal values is used for the calculation of face density ρ_f.

$$\int_\Omega \frac{\partial(\rho\mathbf{u})}{\partial t}\cdot\mathbf{n}_f\, d\Omega \approx \frac{d(\rho_f U_f)}{dt}\,\Omega \tag{3.14}$$

Using the Gauss divergence theorem and single–point quadrature, the semi–discrete

form of the Eq. (3.13) can be written as,

$$\frac{d(\rho_f U_f)}{dt}\,\Omega + \underbrace{\Big[\sum_{e\in\Omega}(\rho_e \mathbf{u}_e U_e)\Delta s_e\Big]\cdot\mathbf{n}_f}_{\mathbb{CONV}} = -\,\frac{\delta p}{\delta n}\Big|_f\,\Omega + \underbrace{\frac{1}{Re}\Big[\sum_{e\in\Omega}(\mu_e(\nabla\mathbf{u}_e+\nabla\mathbf{u}_e^T)\cdot\mathbf{n}_e)\Delta s_e\Big]\cdot\mathbf{n}_f}_{\mathbb{DIFF}} - (\frac{1}{Fr}\mathbf{e}\cdot\mathbf{x})\frac{\delta\rho}{\delta n}\Big|_f\,\Omega + \frac{\varkappa_f}{We}\frac{\delta\phi}{\delta n}\Big|_f\,\Omega \tag{3.15}$$

where $\mathbf{n_e}$ and Δs_e represent the outward unit normal and surface area of the edge 'e' respectively. The derivatives $\frac{\delta p}{\delta n}|_f$, $\frac{\delta \rho}{\delta n}|_f$ and $\frac{\delta \phi}{\delta n}|_f$ indicate the discrete forms of the pressure, density and volume fraction gradient respectively normal at the face f (to see the full discretisation of these normal gradients please refer to Section 4.1). Moreover, $\mathbb{CONV}$ and $\mathbb{DIFF}$ represent the discrete convective and diffusive fluxes and details of their discretisation are dealt with in the sections to follow. In the above equation $\sum_{e\in\Omega}$ implies that the fluxes of edges e are only considered while the contribution of face f is neglected. This is because, at any time instant, outgoing fluxes from the cell m are equal to the incoming fluxes of cell n through the face f and cancel one another. It must be remarked that the control volumes for normal momentum of two different faces of a given cell evidently overlap but does not affect the overall conservation properties, as demonstrated in Section 5.2.

3.3.1 Discretisation of the convective term

The discretisation of convective term in Eq. (3.15) may be written as,

$$\Big[\sum_{e\in\Omega}(\rho_e \mathbf{u}_e U_e)\Delta s_e\Big]\cdot\mathbf{n}_f = \Big[\sum_{e\in\Omega}\begin{pmatrix}\rho_e u_e U_e\\ \rho_e v_e U_e\end{pmatrix}\Delta s_e\Big]\cdot\begin{pmatrix} n_{x,f} & n_{y,f}\end{pmatrix}$$

where u_e and v_e are the Cartesian components of velocity at the center of edge e, U_e is the normal velocity at the edge e and $n_{x,f}, n_{y,f}$ are the components of the unit normal at the face f . The face values of the velocity components (u_e, v_e) are obtained from

the centroidal velocities using a high–resolution CUI scheme [84],

$$\alpha_e = \begin{cases} 3\alpha_m - 2\alpha_n + 4\nabla\alpha \cdot (\mathbf{x}_n - \mathbf{x}_m) & 0 < \tilde{\alpha}_U \leq \frac{2}{13} \\ \frac{5}{6}\alpha_m + \frac{1}{6}\alpha_n + \frac{1}{3}\nabla\alpha \cdot (\mathbf{x}_n - \mathbf{x}_m) & \frac{2}{13} < \tilde{\alpha}_U \leq \frac{4}{5} \\ \alpha_n & \frac{4}{5} < \tilde{\alpha}_U \leq 1 \\ \alpha_m & \text{elsewhere} \end{cases}$$

where α represents the Cartesian velocity components (u, v). Note that the fluxes are calculated at the cell edges e in the same manner as in the case of collocated meshes, although the solution variable is the normal momentum stored at the cell faces. It must be recalled that the CUI scheme is the high–resolution (HR) part of the interface capturing CUIBS scheme discussed in detail in Chapter 2. While CUI scheme is the preferred convection scheme in our studies, the framework is flexible to accommodate other alternate convection schemes as well.

3.3.2 Discretisation of the diffusive term

The discretisation of diffusive term in Eq. (3.15) may be written as,

$$\frac{1}{Re}\Big[\sum_{e\in\Omega}(\mu_e(\nabla\mathbf{u}_e + \nabla\mathbf{u}_e^T)\cdot\mathbf{n}_e)\Delta s_e\Big]\cdot\mathbf{n}_f = \frac{1}{Re}\Big[\sum_{e\in\Omega}\mu_e \begin{pmatrix} 2\frac{\delta u}{\delta x}\Big|_e n_{x,e} + (\frac{\delta u}{\delta y}\Big|_e + \frac{\delta v}{\delta x}\Big|_e)n_{y,e} \\ (\frac{\delta v}{\delta x}\Big|_e + \frac{\delta u}{\delta y}\Big|_e)n_{x,e} + 2\frac{\delta v}{\delta y}\Big|_e n_{y,e} \end{pmatrix}\Delta s_e\Big] \cdot \begin{pmatrix} n_{x,f} & n_{y,f} \end{pmatrix}$$

The viscous fluxes depend on the gradients of velocity components which are themselves computed at the cell centroids. The gradients of all quantities, including the velocity components are obtained using a Green–Gauss gradient reconstruction [85]. The viscous fluxes at the edge e are then evaluated by simple averaging between the centroidal values as [85],

$$\begin{aligned} \frac{\delta\alpha}{\delta x}\Big|_e &= \frac{1}{2}\Big(\frac{\delta\alpha}{\delta x}\Big|_m + \frac{\delta\alpha}{\delta x}\Big|_n\Big) - \mathrm{T_x} \\ \frac{\delta\alpha}{\delta y}\Big|_e &= \frac{1}{2}\Big(\frac{\delta\alpha}{\delta y}\Big|_m + \frac{\delta\alpha}{\delta y}\Big|_n\Big) - \mathrm{T_y} \end{aligned}$$

where the factors $\mathrm{T_x}$ and $\mathrm{T_y}$ avoid odd–even decoupling and are given by [85],

$$\begin{aligned}
\mathrm{T_x} &= \Big[\frac{1}{2}\Big(\frac{\delta\alpha}{\delta x}\Big|_m + \frac{\delta\alpha}{\delta x}\Big|_n\Big)n_{l,x} + \frac{1}{2}\Big(\frac{\delta\alpha}{\delta y}\Big|_m + \frac{\delta\alpha}{\delta y}\Big|_n\Big)n_{l,y} - \frac{\alpha_n - \alpha_m}{\Delta x_{mn}}\Big]n_{l,x} \\
\mathrm{T_y} &= \Big[\frac{1}{2}\Big(\frac{\delta\alpha}{\delta x}\Big|_m + \frac{\delta\alpha}{\delta x}\Big|_n\Big)n_{l,x} + \frac{1}{2}\Big(\frac{\delta\alpha}{\delta y}\Big|_m + \frac{\delta\alpha}{\delta y}\Big|_n\Big)n_{l,y} - \frac{\alpha_n - \alpha_m}{\Delta y_{mn}}\Big]n_{l,y}
\end{aligned}$$

where α refers to the Cartesian velocity components u and v. Furthermore, $n_{l,x}$ and $n_{l,y}$ are the components of the unit vector along the line joining m and n and $\Delta()_{mn}$ is the distance between points m and n. As in the case of convective fluxes, the viscous fluxes are also computed in a manner analogous to those on collocated grids.

3.3.3 Time integration scheme for the normal momentum equation

In order to ensure time–accurate solutions and to be commensurate with the spatial accuracy, we employ a second–order accurate three–point backward differencing scheme for time advancement. Following the numerical algorithms for incompressible flows, the flow solver in the present work adopts a segregated strategy with an incremental fractional step algorithm. This results in a predictor–corrector approach, with the predictor step in discrete form as,

$$\begin{aligned}
\frac{3\rho_f^{n+1}U_f^\star - 4\rho_f^{n+1}U_f^n + \rho_f^{n+1}U_f^{n-1}}{2\Delta t} = &- \mathbb{CONV}(U_f^\star, \mathbf{u}^\star) + \mathbb{DIFF}(U_f^\star, \mathbf{u}^\star) \\
&- \frac{\delta p}{\delta n}\Big|_f - (\frac{1}{Fr}\mathbf{e}\cdot\mathbf{x})\frac{\delta\rho}{\delta n}\Big|_f + \frac{\varkappa_f}{We}\frac{\delta\phi}{\delta n}\Big|_f
\end{aligned} \tag{3.16}$$

where $U_f^\star$ is face normal velocity at the intermediate time level between $n+1$ and n, $\mathbf{u}$ denotes the centroidal velocity vector. $\mathbb{CONV}$ and $\mathbb{DIFF}$ indicate the discrete convective and diffusive flux operators as discussed earlier. This step gives a predicted value for normal momentum whose normal velocities do not, in general, satisfy the continuity equation.

The predictor equation for normal momentum is an intermediate step and is solved using an implicit approach. It may be considered as the solution to a fixed point problem

$G(U_f)$ = 0, where the non–linear functional G consists of the time derivative, discrete convective and viscous fluxes and the discrete pressure gradient. We defer from discussing the details of the solution procedure, but remark that the non–linear system of equations are solved using a Newton–Krylov solver through the open source PetSc libraries [95].

3.3.4 Velocity reconstruction

The discussions on convective and viscous flux calculations, which are carried out as in a collocated framework, are based on the assumption that the centroidal velocities are available. This is however not the case in the present framework, where only the normal momentum is known and is stored at the cell faces. It is therefore necessary to reconstruct the velocities at the centroids from the face–normal velocities and this is achieved through a novel iterative defect correction approach. Stated in mathematical terms, we obtain the centroidal velocities as (where k denotes iteration counter),

$$\mathbf{u}_c^k = \mathbb{A}^{-1}\mathbf{b}(\mathbf{u_c^{k-1}}) \tag{3.17}$$

where $\mathbb{A}$ is a 2 $\times$ 2 geometric matrix and b is a 2-dimensional vector defined respectively as,

$$\mathbb{A}_{i,j} = \sum_f n_i n_j \Delta s_f \tag{3.18}$$

$$\mathbf{b_j} = \sum_f \tilde{U}_f n_i \Delta s_f \tag{3.19}$$

and the corrected face normal velocity is defined as,

$$\tilde{U}_f = U_f - \sum_{i=1}^{2}\sum_{j=1}^{2} u_{c_{i,j}}^{k-1} \Delta x_j n_i \tag{3.20}$$

In the above equation, $u_{c_{i,j}}$ is defined as the j^{th} component of the gradient of the i^{th} velocity component in the cell c, Δx_j is the j^{th} component of distance vector between the centroids of the face f and cell c and n_i is the i^{th} component of the face unit normal. A weighted least–squares approach is used to calculate the gradients appearing

in Eq. (3.20) for the corrected velocities. It has been shown in [96] that the iterative process defined by Eqs. (3.17) and (3.20) indeed converges on different mesh topologies thereby leading to second-order accurate centroidal velocities. It must be noted that the iterative process is necessitated by the fact that the second-order accurate calculation of the centroidal velocities needs the corrected face normal velocities which in turn requires the gradients of the centroidal velocity vector itself to first order accuracy. It may be remarked that the iterative process is not necessary on orthogonal meshes such as those employed in the immersed boundary approach later in the thesis. The face normal velocities are obtained by dividing the normal momentum by the face densities, with the latter obtained through an averaging of the centroidal densities (which are known). It is also important to realise that this reconstruction approach is critical to ensure physically consistent solutions on non–orthogonal meshes and interested readers are referred to [96] for further details.

3.4 Pressure Correction Equation

We employ an incremental fractional step approach as in [97] and for the case of variable density flows, as in this thesis, results in a variable coefficient Poisson equation for pressure correction ($\mathcal{P} = p^{n+1} - p^n$),

$$\sum_{f \in C} U_f^\star \, \Delta s_f = \frac{2\,\Delta t}{3} \sum_{f \in C} \frac{1}{\rho_f^{n+1}} \frac{\delta \mathcal{P}}{\delta n}\Big|_f \, \Delta s_f \tag{3.21}$$

where the left hand side is a known source term (since $U_f^\star$ is calculated from the normal momentum equation) and $\frac{\delta \mathcal{P}}{\delta n}|_f$ denotes the discrete normal gradient of the pressure correction at the faces f. It must be emphasized that the unlike for the normal momentum equation, control volume for the pressure correction equation is the individual cell (C) as shown in Figure 3.3, because the pressure and its correction are stored at the cell centroids. It is easy to see that the above equation is the discrete counterpart of the Poisson equation and is therefore inherently linear. Any non–linearity which is introduced because of the non–orthogonal correction terms for the normal gradient of

pressure correction [2] on unstructured meshes is handled using a defect correction approach. Similar to the advection equation for volume fraction, the above equation can be arranged to form a linear system of equations that reads,

$$\mathbb{A}P = \mathbb{S}$$

where $\mathbb{A}$ is a geometric matrix, P is the vector of pressure correlations at the cell centroids and $\mathbb{S}$ represents the source vector containing left hand side term in the Eq. (3.21) and the gradients of pressure correction arising from non–orthogonality effects. The latter is a “lagged" contribution to the source term and the resulting linear system at every step is solved using open source LiS libraries [86] with a flexible GMRES method that employs SAAMG as preconditioner. This system is solved for several sub–iterations (because of the “lagged" source term) and a suitable termination criterion is $|P^{k+1} - P^k| \leq 10^{-12}$, where superscript k denotes the sub–iterations. Note that for orthogonal meshes, there is only one sub–iteration and few sub–iterations (6–8) suffice for grids with mild to moderate non–orthogonality. The pressure correction is then used to update the pressure to the next time level and also to correct the normal momentum obtained in the predictor step.

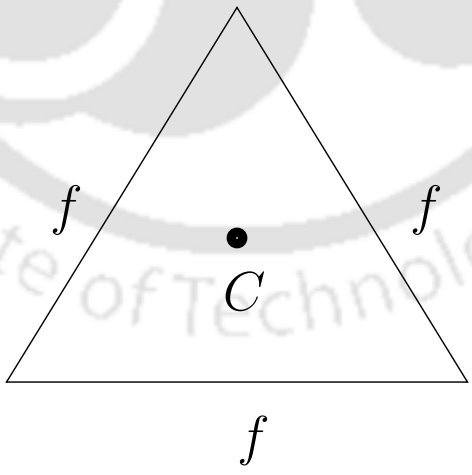

Figure 3.3: The control volume Ω_c for the solution of scalar variables namely pressure correction $\mathcal{P}$ and volume fraction ϕ.

[2] For a clear picture of non–orthogonality in the discrete representation of normal derivatives, please refer to Section 4.1.

3.5 Solution methodology

In this section, we summarise the overall solution methodology for simulation of multiphase flows in this thesis. A finite volume methodology in a hybrid staggered/non–staggered framework is employed, the details of which have been discussed in earlier sections. The flows are assumed to be incompressible for most part of this thesis and therefore an incremental fractional step algorithm, typical of such flows, is adopted in this thesis as well. A segregated solution approach is adopted wherein the advection equation for the volume fraction is first solved implicitly using the known value of velocity field. The density and dynamic viscosity at the centroids are then computed using the volume fractions and are subsequently employed in the solution to the normal momentum equation. The solution to the latter results in an auxiliary momentum (and hence velocity) field that does not satisfy incompressibility. In order to obtain a divergence–free velocity field, an evolution equation for the pressure correction is solved. It must be remarked that the solution to the momentum and pressure correction equations require the face values of density and viscosity. The interfacial values for density are obtained from the centroidal values using volume–weighted averaging whereas the viscosity at the face is determined using harmonic averaging as in [38]. The pressure corrections hence obtained are then used to update the pressure and normal momentum obtained in the predictor step to the next time level. The corrector step is a purely algebraic process which reads,

$$p^{n+1} = \mathcal{P} + p^{n} \tag{3.22}$$

$$(\rho U_f)^{n+1} = (\rho U_f)^{\star} - \frac{2}{3}\frac{\Delta t}{}\left.\frac{\delta \mathcal{P}}{\delta n}\right|_f \tag{3.23}$$

where $\rho^{\star} = \rho^{n+1}$ and follows from the non-dimensional form of the Eq. (3.10). This entire process, which constitutes one outer iteration of the multiphase flow solver is repeated for a finite number of outer iterations (for unsteady cases) or until convergence (for steady–state problems). The overall solution methodology is also schematically shown in the flowchart (see Figure 3.4), for sake of completeness and clarity.

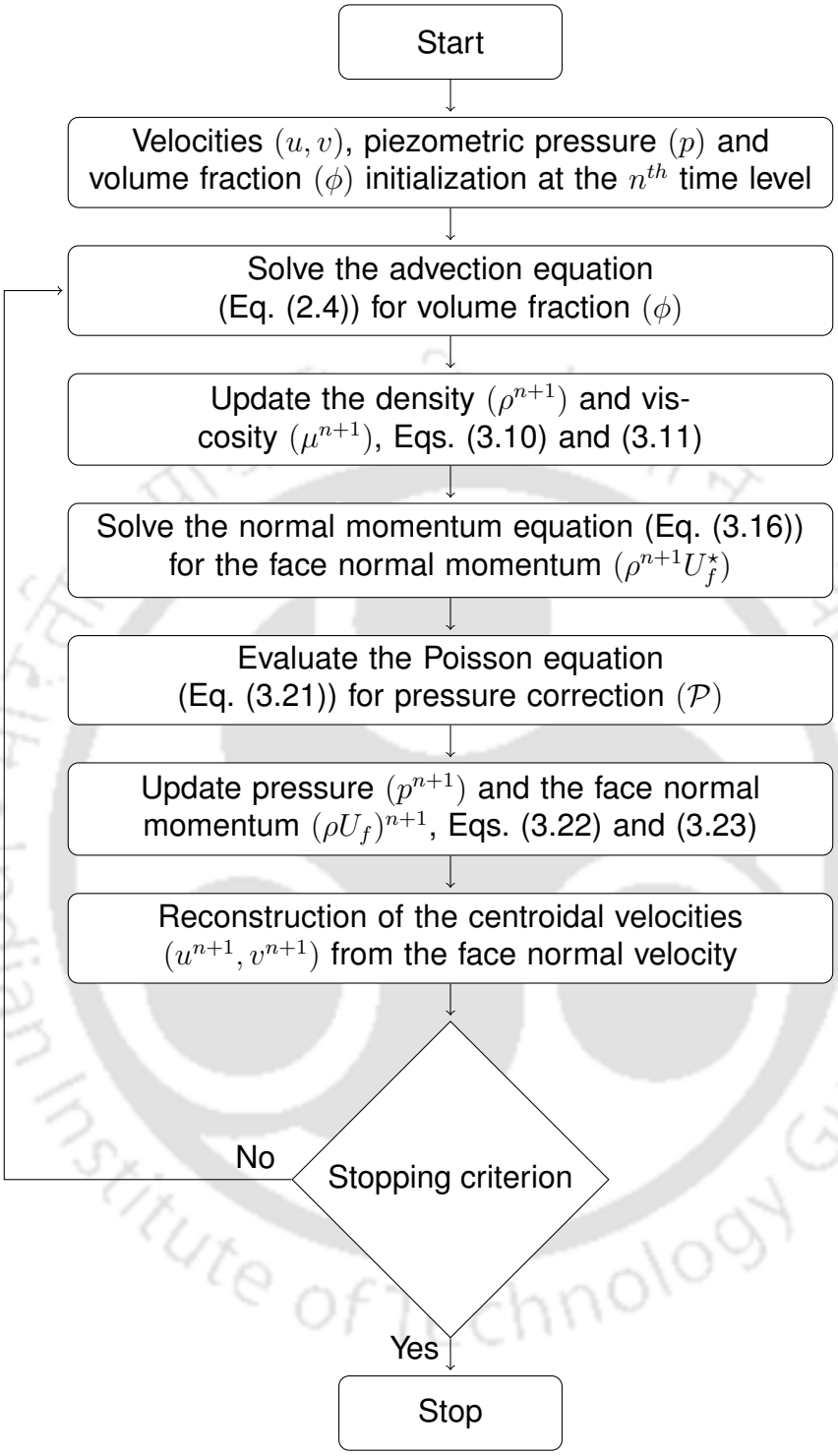

Figure 3.4: Flowchart for solution methodology.

3.6 Preliminary validation

We carry out a primary assessment of the multiphase flow solver by considering two preliminary test problems of interest. We remark that this solver essentially combines

the volume fraction advection with Navier–Stokes equations in a finite volume framework for multi–fluid flows. The two–interface problem and the Rayleigh–Taylor instability are simulated with the proposed solver in this section to examine its performance.

3.6.1 Two fluid interface problem

First, we consider the viscous sloshing in a 0.8×0.6 domain of grid resolution $\Delta x = \Delta y =$ 0.005, with the lighter fluid above and heavier below and the initial interface defined by $y = 0.4 - 0.25x$. No–slip condition is enforced on the horizontal top and bottom walls while the vertical walls are defined as slip walls. The simulation is carried out for a density ratio of 2 and the viscosities are considered equal as in [98].The Reynolds number and Froude number are chosen to be 252 and 1 respectively and timestep is fixed to Δt = 0.005.

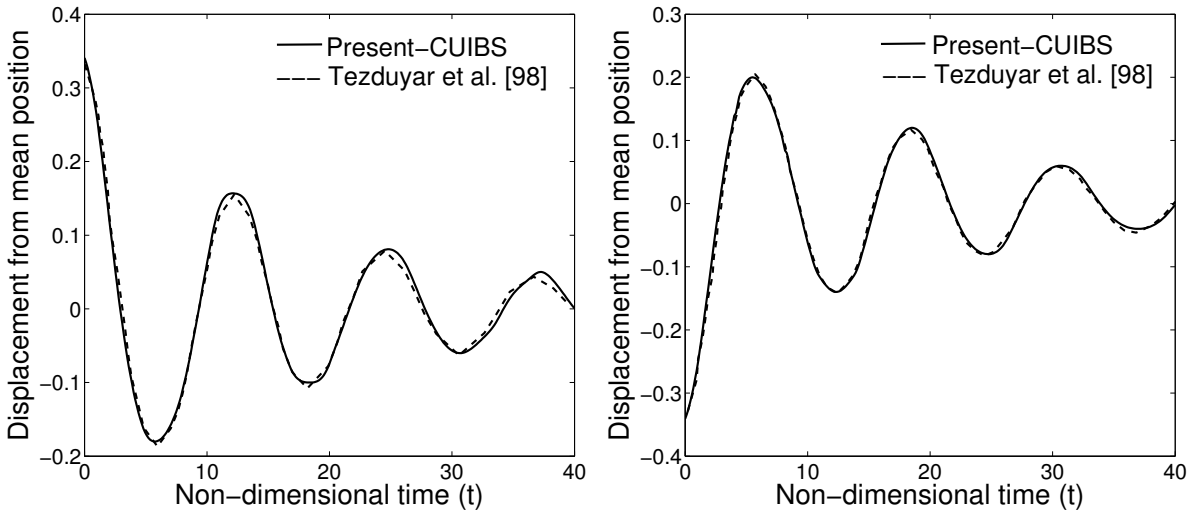

(a) Left wall (b) Right wall

Figure 3.5: The time history of interface location relative to the average height of 0.3 on the (a) left and (b) right walls.

The results of the simulations are compared with those obtained by Tezduyar et al. [98]. Figures 3.5(a) and 3.5(b) show the temporal history of the interface location on the left and right walls, which are in good agreement with the FEM results in [98] and show a damped behaviour indicating a steady state at very long times. Figures 3.6(a)

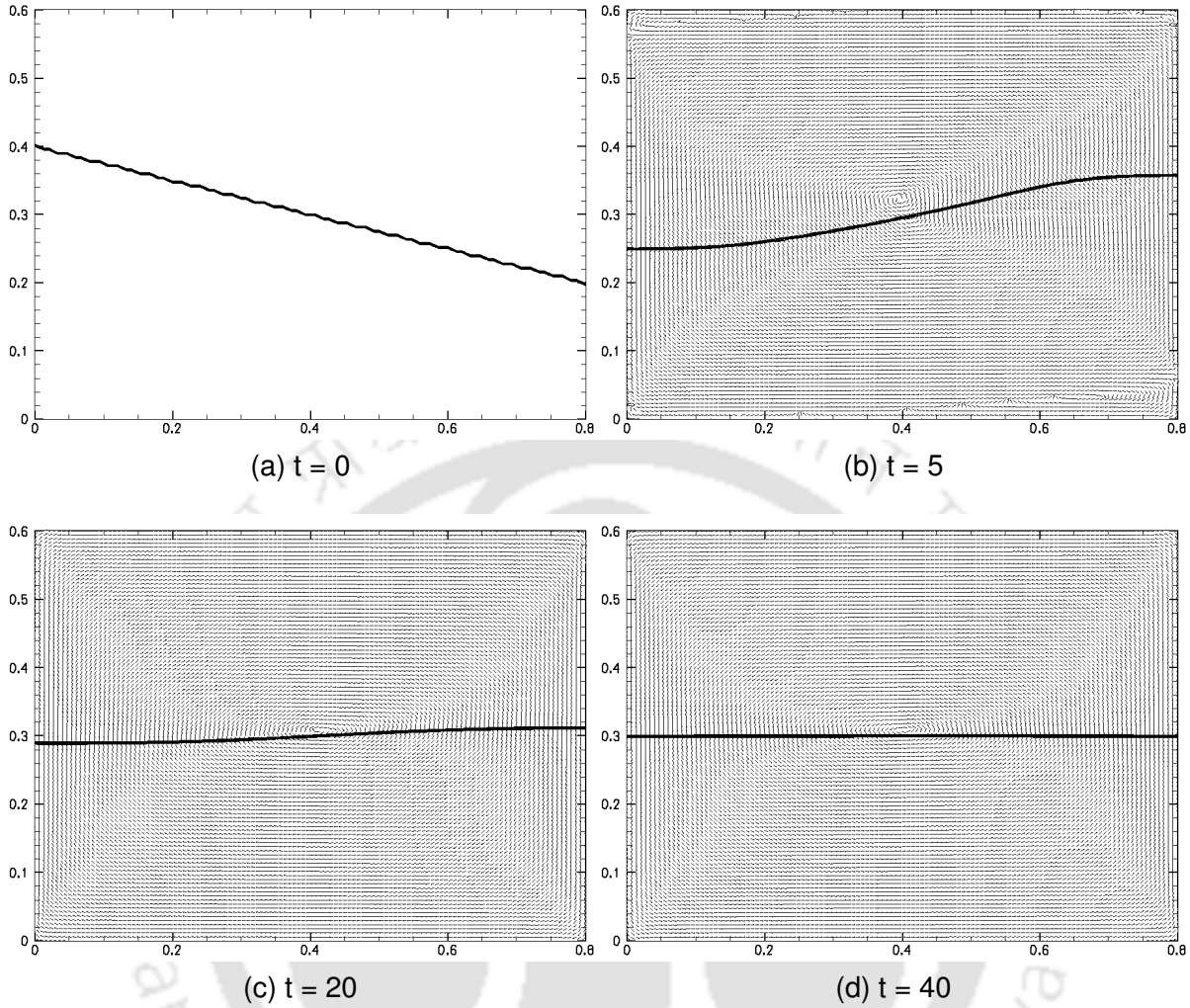

Figure 3.6: Velocity vector with two fluid interface using CUIBS on structured mesh at time instants t = (a) 0 (b) 5 (c) 20 and (d) 40.

to 3.6(d) show the interface at four different time instants (t = 0, 5, 20, 40) indicating that the initial sharp resolution of the interface is preserved to a great extent by the CUIBS scheme.

3.6.2 Rayleigh–Taylor instability

The Rayleigh–Taylor instability is a density–driven problem where a heavier liquid on top is separated from a lighter liquid on the bottom by an interface, and has been simulated by several researchers in the past [99, 100] to test the capability of interface capturing algorithms to tackle complex flow phenomena. This problem is known to be sensitive to grid irregularities and therefore an unstructured grid symmetric about

the vertical centerline is used to minimize any asymmetry errors. A 1×4 rectangular domain is discretised into 21456 triangular elements. No-slip boundary conditions are prescribed on the top and bottom walls and the remaining boundaries are assumed to be slip walls. The density ratio of equal dynamic viscosity fluids is chosen to be 3 and therefore the Atwood number $At = \frac{\rho_H - \rho_L}{\rho_H + \rho_L} = 0.5$. The interface is perturbed to initiate the instability as, $y = 2 + 0.1\cos(2\pi x)$, with Reynolds and Froude number fixed to 1000 and 1 respectively.

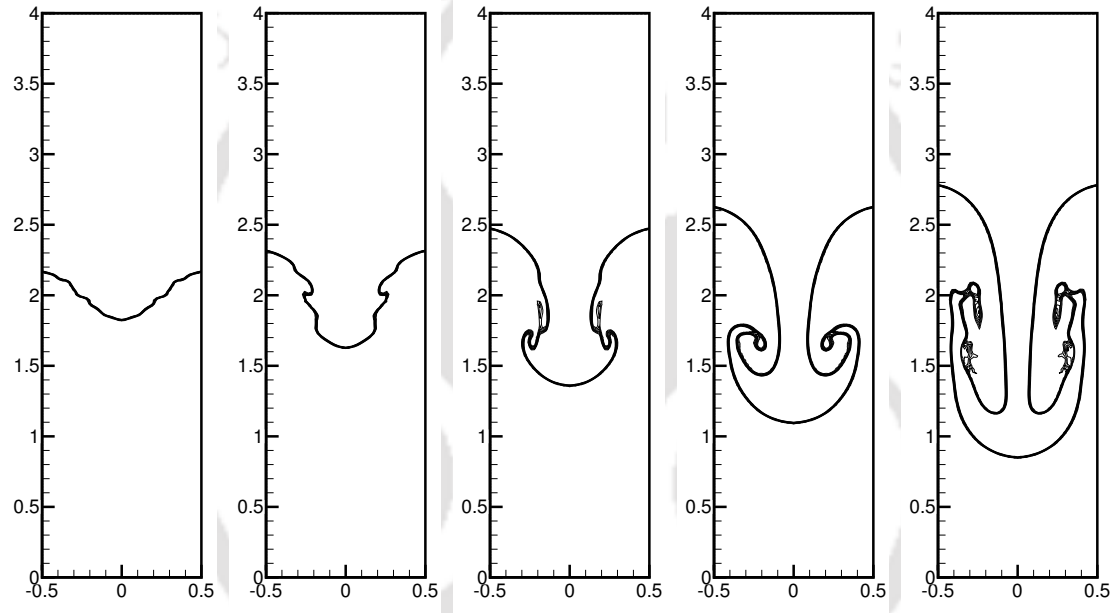

(a) T = 0.5 (b) T = 1 (c) T = 1.5 (d) T = 2 (e) T = 2.5

Figure 3.7: Rayleigh–Taylor instability: Contours of volume fraction using CUIBS scheme at non-dimensional time $T = t\sqrt{At} =$ (a) 0.5 (b) 1 (c) 1.5 (d) 2 and (e) 2.5.

Interface evolution using CUIBS scheme on unstructured mesh are shown in Figures 3.7(a) to 3.7(e) at different time levels of $t\sqrt{At}$ = 0.5, 1, 1.5, 2 and 2.5. It can be observed that the interface is symmetric about center line and instability is described accurately by scheme. In order to obtain grid-independent solutions, the test case is simulated on three unstructured meshes viz. G1, G2 and G3 having 10246, 21456 and 41156 triangular elements respectively. The results presented in Figure 3.8 show that no perceptible differences exist on meshes G2 and G3 and therefore the solutions on G2 are grid-independent. The numerical results obtained herein and anal-

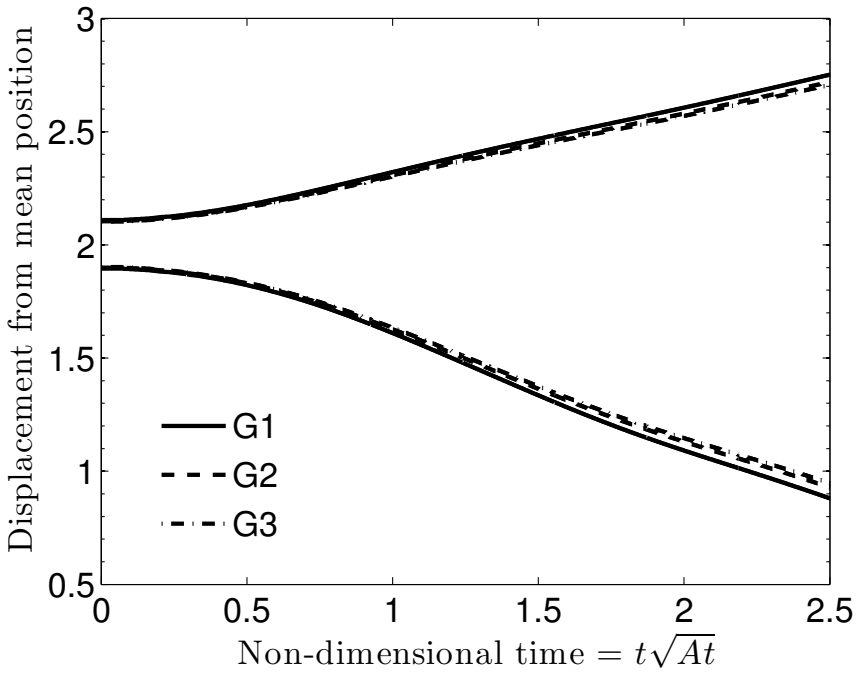

Figure 3.8: The mesh refinement study for Rayleigh-Taylor instability on unstructured meshes G1 (10246), G2 (21456) and G3 (41165) using CUIBS scheme.

ysed further are those obtained using G2. Figure 3.9 plots the position of the rising bubble at the side wall and falling bubble at the mid section of the domain against the non–dimensional time, and are compared with numerical simulations of Guermond and Quartapelle [99] and Tryggvason [100]. The agreement of the results from the present simulations with those in [99,100] is excellent, and further validates the robustness and efficacy of the solver to handle complex flow phenomena in realistic fluid flows.

It can be observed that the simulations are carried out for low density ratios, although, many multiphase flows are subjected to high density contrasts. Multiphase algorithms including the VOF method often lead to the anomalous results in such cases as also reported in literature. In the next chapter, we will explore the possible reasons for numerical instabilities in high density ratio flows and propose a consistent and well balanced algorithm precisely for numerical simulations of large density contrasts.

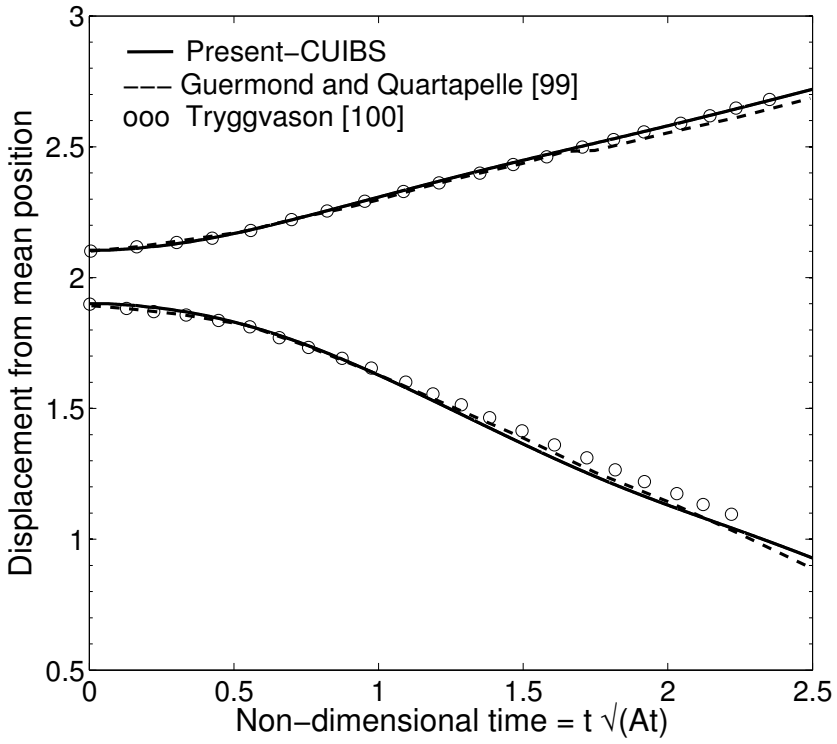

Figure 3.9: Position of rising and falling bubbles versus time on unstructured meshes using CUIBS scheme.

CHAPTER 4

A WELL BALANCED AND CONSISTENT FORMULATION[‡]

Numerical simulations of realistic multiphase flows are often plagued by numerical instabilities owing to high density ratios of the fluids involved in the studies. Furthermore, the dynamics of multiphase flows in several applications are influenced by surface tension and gravity. The focus of this chapter is on the need to and means of accounting for large interfacial and body forces in multiphase flow simulations. We also attempt to understand the reasons behind reported difficulties in large density ratio flows (of which we experienced a few) and evolve a numerical strategy to perform robust and stable simulations of multiphase flows with arbitrarily large density contrasts. The approach discussed in this chapter is investigated using a large number of test problems covering a wide range of scenarios both on structured and unstructured meshes. A few realistic scenarios are also simulated to demonstrate the efficacy of the formulation developed herein for multiphase simulations with high density and viscosity ratios as well as large interfacial tension and body forces.

[‡]The contents in this chapter have been published as J.K. Patel and G. Natarajan, "A novel consistent and well-balanced algorithm for simulations of multiphase flows on unstructured grids", Journal of Computational Physics 350 (2017).

4.1 Balanced force algorithm

As discussed in the introduction, one of the critical aspects of numerical discretisation for multiphase flows is the need for ensure a balance of forces in the momentum equation. While collocated approaches in [32–34] adopt different methodologies that require modifications in momentum interpolation to achieve the balance, the present staggered/non–staggered framework allows for a relatively straightforward and arguably “natural" approach for well–balanced discretisation.

One can easily see that the terms corresponding to pressure, surface tension and body forces in the normal momentum equation involve gradients of scalar quantities viz. p, ϕ and ρ respectively. The key to a well–balanced formulation is to discretise all these gradients in an identical manner. Unlike the collocated framework, the forces in the normal momentum equation involve only the normal derivatives (see Eq. (3.15)) which may be discretised accounting for non–orthogonal effects as,

$$\frac{\delta\alpha}{\delta n}\Big|_f = \underbrace{\frac{\alpha_n - \alpha_m}{\Delta r}}_{\text{orthogonal part}} + \underbrace{\frac{\nabla\alpha_n \cdot \Delta\mathbf{r}_n - \nabla\alpha_m \cdot \Delta\mathbf{r}_m}{\Delta r}}_{\text{non–orthogonal part}} \tag{4.1}$$

where α is any scalar quantity ($= \rho, p, \phi, \mathbb{P}$) and Δr denotes the distance between the points m' and n'. The quantities $\Delta\mathbf{r}_m$, $\Delta\mathbf{r}_n$ are the vectors along the line joining the points m and m', n and n' respectively (see Figure 4.1) and contribute to the non–orthogonal correction. It must also emphasised that normal derivatives of pressure in the momentum equation, Eq. (3.15) and momentum update, Eq. (3.23) must necessarily have the same discretisation as also the pressure correction in the Poisson equation, Eq. (3.21). The gradients appearing in the non–orthogonal contribution are estimated using a standard Green–Gauss approach [85].

A different and possibly naive approach to determine the normal gradients appearing in the force terms is to use an alternate discretisation defined by,

$$\frac{\delta\alpha}{\delta n}\Big|_f = \overline{\frac{\delta\alpha}{\delta x}} n_{x,f} + \overline{\frac{\delta\alpha}{\delta y}} n_{y,f} \tag{4.2}$$

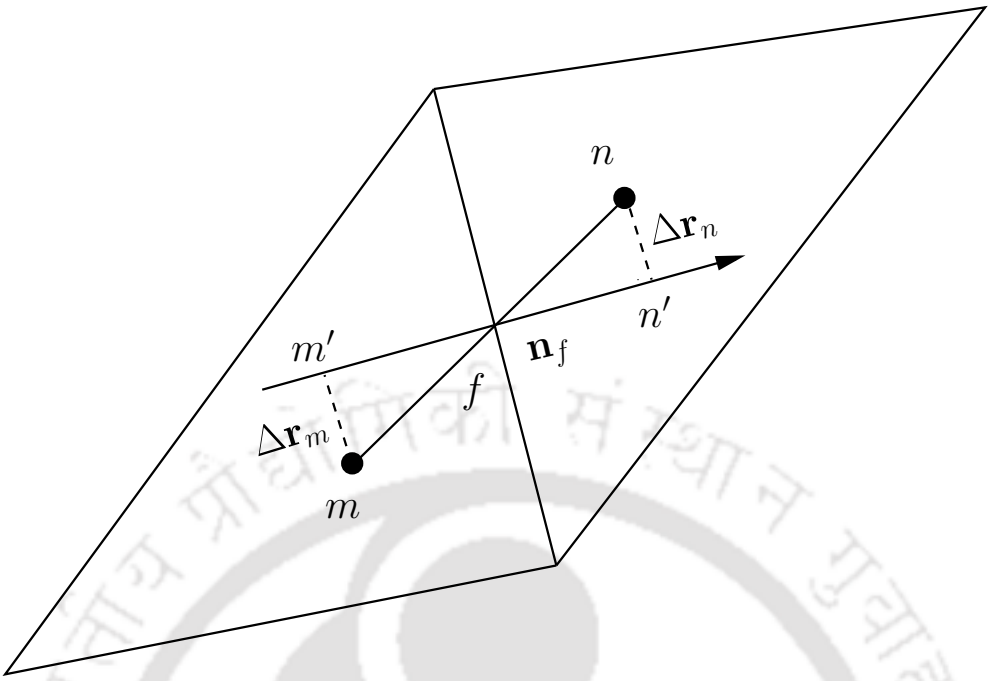

Figure 4.1: The projections of the centroids on normal to the face f.

where the quantities $\overline{\frac{\delta \alpha}{\delta x}}$ and $\overline{\frac{\delta \alpha}{\delta y}}$ are obtained using a linear interpolation of these gradients at centroids of cells (m and n) sharing the face 'f' (see Figure 4.1) and $n_{x,f}$ and $n_{y,f}$ are the components of the unit normal to the face. The use of Eq. (4.1) for pressure gradient and Eq. (4.2) for density and/or volume fraction gradients (or vice–versa) would however result in an unbalanced formulation. We shall discuss its implications for surface tension and gravity dominated flows in Section 4.3.

4.2 Consistent discretisation of governing equations

The transport of mass and momentum in a consistent fashion at the discrete level is necessary to obtain robust and stable solutions for high density and high shear flows. In the present work, we adopt the philosophy in [35] within a VOF framework to achieve discrete consistency for the transport equations on arbitrary polygonal meshes. The inherent and fundamental principle behind a consistent approach is to ensure that the transporting velocity and transported quantities are discretely similar in both the mass and momentum equations. This means that the convective fluxes in the VOF equation, Eq. (2.4), as well as the normal momentum equation, Eq. (3.15), must be evaluated

necessarily using the same convective scheme.

In this study we employ the CUI scheme, which is a high-resolution upwind–biased scheme for the discretisation of the convective fluxes in the momentum and volume fraction equations. One can obtain the normalised face values of quantities in the convective fluxes using this scheme as,

$$\tilde{\alpha_f} = \begin{cases} 3\tilde{\alpha}_U & 0 < \tilde{\alpha}_U \leq \frac{2}{13} \\ \frac{5}{6}\tilde{\alpha}_U + \frac{1}{3} & \frac{2}{13} < \tilde{\alpha}_U \leq \frac{4}{5} \\ 1 & \frac{4}{5} < \tilde{\alpha}_U \leq 1 \\ \tilde{\alpha}_U & \text{elsewhere} \end{cases} \tag{4.3}$$

where α is any transport quantity $(= u, v, \rho, \phi)$ and $\tilde{\alpha} = \dfrac{\alpha - \alpha_{FU}}{\alpha_D - \alpha_{FU}}$, with the subscripts U,D and FU referring to the upwind, downwind and far upwind cells respectively for the face f. The CUI scheme, which has also been discussed in Section 2.6.2, is nominally second–order accurate on unstructured meshes and ensures boundedness by construction [84]. It is possible to use other high–order accurate schemes as long as the same scheme is employed for convection of volume fraction and momentum. The use of different schemes for volume fraction and momentum transport leads to an inconsistent approach. We show that an inconsistent transport, realised herein by using a first–order upwind scheme in place of CUI for momentum transport could be detrimental for multiphase flows under some conditions as discussed in Section 4.3. It must be also be remarked that any choice of dissimilar schemes for mass and momentum transport would also lead to inconsistency, irrespective of their orders of accuracy as demonstrated later in the chapter.

4.3 Numerical tests

We investigate the role and need of consistent and fully–balanced formulations, as proposed in Sections 4.1 and 4.2 for multiphase simulations through a series of nu-

merical experiments in this section. A wide range of test problems of varying levels of complexity are tested on both structured and unstructured meshes to analyse the implications of unbalanced formulation as well as inconsistent transport. These studies are then employed to arrive at salient conclusions on the performance of the proposed algorithm. We emphasise that the all dimensionless numbers in the studies are defined based on the properties of the less denser fluid (denoted by subscript L) which is also considered to be the less viscous one.

4.3.1 Static droplet

We first consider the case of a static droplet in an inviscid fluid in the absence of gravity. The droplet of diameter D = 0.5 is placed at the center of a 1 $\times$ 1 square cavity. It must be remarked that the velocity scale used in defining the dimensionless numbers is chosen here as $\sqrt{\frac{\sigma}{\rho_L D}}$, while the length scale is the diameter of the droplet. Studies are carried out on a 50 $\times$ 50 Cartesian grid as well as a triangulated grid with 2436 elements at two different density ratios. All simulations are carried out at We = 1 with a timestep Δt = 0.001.

The balanced and unbalanced formulations are compared by considering the following two quantities,

$$\begin{aligned} L_\infty(\mathbf{u}) &= \max|\mathbf{u}| \\ E(\Delta p_{total}) &= \frac{|\Delta p_n - \frac{\kappa}{We}|}{\frac{\kappa}{We}} \end{aligned}$$

While the first is a measure of spurious currents, the second expresses the deviation of the numerically computed pressure jump ($\Delta p_n = p_{in} - p_{out}$, difference between the average computed pressures inside and outside of the droplet) from the exact pressure jump as given by the Young–Laplace law. The inside of the droplet is defined by all cells with a volume fraction ϕ lesser than 0.5 and the outlet by those with ϕ greater than 0.5 with ϕ = 0.5 denoting the interface.

Table 4.1 shows the spurious currents and pressure error jumps on the two grids

Table 4.1: Spurious currents and pressure jump errors for inviscid static droplet with exact curvature on structured and unstructured mesh. The timestep is fixed to Δt = 0.001 with We = 1.

Algorithm	Time	$\frac{\rho_H}{\rho_L}$	Structured		Unstructured	
			$L_\infty(\mathbf{u})$	$E(\Delta p_{total})$	$L_\infty(\mathbf{u})$	$E(\Delta p_{total})$
Unbalanced	Δt	10	5.41×10^{-6}	1.47×10^{-1}	2.97×10^{-5}	7.56×10^{-1}
		10^3	9.73×10^{-6}	2.43×10^{-1}	4.47×10^{-5}	8.52×10^{-1}
	$50\Delta t$	10	2.11×10^{-3}	4.39×10^{-1}	9.84×10^{-3}	8.41×10^{-1}
		10^3	7.11×10^{-3}	4.96×10^{-1}	1.01×10^{-2}	8.95×10^{-1}
Balanced	Δt	10	1.09×10^{-14}	1.15×10^{-3}	3.95×10^{-12}	8.52×10^{-3}
		10^3	1.89×10^{-14}	1.20×10^{-3}	6.21×10^{-12}	8.73×10^{-3}
	$50\Delta t$	10	1.71×10^{-13}	2.10×10^{-3}	3.32×10^{-11}	8.16×10^{-3}
		10^3	2.01×10^{-13}	2.16×10^{-3}	6.32×10^{-11}	9.24×10^{-3}

when exact curvature is specified. It is evident that the balanced algorithm maintains near machine–zero values of spurious currents on either mesh even at large times, independent of the density ratio. On the contrary, the unbalanced formulation produces comparatively larger currents which quickly increase with time. The effect of the balanced algorithm can also be observed in the errors in pressure jump where the errors are lower by two orders of magnitude as compared to the unbalanced formulation. It must be remarked that the errors are larger on unstructured grids as compared to the structured grids for both formulations and can be attributed to the relative coarseness of the unstructured grids employed. However, the errors in pressure jump on the structured meshes using the balanced formulation in the present study are lower than those reported in a similar study [32], where a similar grid resolution was employed. This may be possibly attributed to differences in the implementation of the balanced algorithm between the present study and those in [32].

We further consider the performance of the two formulations when the interface curvature is calculated. The evolution of the total kinetic energy, which must be ideally zero, is again a measure of spurious currents and is shown in Figures 4.2(a) and 4.2(b) for both formulations on the two different meshes. We observe that the spurious currents are larger for this case (as compared to imposing exact curvature) but remain bounded at large times when a balanced formulation is employed. This is in contrast

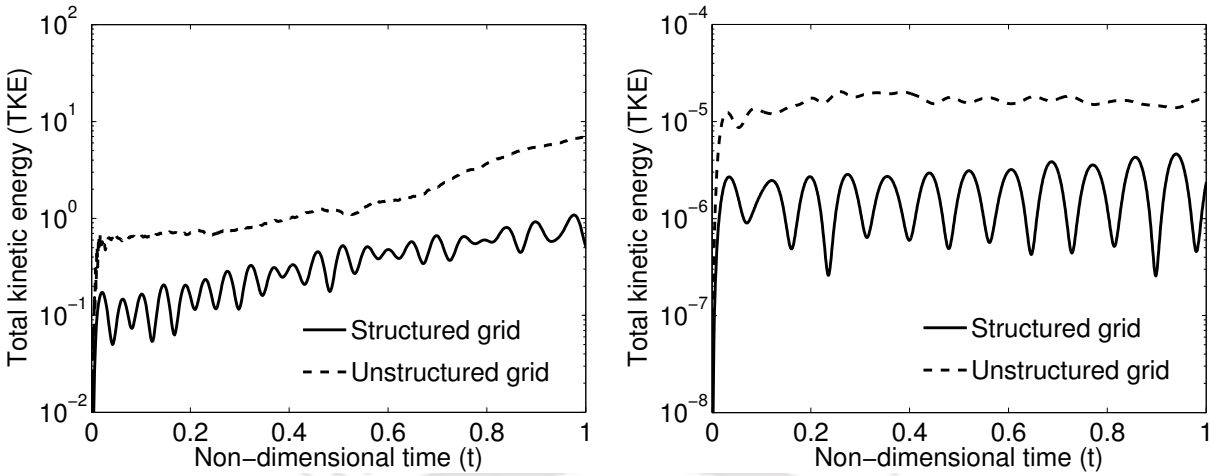

(a) Unbalanced algorithm (b) Balanced algorithm

Figure 4.2: The evolution of TKE with time for inviscid static droplet using Ubbink curvature model in (a) unbalanced and (b) balanced algorithms. The simulations are performed for density ratio $\frac{\rho_H}{\rho_L}$ = 10 and We = 1 with timestep Δt = 0.001.

to the conclusions in [32] where the use of CSF model with convolution of volume fraction for curvature calculation led to a constant increase in spurious currents even for a balanced formulation. The boundedness of the spurious currents in the present case, even when a less accurate curvature calculation is likely due to the specific approach adopted to effect the discrete balance. The methodology in [32] which uses a collocated framework, involves interpolations of quantities from cells to faces (and vice–versa) while the present approach, on account of its hybrid staggered/non–staggered framework, achieves the balance in a relatively more straightforward manner as described in Section 4.1. Not surprisingly, the unbalanced formulation indeed shows large spurious currents that increase with time. These results highlight the importance of the balanced formulation and we believe that the present implementation would suffice to handle more complex problems, although improved curvature calculations using the approaches in [32, 34] would definitely be beneficial in further lowering the magnitude of spurious currents.

4.3.2 Stationary water column in tank

The importance of balanced formulation when body forces are dominant in multiphase flows is investigated using a stationary water column. A tank of unit height and width

is filled up to half of its height with water. We assume an inviscid flow with a density ratio of 1000 and Fr = 1. The length and velocity scales are chosen as W and $\sqrt{gW}$, where W is the width of the tank. Simulations are carried out on a 100$\times$100 Cartesian mesh using Δt = 0.001. The pressure contours at time t = 1 using the unbalanced and balanced formulations are shown in Figures 4.3(a) and 4.3(b) respectively. It is evident that the unbalanced formulation generates significant spurious currents even at smaller times and predicts an erroneous pressure jump across the interface. The balanced formulation however estimates the exact pressure jump (which in this case is 499.5) and keeps the spurious currents to very low values of $\mathbf{O}(10^{-7})$ even at large times.

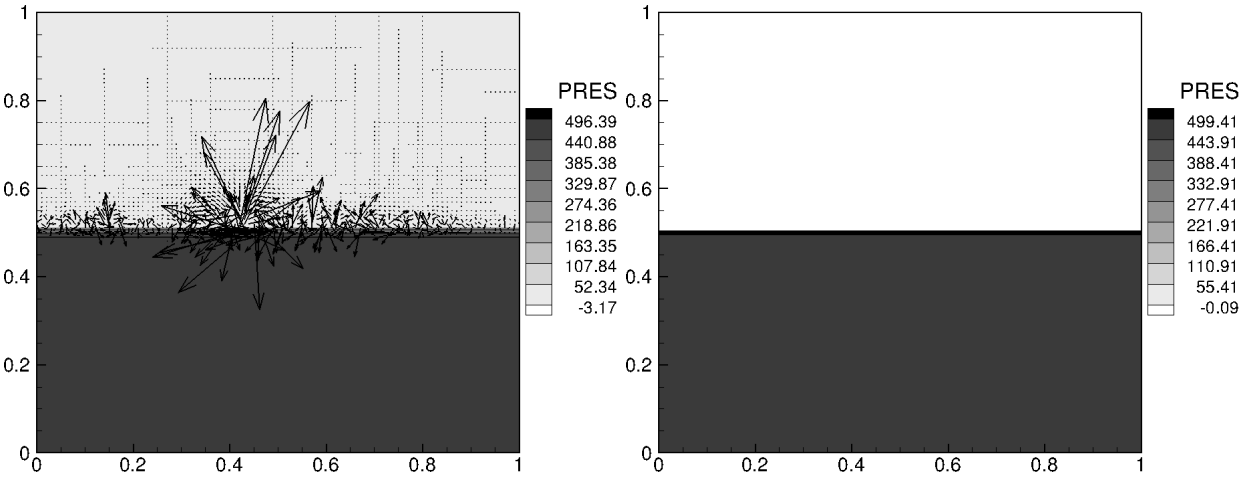

(a) Unbalanced formulation (b) Balanced formulation

Figure 4.3: Plots of the piezometric pressure superimposed with velocity vectors for $\frac{\rho_H}{\rho_L}$ = 1000, in inviscid stationary water column with (a) unbalanced and (b) balanced formulations. The scale for the vectors are identical in both figures.

While the balanced formulation discussed herein treats gravity as an interfacial force, a volumetric force treatment of the body force is also possible. The body force, in such a case, in simply $\rho_f g$ and is lumped at the face center, which may be considered as the centroid of the momentum control volume as well (see Figure 3.2). Following this approach, the pressure is hydrostatic and not piezometric. This is reproduced in our numerical simulations as well, where Figure 4.4 shows the correct linear pressure variation and no significant spurious currents are observed in this case even at t =

20. This is in contrast to the conclusions in [36] where the cell–centered treatment of gravity, albeit in a collocated framework, resulted in significant spurious currents and pressure errors. This study therefore points to the fact that use of identical operators for pressure and body forces are therefore not essential and other body forces may similarly be treated as volumetric forces lumped at the faces. Nevertheless, we shall continue with the use of piezometric pressure and interfacial treatment of gravity in the studies to follow.

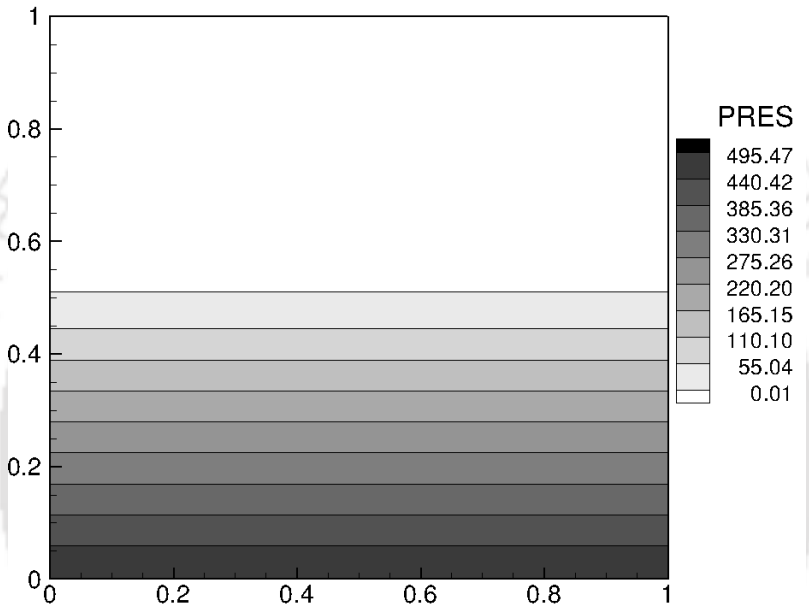

Figure 4.4: Pressure variation superimposed with velocity vectors for $\frac{\rho_H}{\rho_L}$ = 1000, in inviscid stationary water column at t = 20. The velocities are $\mathrm{O}(10^{-7})$.

4.3.3 Convection of large density droplet

We now examine the importance of consistent formulation by considering the convection of a large density droplet in a stagnant fluid. A droplet of diameter D = 1 centered in a 3×3 domain is moved with constant unit velocity (U = 1) in an outer stagnant fluid. We choose a uniform grid with $\Delta x = \Delta y =$ 0.01 and a density ratio of 10^6. The timestep for the simulation is $\Delta t = 10^{-4}$ and the simulation is carried out till t = 1. Gravity, surface tension and viscous effects are neglected in this study to focus solely on the discrete mass–momentum transport. The circular droplet shapes are significantly distorted in inconsistent formulation as shown in Figure 4.5(a). This is due to dissimilar

choice of convection schemes which leads to discretely inconsistent transport of mass and momentum and hence the spurious currents. The consistent formulation, on the other hand, largely preserves the shape of the droplet as the time progresses (shown in Figure 4.5(b)) despite some diffusion of the interface which is likely due to the coarser mesh resolution.

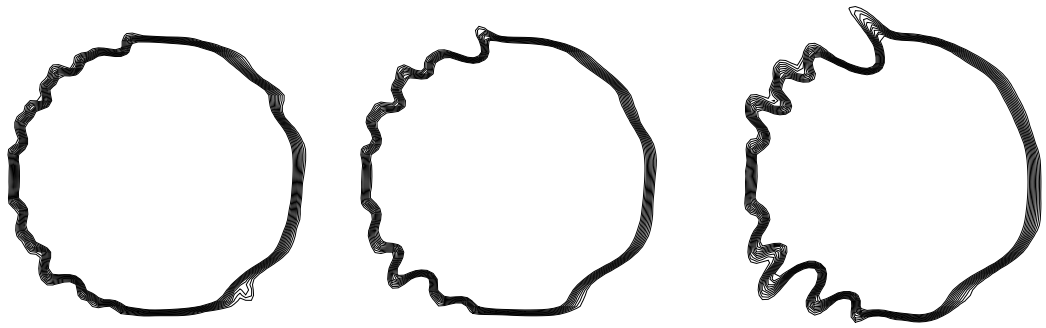

(a) Inconsistent formulation

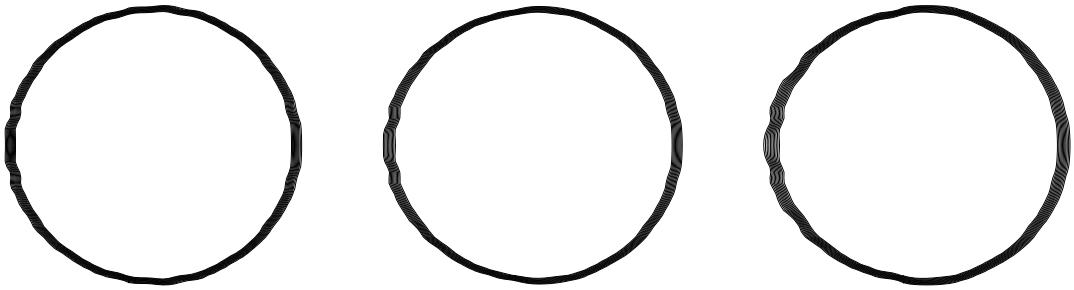

(b) Consistent formulation

Figure 4.5: Shape of the droplet of density ratio $\frac{\rho_H}{\rho_L}$ = 10^6 moving at constant velocity U = 1 with timestep Δt = 10^{-4} using (a) inconsistent and (b) consistent formulations.

4.3.4 Translating droplet

Having discussed the effects of balanced formulation and consistent transport separately, we now discuss their combined effect in this subsection. A viscous drop is placed in a channel of length 5 and height 3 at (1, 1.5). The drop has a diameter D = 1 and the domain is discretised using a Cartesian mesh with $\Delta x = \Delta y =$ 0.02. We specify a uniform inlet velocity of unity and Neumann boundary condition at outlet with

the lateral surfaces being slip boundaries. The liquid inside the droplet is initialized to same velocity as the inlet and only surface tension effects are accounted for by specifying the exact curvature [1], whilst neglecting gravity.

Studies are first performed at We = 1 for two different Reynolds numbers and density ratios (10 and 1000) by considering fluids of equal dynamic viscosity. A timestep of Δt = 0.001 is chosen for the simulations which are carried out up to t = 3.

Figures 4.6(a) to 4.6(d) show the maximum error in the velocity in the domain relative to the background fluid flow and therefore is a direct measure of the spurious currents. We see from Figures 4.6(a) and 4.6(c) that for an inconsistent formulation, the spurious currents are nearly independent of whether a balanced approach is employed or not, for a given Reynolds number and density ratio. A more interesting fact evident from these figures is that although the spurious currents are the highest for the largest density ratio at Re = 10, they are quite significant even for a density ratio of 10 at Re = 1000. It is easy to see that the spurious currents in these two cases are equal or more than the background velocity itself, causing unphysical deformation of the droplet (not shown here for sake of brevity) as time progresses. On the other hand, the use of a consistent formulation exhibits much smaller spurious currents in comparison (as shown in Figures 4.6(b) and 4.6(d)), with the use of a balanced force approach leading to a reduction in spurious currents by nearly an order of magnitude as compared to an unbalanced force approach. We also remark that only the use of a consistent formulation closely preserved the circular shape of the droplet in all cases.

We conduct a second study to investigate the influence of viscosity ratio on the numerical results but keep the Reynolds number and density ratio constant at 10 and 1000 respectively. Figures 4.7(a) and 4.7(b) show the results employing a balanced force approach with inconsistent and consistent transport respectively for viscosity ratios of 1 and 1000. We observe that the spurious currents are significantly smaller at larger (realistic) viscosity ratios, although the consistent formulation still produces

[1] It is not correct to apply the exact curvature when the drop deforms, but we still do so to avoid spurious errors that would arise from curvature calculations.

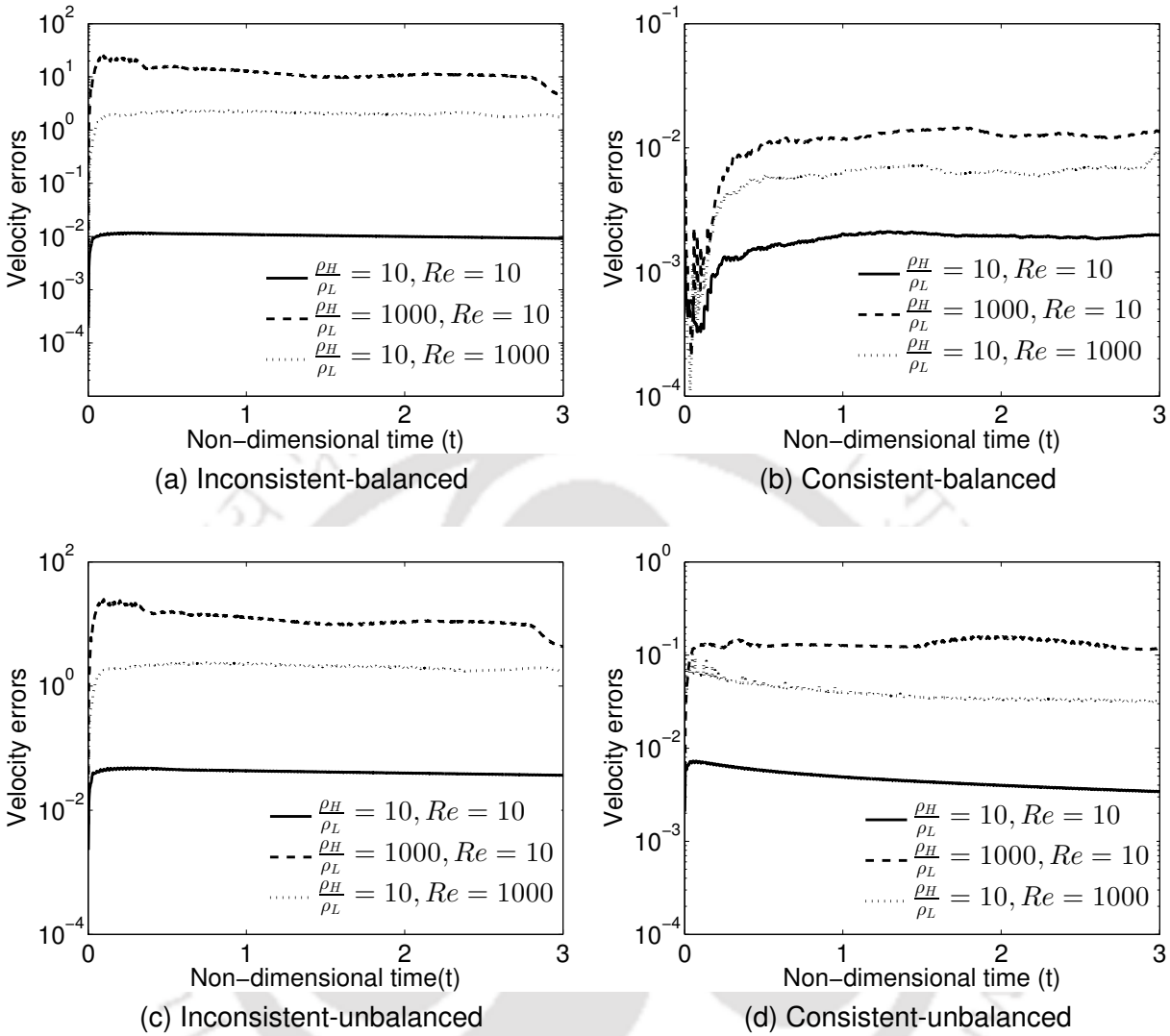

Figure 4.6: L_∞ norm of the velocity error relative to the background fluid moving with velocity U = 1 for We = 1, $\frac{\mu_H}{\mu_L}$ = 1 and Δt = 0.001 using different formulations: (a) inconsistent-balanced (b) consistent-balanced (c) inconsistent-unbalanced (d) consistent-unbalanced.

lesser currents as compared to the inconsistent formulation. This may be possibly attributed to the pronounced damping at larger viscosity ratios. For the smaller viscosity ratio, as also observed in the earlier study, only the consistent approach preserves the shape of the droplet and results in acceptably low values of spurious currents.

A third study is conducted at low Capillary numbers for static and moving droplets with both exact and calculated curvature. We choose We = 0.01 and Re = 10, which corresponds to a capillary number of Ca = 0.001, with large density and viscosity ra-

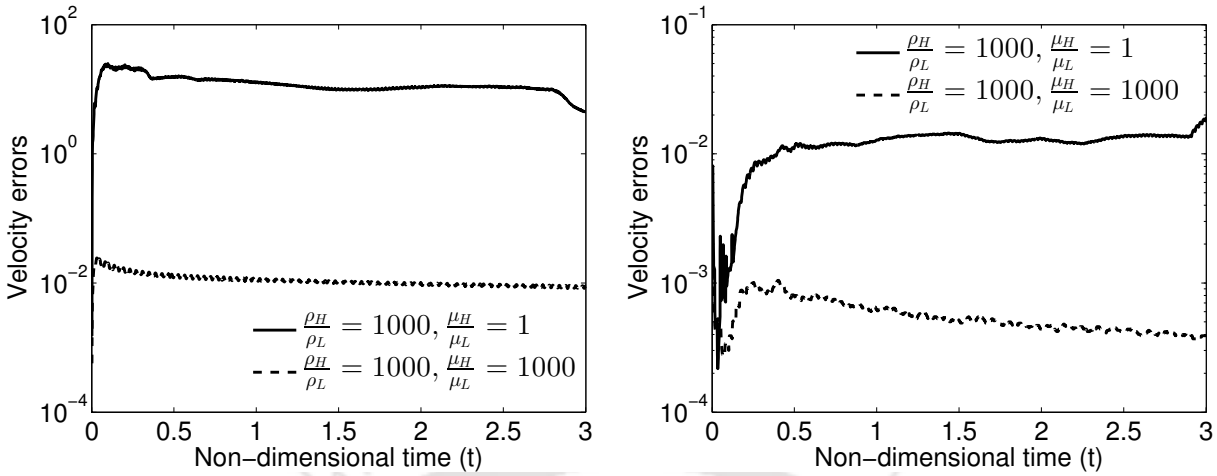

(a) Inconsistent-balanced (b) Consistent-balanced

Figure 4.7: L_∞ norm of the velocity error relative to the background fluid moving with velocity U = 1 for We = 1, Re = 10 and Δt = 0.001 using (a) inconsistent-balanced and (b) consistent-balanced formulations.

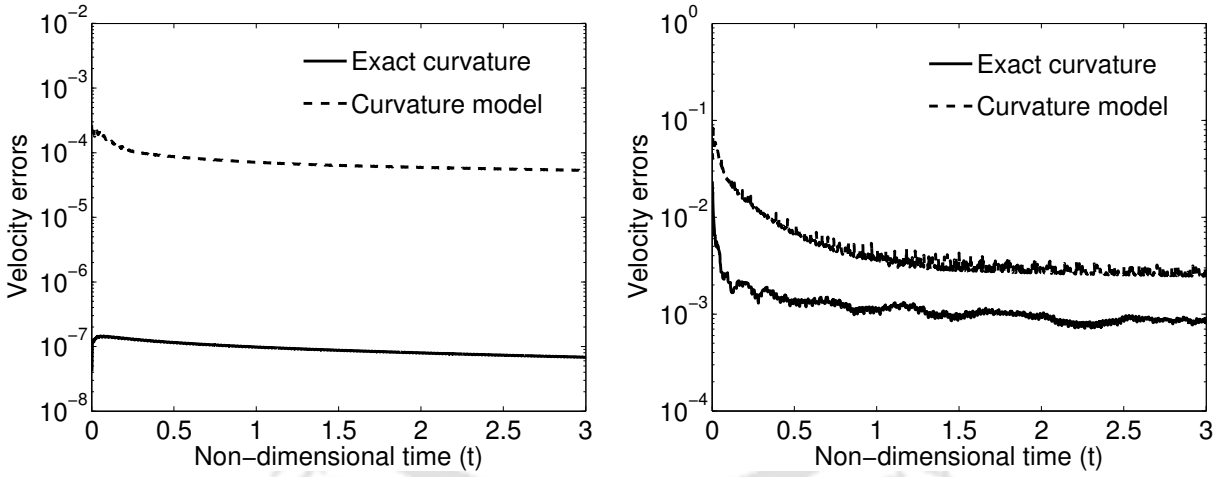

(a) Static (b) Moving

Figure 4.8: L_∞ velocity error of a droplet for We = 0.01, Re = 10, $\frac{\rho_H}{\rho_L}$ = 1000, $\frac{\mu_H}{\mu_L}$ = 1000 and Δt = 0.001 in a consistent-balanced formulation for (a) static and (b) moving cases.

tios (both 1000). Simulations are performed using only the consistent and balanced formulation for the case of the static (specifying zero inlet velocity) and the translating droplet. The results in Figures 4.8(a) and 4.8(b) show that the calculation of curvature introduces higher spurious currents as compared to exact specified interface curvature in both static and moving cases. Furthermore, the increase in spurious currents due to errors in curvature calculation are less pronounced in the moving case but are

more prominent in the static case. While one could argue that the moving and static problems are essentially equivalent (differing by only the constant background velocity field), the calculated spurious errors appear to be significantly different, for a given curvature calculation. While this result is surprising and requires further investigation it appears to be consistent with the observations in the recent investigation of [30], who showed that the use of a moving reference frame in slug flows led to significantly reduced spurious currents as opposed to calculations on a stationary fixed reference frame with moving bubbles. Nevertheless, these studies clearly demonstrate that the consistent and balanced force algorithm performs the best leading to acceptably low spurious currents at high density ratios and even at low Capillary numbers where traditional algorithms are known to often experience difficulties.

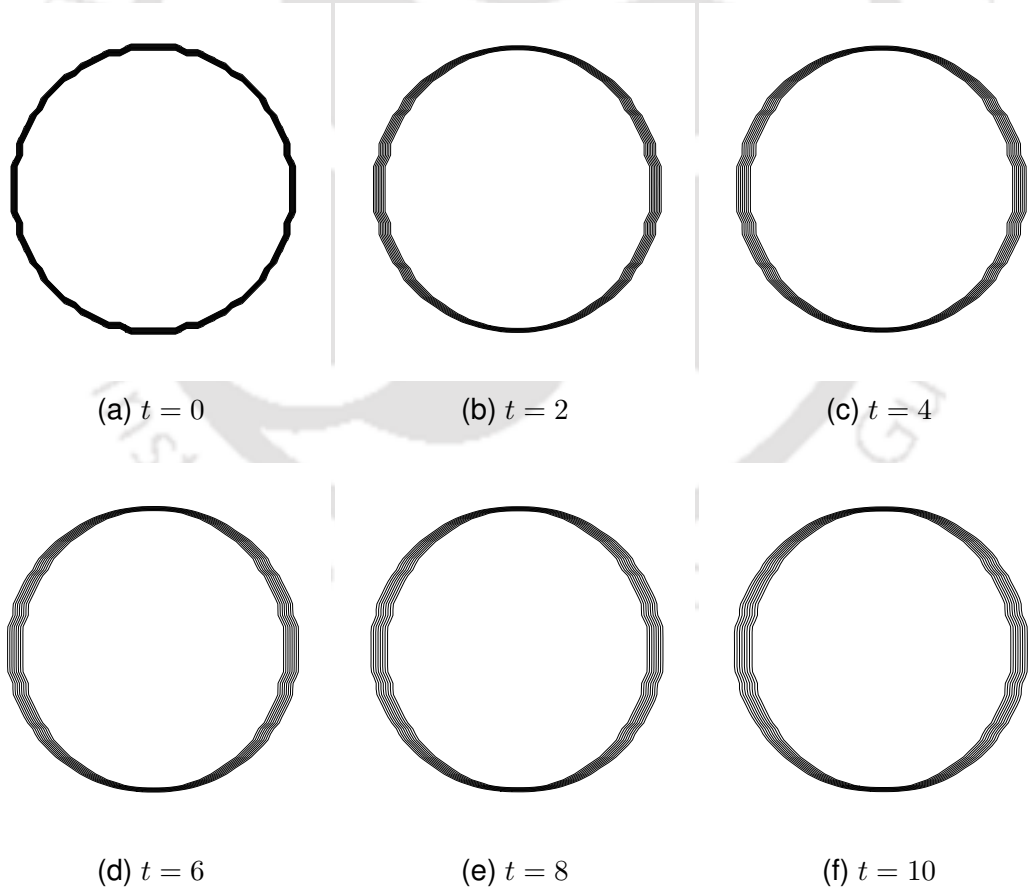

(a) $t = 0$ (b) $t = 2$ (c) $t = 4$

(d) $t = 6$ (e) $t = 8$ (f) $t = 10$

Figure 4.9: Line contours of volume fraction at time levels $t =$ (a) 0 (b) 2 (c) 4 (d) 6 (e) 8 and (f) 10 moving with velocity U =1 for Re =10, $\frac{\rho_H}{\rho_L}$ =1000, We =1, $\frac{\mu_H}{\mu_L}$ =1 and Δt =0.001 using the consistent–balanced formulation.

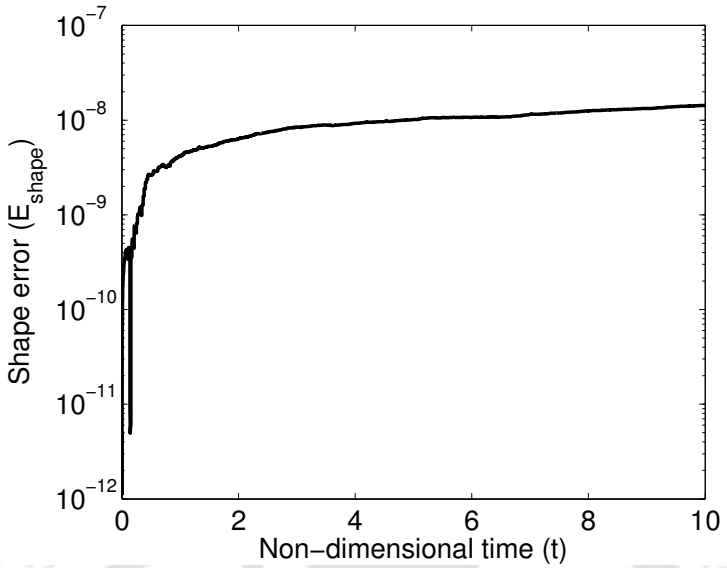

Figure 4.10: Volume/shape error of a translating droplet moving with velocity U =1 for Re =10, $\frac{\rho_H}{\rho_L}$ =1000, We =1, $\frac{\mu_H}{\mu_L}$ =1 and Δt =0.001 using the consistent–balanced formulation.

We also quantify the volume/shape losses in the proposed algorithm by considering the translation of the droplet at $We = 1$, $Re = 10$ with a density ratio equal to 1000 and unit dynamic viscosity ratio using the consistent transport and balanced force formulation. For this case we use a longer 12×3 computational domain with same grid resolution as employed in the previous studies. The upwind–biased CUI scheme is indeed prone to interface diffusion and we attempt to investigate this interface diffusion and associated volume losses in this numerical experiment. Figures 4.9(a) to 4.9(f) show the interface diffusion at different time instants in the course of simulation. While one can clearly see that the interface diffuses over time, the diffusion is observed to be limited within 2–3 cells even at long times. We also calculate the shape errors as,

$$E_{shape} = \frac{\sum_{i=1}^{N} |\phi_c^n \Omega_c - \phi_c^0 \Omega_c|}{\sum_{i=1}^{N} \phi_c^0 \Omega_c} \tag{4.4}$$

where N is the total number of control volumes in the domain and superscripts n and 0 denote the numerical and initial volume fractions. The temporal history of E_{shape} is presented in Figure 4.10 and is acceptably low and remains bounded at long times. This study establishes the fact that the interface–free reconstruction approach in conjunc-

tion with consistent mass/momentum transport and well–balanced approach is an ideal methodology for computations of realistic flow phenomena with high density ratios.

4.3.5 Two fluid Poiseuille flow

The Poiseuille flow of two immiscible fluids in a channel provides an ideal test case to highlight the importance of consistent formulation in gravity–dominated flows. We consider a horizontal channel with dimensions of [0,5]×[-1,1] which is discretised using a uniform Cartesian mesh with Δx = Δy = 0.02. We set the inlet and outlet pressures to zero and apply the gravity in the flow direction. The velocity scale is here chosen as $\sqrt{gW}$ and the width of the channel W is chosen as the length scale. We neglect the effects of surface tension in this study and carry out simulations for four different sets of parameters as shown in Table 4.2. The analytical fully developed profile may be easily derived as,

$$U = \begin{cases} \dfrac{Re}{Fr}\left[\left\{\dfrac{1}{2(1+\beta)} + \dfrac{\beta y}{2(1+\beta)} - \dfrac{y^2}{2}\right\} - \alpha\left\{\dfrac{1}{2(1+\beta)} - \dfrac{y}{2(1+\beta)}\right\}\right] & \text{if } y \geq 0 \\ \dfrac{Re}{Fr}\left[\left\{\dfrac{1}{2(1+\beta)} + \dfrac{y}{2(1+\beta)}\right\} - \alpha\left\{\dfrac{1}{2(1+\beta)} - \dfrac{y}{2\beta(1+\beta)} - \dfrac{y^2}{2\beta}\right\}\right] & \text{if } y < 0 \end{cases}$$

where $\alpha = \frac{\rho_H}{\rho_L}$ and $\beta = \frac{\mu_H}{\mu_L}$ represent the density and viscosity ratios respectively.

Table 4.2: Simulation parameters for two fluid Poiseuille flow.

Test	Re	$\frac{\rho_H}{\rho_L}$	$\frac{\mu_H}{\mu_L}$	Fr	We	Δt
C1	10	10	1	1	–	0.001
C2	10	1000	1	100	–	0.001
C3	10	1000	100	1	–	0.001
C4	1000	10	1	1	–	1×10^{-6}

The velocity profiles at the outlet obtained with both consistent and inconsistent formulations, which is balanced in either case, are shown in Figures 4.11(a) to 4.11(d) for the four different cases. It is easy to see that the steady state solutions obtained using a consistent formulation agree well with the analytical result in all cases. The inconsistent formulation, on the other hand, performs as well as the consistent formulation in

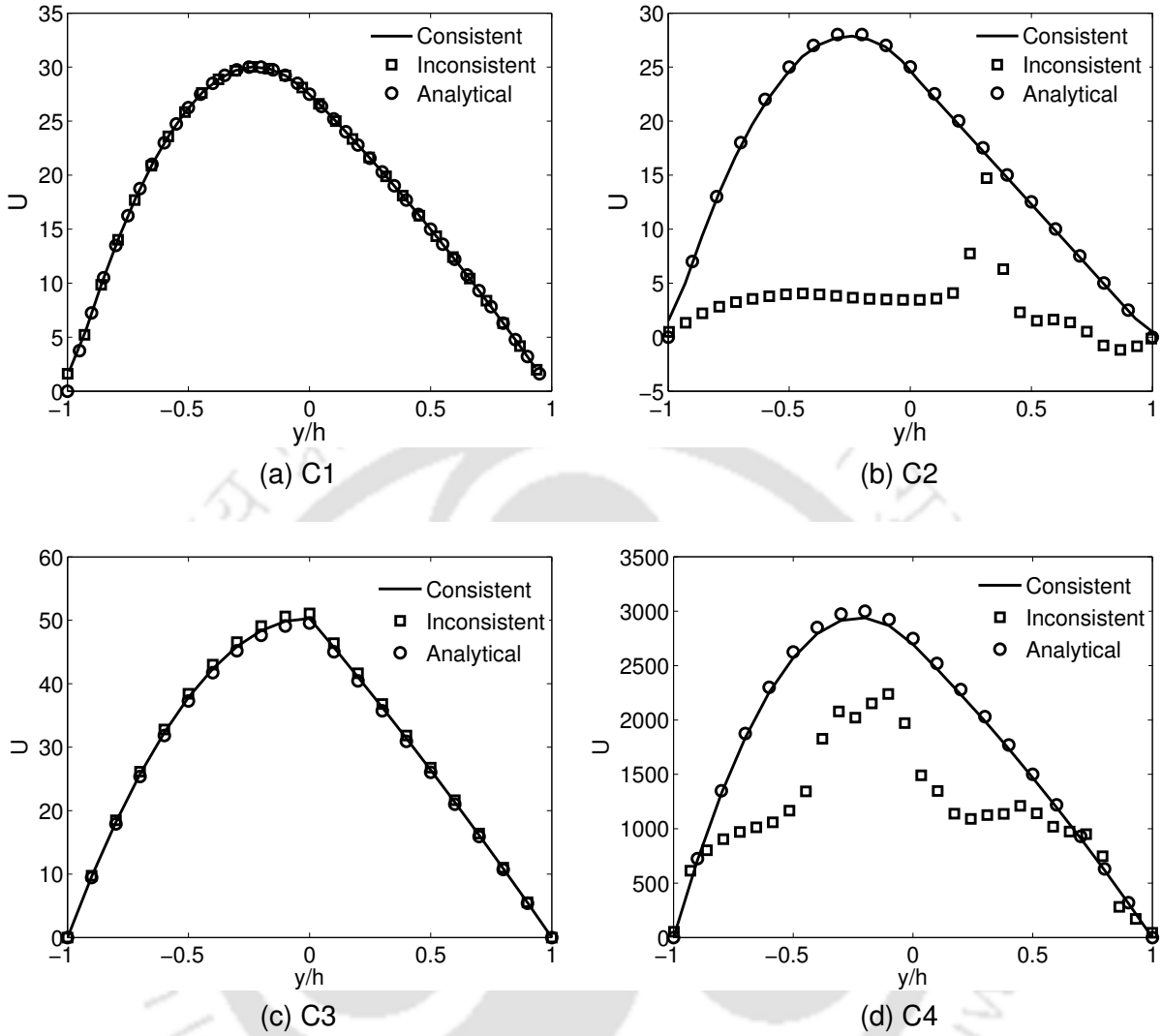

Figure 4.11: Non–dimensional velocity profiles in two fluid Poiseuille flow for test cases (a) C1 (b) C2 (c) C3 and (d) C4.

cases C1 and C3 but fails completely in cases C2 and C4. This is also evident in the significant distortion of the interface shown in Figures 4.12(a) and 4.12(b). It must be remarked that while C2 represents a flow with high density ratio, case C4 involves a much smaller density ratio albeit at a larger Reynolds number. While cases C1, C2 and C4 involve unit viscosity ratio, Case C3 considers more realistic density and viscosity ratios and results in stable and accurate solution using both formulations, though at a lower Reynolds number.

While the use of dissimilar schemes for convection lead to an inconsistent trans-

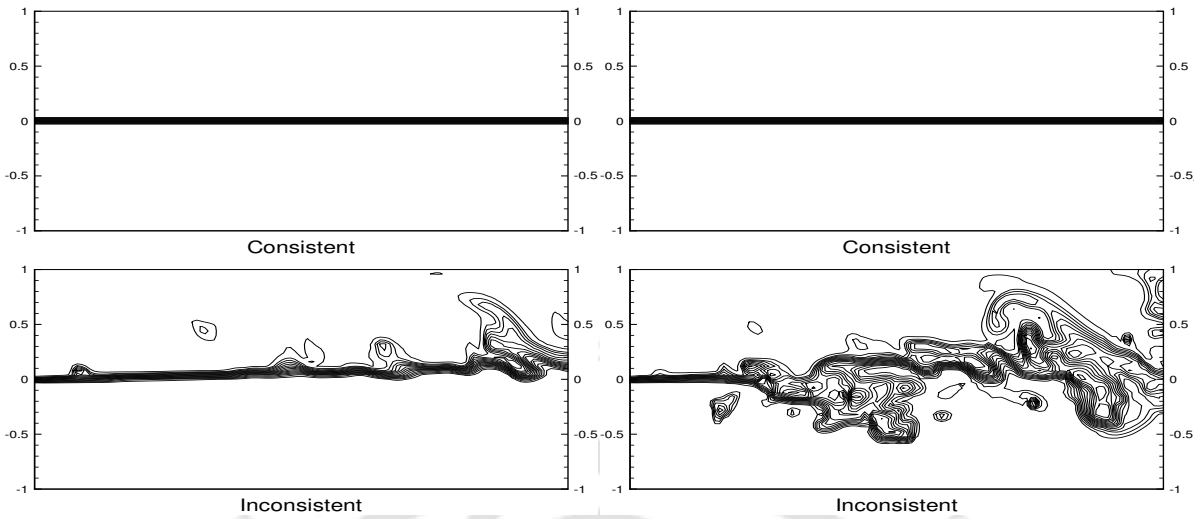

(a) C2 (b) C4

Figure 4.12: The distortion of the interface using consistent and inconsistent formulations for test cases (a) C2 and (b) C4.

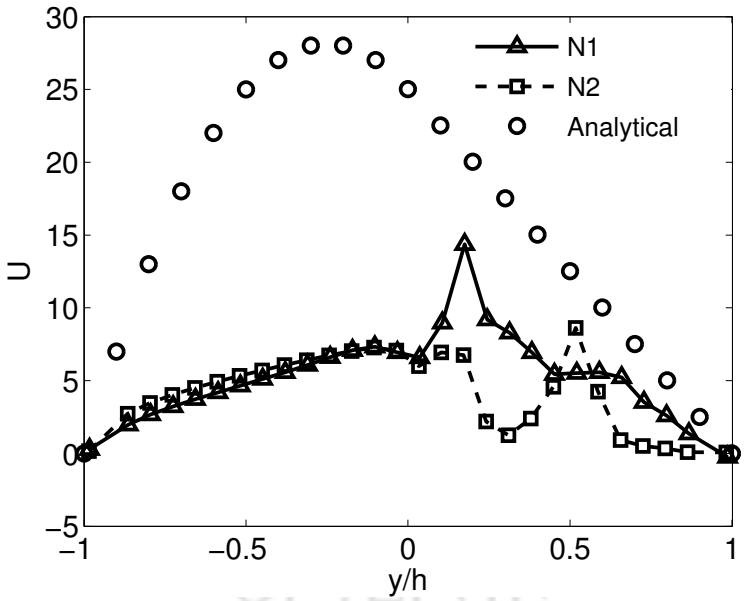

Figure 4.13: Non–dimensional velocity profiles in C2 for two fluid Poiseuille flow.

port and unstable solutions for cases C2 and C4, one could argue that the different orders of accuracy of convective schemes used in the inconsistent formulation (1 for upwind and 2 for the CUI scheme) may be the source of instability. In order to investigate if this is indeed the case, we repeated the case C2 (which is more stringent) using dissimilar convection schemes of second–order accuracy for both mass and momentum transport. While the scheme N1 uses the high resolution scheme in [22] for

momentum and CUI for volume fraction, scheme N2 adopts CUI for momentum and compressive CUIBS scheme for volume fraction [84]. The velocity profiles obtained using these schemes are presented in Figure 4.13 and show that anomalous velocities are obtained in both cases, which underscore the fact that the dissimilar advection schemes themselves and not their orders of accuracy is responsible for the error. This also strongly suggests that the use of a consistent formulation may be necessary for high density multiphase flow simulations and in particular those involving high shear.

4.3.6 Simulations of flow instabilities

Flow instabilities are ubiquitous in many applications and can involve high density ratios and/or high shear. We consider the simulations of (a) Rayleigh–Taylor and (b) Kelvin–Helmholtz instabilities to investigate the importance of consistent and inconsistent formulations in such flows. In these studies, we neglect the effects of surface tension for the sake of simplicity.

4.3.6.1 Rayleigh–Taylor instability

We choose a rectangular domain [-0.5,0.5]$\times$[0,4] for the simulations which is triangulated into 22256 elements. The velocity scale and length scale are chosen as $\sqrt{gW}$ and the width of the domain W respectively. In order to avoid any effects of mesh asymmetry on the interface dynamics, we construct the unstructured mesh symmetric about the vertical centerline. The interface is initially perturbed as $y = 2 + 0.1\cos(2\pi x)$ and timestep is fixed to Δt = 0.001. We study the instability for two cases, of low and high Atwood numbers in moderate and strong gravity fields respectively.

The first case following the numerical studies of Wang et al. [101] has an Atwood number 0.5 which corresponds to a density ratio of 3 and the viscosity ratio is also chosen as 3. The other dimensionless parameters for the simulation are Re = 256, Fr = 1. The interface morphology at different time instants using inconsistent and consistent formulations are shown in Figures 4.14(a) and 4.14(b). The time evolution of the interfaces show excellent qualitative agreement while remaining symmetric, indepen-

dent of whether a consistent approach is employed. This is also reflected in the bubble and spike positions shown in Figure 4.15, which agree well with the results of Wang et al. [101].

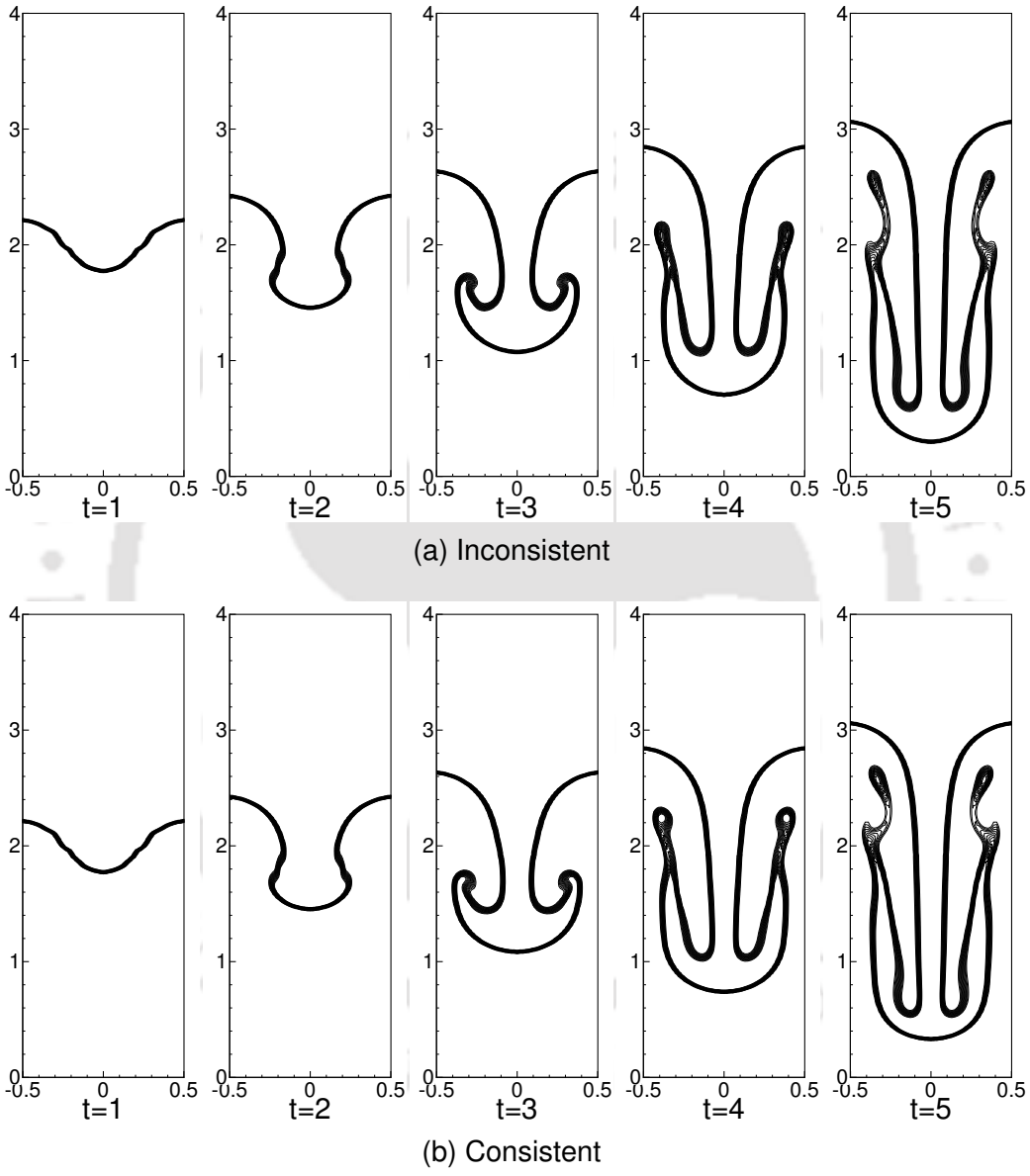

Figure 4.14: Time plots of Rayleigh–Taylor instability for $\frac{\rho_H}{\rho_L}$ = 3, $\frac{\mu_H}{\mu_L}$ = 3, Re = 256 and Fr = 1 on unstructured grid using (a) inconsistent and (b) consistent formulations.

For the second case, we choose a strong gravity field corresponding to Fr = 0.1 for a density ratio of 7, that translates to a moderately large Atwood number of 0.75. We choose a larger Re = 1000, while keeping the viscosity ratio equal to unity. The position of the interface at different instants of time using inconsistent and consistent

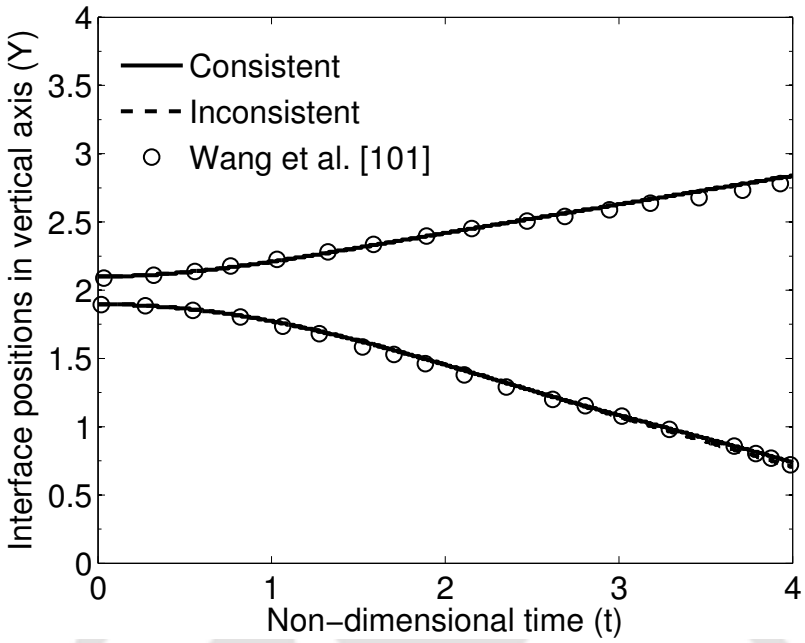

Figure 4.15: Time history of the interface position on left wall (top three lines) and at the vertical centerline (bottom three lines) for low At = 0.5.

formulations are shown in Figures 4.16(a) and 4.16(b) respectively. It is evident that the inconsistent formulation converges to a non–physical solution with a significant symmetry breaking at large times leading to a distorted interface. On the contrary, the consistent formulation preserves the symmetry about the vertical centerline correctly predicting a central spike even on the unstructured mesh.

The results show that the use of an inconsistent formulation leads to a robust and accurate simulation when employed for a low Atwood number case, while it results in anomalous results for larger Atwood and Reynolds numbers in a stronger gravitational field.

4.3.6.2 Kelvin–Helmholtz instability

We now perform viscous simulations of shear instability in a unit square domain. The domain is discretised into a uniform 200$\times$200 mesh and periodic boundary conditions are applied in the x-direction while slip velocities are provided in the y-direction. The two fluids which have a density ratio of 2 and equal viscosities are separated by an interface at the mid plane corresponding to y = 0.5. We initialise the velocity field and

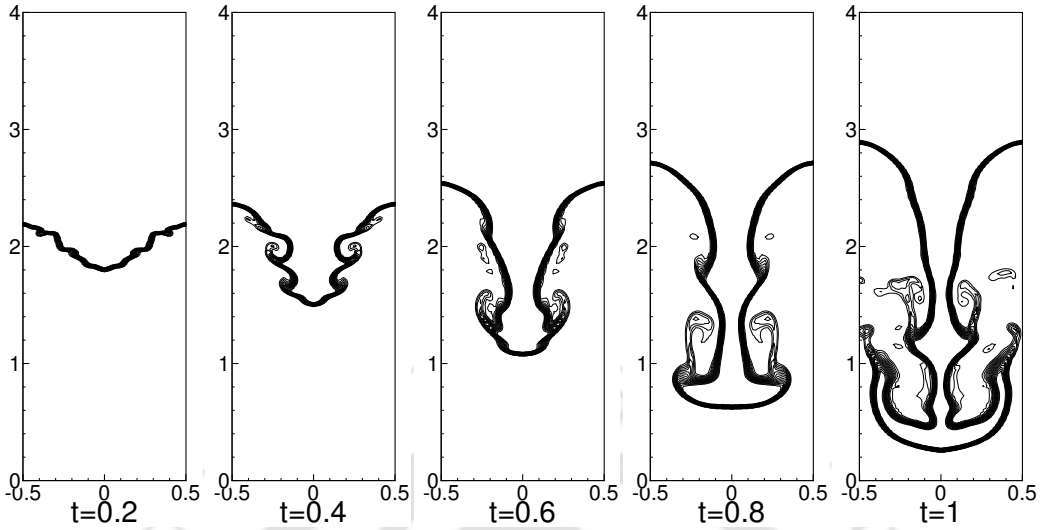

(a) Inconsistent

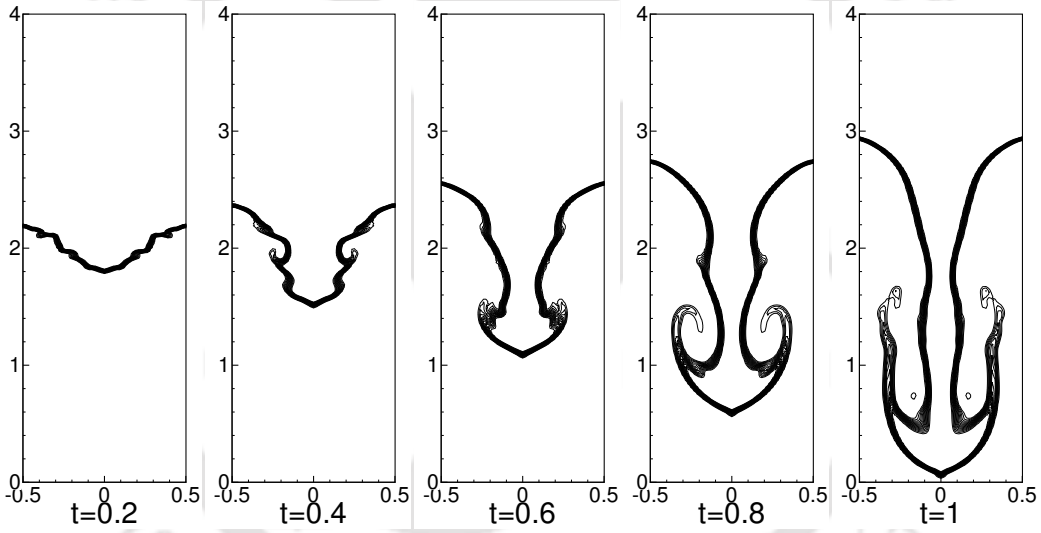

(b) Consistent

Figure 4.16: Time plots of Rayleigh–Taylor instability for $\frac{\rho_H}{\rho_L}$ = 7, $\frac{\mu_H}{\mu_L}$ = 1, Re = 1000 and Fr = 0.1 on unstructured grid using (a) inconsistent and (b) consistent formulations.

volume fraction in the domain as follows [102].

$$u = \tanh\left(\frac{y - 0.5 - 0.01\sin(2\pi x)}{0.01}\right) \tag{4.5}$$

$$v = 0 \tag{4.6}$$

$$\phi = 0.5\left(1 + \tanh\left(\frac{y - 0.5 - 0.01\sin(2\pi x)}{0.01}\right)\right) \tag{4.7}$$

Simulations are carried out using $\Delta t = 5 \times 10^{-4}$ up to t = 1 using both consistent

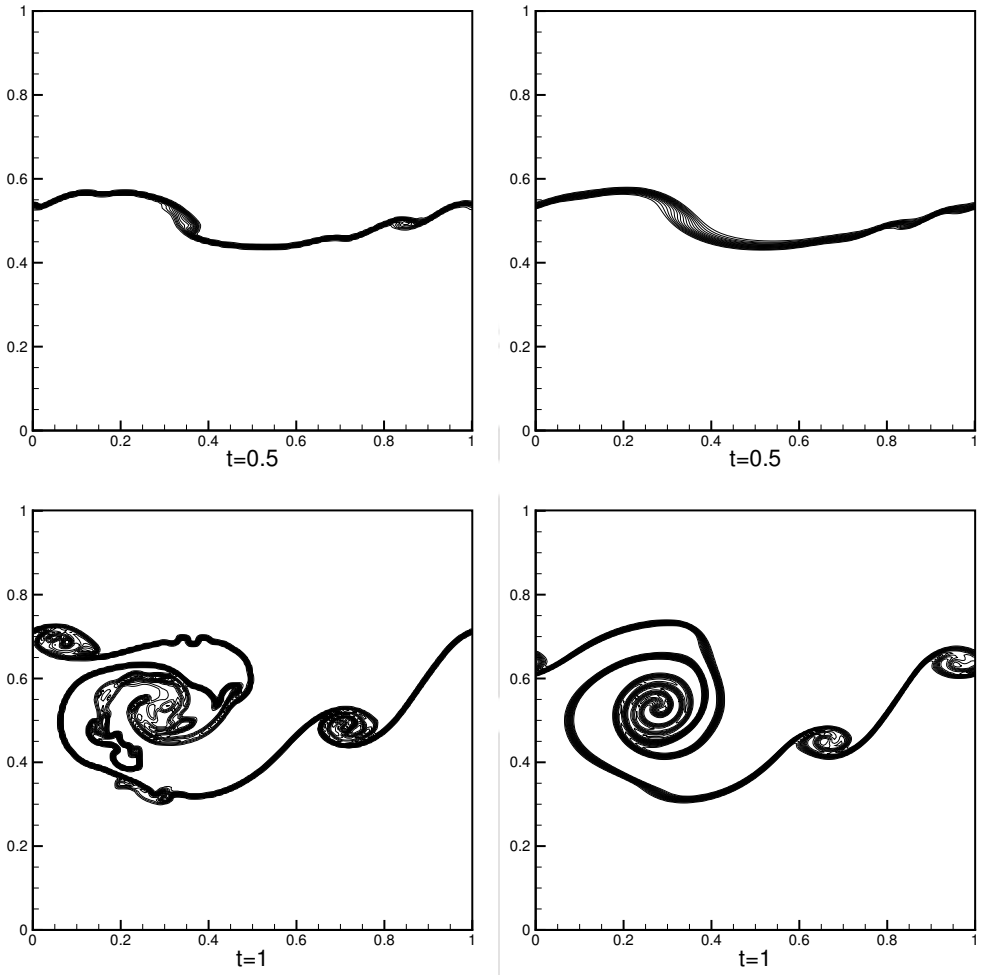

(a) Inconsistent formulation (b) Consistent formulation

Figure 4.17: The volume fraction profile of Kelvin–Helmholtz instability for $\frac{\rho_H}{\rho_L}$ = 2, $\frac{\mu_H}{\mu_L}$ = 1 and Re = 5000 using (a) inconsistent and (b) consistent formulations.

and inconsistent formulations. In these studies, we choose Re = 5000 and neglect the effects of gravity to focus on the effect of high shear. Figures 4.17(a) and 4.17(b) show the interface between the fluids using the two approaches at t = 0.5 and t = 1 respectively. It is evident that the inconsistent formulation introduces errors which cause anomalous deformation of the interface while also leading to a completely different roll–up pattern, as compared to the consistent formulation.

The results for the simulation of R–T and K–H instabilities further underline the importance of consistent mass–momentum transport in flows with high density ratio as well as high shear. Coupled with a balanced force framework, we believe that

a consistent formulation as described in this work, presents a robust approach for simulating complex multiphase flows involving large density contrasts and high shear such as those encountered in primary atomization.

4.3.7 Rising bubble in stagnant fluid

We now consider a multi–physics test case, involving both effects of gravity and surface tension, that has been the subject of many investigations using multiphase flow solvers. We simulate the rise of an air bubble in stagnant water using the benchmark studies of Hysing et al. [103] and choose Re = 3.5, We = 0.125 and Fr = 1 with the density and viscosity ratios being 1000 and 100 respectively. This test case is a challenging one for multiphase flow solvers, in particular because the bubble lies in a regime where break–up can possibly occur. The bubble of diameter D = 1 is initially positioned at (1, 1) in a computational domain of 2$\times$4 which is discretised into 80426 triangular elements, ensuring grid symmetry about the centerline of the channel. The length and velocity scales are the diameter of the bubble D and $\sqrt{gD}$ respectively. Simulations are carried out up to t = 4.2 with a timestep of Δt = 0.001 with both consistent and inconsistent formulations.

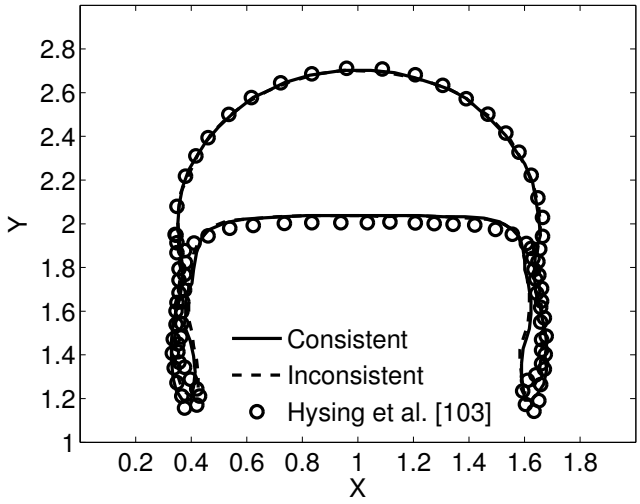

Figure 4.18: Comparison of the bubble shape at time t = 4.2.

The rising bubble continuously deforms due to buoyancy and drag with the surface

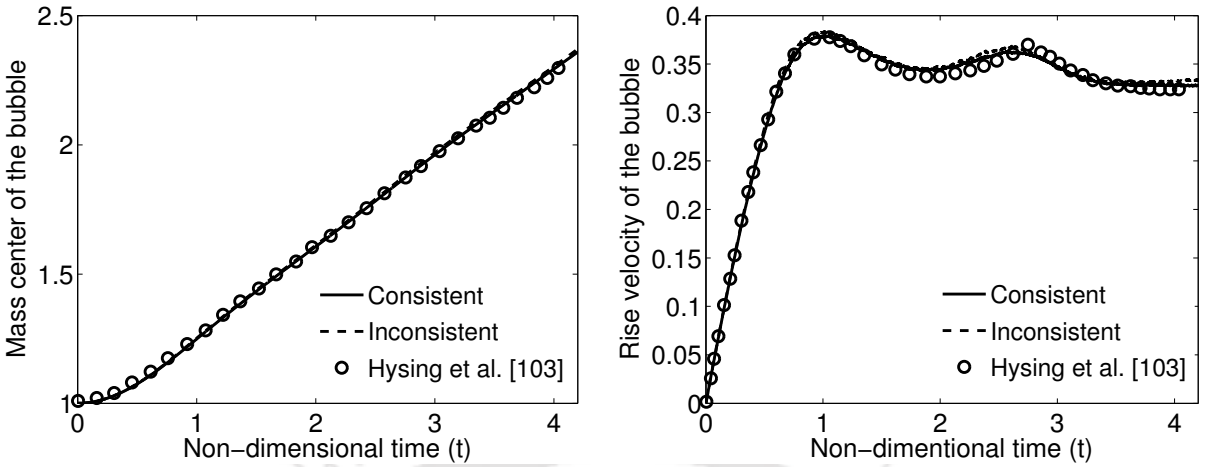

(a) Bubble mass center (b) Rising velocity

Figure 4.19: Time evolution of (a) bubble mass center (b) rising velocity for $\frac{\rho_H}{\rho_L}$ = 1000, $\frac{\mu_H}{\mu_L}$ = 100, Re = 3.5, We = 0.125 and Fr = 1 on unstructured grid.

tension trying to provide a stabilising effect. The shape of the bubble at t = 4.2 shown in Figure 4.18 is compared with those in [103] and shows a very good agreement when employing either formulation. Interestingly, the evolution of mass center of the bubble and rise velocity obtained from both formulations (see Figures 4.19(a) and 4.19(b)) also agree well with the results in [103].

We repeat this experiment with a viscosity ratio of unity while keeping all other parameters unchanged. The shapes of the bubble at three different time instants are shown in Figures 4.20(a) and 4.20(b) for the inconsistent and consistent formulations respectively. While a validation study for this test is not available, the inconsistent formulation introduces non–physical distortion of the interface while the consistent formulation largely preserves the left–right symmetry of the bubble. The results from these numerical experiments show that the inconsistent formulations may lead to physically consistent solutions even for high density ratios under some conditions but could fail in other scenarios.

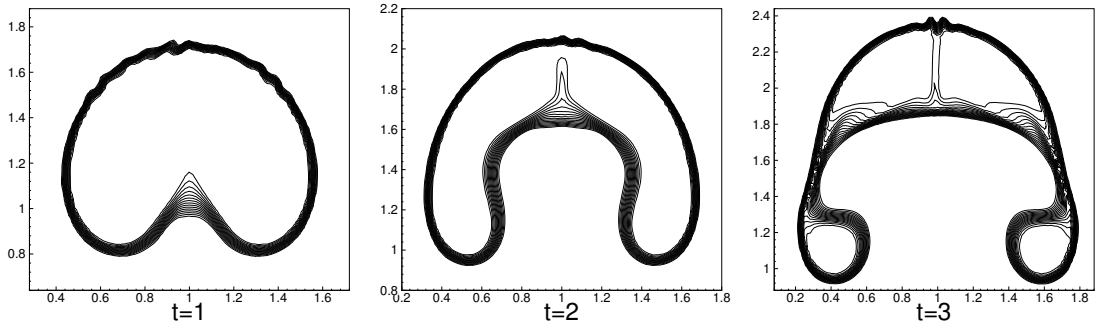

(a) Inconsistent formulation

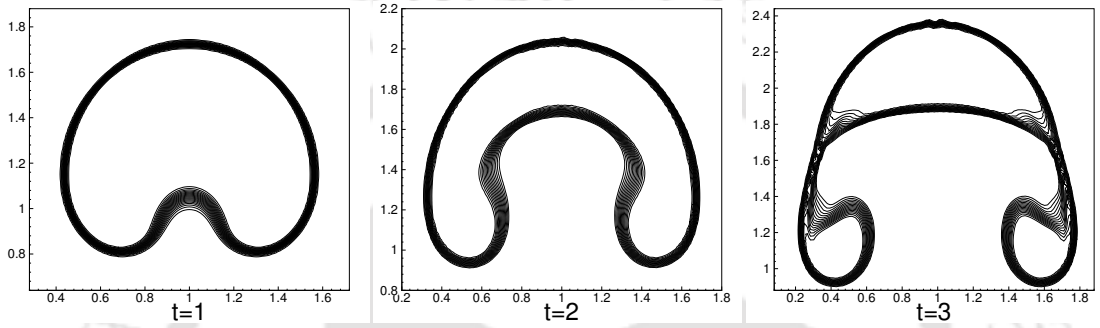

(b) Consistent formulation

Figure 4.20: Shape of the rising bubble in (a) inconsistent and (b) consistent formulations at different times on unstructured grid for $\frac{\rho_H}{\rho_L}$ = 1000, $\frac{\mu_H}{\mu_L}$ = 1, Re = 3.5, We = 0.125 and Fr = 1.

4.3.8 Droplet splashing on thin liquid film

To assess the importance of consistent transport in multiphase simulations we consider the problem of a droplet splashing on a thin layer of liquid. This problem is representative of real–life applications such as inkjet printing and involves complex flow physics, which necessitates a robust and accurate flow solver. For the simulations, we consider a 6×2 rectangular domain with a uniform grid resolution of $\Delta x = \Delta y$ = 0.01. A thin layer of liquid is filled to $(\frac{1}{10})^{th}$ the domain height and a droplet of the same liquid with diameter D = 1, centrally placed just above the layer is given an initial downward velocity of U = 1 (downward). We consider that the working fluids are air and water which correspond to realistic density and viscosity ratios of 815 and 55 at room temperature. Since the impact occurs very quickly, gravity does not play a major role in this case and may be neglected. Simulations are carried out at Re = 66 and We = 0.126 using a timestep Δt = 0.001 up to t = 1.5.

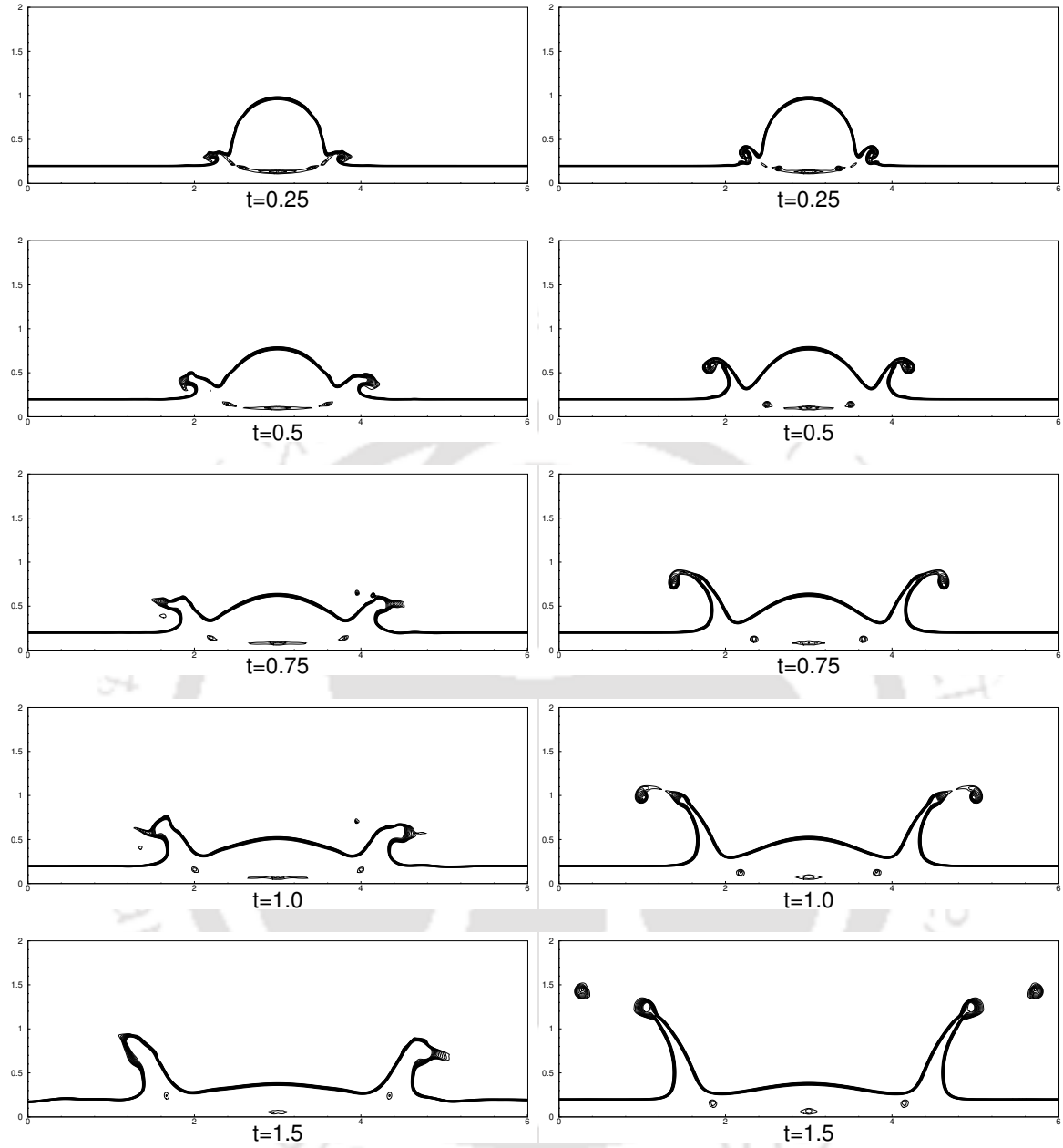

(a) Inconsistent formulation (b) Consistent formulation

Figure 4.21: Instantaneous profile of droplet splashing on thin liquid layer for $\frac{\rho_H}{\rho_L}$ = 815, $\frac{\mu_H}{\mu_L}$ = 55, Re = 66 and We = 0.126 using (a) inconsistent and (b) consistent formulations.

The process of splashing is pictorially represented in Figures 4.21(a) and 4.21(b) respectively for inconsistent and consistent formulations. We observe significant differences between the two formulations with the former exhibiting unphysical asymmetry of the solution at later times (t > 1). The consistent formulation predicts a symmetric splash leading to the "crown" at t = 1.5 and the results agree favourably in the quali-

tative sense with those in Li et al. [104] (where the Re = 1000 based on heavier fluid properties). However, unlike in the results in [104] which were obtained using a Lattice Boltzmann method, we observe satellite droplets (which are diffused due to a relatively coarse mesh) and air entrapment in the thin layer. There is however no physical mechanism to generate satellite droplets in planar flows and the flow scenario simulated herein is not realistic.

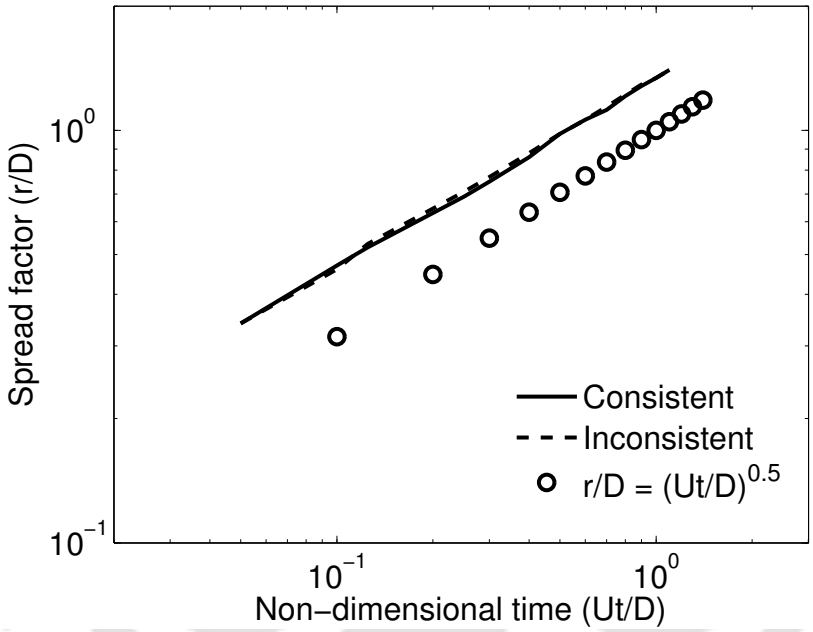

Figure 4.22: The evolution of spread factor with non-dimensional time for Re = 66.

Figure 4.22 shows the temporal evolution of the spread factor $\frac{r}{D}$, where r is the crown radius with the dimensionless time $\frac{Ut}{D}$. Despite being a two–dimensional simulation, the evolution of crown radius follows a power–law defined by $\frac{r}{D} = (\frac{Ut}{D})^{0.5}$, irrespective of the consistency of the formulation. We remark that this agreement for an inconsistent formulation is misleading, since it wrongly predicts the complex underlying physics of the impact.

We further repeat this test case at a lower Re = 6.6 with all other conditions identical and results from both the formulations appear to agree reasonably well with one another and also with those reported in [104]. This can be observed in Figures 4.23(a)

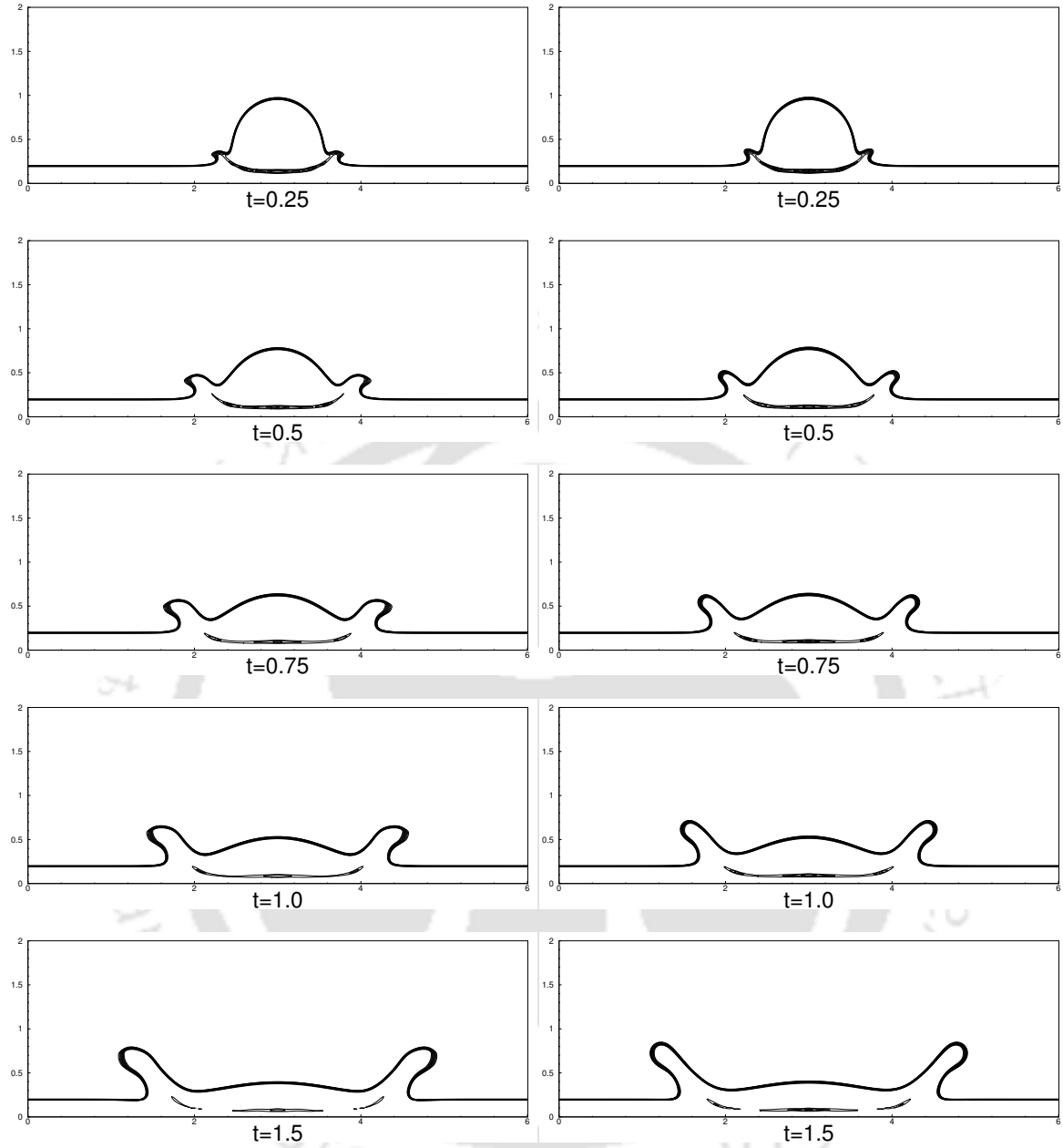

(a) Inconsistent formulation (b) Consistent formulation

Figure 4.23: Instantaneous profile of droplet splashing on thin liquid layer for $\frac{\rho_H}{\rho_L}$ = 815, $\frac{\mu_H}{\mu_L}$ = 55, Re = 6.6 and We = 0.126 using (a) inconsistent and (b) consistent formulations.

and 4.23(b), which show the droplet splashing at the lower Re using the two formulations, where no secondary droplet formation is seen and a thicker liquid sheet emanates after impact. This corroborates the fact that while the consistent formulation can handle a wide variety of density ratios including high density contrasts, an inconsistent formulation could work equally well under a specified set of conditions. While

not necessarily the case, these specified conditions can correspond to realistic scenarios (as in the bubble rising case, see Section 4.3.7) which might also explain why existing multiphase solvers have not deeply addressed the critical issue of consistent advection.

4.3.9 Collapse of a water column

As a final test of balanced and consistent advection, we choose the widely researched problem of collapse of a water column [22, 41], owing to its importance in free surface flows where large distortions of the interface are common. We discretise the domain which is a 7 $\times$ 2 rectangular tank using a triangulated mesh of 78668 elements. A 1 $\times$ 1 water column placed at the left corner surrounded by air, leading to density and viscosity ratios of 815 and 63 respectively. For left and bottom walls we provide no-slip condition and the remaining tank walls are assumed to be slip boundaries. The Reynolds number for the simulation is chosen to be 2950, while Weber number is 0.54 and the Froude number is unity. The velocity and length scales in defining these dimensionless numbers are $\sqrt{gH}$ and the height of the water column H respectively. The simulation is carried out using Δt = 0.001 by employing consistent and inconsistent formulations up to a final time of t = 4.

Figures 4.24(a) and 4.24(b) show the contour plots of density at time t = 0, 1, 2, 3, and 4 for inconsistent and consistent formulations respectively. While comparing both the formulations, it is seen that the density front (position of the interface at the bottom wall) using the inconsistent formulation moves at a slow rate in the initial stages and gets completely distorted in later stages. The consistent formulation, on the other hand, shows an error–free evolution of the front which is in good agreement with the experimental data of Martin and Moyce [105] as can be seen in Figure 4.25. The time history of the evolution of the leading edge using the inconsistent formulation is obviously unphysical as can also be seen from Figure 4.25 and is a direct consequence of dissimilar transport of mass and momentum at the discrete level. This study provides a strong justification for the need to employ consistent transport of mass and momentum in the simulation of high Re and high density ratio free surface flows which are of

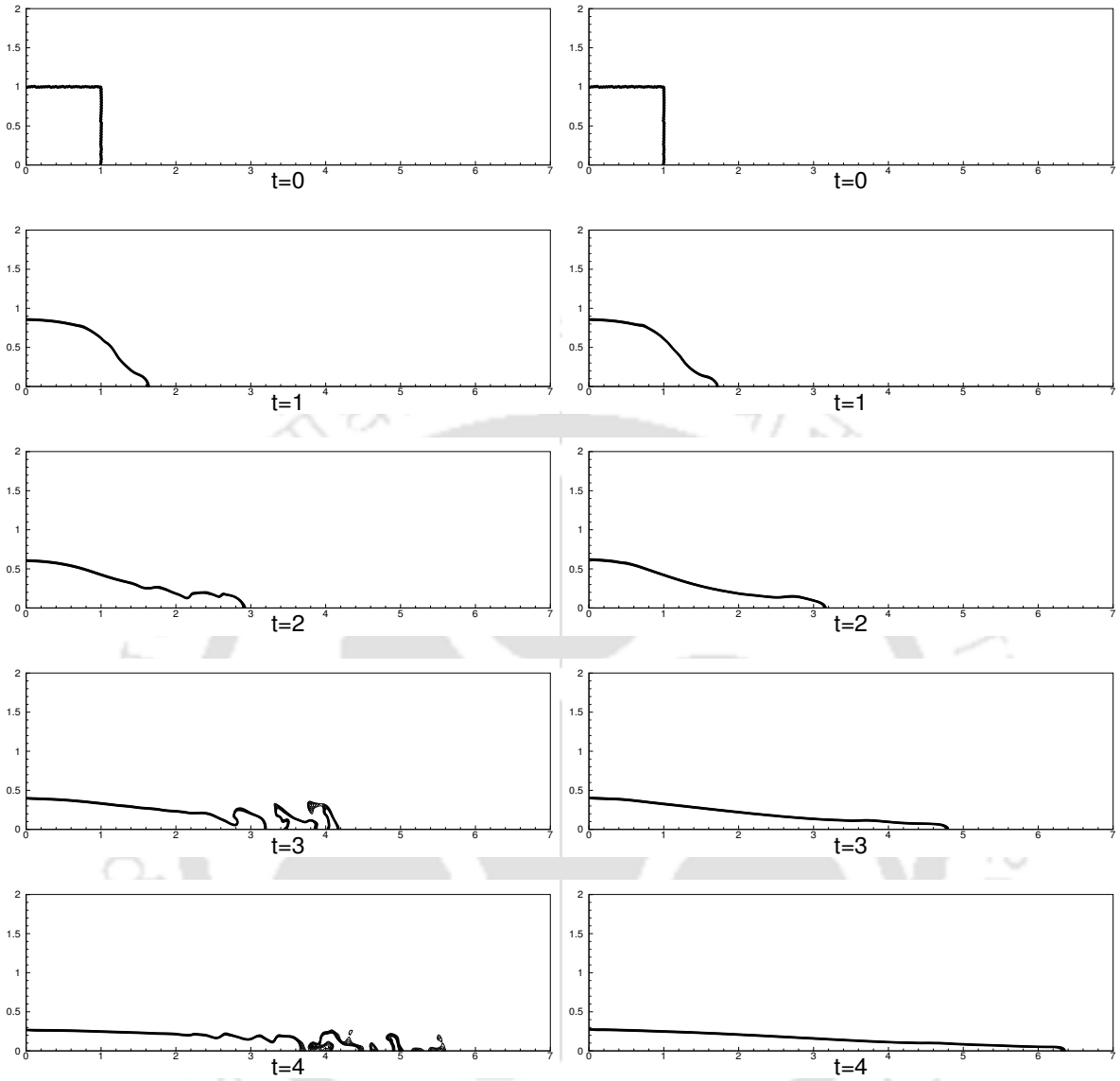

(a) Inconsistent formulation (b) Consistent formulation

Figure 4.24: Instantaneous profiles of collapse of water column for $\frac{\rho_H}{\rho_L}$ = 815, $\frac{\mu_H}{\mu_L}$ = 63, Re = 2950, We = 0.54 and Fr = 1 using (a) inconsistent and (b) consistent formulations.

practical interest.

4.4 Discussions and comparison with alternative algorithms

The proposed algorithm combines elements of balanced force treatment and consistent mass momentum transport within a novel staggered/non–staggered framework

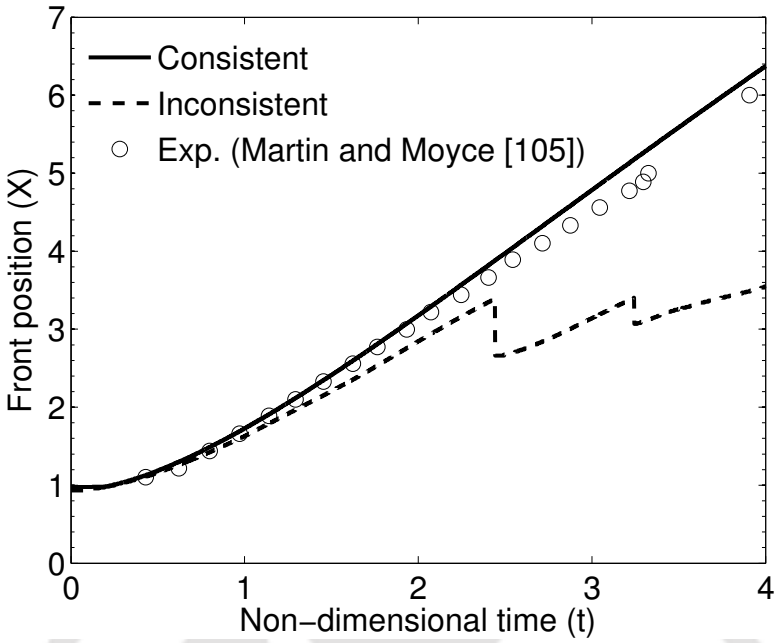

Figure 4.25: The front position of collapsing water column in air.

for multiphase flow simulations. Unlike collocated approaches in [33–35] the present algorithm does not necessitate modifications to the momentum interpolation while incorporating interfacial and body forces. Furthermore, our framework also differs from the staggered framework of [38, 106] in that a collocated treatment is applied for flux calculations and there is no need for use of dual grids for consistent transport.

The key features that make the present algorithm unique for multiphase flow simulations are the specific implementations of force balancing and consistent transport. The use of “normal" momentum equation (Eq. (3.15)) results in pressure appearing as a “normal" derivative both in the transport equation as well as in the Poisson equation (Eq. (3.21)). Furthermore, other force terms (gravity/surface tension) also appear as normal derivatives of suitable scalars, facilitating an identical treatment of these quantities along with pressure. The consistent transport of mass and momentum is realised using identical convective schemes to transport volume fraction and normal momentum respectively. It is important to note that despite the choice of different control volumes to discretise the quantities in mass and momentum equations, the choice of similar convective schemes remains the critical component to ensure a physically consistent solution. While the balanced force philosophy has been previously employed by other

researchers [32–34], the present study provides a novel implementation that naturally couples pressure and surface tension/gravity effects. The methodology proposed in this work is generic and applicable to arbitrary polygonal meshes and has been tested extensively on gravity and surface tension dominated flows. The consistent transport of mass and momentum, while inspired by the work in [35] differs in that we employ a high resolution bounded convective scheme within a VOF framework that ensures consistent errors in discrete transport of volume fraction and normal momentum. Interestingly, we also show through a series of extensive numerical experiments that an inconsistent approach can perform as well as a consistent approach for some problems (and in possibly realistic conditions), although the latter represents the “fail–safe" implementation for flows with high shear and/or density contrasts.

We shall now examine, albeit heuristically, conditions under which an inconsistent treatment would suffice for simulating large density ratio flows. Indeed, many of the present multiphase solvers treat the convective terms in the LS/VOF equation and momentum equation with different schemes for discrete transport [34, 38, 103]. Table 4.3 summarises the results of various studies carried out in this work using the inconsistent formulation, with the relevant parameters, as discussed in Section 4.3. The table also shows the values of a new parameter Re^* which is defined as,

$$Re^* = \frac{Re(\frac{\rho_H}{\rho_L} - 1)U_{char}}{\frac{\mu_H}{\mu_L}} \tag{4.8}$$

where Re is the Reynolds number defined based on properties of the lighter fluid and U_{char} is the characteristic velocity scale driving the flow. For flows that are gravity–dominated, such as the two–fluid Poiseuille flow and Rayleigh–Taylor instability, $U_{char} = \frac{1}{\sqrt{Fr}}$, while for other problems it is equal to the velocity of bulk motion. For flows with large density ratios, Re^* may then be also interpreted as the Reynolds number based on properties of the heavier fluid. However, in general, Re^* is a Reynolds number–like parameter involving the differences in densities of the heavier and lighter fluid as well as their viscosity ratios. A quick look at the calculated values of Re^* in Table 4.3 indicate that the inconsistent formulation would results in physically consistent solutions $(\checkmark)$ for

values of Re^* lesser than 100 while the solutions would be anomalous for larger values of Re^*, typically exceeding 1000. While such a criterion based on Re^* does involve a certain degree of arbitrariness, we believe that it could prove to be a useful rule–of–thumb to decide apriori if simulations using an inconsistent approach (as incorporated in many existing legacy solvers) could lead to a successful numerical simulation of large density ratio multiphase flows or if a consistent formulation is absolutely necessary. From the extensive numerical experiments presented in Section 4.3, one can also conclude that the need for consistent formulations are not driven solely by the density ratio but by a multitude of factors, including the viscosity ratio and body forces. However, we emphasise that a consistent and balanced force algorithm is always the safe bet in unsteady multiphase simulations, particularly those involving instabilities and complex physics, since the spurious currents resulting from unbalanced and/or inconsistent transport could lead to a radically different and completely non–physical numerical solution.

Table 4.3: The value of Re^* for different test cases using inconsistent formulation.

Test case	$\frac{\rho_H}{\rho_L}$	$\frac{\mu_H}{\mu_L}$	Re	We	Fr	U	Re^*	Physically consistent
Translating droplet	10	1	10	1	–	1	90	✓
	1000	1	10	1	–	1	9999	×
Poiseuille flow	10	1	10	–	1	–	90	✓
	1000	1	10	–	100	–	999.9	×
	1000	100	10	–	1	–	99.9	✓
	10	1	1000	–	1	–	9000	×
Rayleigh–Taylor	7	1	1000	–	0.1	–	18974	×
Kelvin–Helmholtz	2	1	5000	–	–	1	5000	×
Bubble rising	1000	100	3.5	0.125	1	–	34.96	✓
	1000	1	3.5	0.125	1	–	3496	×
Droplet splashing	815	55	66	0.126	–	1	976.8	×
	815	55	6.6	0.126	–	1	97.68	✓
Collapse of water column	815	63	2950	0.54	1	–	43660	×

CHAPTER 5

DIFFUSE INTERFACE IMMERSED BOUNDARY METHOD FOR FLUID-RIGID STRUCTURE INTERACTIONS[§]

The existence of one or more solid bodies in the flow field is common in many practical and industrial applications. As mentioned in the literature review, several numerical techniques have been developed to simulate such flow circumstances. In this chapter, we present a novel diffuse interface immersed boundary method (DIIBM) for fluid–structure interactions. The proposed methodology augurs perfectly with the volume–of–fluid framework for multiphase flows and is thus capable of handling multibody–multifluid interactions. The salient details pertaining to the DIIBM approach and its implementation for multiphase flows in finite volume framework are discussed. Extensive numerical experiments ranging from the flow past a cylinder to sedimentation of the particles in stratified media are carried out to demonstrate the accuracy and utility of the proposed methodology.

[§]The contents in this chapter are part of the manuscript titled "Diffuse interface immersed boundary method for multi–fluid flows with arbitrarily moving rigid bodies", Journal of Computational Physics 360 (2018).

5.1 Diffuse interface immersed boundary method

In this section, we discuss the proposed diffuse interface immersed boundary–finite volume (IB–FV) flow solver for incompressible multiphase flows. The diffuse interface IB approach is based on the work of [63] which employs an indicator function for the solid bodies, referred to as solid fraction, in order to construct “hybrid" momentum equations which are solved everywhere in the domain, including within the solid body. The underlying idea in [63], which considers only single–phase flows, is that the solid is considered to be occupied by the same fluid as outside. We extend this principle to multi–fluid flows with multiple rigid bodies in this work using principles of volume–of–fluid approach for handling fluid–fluid interfaces while using an analogous volume–of–solid approach as also in [63], implemented differently for fluid–solid interfaces. Importantly, the present diffuse IB methodology has the following salient differences from those described for single phase flow and heat transfer problems in [63, 64].

1. We assume that the solid(s) are filled with a “virtual" fluid which has a density and dynamic viscosity which is highest among all the fluids involved in the simulation. This is unlike the approaches in [63, 64] which considers only a single fluid. Evidently, our approach is more generic and reduces to those in [63, 64] for a single phase flow.

2. The calculation of solid fractions, which are necessary for the “hybrid" momentum equations are obtained by solving advection equations that govern the motion of the body. In the studies in [63, 64] these quantities are obtained using geometric means without the need for solving additional PDEs. Employing an advection equation for solid fraction(s) is quite natural in a multiphase flow setting, since advection equations are anyway solved for the (fluid) volume fraction(s).

We now discuss the choice of “virtual" fluid, specific construction of the “hybrid" momentum equations involving solid–fluid coupling as well as the tracking of rigid solids under the action of forces and moments exerted on them due to the surrounding fluids and other solids in the vicinity.

5.1.1 Choice of virtual fluid for multiphase flows

While the choice of the fluid that occupies the solid is trivial for single phase flows since there is only one fluid, it poses a non–trivial issue for multiphase flows. One must realise that the solids (either stationary or in motion) can be simultaneously in contact with two or more fluids, with the fluids themselves sharing an interface. While any of the fluids can be chosen to fill the solid(s) in multiphase flows, we choose to employ a “virtual" fluid which has density and dynamic viscosity equal to the largest of all fluids in the problem [1]. This choice is driven by physical and numerical considerations pertaining to computations of fluid properties at the cell faces in the vicinity of the solid–fluid interface. We calculate the density and viscosity at the face (needed because the momentum equations are solved at the cell faces) using a harmonic averaging of the values in cells sharing the face. This may be well understood using the illustrative example in Figure 5.1, where the values of density ρ_f and dynamic viscosity μ_f at the faces are equal to 2 (for f near the solid) when the solid interface lies in the lighter fluid while they are both equal to 1000 when the solid interface falls in the heavier fluid. One can easily see that the fluid properties on the cell faces in the vicinity of the solid are nearly the same as that of the fluid with which the solid (or its part thereof) is in contact with. This shows that the use of a harmonic averaging along with the choice of the densest and most viscous “virtual" fluid allows one to obtain face values of the fluid properties (employed in the computations) that are physically consistent.

5.1.2 Calculation of solid fractions

The proposed diffuse IB methodology treats the solid–fluid interfaces analogous to fluid–fluid interfaces, since the solid is assumed to be containing a “virtual" fluid. Subsequently, one can therefore define a solid volume fraction [2] for each cell analogous to the fluid volume fraction in the VOF approach. The solid fractions φ are therefore obtained by solving an advection equation which reads,

[1] Typically, the densest fluid is also the most viscous which means that the heaviest fluid in the simulation is assumed to occupy the solid(s) at all times.

[2] In this work, we shall refer to the fluid volume fractions and solid volume fractions simply as volume fractions and solid fractions respectively.

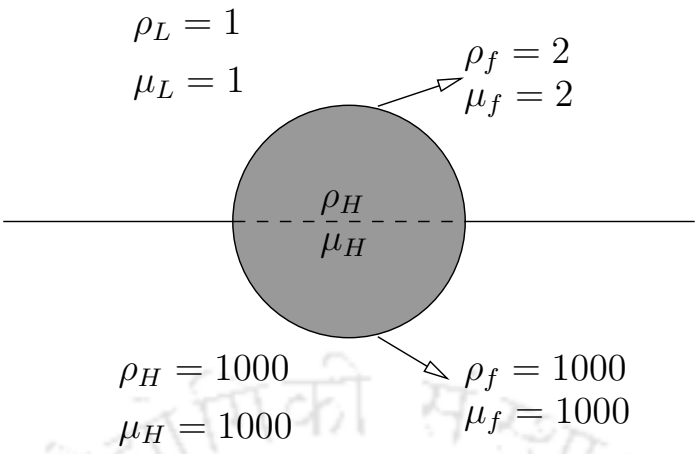

Figure 5.1: Virtual fluid inside the solid domain with harmonic averaging.

$$\frac{\partial \varphi_i}{\partial t} + \mathbf{V}_i^n \cdot \nabla \varphi_i = 0 \qquad i = 1, 2, ..., N_s \tag{5.1}$$

where N_s is the number of solids in the domain and for each solid i the corresponding solid fraction φ_i is initialized as,

$$\varphi_i(\mathbf{x}, t) = \begin{cases} 1 & \text{if } \mathbf{x} \in i^{th} \text{ solid} \\ 0 & \text{elsewhere} \end{cases} \tag{5.2}$$

It should be noted that the velocity of the solid V is used for the advection of solid fraction, analogous to the VOF approach which employs the local fluid velocity. The solid velocity is known in case the motion is imposed and for problems where the motion is induced can be obtained by solving the equations governing the body dynamics as discussed in Section 5.1.4. The use of an Eulerian approach to solid tracking as opposed to use of Lagrangian markers is not new and has been previously employed in [62, 70]. This advection equation is then discretised with the same second–order accurate temporal scheme as for Eq. (2.4),

$$\Omega_c \frac{3\varphi_c^{n+1} - 4\varphi_c^n + \varphi_c^{n-1}}{2\Delta t} + \sum_{f \in C} \varphi_f^{n+1} V_f^n \Delta s_f = 0 \tag{5.3}$$

While the control volumes for ϕ and φ are indeed identical, we employ the CUIBS scheme [84] instead of the CUI for solid fraction advection. This choice is motivated by

the fact that CUIBS is an interface sharpening scheme which can preserve the solid geometry more accurately. It must be emphasised that the disparate discrete treatment of solid and fluid volume fractions do not lead to inconsistencies and akin to the volume fraction equation, the Eq. (5.3) is solved implicitly using the GMRES solver in conjunction with algebraic multigrid preconditioner using the LiS libraries. We also remark that we treat fluid–fluid and fluid–solid interfaces in similar fashion, devoid of any interface reconstruction, resulting in a relatively straightforward implementation that can be adopted into any standard finite volume flow solver. While it is logical to argue that the use of a diffuse representation could become inaccurate, we show through extensive numerical studies that this is not true. Furthermore, one can approach the accuracy of a sharp interface representation by combining this Eulerian approach with geometry and solution based adaptive mesh refinement, which is however not in the scope of the present study.

5.1.3 Enforcing boundary conditions

The diffuse interface immersed boundary method proposed in the present work is based on the work in [63] and employs the solid fraction to construct a “hybrid" momentum equation that is solved everywhere in the domain. The resulting momentum equation(s) must satisfy the following conditions.

1. In regions fully occupied by fluid(s) (in which case $\varphi = 0$), it must reduce to the Navier–Stokes equations that govern the fluid flow.

2. In regions fully occupied by solid(s) (in which case $\varphi = 1$), it must reduce to the no–slip boundary conditions. This is because since a “virtual" fluid is filled within the solid(s) and the geometries are assumed rigid, the “virtual" fluid must move with the same velocity as the rigid solid which it occupies.

3. In regions occupied by both fluid and solid ($0 \leq \varphi \leq 1$), it must be a suitable combination of the Navier–Stokes equations and the no–slip boundary conditions. This allows the velocity field to transition smoothly from fully solid regions to fully

fluid regions and plays a significant role in ensuring that there are negligible spurious oscillations in force and moment histories.

These conditions are satisfied by using a convex blending of the Navier–Stokes equations and physical boundary employing the solid fractions to construct the “hybrid" momentum equations which are valid everywhere in the domain. The resulting equation in the present staggered/non–staggered framework reads,

$$(1-\sum_{i=1}^{N_s}\varphi_{fi})\left[\frac{\rho_f^{n+1}(3U_f^\star-4U_f^n+U_f^{n-1})}{2\Delta t}\,\Omega+\mathbb{C}(U_f^\star,\mathbf{u}^\star)-\mathbb{D}(U_f^\star,\mathbf{u}^\star)+\frac{\delta p}{\delta n}\Big|_f\,\Omega+\frac{\rho_f}{Fr}\mathbf{e}\,\Omega\right] + \sum_{i=1}^{N_s}\varphi_{fi}\rho_f^{n+1}\frac{3(U_f^\star-V_i^n)}{2\Delta t}\,\Omega=0 \tag{5.4}$$

where N_s indicates the number of solids and φ_{fi} is the face solid fraction of the i^{th} solid calculated using the volumetric averaging of the values at centroids of cell sharing the face. It is easy to see that this equation recovers the normal momentum equation for the fluid faces when φ_i = 0 and enforces the solid velocity V_i^n for the solid faces that correspond to φ_i = 1. As discussed in Section 3.3.3, this “hybrid" normal momentum equation is implicitly solved using a Newton–Krylov solver with the help of PetSc libraries. The present work is a generalisation of the IB methodology in [63] to handle complex moving rigid bodies in multiphase flows and is simple and easy to implement requiring minimal effort. We refer to this approach as diffuse IB because the computed solid fractions are cell–averaged quantities and the sharp representation of the geometry is lost with the solid–fluid interface smeared over one or two cell widths.

A closer look shows that the momentum equation in the present IB–FV approach is indeed different from those used in conformal mesh based approaches. While the latter solve the Navier–Stokes equations, the IB–FV approach uses a “hybridisation" that is dictated by the solid fraction. Nevertheless, it is interesting to note that the Poisson equation for pressure correction for the present diffuse interface IB approach is devoid of solid fractions with its discrete form in Eq. (3.21) solved everywhere, including inside the solid(s). By not choosing to discriminate the Poisson equation in solid

and fluid regions, via the solid fractions, we discretely preserve its elliptic character and the pressure inside the solid(s) evolves to adjust to the pressure outside of it. This approach of solving the Poisson equation without discriminating between regions occupied by the real and “virtual" fluids is simple and easy to implement and is a clear departure from those employed in sharp interface IB methods. Importantly, unlike the sharp interface IB methods, the proposed methodology does not involve interpolations for momentum (and hence velocities) and pressure and its implications for numerical simulations will be discussed in the following sections.

5.1.4 Flow induced motion and rigid body dynamics

The velocity of the solid object V_i appearing in Eqs. (5.3) and (5.4) is known if the motion of the rigid body is imposed. In the case of induced motion, the velocities of solid object(s) are obtained from the Newton's second law.

$$\hat{M}_i \frac{\mathrm{d}\hat{\mathbf{V}}_{ti}}{\mathrm{dt}} = \hat{\mathbf{F}}_i + \hat{\mathbf{F}}_i^{rep} + \hat{M}_i \mathbf{g} \tag{5.5}$$

$$\hat{J}_i \frac{\mathrm{d}\hat{\boldsymbol{\omega}}_i}{\mathrm{dt}} = \hat{\mathbf{T}}_i \tag{5.6}$$

where $\hat{M}_i$ is the mass of i^{th} solid, $\hat{\mathbf{V}}_{ti}$ is the translational velocity and $\hat{\boldsymbol{\omega}}_i$ represents the angular velocity of the bodies. In addition, $\hat{\mathbf{F}}_i$ represents the sum total of hydrodynamic and buoyancy forces, $\hat{\mathbf{F}}_i^{rep}$ is the repulsive force between two solid bodies, $\hat{J}_i$ is the mass moment of inertia and $\hat{\mathbf{T}}_i$ represents the net torque about the center of mass (x_{com}, y_{com}). The above equations can be suitably non–dimensionalised and the dimensionless form of the equations read,

$$\mathbf{V}_{ti}^{n+1} = \mathbf{V}_{ti}^{n} + \frac{\mathbf{F}_i}{M_{red}}\Delta t + \frac{\mathbf{F}_i^{rep}}{M_{red}\,\rho_L D^2}\Delta t + \frac{1}{Fr}\mathbf{e}\Delta t \tag{5.7}$$

$$\boldsymbol{\omega}_i^{n+1} = \boldsymbol{\omega}_i^{n} + \frac{\mathbf{T}_i}{J_i}\Delta t \tag{5.8}$$

where $\mathbf{F}_i = \frac{\hat{\mathbf{F}}_i}{\rho_L U^2 D}$ and $\mathbf{T}_i = \frac{\hat{\mathbf{T}}_i}{\rho_L U^2 D^2}$. The non–dimensionalisation also results in reduced mass and moments of inertia defined by $M_{red} = \frac{\hat{M}_i}{\rho_L D^2}$ and $J_{red} = \frac{\hat{J}_i}{\rho_L D^4}$ respectively. These equations are temporally discretised using the explicit Euler scheme and are solved to obtain the translational and angular velocities. The velocity field within

the solid body (dropping the subscript denoting the solid) is determined as,

$$\mathbf{V} = \mathbf{V}_t + \boldsymbol{\omega} \times \mathbf{r}$$

The face normal velocity appearing in the hybrid normal momentum equation Eq. (5.4), that enforces the no–slip boundary condition, easily follows by taking the dot product as $V_f = \mathbf{V} \cdot \mathbf{n_f}$.

5.1.5 Calculating forces and moments

The dimensionless forces and torques $(\mathbf{F}_i, \mathbf{T}_i)$ acting on the solid(s) due to the surrounding fluid flow can be calculated through direct surface integration of pressure and viscous forces.

$$\mathbf{F}_i = \int_{\Gamma_i} (-p\mathbf{n_f} + \frac{\mu_f}{Re}(\nabla\mathbf{u} + \nabla\mathbf{u}^T) \cdot \mathbf{n_f}) \, \mathrm{d}\Gamma_i \tag{5.9}$$

$$\mathbf{T}_i = \int_{\Gamma_i} (\mathbf{x} - \mathbf{x}_{com,i}) \times (-p\mathbf{n_f} + \frac{\mu_f}{Re}(\nabla\mathbf{u} + \nabla\mathbf{u}^T) \cdot \mathbf{n_f}) \, \mathrm{d}\Gamma_i \tag{5.10}$$

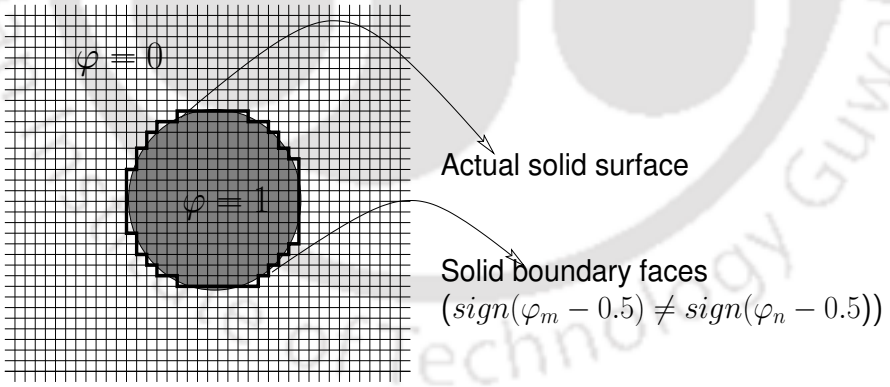

Figure 5.2: Staircase representation of the solid boundaries. The sign() function gives 1 if the argument is positive and -1 otherwise.

where Γ_i is the boundary of the i^{th} solid and we define drag, lift and momentum coefficients related to dimensionless forces as C_D=$2F_{ix}$, C_L=$2F_{iy}$, and C_M=T_i respectively. This boundary, over which the integral is carried out, needs attention because it neither conforms to the underlying grid nor has markers indicating its position. We define a constant S for each solid as $S = \varphi - 0.5$. If any two cells sharing a common

face of the underlying mesh have values of S with opposite signs we consider that face to be part of the boundary of that solid. This allows us to approximate the body using a stair–step representation as shown in Figure 5.2, for the purpose of computation of aerodynamic coefficients. While there would be a noticeable difference between this approximate representation and the true body contour, this approach leads to acceptably accurate forces and moments. The use of an approximate approach discussed herein is justified since the interface is itself not sharply represented by the IB methodology. Furthermore, the inaccuracies incurred by this representation can be reduced significantly using adaptive mesh refinement in the body vicinity, which is however not part of the present study.

In fluid–solid interactions where there are more than one solid bodies it is very likely that the bodies will come in contact with each other. In order to prevent inter–penetration of the solid bodies, we employ the repulsive force model of Glowinski et al. [54]. This model applies an artificial short–range force to maintain a minimum distance between the solids. The repulsive force exerted on the solid object 'i' by the neighboring bodies 'j' is given by [54],

$$\mathbf{F}_i^{rep} = \sum_{j=1, j\neq i}^{N_n} \mathbf{F}_{i,j}^{rep}, \tag{5.11}$$

$$\mathbf{F}_{i,j}^{rep} = \frac{M_{red}\ \rho_L D^2}{\epsilon\ Fr} \left(max\left\{0, -\left[\frac{d_{ij} - r_i - r_j - \delta}{\delta}\right]\right\}\right) \frac{\mathbf{x}_{com,i} - \mathbf{x}_{com,j}}{d_{ij}} \tag{5.12}$$

where N_n is the number of neighboring bodies, $\mathbf{x}_{com}$ is position vector of the center of mass, d_{ij} is the distance between the mass center of the bodies i and j. The parameter δ is the distance between the boundaries of the bodies, exceeding this value repulsive force has no effect. In this model, the repulsive force is exerted on the object in the direction along the line joining the mass center of the objects and ϵ is grid dependent parameter. In the present studies we choose $\delta = 2\Delta x$ and $\epsilon = (\Delta x)^2$ following the recommendations in [54].

5.1.6 Multiple fluid methodology

The proposed immersed boundary method is capable of handling multiple fluid–solid interactions wherein the fluids are considered to be immiscible. The single fluid formulation allows us to determine the mixture density and viscosity as functions of the volume fraction ϕ as,

$$\rho = (1 - \sum_{k=1}^{N_f-1} \phi_k) + \sum_{k=1}^{N_f-1} \phi_k \frac{\rho_k}{\rho_L} \tag{5.13}$$

$$\mu = (1 - \sum_{k=1}^{N_f-1} \phi_k) + \sum_{k=1}^{N_f-1} \phi_k \frac{\mu_k}{\mu_L} \tag{5.14}$$

where N_f is the total number of fluids present in the computational domain. Here, ρ_k and μ_k denote the density and dynamic viscosity of the k^{th} fluid. It is clear from these expressions that for a case with N_f fluids in the domain, a total of $(N_f - 1)$ volume fractions need to be solved. The fluid volume fractions are governed by simple advection equations and are solved using the VOF method to capture the interface kinematics. The equations for the $(N_f - 1)$ volume fractions read,

$$\frac{D\phi}{Dt} = \frac{\partial \phi_k}{\partial t} + \mathbf{u} \cdot \nabla \phi_k = 0 \qquad k = 1, 2, ..., (N_f - 1) \tag{5.15}$$

The volume fraction equations are also discretised on the same control volume (cell C) as the pressure and the fully discrete advection equation for any fluid reads,

$$\Omega_c \frac{3\phi_c^{n+1} - 4\phi_c^n + \phi_c^{n-1}}{2\Delta t} + \sum_{f \in C} \phi_f^{n+1} U_f^n \Delta s_f = 0 \tag{5.16}$$

where U_f is the local fluid velocity obtained from the Eq. (5.4). It is also easy to see that the incompressibility constraint has been implicitly enforced to recast the volume fraction equations in a conservative form before the discretisation is carried out. The discrete implicit discretisation of the equation can be found in the Section 2.1. Furthermore, a well balanced and consistent formulation is implemented (see Chapter 4) in order to simulate large density multiphase flows.

5.1.7 Immersed boundary–finite volume algorithm

The complete solution methodology for the proposed diffuse interface immersed boundary finite volume framework can be summarised in the Figure 5.3,

We remark that the forces required to calculate the solid velocities are those obtained in the previous timestep, which is essentially a “weak" coupling in terms of fluid–structure interaction. The problems considered herein involve rigid structures and as discussed in [48], the “weak" coupling remains numerically stable and can be effected at a much lower computational cost than its “strong" coupling counterpart.

5.1.8 Comparison with the Brinkman penalization method

The diffuse interface IB method discussed in this work employs a unique strategy which solves a solid fraction–hybridised equation for momentum and a solid fraction–free Poisson equation for pressure everywhere in the domain. We briefly demonstrate that the present approach has a few striking similarities with the Brinkman penalization method [58–60] which was originally developed for porous media flows. The Brinkman penalisation method uses permeability and porosity as parameters to penalize the momentum equation for enforcing boundary conditions. The penalized momentum equation reads,

$$\frac{\partial \mathbf{u}}{\partial t} + \mathbf{u} \cdot \nabla \mathbf{u} - \frac{1}{Re} \nabla^2 \mathbf{u} + \nabla p = -\frac{1}{\eta} \chi (\mathbf{u} - \mathbf{v_s}) \tag{5.17}$$

where $\mathbf{v_s}$ is solid velocity, $\eta << 1$ is porosity coefficient and χ is the mask function which is assigned a value of 1 inside the solid and zero elsewhere. Similar to Eq. (5.4), the above equation is also valid for the entire domain with the no–slip boundary condition realised through the term on the right side of the equation. The fluid flow inside the pores is assumed to be governed by the Darcy's law.

$$\mathbf{v} = -\frac{K}{\mu} \nabla p \tag{5.18}$$

This equation relates the Darcy velocity to the pressure gradient driving the flow. It can be seen that the Darcy velocity becomes very small as the permeability (K) ap-

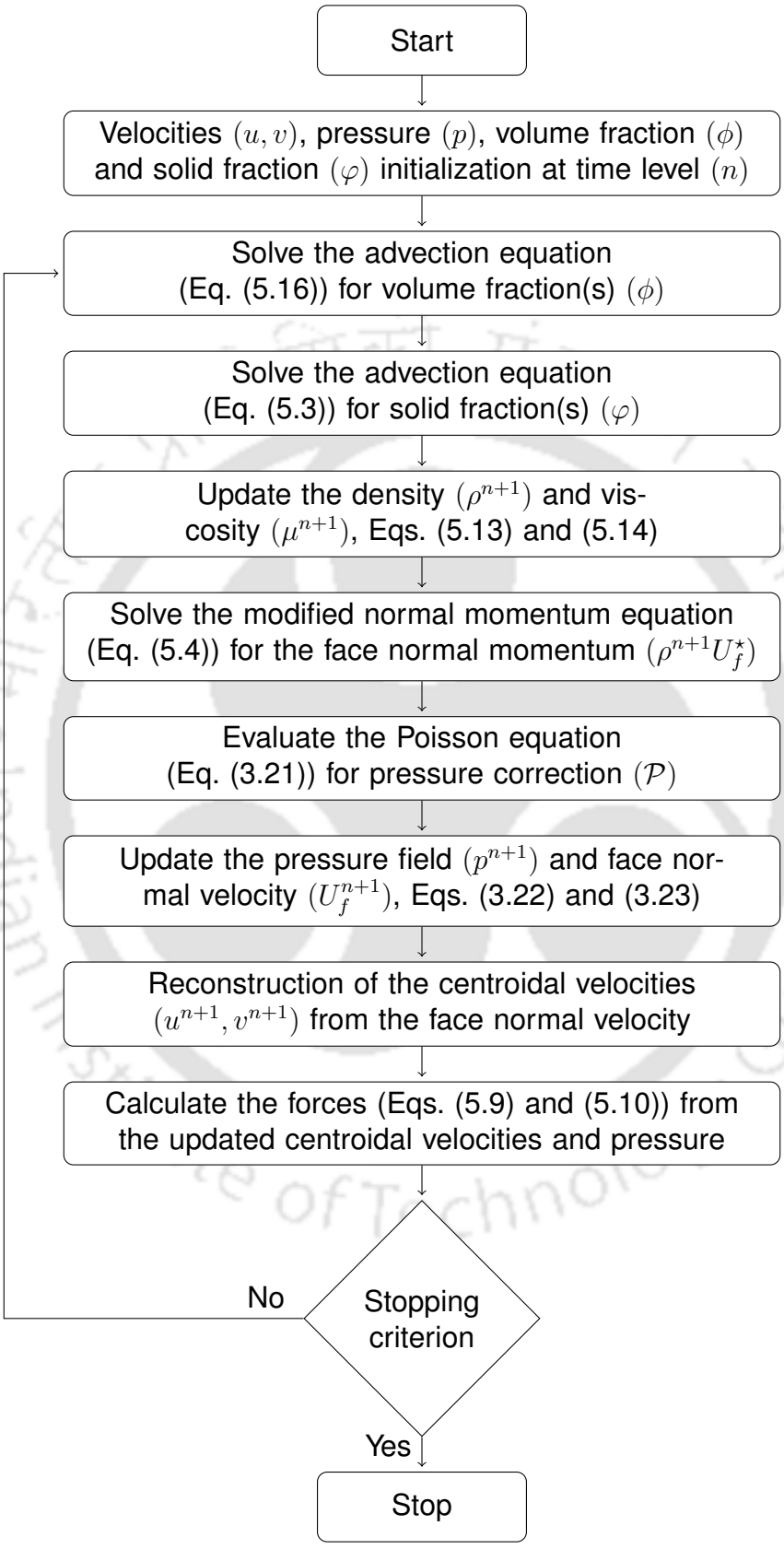

Figure 5.3: Flowchart for solution methodology.

proaches zero. Recall that in the present algorithm (described in Section 5.1.7), the solutions of the pressure correction equation are used to update the face normal velocity everywhere in the domain as,

$$U_f^{n+1} = U_f^{\star} - \frac{2\,\Delta t}{3}\frac{1}{\rho^{n+1}}\frac{\delta \mathcal{P}}{\delta n}\Big|_f \tag{5.19}$$

In this equation $U_f^{\star}$ is obtained from the Eq. (5.4), which is zero in case of stationary body and is known (prescribed or computed) in case of moving bodies. However, the updated face velocities U_f^{n+1} are not zero, but proportional to the pressure correction gradient $\frac{\delta \mathcal{P}}{\delta n}|_f$. A direct comparison of Eqs. (5.18) and (5.19), show that the updated face normal velocities behave analogous to the Darcy velocity with the velocities in a stationary rigid solid having a non–zero but very small value. This comparison gives a greater insight on the diffuse interface IB approach discussed in this work, which can also be interpreted as a simple but distant variant of the Brinkman penalisation approach.

5.2 Studies on discrete conservation

The IB–FV solver proposed in this work is investigated in this section for its discrete conservation properties. While use of finite volume methods on traditional body–fitted grids with the conservative form of the Navier–Stokes equations guarantee discrete conservation, we address this issue for the present diffuse IB methodology in the hybrid staggered/non–staggered framework. This study, in the context of IB approaches, is also relevant because the lack of mass conservation has been reported to be the source of spurious force oscillations in case of moving body simulations [65, 67].

We consider 5×4 rectangular domain, discretised into 250×200 rectangular elements, to examine the efficacy of the diffuse interface IB method to conserve the mass discretely. A channel inclined at 30^o to the horizontal is embedded within this Cartesian mesh and the walls of the channel are not aligned with the underlying mesh as shown in Figure 5.4. Our interest is to simulate the laminar flow through the channel using the IB–FV solver and we apply a constant velocity (U_∞=1) at the inlet and Neumann

BCs for the velocity at the outlet, with the inlet and outlet boundaries coinciding with the the domain boundaries. We choose a Reynolds number (based on inlet height and velocity) equal to 10 and carry out the simulation to steady state with a timestep of Δt = 0.001.

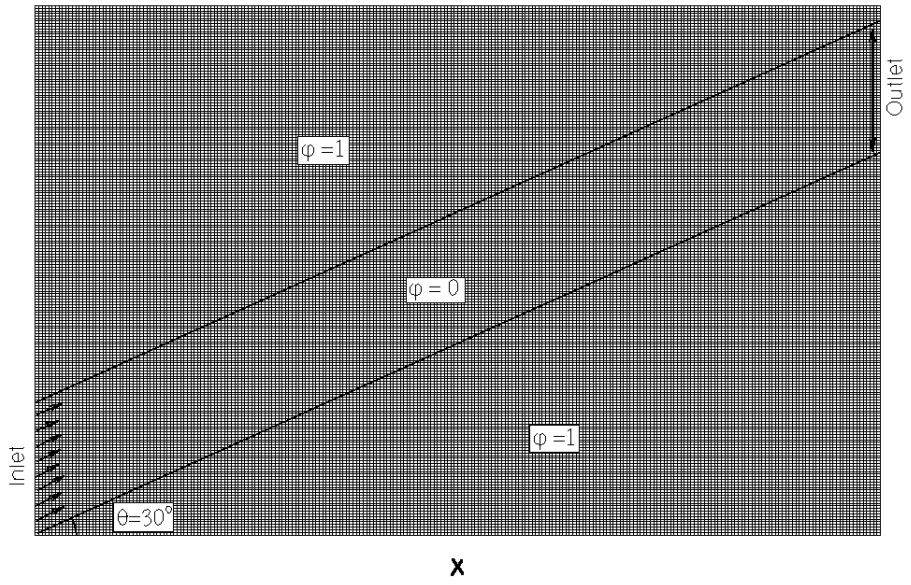

Figure 5.4: Schematic representation of the inclined channel using solid fraction φ in a background rectangular domain discretised into structured elements.

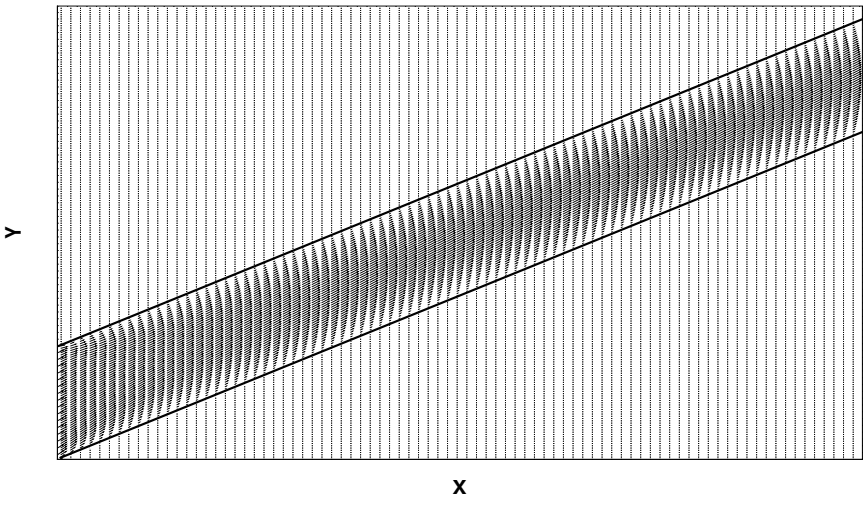

Figure 5.5: Velocity vectors in the domain showing parabolic velocity profiles inside the channel.

Figure 5.5 shows the velocity vectors in the entire domain at the steady state.

Clearly, there is no (numerically very small) velocity field present in the domain outside of the channel. This demonstrates that no unphysical velocities are generated despite the boundary faces not being aligned with the mesh. Specifically, the the flow becomes fully developed at the outlet and the velocity distribution across the channel is parabolic and the computed profiles agree well with the theoretical result as shown in Figure 5.6. A very small velocity at the channel boundaries, amounting to 0.008 in Figure 5.6, is a consequence of the convex blending between Navier-Stokes equation and the no-slip boundary condition. Clearly, the diffuse nature of the solid interface means that one cannot expect an exact zero velocity although we remark that these velocities are not unphysical and do not pollute the numerical solution. The good agreement between the analytical and numerical results for this problem involving non–conformal boundaries is a testimony to the fact that the mass and momentum conservation laws are discretely satisfied. This is further confirmed by computing the temporal history of the local maximum divergence $|\nabla \cdot \mathbf{u}|$ in the domain which is presented in Figure 5.7. One can see that the velocities are nearly solenoidal with the maximum values of $\mathbf{O}(10^{-10})$ which is proof of discrete local mass conservation. This numerical exercise can be construed as a demonstration of discrete conservation not only for the diffuse IB framework, but also for the hybrid staggered/non–staggered framework in which the momentum control volumes are overlapping. We remark that the discrete momentum conservation for the hybrid staggered/non–staggered framework has also been studied in [107] and the physically consistent results obtained in the present work, as demonstrated in the later sections, is a consequence of the discrete conservation properties of the IB–FV solver.

5.3 Studies on spatial and temporal accuracy

5.3.1 Taylor-Green vortex

A pertinent issue, apart from discrete conservation, related to immersed boundary techniques is the spatial and temporal accuracy of the approach. To investigate the order of accuracy of the present solver, we consider the Taylor–Green vortex problem [57], with an embedded solid. We choose a 0.5×0.5 domain for the computations and

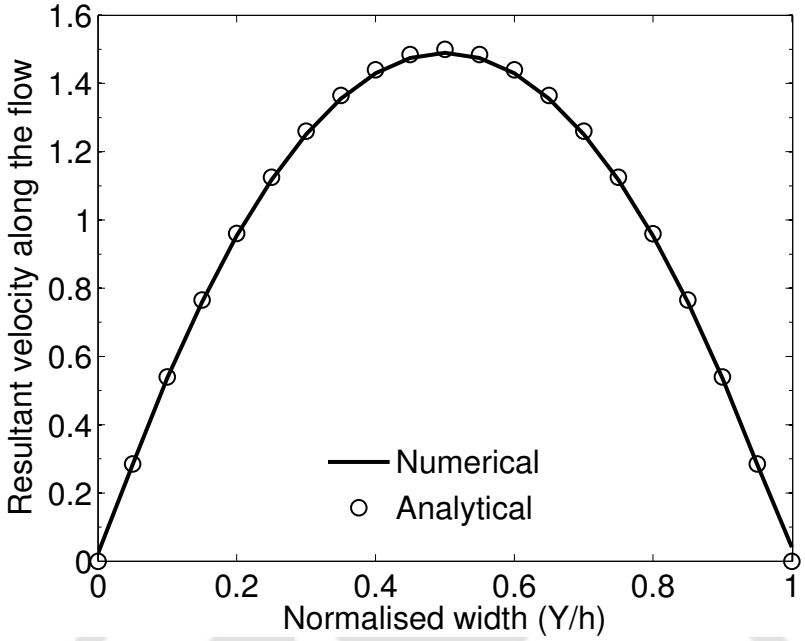

Figure 5.6: The resultant velocity profile along the normalised channel width.

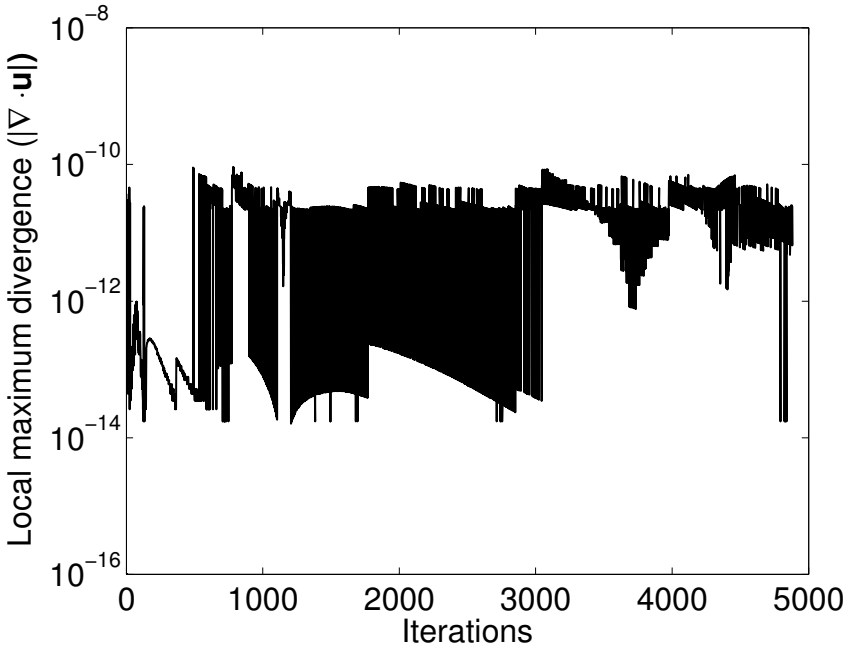

Figure 5.7: Local maximum divergence in the entire computational domain.

the analytical solution, shown below, is specified at the boundaries.

$$u = -\cos(2\pi x)\sin(2\pi y)e^{\frac{-8\pi^2 t}{Re}} \quad (5.20)$$

$$v = \sin(2\pi x)\cos(2\pi y)e^{\frac{-8\pi^2 t}{Re}} \quad (5.21)$$

$$p = \frac{-(\cos(4\pi x)+\cos(4\pi y))}{4}e^{\frac{-16\pi^2 t}{Re}} \quad (5.22)$$

The solid, which is a square of side 0.25 is positioned at the center, inclined at an angle of 45^o, so that the body is not aligned with the underlying mesh. The exact solution is prescribed at all times within the solid [3], which is kept stationary in one case and rotated with a constant angular velocity $\omega = 2\pi$ in another case. The numerical solutions are allowed to evolve everywhere outside of the solid region and the L_∞ error norms for velocity and pressure are considered for accuracy studies.

We study the spatial accuracy by considering uniform Cartesian meshes of different grid resolutions (Δx = 0.025, 0.0125, 0.00625, 0.003125) with a constant timestep Δt = 0.001. It can be seen that the IB–FV solver demonstrates a nominal second order accuracy for velocity errors (see Figure 5.8(a)), both in the stationary and moving body cases. Interestingly, the pressure errors however decay at a rate close to unity and we briefly discuss this aspect in the following section. In order to determine the temporal accuracy, we use four time steps (Δt = 0.01, 0.005, 0.0025, 0.00125) on the same grid, which is chosen as the coarsest one (Δx = 0.025). We find that the solver has second order temporal accuracy as well, as seen in Figure 5.8(b), for both the stationary and moving body cases. We also present the spatial and temporal studies of the solver in Figures 5.9(a) and 5.9(b) in absence of any solid which confirms the second-order spatial and temporal accuracies of the underlying finite volume solver as well. It must be noted that the moving body case and associated accuracy studies are an exposition of the ability of the proposed methodology to accurately handle moving solid interfaces. One can conclude from these numerical experiments that the IB–FV solver is nominally second–order accurate, in both space and time.

5.3.2 Taylor-Couette problem

The accuracy study using the Taylor-Green vortex, despite having been employed by several authors to demonstrate the accuracy of IB-FV solver, is not realistic in that the exact solution is always prescribed inside the body. Therefore, we now consider Taylor-Couette problem where the flow occurs between the two concentric cylinders due to

[3]The solid body herein is actually a region where the exact analytical solution to the Taylor–Green vortex problem is forced and not the physical no–slip conditions.

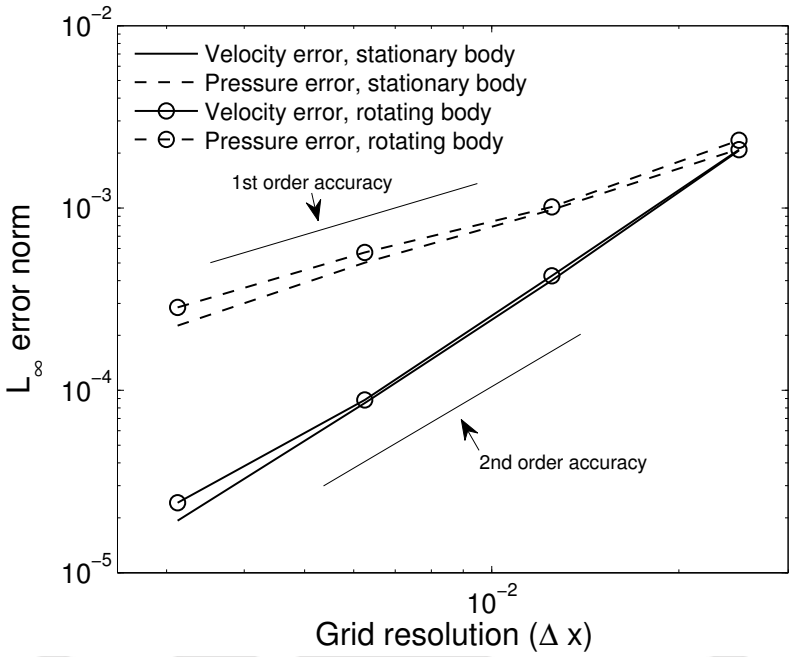

(a) Spatial accuracy

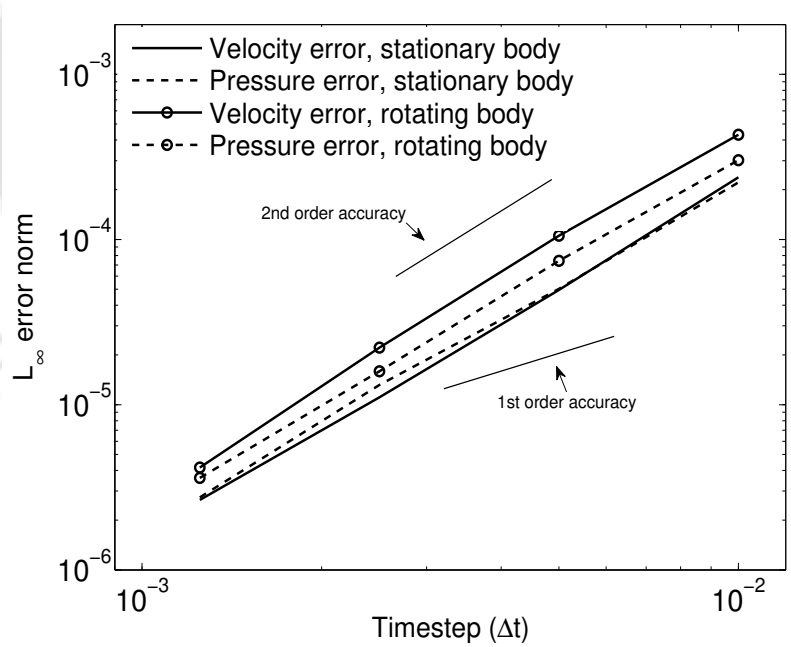

(b) Temporal accuracy

Figure 5.8: L_∞ error norm for velocities $\mathbf{u}$ and pressure p for stationary and rotating square body showing (a) spatial and (b) temporal accuracies.

the constant angular motion of inner cylinder. The computational domain is shown in Figure 5.10 with the inner cylinder of diameter D_1 = 0.4 moving with a constant angular velocity $\omega = \pi$ while the outer cylinder of diameter D_2 = 0.8 remains stationary. The

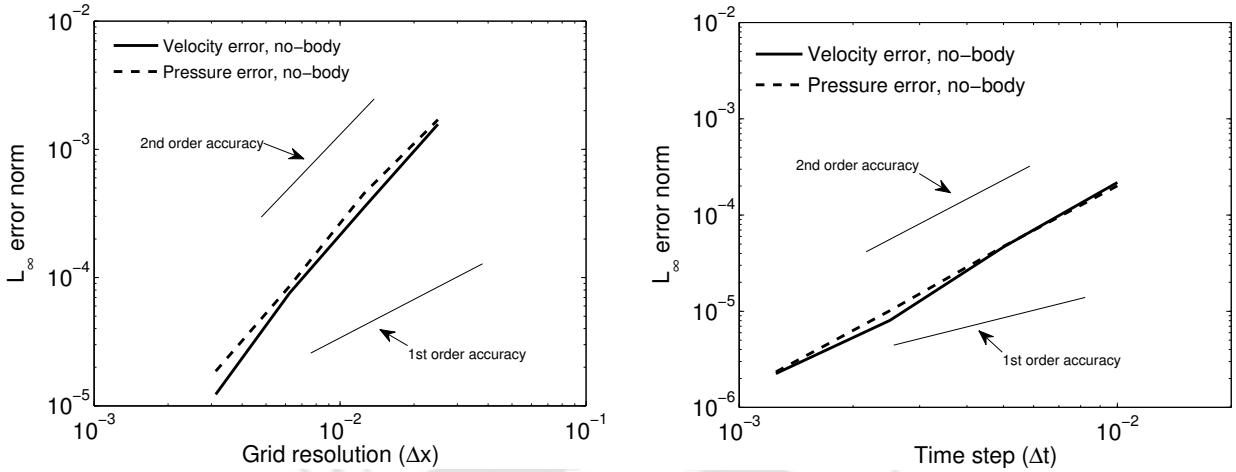

(a) Spatial accuracy (b) Temporal accuracy

Figure 5.9: L_∞ error norm for velocities $\mathbf{u}$ and pressure p for solver without any solid showing (a) spatial and (b) temporal accuracies of the finite volume flow solver.

two cylinders are immersed in a larger computational domain of size [-0.5,0.5] $\times$ [-0.5,0.5] whose outer boundaries are given no-slip boundary condition. The cylinders are considered to be rigid and impermeable solids and the no-slip boundary condition is enforced on the cylinder surfaces via the immersed boundary approach. The analytical solution for this case is,

$$u = \frac{\omega R_1^2}{R_2^2 - R_1^2}\left(\frac{R_2^2}{r^2} - 1\right) y \tag{5.23}$$

$$v = -\frac{\omega R_1^2}{R_2^2 - R_1^2}\left(\frac{R_2^2}{r^2} - 1\right) x \tag{5.24}$$

$$p = \left(\frac{\omega R_1^2}{R_2^2 - R_1^2}\right)^2 \left(\frac{r^2}{2} - \frac{R_2^4}{2r^2} - R_2^2 \log(r^2)\right) \tag{5.25}$$

where $R_1 = D_1/2$, $R_2 = D_2/2$ and $r = \sqrt{x^2 + y^2}$. The numerical simulations are performed with a constant time step Δt = 0.001 on four structured meshes of gradually increasing resolution (Δx = 1/16, 1/32, 1/64 and 1/128) for Re = 200, based on cavity dimensions. The L_∞ error norms for velocity and pressure are shown in Figure 5.11. We observe that the IB–FV solver exhibits first order accuracy in L_∞ norms. This result is in contrast to the Taylor-Green vortex study in Section 5.3.1 where the imposition of exact boundary conditions inside the solid led to nearly second order accuracy for velocity errors in both the error norms. It must be remarked that the pressure errors

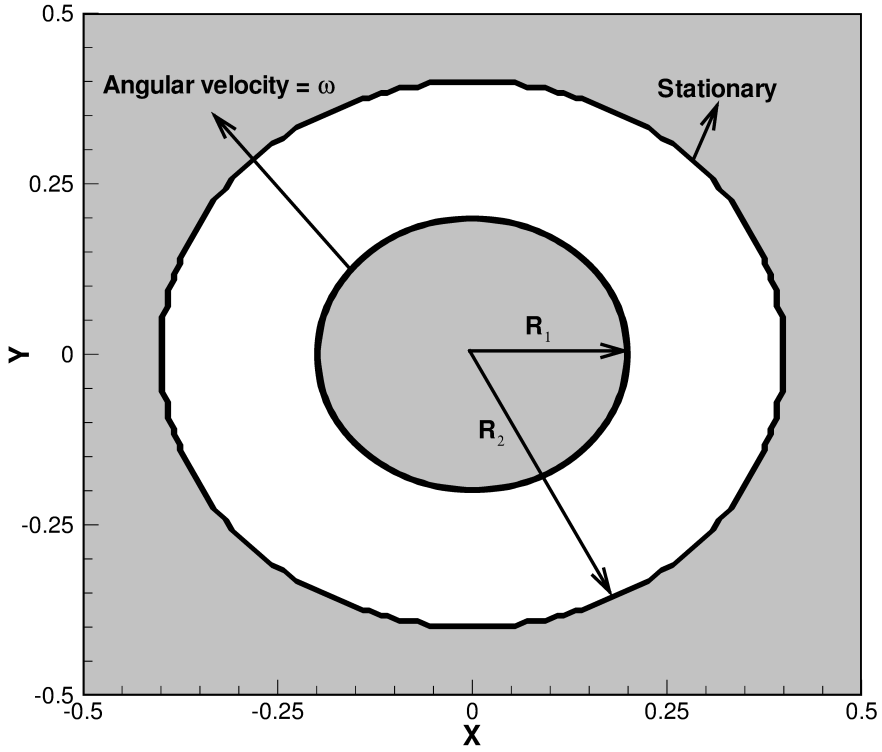

Figure 5.10: Computational domain for Taylor-Couette problem.

for this test case also diminishes linearly with grid refinement in the L_∞ norm as was also observed in the studies in Section 5.3.1. This behaviour of pressure errors in the context of immersed boundary methods has also been previously reported [108]. It must also be emphasised that it is the velocity errors that are more important than the pressure errors, since it is the gradient of pressure that plays a pivotal role in incompressible flows and not the pressure itself. We also remark that the order of accuracy in L_1 norm for this case is however close to 2 but is not shown here for reasons of brevity. This proves that the flow solver, even for realistic scenarios involving the no-slip boundary condition, shows nominal second order accuracy in space. As a further validation of the IB-FV solver for the Taylor-Couette problem, we compare the u and v velocity profiles at sections $x = 0$ and $y = 0$ respectively, obtained using the finest mesh, with the analytical solutions as shown in Figures 5.12(a) and 5.12(b), where the agreement is excellent.

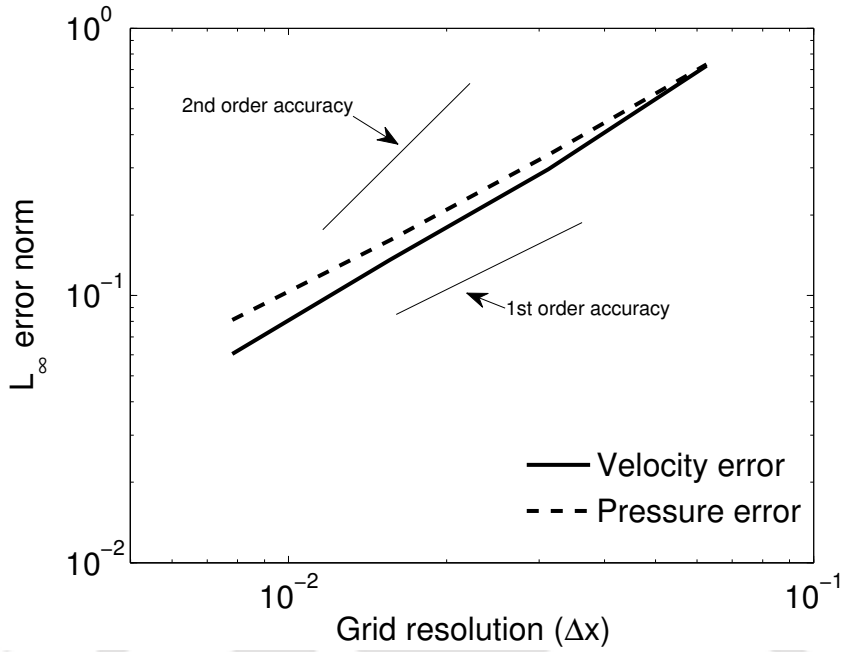

Figure 5.11: L_∞ error norm for velocities $\mathbf{u}$ and pressure p for Taylor-Couette problem showing spatial accuracy.

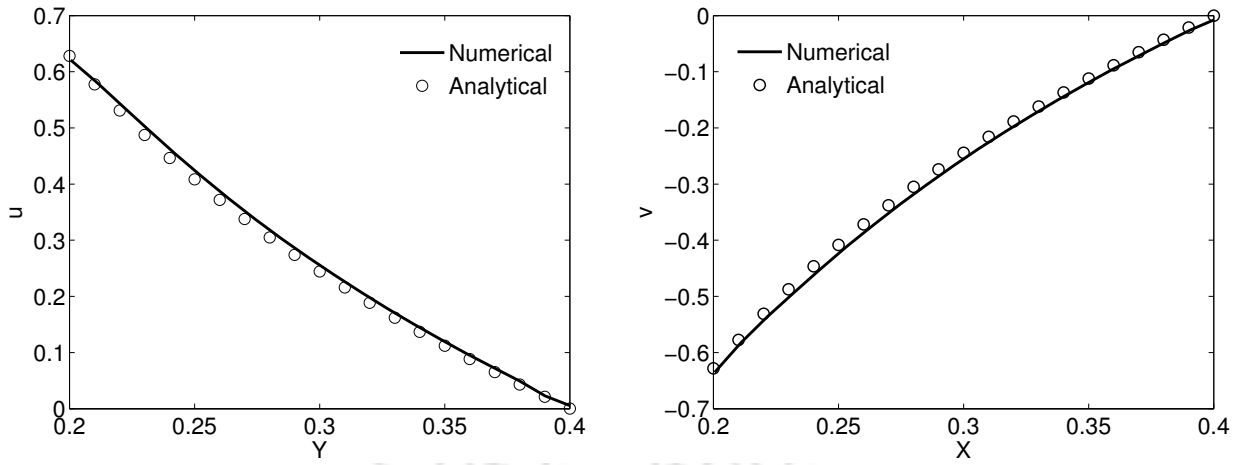

(a) u-velocity profile (b) v-velocity profile

Figure 5.12: Comparison of the obtained numerical and analytical solutions showing (a) u velocity profile at x =0 and (b) v velocity profile at y =0.

5.4 Results and discussions

We have shown in earlier sections that the proposed diffuse interface immersed boundary–finite volume (IB–FV) flow solver exhibits nominal second-order accuracy in space and time and has excellent mass and momentum conservation. We devote this section to

investigate several test problems involving single and multi–fluid flows, stationary and moving bodies as well as imposed and induced motions to thoroughly evaluate the efficacy of the IB–FV solver. These test cases span a large spectrum of flow scenarios in the laminar regime and serve to highlight the scope and utility of the proposed diffuse interface IB methodology for complex flow applications such as two–particle sedimentation in stratified media.

5.4.1 Flow past a stationary circular cylinder

We begin our studies by investigating the steady and unsteady laminar flows past a circular cylinder using the IB–FV solver. The computational domain is $30D \times 8D$ channel, in which a circular cylinder of diameter D = 1 is placed at $8D$ from the inlet. A constant velocity of unity is specified at the inlet and the Neumann boundary condition is provided at the outlet. The top and bottom walls of the channel are considered to be slip walls. To resolve the geometry of the cylinder accurately and to preserve the sharpness of the solid–fluid interface to a reasonable extent, a fine uniform mesh ($\Delta x = \Delta y = 0.02$) is used in the vicinity of the cylinder. The grid is stretched gradually in both directions, leading to a non–uniform Cartesian mesh. The simulations are performed for Re_D = 40 and 200 with a timestep of Δt = 0.001.

The lift and drag histories for both cases are shown in the Figure 5.13. The solutions for the Re = 40 case are steady and exhibit symmetrical recirculation zones in the wake while those for Re = 200 reproduce the unsteady Karman vortex street. The lift and drag coefficients (mean values in unsteady case) as well as the recirculation zone length (in the steady case) are tabulated in Table 5.1. The results from the present solver are in excellent agreement with those of previous researchers [57, 109, 110] and provides a primary validation of the IB–FV solver, albeit for the stationary body case in single phase flow.

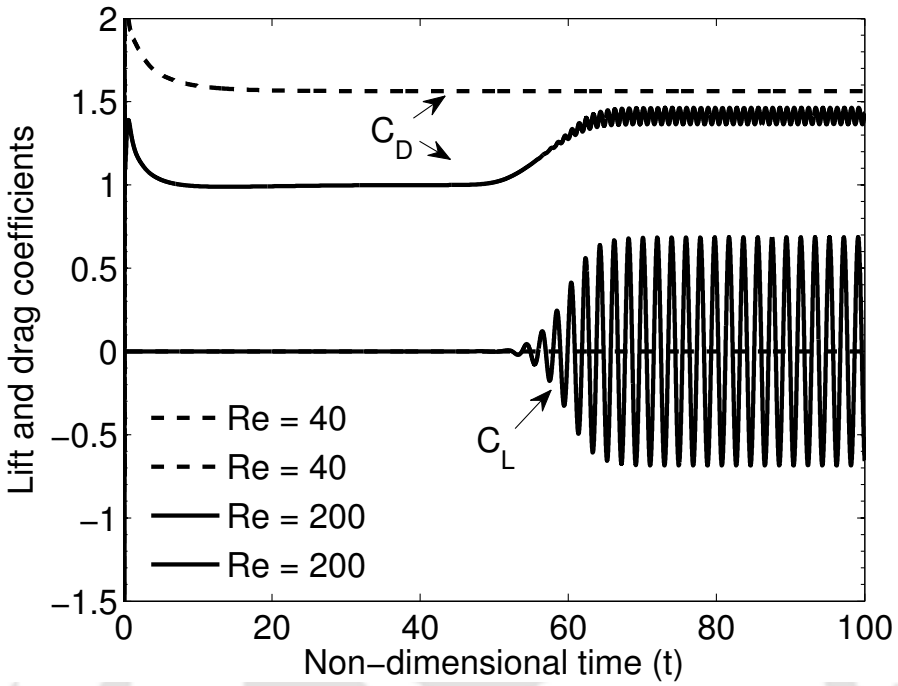

Figure 5.13: Drag and lift coefficient for the flow past a stationary cylinder.

Table 5.1: Drag and lift coefficient for the flow past a cylinder.

Authors	Re = 40		Re = 200	
	C_D	l_w	C_D	C_L
Present	1.56	2.23	1.35±0.04	±0.69
Pan [63]	1.5	2.19	1.27±0.04	±0.6
Choi et al. [109]	1.52	2.25	1.36±0.048	±0.65
Apte et al. [57]	1.54	-	-	-
Mittal et al. [111]	1.53	-	-	-
Russell and Wang [112]	1.6	2.29	-	-
Zhang et al. [110]	-	-	1.37±0.03	±0.71

5.4.2 Flow past a stationary airfoil

The incompressible viscous flow past an airfoil is studied numerically to understand the ability of the IB approach in treating thin streamlined solids. The NACA 0008 airfoil at two different angle of attacks ($\alpha = 0^\circ$ and 4°) are used for the simulations. The computational domain and boundary conditions are similar to the previous test case, except that a non–uniform Cartesian background mesh which is more finer (Δx = 0.01, Δy = 0.01) near the airfoil and progressively coarsening as one moves away from it is employed. This helps to accurately resolve the thin geometry including the sharp

trailing edge. We ensure that the flow is laminar by choosing a Reynolds number Re_c = 2000 as also in [111] with the the timestep for simulations taken as Δt = 0.001.

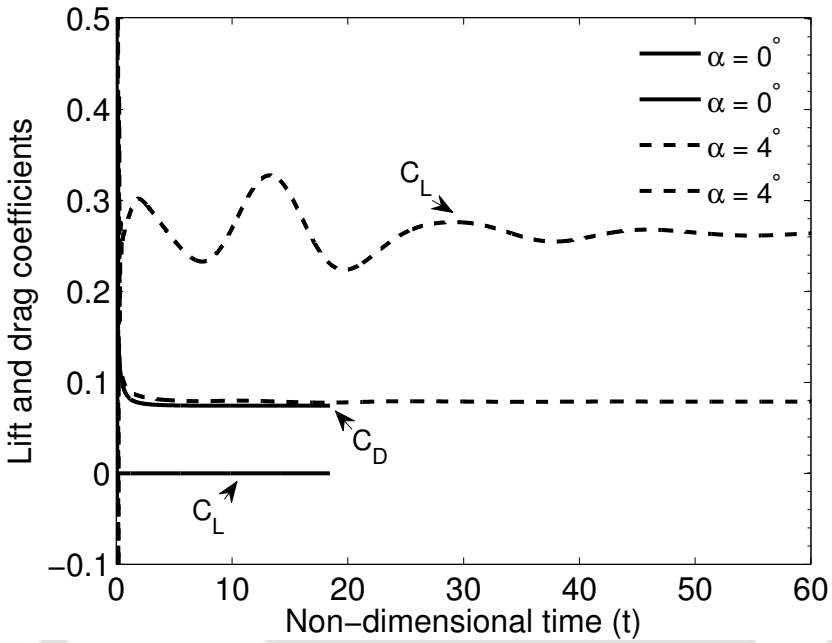

Figure 5.14: Drag and lift coefficient for the flow past an airfoil for $Re_c = 2000$.

Table 5.2: Drag and lift coefficient for the flow past an airfoil for $Re_c = 2000$.

Authors	$\alpha = 0°$		$\alpha = 4°$	
	C_D	C_L	C_D	C_L
Present	0.075	-	0.080	0.264
Mittal et al. [111]	0.078	-	0.081	0.273
Kroo and Kunz [113]	0.076	-	0.080	0.272

The lift and drag coefficient histories for the simulations at the two angles of attack are shown in Figure 5.14. The time taken to reach steady state for the larger angle of attack is more although the flow remains unseparated. In Table 5.2, the obtained lift and drag coefficients at steady state are compared with the the numerical findings in [111,113]. It can be observed that the agreement between present results and those in published literature is reasonable. In addition to this, we also present the variation of pressure coefficient along the airfoil surface for $\alpha = 4°$ in Figure 5.15. To effect comparison, we also show results obtained on a triangulated body fitted grid with ap-

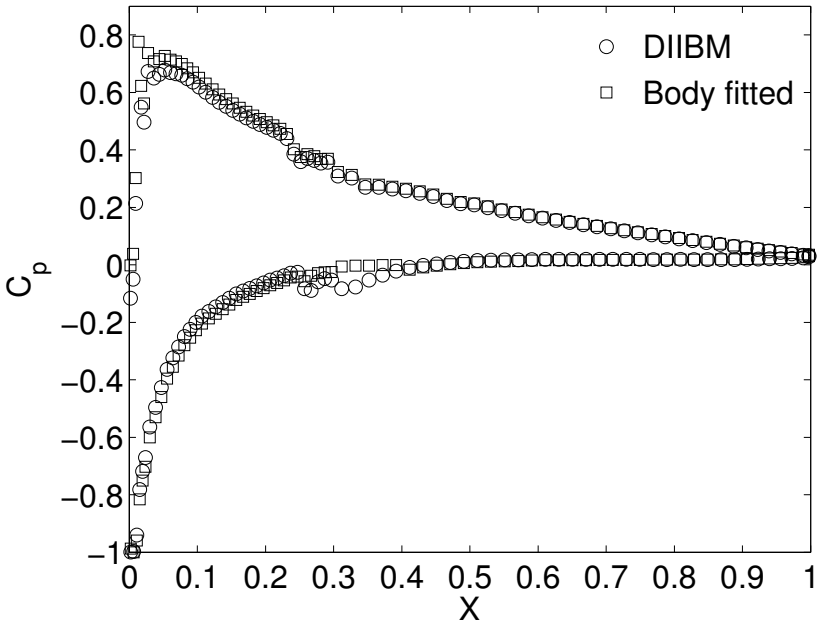

Figure 5.15: Pressure coefficient for flow over NACA 008 at $\alpha = 4°$ for $Re_c = 2000$.

proximately same number of elements as the case of background Cartesian mesh. While some deviations between the pressure distributions from the IB approach and body–fitted grids are seen, the overall agreement is quite satisfactory. The deviations may be attributed to the fact that the IB approach is non–conformal and adaptive refinement in the vicinity of the airfoil, especially at the leading and trailing edges, is expected to reduce these differences.

5.4.3 Flow induced by inline oscillating circular cylinder

In order to assess the ability of the solver for moving body problems, we examine the inline oscillation of a circular cylinder as also studies in [114]. The details of the computational domain and the grid are same as those in Section 5.4.1. The solution procedure is also similar to the stationary cylinder case, except that there is no inlet velocity (quiescent medium) and that the cylinder oscillates with an imposed velocity $U = \frac{2\pi}{KC} A\, cos(\frac{2\pi}{KC} t)$ where A is the amplitude and $KC = \frac{2\pi A}{D}$ is the Keulegan–Carpenter number.

Following the studies in Dütsch et al. [114], we use Re_D = 100 and KC = 5 with

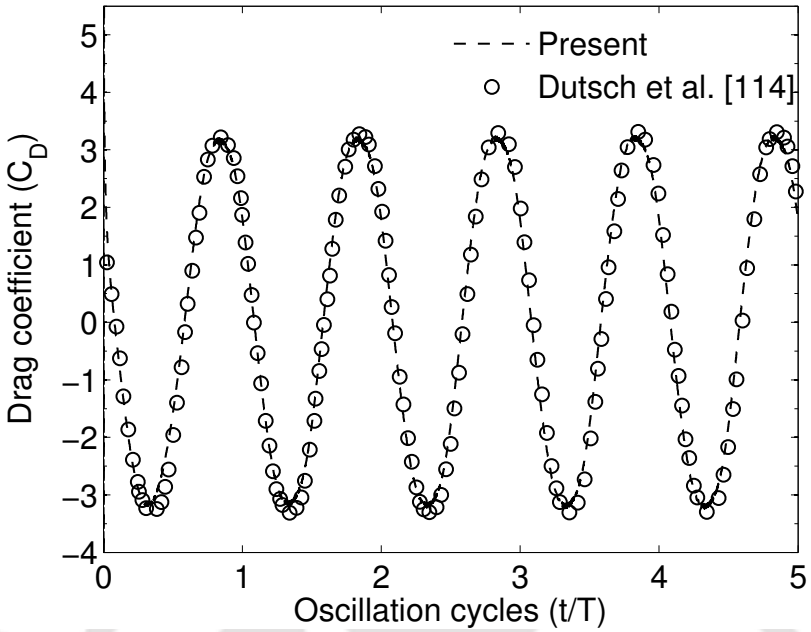

(a) $\Delta x = 0.02$, $\Delta t = 0.001$

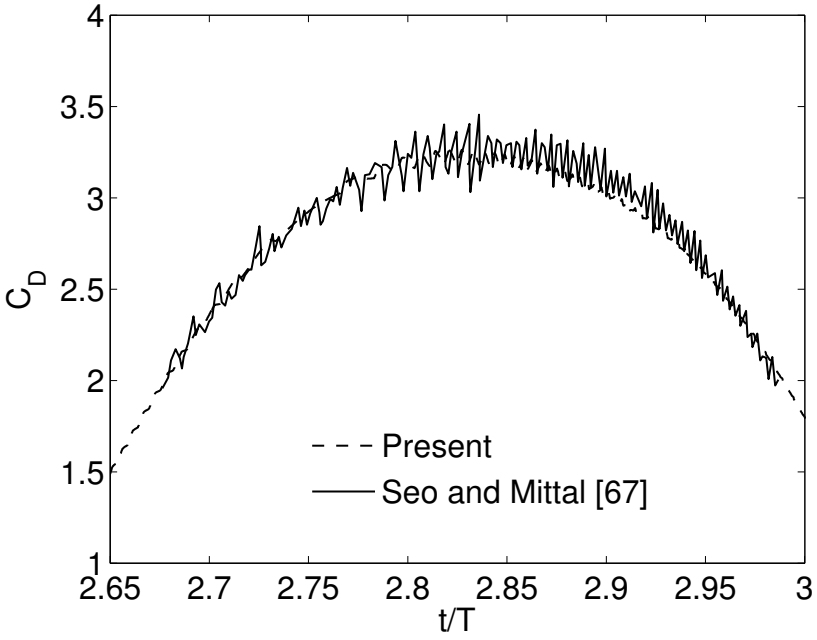

(b) Spurious oscillations (enlarge view)

Figure 5.16: Inline oscillation of a circular cylinder in stagnant fluid for $Re = 100$ and $KC = 5$ (a) validation with Dütsch et al. [114] (b) comparison of spurious oscillation with Seo and Mittal [67].

Δt = 0.001. The history of the drag force (C_D) acting on the cylinder is plotted in Figure 5.16(a) and shows a periodic behaviour which also agrees well with the published results in [114]. Furthermore, the force histories show a smooth variation over

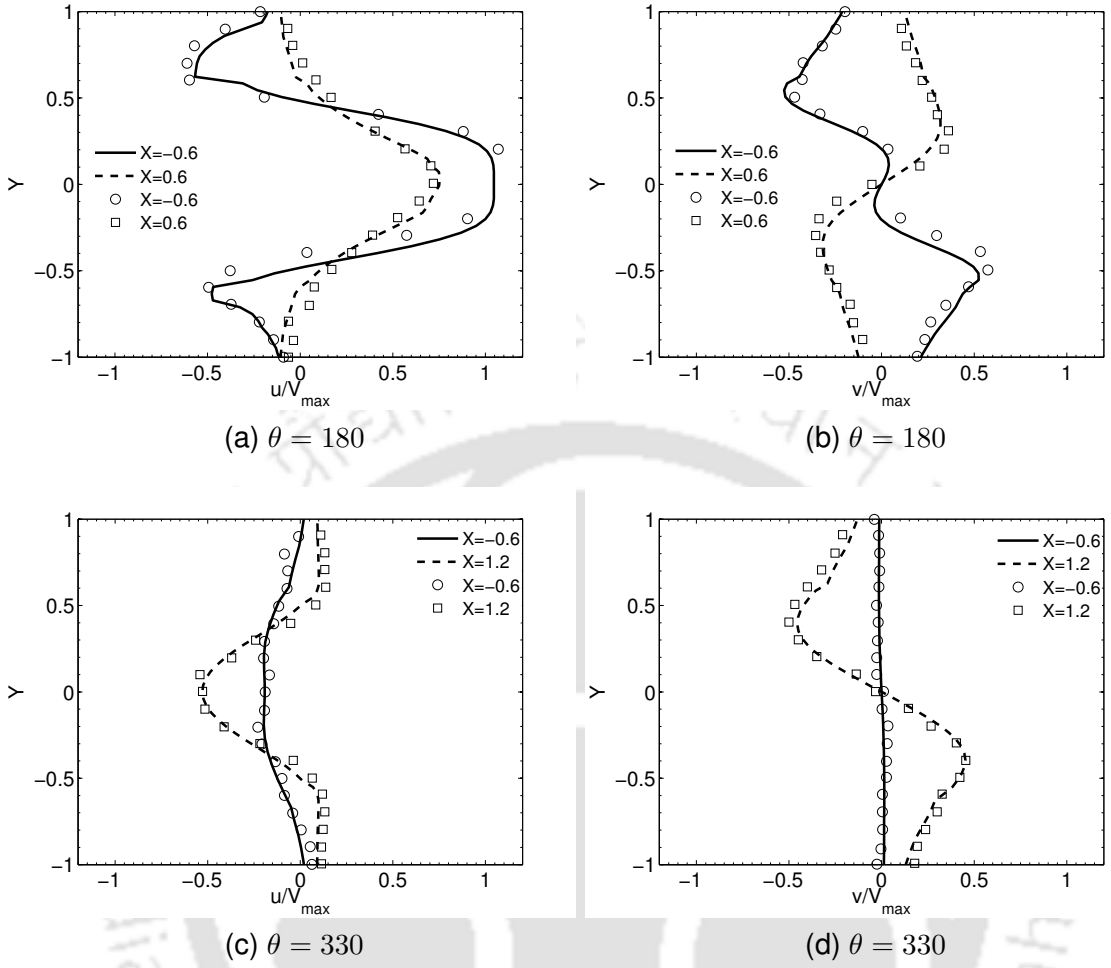

(a) $\theta = 180$ (b) $\theta = 180$

(c) $\theta = 330$ (d) $\theta = 330$

Figure 5.17: Velocity profiles for phase angle $\theta = \frac{2\pi}{KC}t =$ (a) 180 (b) 180 (c) 330 and (d) 330, at the cross section X, the lines show the present results and symbols are experimental data of Dütsch et al. [114].

several oscillation cycles and no spurious force oscillations are observed. This is an important observation, since sharp interface IB methods such as those in [65, 67] are prone to non–physical oscillations in force histories for moving body simulations. The approaches in [65, 67] are therefore complemented with special measures to suppress these oscillations. Figure 5.16(b) shows a comparison of the drag coefficients from the proposed diffuse IB–FV solver and those from [67] over a short time interval, during which the cylinder also changes its direction of motion. In comparison to the results from the proposed methodology, those from [67] where a ghost–cell IB approach is used on a mesh with finer resolution with larger timestep than used herein show appreciable spurious oscillations. The near–negligible spurious oscillations observed in

the present study is likely a manifestation of the discrete mass conservation of the diffuse IB approach demonstrated earlier in Section 5.2. The interface diffusion in the computational process does not hamper the solution accuracy as shown in Figures 5.17(a) to 5.17(d) which depict the velocity profile for two different phase angles ($\theta = \frac{2\pi}{KC}t = 180^o, 330^o$). The numerical results from the present study agree well with the experimental results in [114] underlining the ability of the present solver to handle moving body problems with ease while avoiding spurious force oscillations without the need for special sophisticated techniques. The latter characteristic is critical for fluid–structure interaction problems and makes the proposed IB–FV solver a simple–to–implement and accurate methodology for this class of problems.

5.4.4 Sedimentation of a circular particle

Having examined the ability of the IB–FV solver for imposed body motion, we consider the more complex case of induced body motion. We first simulate the sedimentation of a circular particle by only considering the translational degrees of motion. A particle of diameter D = 1 is centered at (4D, 20D) of the 8D$\times$24D rectangular domain. The no-slip condition is given to the all walls. We choose a density ratio of the particle to background fluid is, $\frac{\rho_S}{\rho_L}$ = 1.25 in accordance with the parameters in Blasco et al. [56]. The Froude number is set to $\frac{U^2}{gD}$ = 1 and Reynolds number based on the fluid density is, $\frac{\rho_L\sqrt{gD}D}{\mu_L}$ = 39.13. In this test case we also study the dependence of grid on particle trajectories and terminal velocity using four different grid resolutions $D/\Delta x$ = 15, 20, 30 and 50. The timestep of Δt = 0.001 is used for all the cases.

Initially particle accelerates due to gravity, thereafter buoyancy and drag forces balance the weight and particle moves with constant terminal velocity. In Figure 5.18 the time history of the vertical downward velocity on all grid resolutions is depicted. For $D/\Delta x$ = 15 and 20, particle attains the terminal velocity early compared to the finer meshes. The relatively poor resolution of the circular geometry on the coarser mesh leading to a higher drag could be the cause of low terminal velocity. For finer grid resolutions, we observe higher terminal velocities which are nearly identical to each other and further increase in grid resolution does not impact the solution. The results on $\frac{D}{\Delta x}$ =

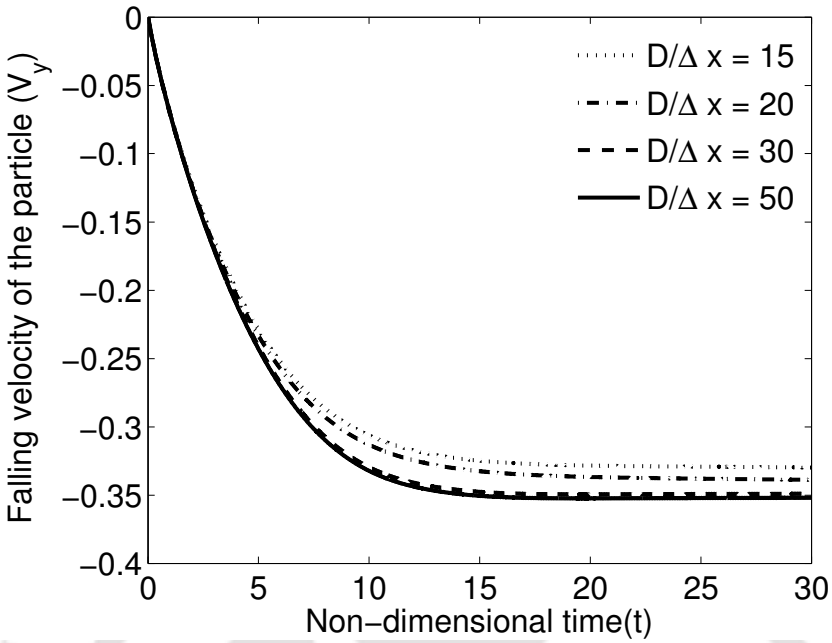

Figure 5.18: Sedimentation of single particle of density ratio $\frac{\rho_S}{\rho_L}$ = 1.25, for Re = 39.13.

30 are therefore grid-independent and agree excellently with those reported in Blasco et al. [56] for a similar grid resolution.

5.4.5 Roll motion of a rectangular barge

Next we examine the capability of the solver for purely rotational degree of freedom by simulating the free decay motion of a rectangular barge, floating on the free surface. The barge of length L = 1 and width $b = \frac{L}{3}$, half submerged in water and initially inclined at 15° as shown in Figure 5.19 is allowed to only rotate about an axis passing through its center of mass. The barge is immersed in a domain of 20L$\times$5L with a uniform grid resolution $\Delta x = \Delta y$ = 1/50. To avoid the wall effects on barge, slip boundary condition is provided on the lateral and top walls while the no–slip condition is prescribed at the bottom wall of the domain. The tank is filled with water up to the height of $3L$, and the water–air density and viscosity ratios are $\frac{\rho_H}{\rho_L}$ = 833 and $\frac{\mu_H}{\mu_L}$ = 55 respectively. The motion of the barge is driven by gravity and values of Froude number $\frac{U^2}{gL}$ and the Reynolds number $\frac{\rho_L\sqrt{gL}L}{\mu_L}$ are fixed to 1 and 34310 respectively. A timestep of Δt = 0.001 is used for the calculations for this test case which considers only the rotational degree of freedom.

The initial unstable position of the barge causes an imbalance between the forces causing it to move and induce velocities in the surrounding fluids which then exert forces that affects its motion (including position and velocity). The motion of the barge, as can also be expected intuitively, is periodic but the amplitude decays over time due to viscous damping. A mesh refinement study is carried out for this test case on three uniform grid resolutions ($D/\Delta x$ = 20, 50 and 80) and the time history of the barge inclination is presented in Figure 5.20. It can be seen that except on the coarsest mesh, the damping pattern on other meshes are nearly identical. This means that the numerical solutions on the mesh with $D/\Delta x = 50$ is grid-independent and all results shown for this case employ this mesh. Figure 5.21 shows the variation of angle of inclination of the barge with time which clearly shows damped oscillations that show good agreement with the experimental measurements of Jung et al. [115] and excellent agreement with the numerical results of Calderer et al. [53]. While the numerical decay is slower than that reported experimentally, because frictional effects in the experimental apparatus and possible turbulence are not accounted for, the present simulations are in better agreement with the experimental results than those of [53]. This numerical experiment not only demonstrates the ability of the IB–FV approach for fluid–structure interactions but also highlights its capability to deal with rigidly moving bodies in presence of multiple fluids with large density and viscosity contrasts.

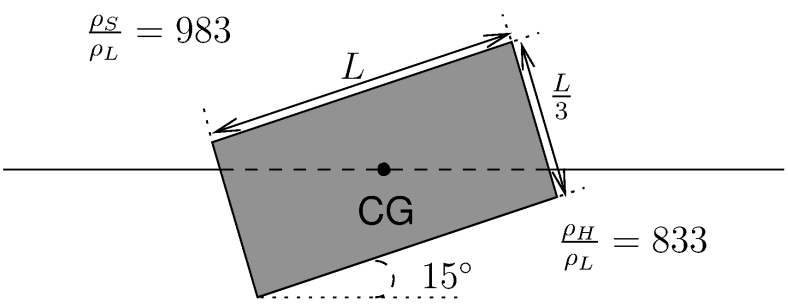

Figure 5.19: Schematic representation of the rectangular barge.

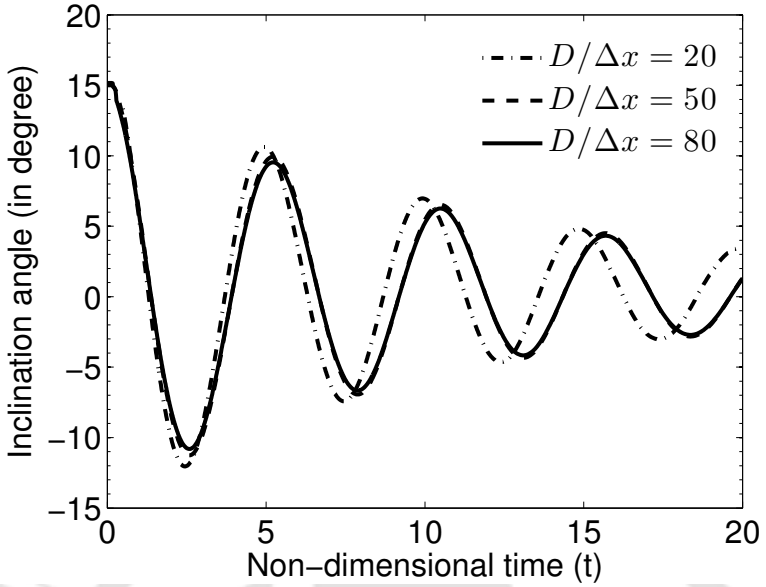

Figure 5.20: Mesh refinement study for the roll motion of rectangular barge.

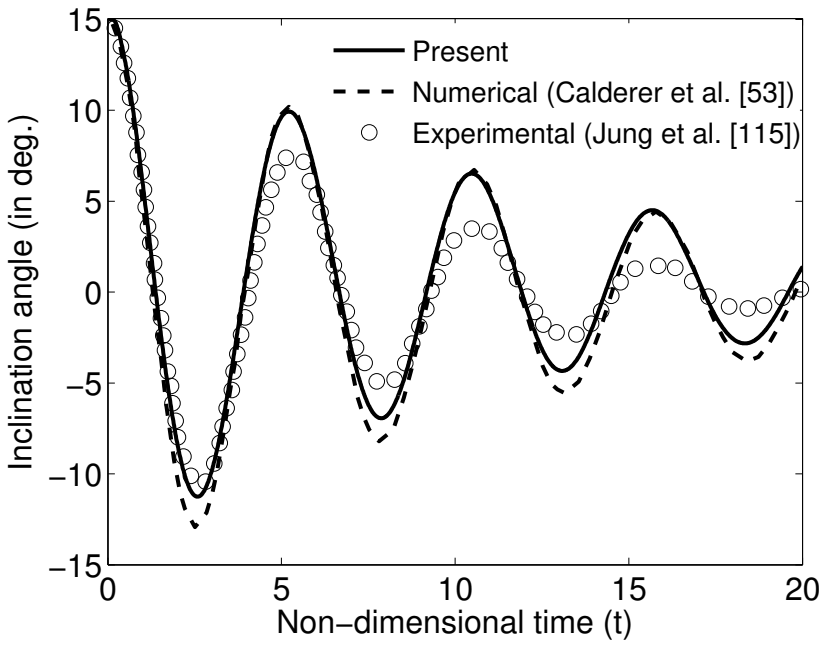

Figure 5.21: Angle of inclination of the rectangular barge of density ratio $\frac{\rho_S}{\rho_L}$ = 983 during oscillations initially inclined at 15°.

5.4.6 Water entry of a circular cylinder

We begin our investigations on the efficacy of the solver for multi–fluid flows with fluid–structure interaction by simulating the water entry of a circular cylinder. We choose a rectangular computational domain of cross-section 8D$\times$10D, which is discretised with a

uniform grid of resolution $\Delta x = \Delta y =$ 1/50. The lateral walls of the domain are treated as the slip walls and no-slip boundary condition is provided on the top and bottom walls. A cylinder of diameter D = 1 is initially placed in the air and the water–air density and viscosity ratios are $\frac{\rho_H}{\rho_L}$ = 833 and $\frac{\mu_H}{\mu_L}$ = 55 respectively. We perform three different test cases to thoroughly analyse the dynamics of the cylinder: (i) cylinder falling with constant velocity (ii) neutrally buoyant cylinder in free fall and (iii) half buoyant cylinder in free fall. Simulations are carried out with Froude number $\frac{U^2}{gD}$ = 1 (for cases (ii) and (iii)) and Reynolds number $\frac{\rho_L \sqrt{gD} D}{\mu_L}$ = 7618 and a time step of Δt = 0.001 is employed in all studies.

5.4.6.1 Cylinder falling with constant velocity

We start with the case of a solid cylinder moving with a constant downward velocity V = -1. The domain is filled with water up to the height of $6D$ from the bottom and the cylinder is centered D above the water surface. As soon as the cylinder strikes the water surface, an impact force also known as slamming force starts acting on the cylinder. Figure 5.22 reveals the magnitude of the slamming coefficient, $C_s = \frac{2F_{iy}}{\rho_H/\rho_L}$, with the non-dimensional time t corresponding to the cylinder–water impact. On impact, high pressure fields are generated around the surface of contact which lead to the maximum slamming coefficient. Thereafter, C_s decreases abruptly to the minimum value as the cylinder continues to submerge in water. It can be seen from Figure 5.22 that the present results significantly underpredict the slamming coefficient when compared with the experimental measurements of Campbell and Weynberg [116] at and immediately after impact. The agreement between the numerical simulations and experiments is quite good in the later stages after impact (during motion when cylinder is fully submerged in water) and our predictions are quantitatively similar to those of Kleefsman et al. [117].

We also compute the time history of cylinder volume (area in two dimensions) as it moves through air, strikes the surface and then moves in water. The error between the exact and numerical volumes, $(A_n - A_e)$, as a function of time is plotted in Figure 5.23. One can easily see that despite the grid being non–conformal to the body

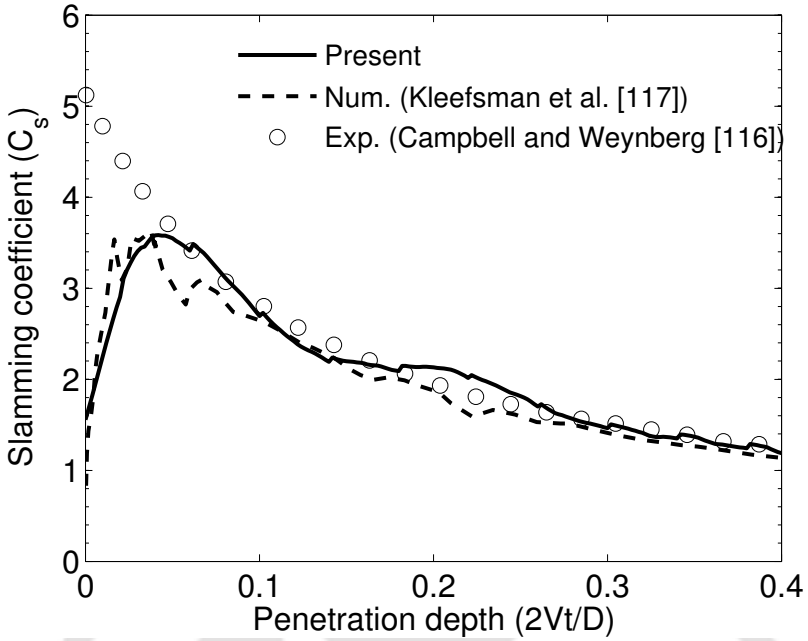

Figure 5.22: Water entry of the circular cylinder with the constant velocity V = -1.

and the description of the cylinder realised using an Eulerian approach, the errors remain acceptably low of the $\mathbf{O}(10^{-4})$. We remark that the IB–FV approach does a good job of preserving the geometry (shape) of the rigid solid(s) while accurately predicting the dynamics for this test problem.

5.4.6.2 Neutrally buoyant cylinder freely falling in water

We turn our attention to freely falling bodies in multiphase flows by considering a neutrally buoyant cylinder to fall freely in a tank (which is the computational domain itself) of water depth $3D$. The distance between the bottom of the cylinder and free surface is $4.55D$ and the cylinder and water assume to have equal density. We choose the same grid as in the earlier study and carry out simulations up to t = 5.2 with a timestep of Δt = 0.001. The dynamics of the problem are encapsulated in Figures 5.24(a) to 5.24(f) which show the free surface deformation at different time instants. We see that the cylinder touches the free surface at t = 2.83 and jets emerge from the side of the cylinder and keeps growing as the cylinder submerges in the fluid and gets fully wetted, reaching the bottom of the domain at t = 5.2, where it settles. It must be noted that this would be the final stable position for the cylinder if a longer domain (not shown here)

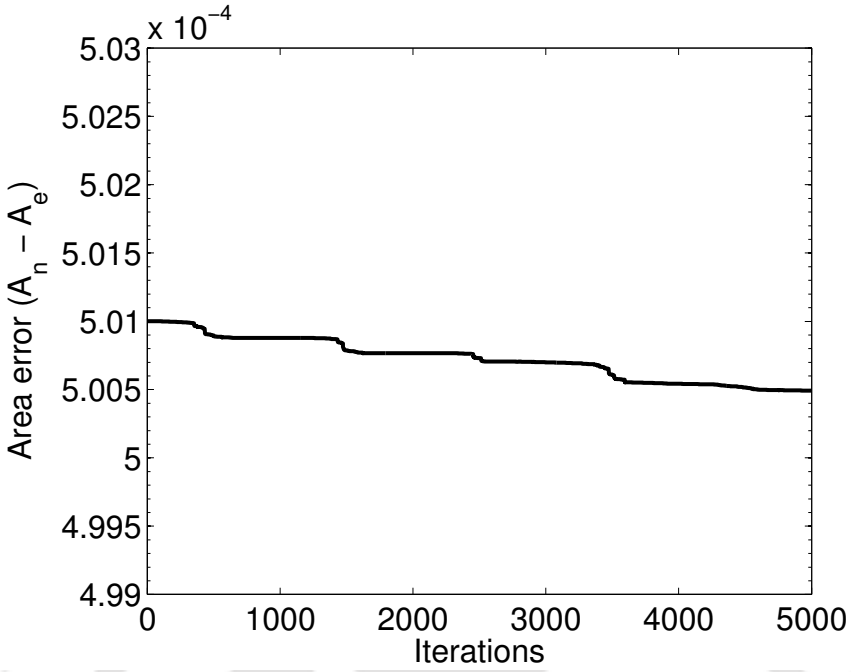

Figure 5.23: Area error of a circular cylinder in water entry with the constant velocity V = -1.

were to be chosen and our results qualitatively agree with the experimental observations of Greenhow and Lin [118]. We also see that the quantitative comparisons of the depth of penetration from the present solver with the numerical predictions using CIP method in [119] are excellent as shown in Figure 5.25 and fairly agree with the limited experimental data in [118].

5.4.6.3 Half buoyant cylinder freely falling in water

While the previous numerical experiment considered equal densities for cylinder and the liquid, we now consider the equally challenging scenario of a freely falling cylinder whose density is half that of water. The grid and simulation parameters are chosen same as the previous study, except that the simulation is run longer up to t = 7.5 and we attempt to understand the evolution of the flow through the free surface deformation at different time instants. A closer look at Figures 5.26(a) to 5.26(f) clearly show that the flow dynamics is expectedly different from the neutrally buoyant case. The time of impact is nearly the same as the neutrally buoyant case (since the air resistance is negligible) and one can observe distinct water jets at t = 3.5 with the radius of the air cavity increasing as the cylinder moves down into the liquid. At t = 4.7, the cylinder

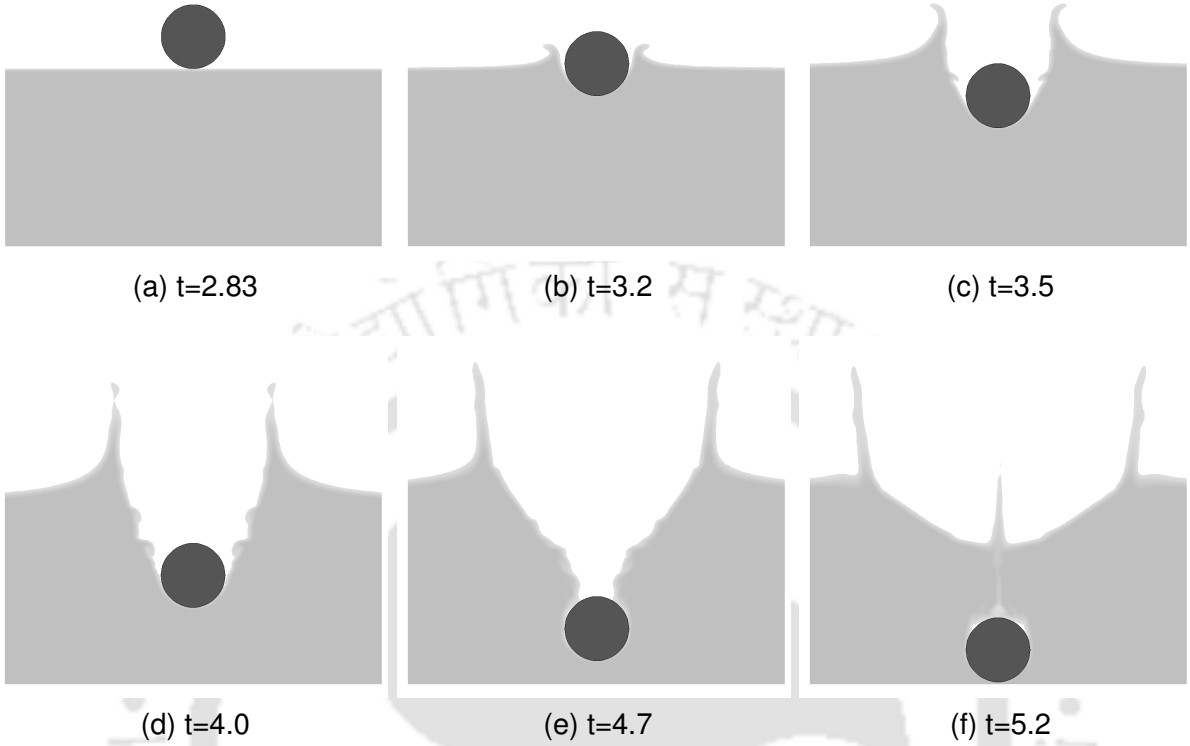

Figure 5.24: Free surface deformation at different time instants t = (a) 2.83 (b) 3.2 (c) 3.5 (d) 4.0 (e) 4.7 and (f) 5.2 during water entry of a neutrally buoyant cylinder.

starts experiencing a net upward force causing it to reverse the direction of motion and as the cylinder rises the water layer is pushed up as can be seen at t = 6.5. The variation of the depth of penetration as time progresses is shown in Figure 5.27, which shows a very good agreement with the experimental results of Greenhow and Lin [118] and the BEM computations of Sun and Falistin [120]. Our results with the diffuse interface IB–FV solver also show that the cylinder finally floats on the surface, settling at approximately the same location it reaches at t = 7.5.

The experiments with the freely falling cylinders, while two–dimensional, account for all three degrees of freedom (two translational and one rotational) and brings out the ability of the IB methodology to simulate rigidly moving solid(s) and their interaction with more than one fluid. It must be remarked that we have not accounted for surface tension in these calculations (as also in the case of decay of the rolling motion of the barge), but the excellent agreement of the results with other computations indicate

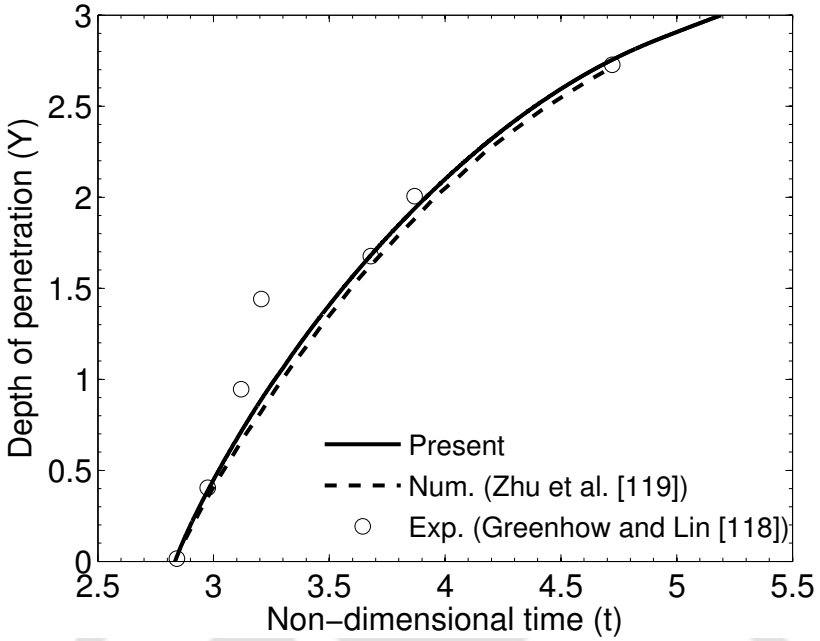

Figure 5.25: Depth of penetration of a neutrally buoyant cylinder (extreme bottom) from the free surface for Re = 7618 and Fr = 1.

that surface tension effects are sub–dominant in these scenarios. We also emphasise that the flow solver is equipped to handle interfacial tension between immiscible fluids with large density ratios as shown in Chapter 4, but we defer from performing these computations for sake of consistency in comparing with other published results.

5.4.7 Sedimentation of circular particles

In order to assess the performance of the flow solver for problems with multiple moving bodies, we focus on the sedimentation of circular particles in quiescent medium. Particle sedimentation studies have vast applications in engineering and has been the subject of experimental and numerical investigations. We analyse the potential of the IB–FV solver in resolving the dynamics of flow due to arbitrary motion of two identical particles in two different environments. We first study the problem with a homogeneous single fluid environment which has also been studied by other researchers [54, 56] and then investigate the differences arising from a discretely stratified environment.

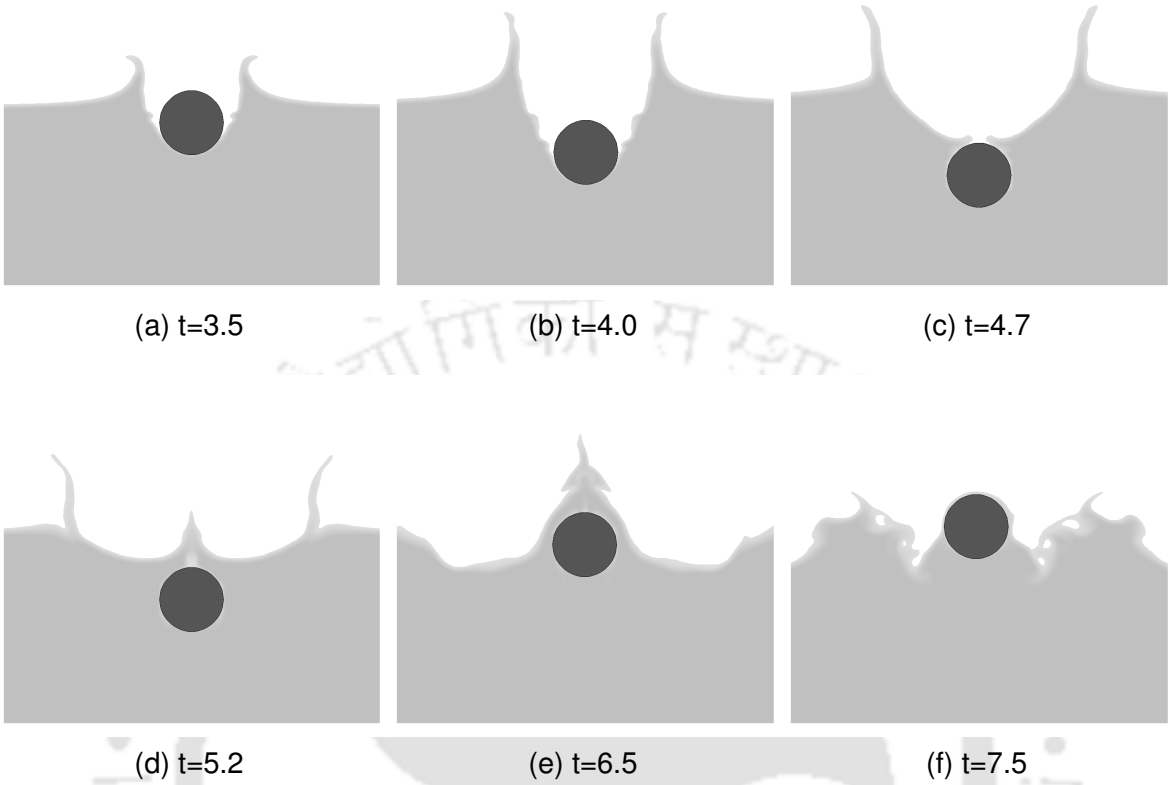

(a) t=3.5 (b) t=4.0 (c) t=4.7

(d) t=5.2 (e) t=6.5 (f) t=7.5

Figure 5.26: Free surface deformation at different time instants t = (a) 3.5 (b) 4.0 (c) 4.7 (d) 5.2 (e) 6.5 and (f) 7.5 during water entry of a half buoyant cylinder.

5.4.7.1 Two–particle sedimentation in homogeneous medium

We consider two identical circular particles of density ratio $\frac{\rho_S}{\rho_L}$ = 1.5 and diameter D = 1 dropped from the center line of a rectangular domain 8D$\times$24D at heights of (4D, 20D) for the trailing particle and (4D, 18D) for the leading particle. The domain is discretised with a uniform grid of resolution $\Delta x = \Delta y =$ 0.025 and the no–slip condition is enforced on all domain boundaries. Simulations were carried out for Reynolds number $\frac{\rho_L \sqrt{gD} D}{\mu_L}$ = 391.3 and Froude number $\frac{U^2}{gD}$ = 1 with a timestep of Δt = 0.001.

The sedimentation of the two particles aligned vertically exhibits the well–known phenomena of drafting, kissing and tumbling (DKT) that has been observed by several researchers. Our numerical results also reproduces this phenomenon which is evident from Figures 5.28(a) to 5.28(d), which show the position of the two particles in the domain at different instants of time. It can be seen that the particles begin to accelerate

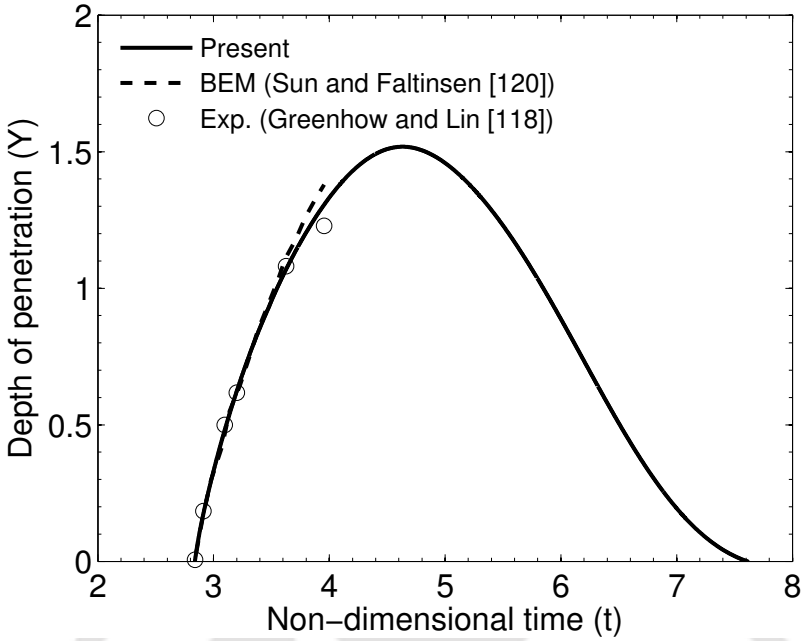

Figure 5.27: Depth of penetration of a half buoyant cylinder (extreme bottom) from the free surface for Re = 7618 and Fr = 1.

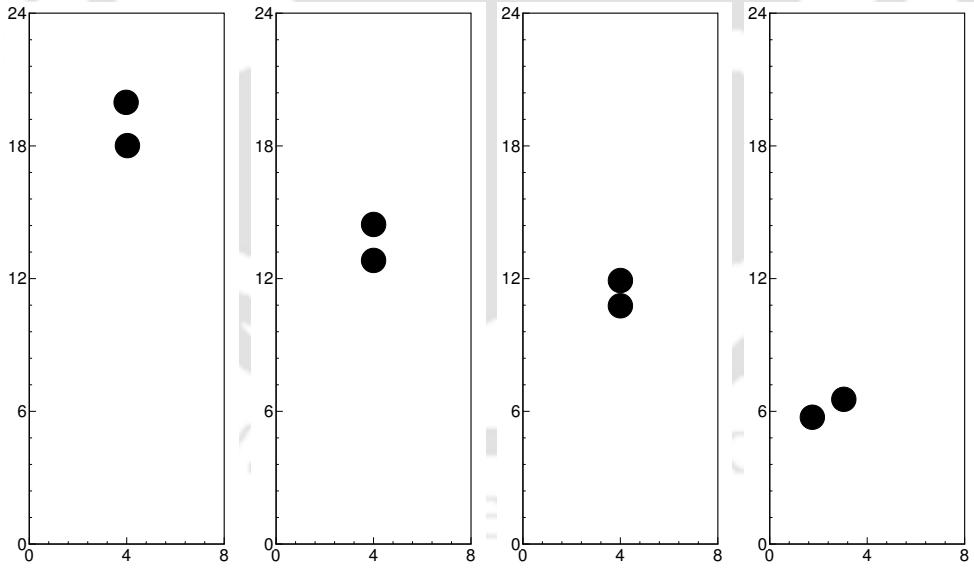

Figure 5.28: The position of two circular particles showing (a) initial position, (b) drafting, (c) kissing and (d) tumbling at different time levels for Re = 391.3 and particles density ratio $\frac{\rho_S}{\rho_L}$ = 1.5.

downward due to gravity and the trailing particle comes under the influence of the wake of the leading particle shortly afterwards. The trailing particle therefore experiences lesser drag and achieves a higher velocity as can be seen in Figure 5.29(b) and this

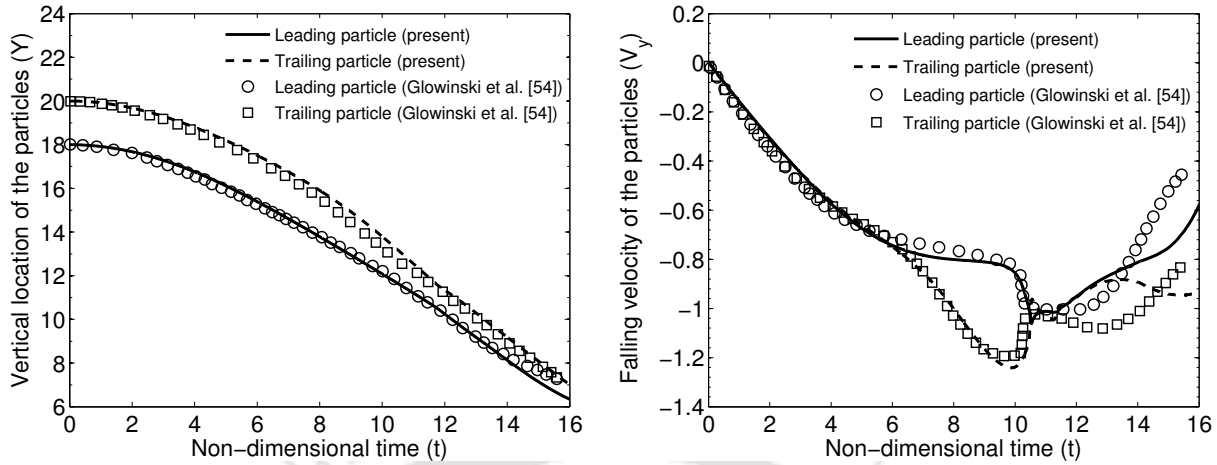

(a) Vertical location (b) Falling velocity

Figure 5.29: Sedimentation of two circular particles of density ratio $\frac{\rho_S}{\rho_f}$ = 1.5: time histories of (a) the vertical location of the particles center (y) (b) falling velocity of the particles (V_y).

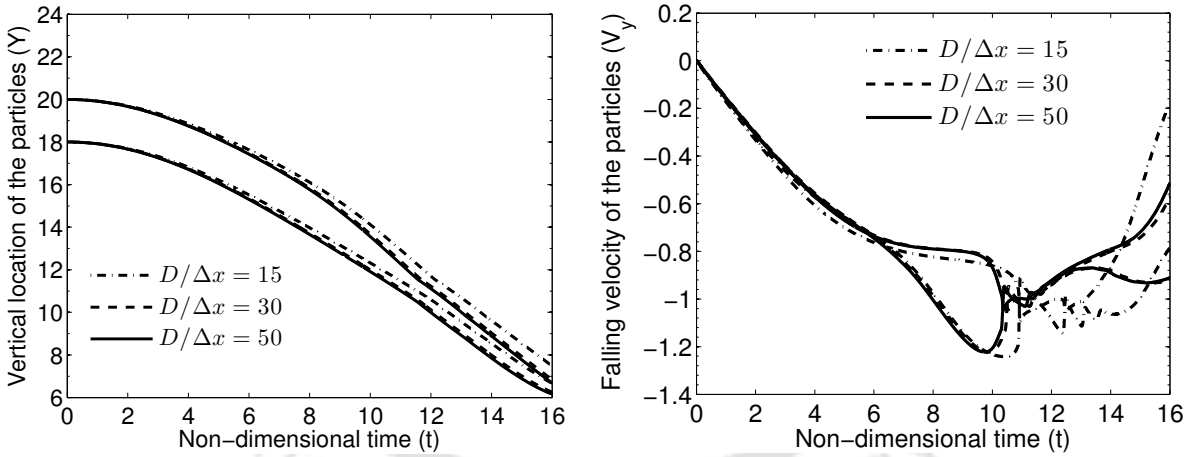

(a) Vertical location (b) Falling velocity

Figure 5.30: Mesh refinement study for sedimentation of two circular particles of density ratio $\frac{\rho_S}{\rho_f}$ = 1.5: time histories of (a) the vertical location of the particles center (y) (b) falling velocity of the particles (V_y).

phenomenon is called drafting. Subsequently, the trailing particle catches up with the leading particle and touches it which is known as kissing and may be observed at t = 11 for this case. The particles remain in contact [4] and the two move together as if they were a single elongated body for a short time. This position is however unstable

[4]When the minimum separation between particles as defined by the repulsive force model is attained we say that they are in contact. No physical contact is allowed to occur to avoid anomalous “piercing" of solids.

and the particles drift apart from each other under the action of repulsive forces at time t = 16 while continuing their downward motion and this phenomenon is referred to as tumbling. The time history of the vertical location and falling velocities of the particles obtained using the IB–FV solver are shown in Figures 5.29(a) and 5.29(b). The present results are compared with the computed results of Glowinski et al. [54] which employed a fictitious domain method. Despite the reasonably good agreement of the vertical positions and the velocities in drafting and kissing phases, one can clearly notice a significant discrepancy in the velocities in the tumbling phase. This is possibly because the dynamics of the particle in the tumbling phase is very sensitive to grid resolution. In order to confirm the grid-independency of the reported results we have carried out simulations on two other uniform grid resolutions viz. $D/\Delta x$ = 15 and $D/\Delta x$ = 50. These grids represent mesh resolutions that are respectively coarser and finer than the one considered in this study. A comparison of the time histories of vertical location and falling velocity on the three grids presented in Figures 5.30(a) and 5.30(b) show that there are noticeable differences between the predictions on the coarsest mesh and those obtained on the two finer meshes. However, the results on $D/\Delta x$ = 30 and 50 show excellent agreement demonstrating that the mesh resolution defined by $D/\Delta x = 30$ suffices for solutions to be grid-independent. The source of differences in computational predictions shown in Figure 5.29(b) may therefore be attributed to differences in solution methodology as well as the repulsive force model and this has also been previously reported by Di and Ge [121]. While the issue of sensitivity of the tumbling phase needs more attention, this experiment gives credence to the IB–FV solver as a numerical approach that can mimic the complex physics in two–particle sedimentation with reasonable accuracy.

5.4.7.2 Two–particle sedimentation in discretely stratified medium

We extend the problem of two–particle sedimentation discussed earlier to a more complex scenario involving multiple fluids in a stratified environment. We consider the same computational domain as in the earlier study, which is filled with four fluids of progressively increasing density starting from 1 to 1.15 (in steps of 0.05) to equal heights as we go from the top to the bottom. The details of the grid, simulation parameters and

solution procedure are identical to those discussed in the earlier case, except that the leading and trailing particles are dropped from $20D$ and $22D$ respectively. We ensure that the initial location of the two particles are in the same fluid (which is also the least dense) and all fluids are assumed to have the same dynamic viscosity. The flow dynamics showing the interaction between particles and with the surrounding fluids is depicted in Figures 5.31(a) to 5.31(f) where one can observe the complex particle motions. A closer look however reveals that the particle dynamics show similarities yet differ from those reported for the homogeneous fluid environment. Unlike the previous case where the fluid forces are purely due to a single fluid, the drag and buoyancy forces in case of stratified environment would depend on the fluid with which the solid(s) are in contact with at different instants leading to a complex interplay of forces that in turn affect the motion. While one can observe drafting (at t = 9) and tumbling in the later stages (beyond t = 14), the kissing phase seen in the earlier study appears to have been modified. In particular, the particles first kiss each other around t = 11, followed by a separation phase before they come into contact at t = 14. This leads to a kissing-separation-kissing phenomenon that is evident in the temporal histories of vertical position and velocities of the leading and trailing particles depicted in Figures 5.32(a) and 5.32(b).

We must remark that sedimentation in stratified media is sparsely investigated and while there have been studies with linearly stratified fluids in the past [122], we are not aware of similar efforts with discretely stratified fluids. This test case was primarily motivated by the need to explore the versatility of the IB–FV solver for multiple solids and multiple fluids with flow induced motion. The present results cannot be therefore compared with other benchmarks and can only be verified by independent numerical investigations or even experiments. However, these results are physically consistent in that they qualitatively reproduce the four stages – drafting, kissing, separation and tumbling, which have been previously reported in [122] for sedimentation in continuously stratified media. The dynamics of flow induced motion of particles and their trajectories pose an interesting and challenging problem to analyse, which is however beyond the scope of the current work.

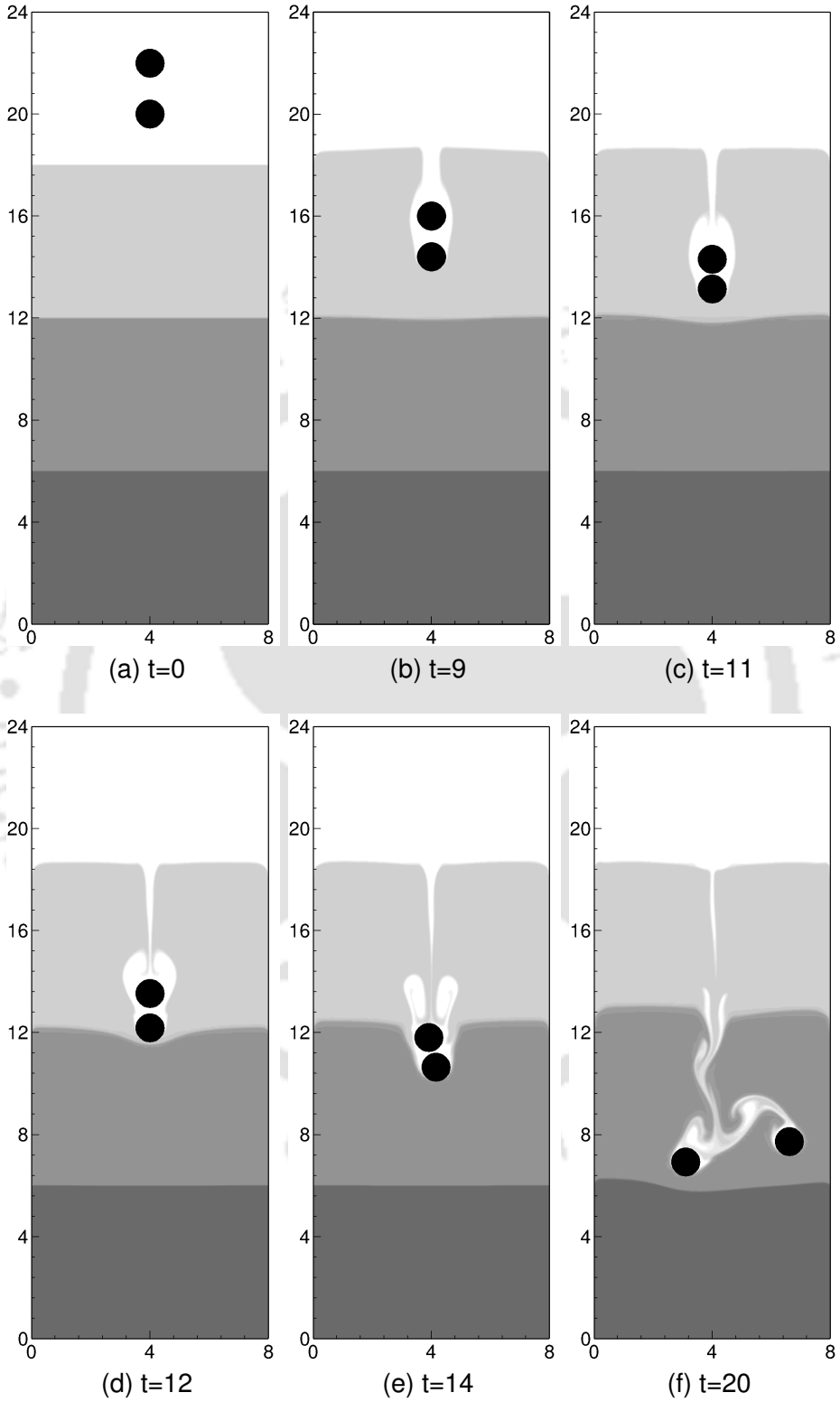

Figure 5.31: Sedimentation of two circular particles of density ratio $\frac{\rho_S}{\rho_L}$ = 1.5 in discrete stratified fluid of density ratio $\frac{\rho_H}{\rho_L}$ = 1, 1.05, 1.1, 1.15 (top to bottom) showing (a) initial position (b) drafting (c) kissing (d) separation (e) kissing and (f) tumbling.

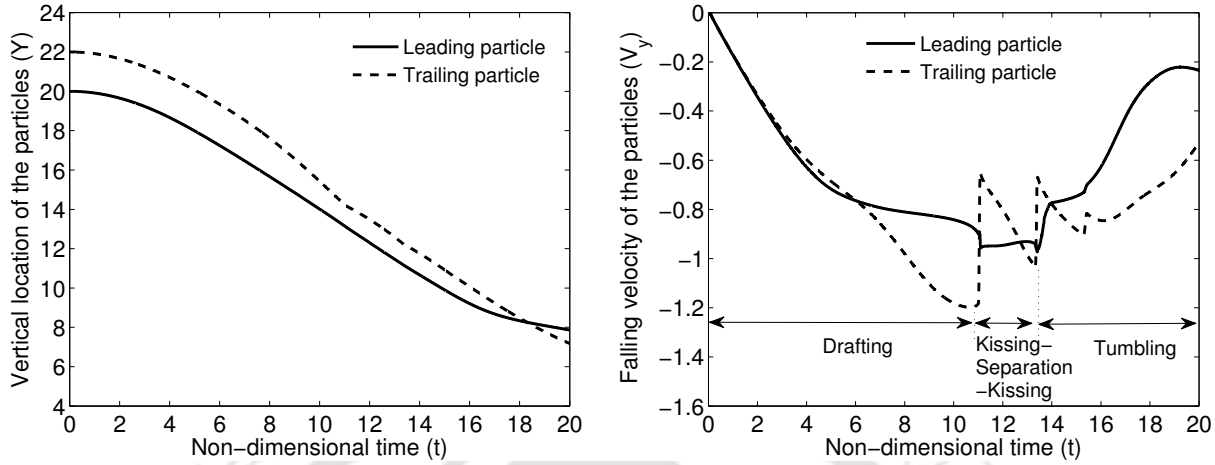

(a) Vertical location (b) Falling velocity

Figure 5.32: Sedimentation of two circular particles of density ratio $\frac{\rho_S}{\rho_L} = 1.5$ in discrete stratified fluid: time histories of (a) the vertical location of the particles center (Y) (b) falling velocity of the particles (V_y).

We can therefore see that our results quantitatively reproduce the DKT phenomena and qualitatively exhibit the DKSKT phenomena in homogeneous and stratified media respectively, which highlight the efficacy of the proposed diffuse interface immersed boundary method.

CHAPTER 6

SIMULATING MISCIBLE FLUID FLOWS

Miscibility refers to the ability of the fluid to completely dissolve into another fluid thus forming a homogeneous solution. In the previous chapters, we have discussed the numerical framework for simulations of immiscible fluid flows, where the fluids are separated by a distinct interface. On the other hand, there exists no sharp interface between miscible fluids and one can extend the immersed boundary–finite volume framework for such scenarios by suitably accounting for the mixing effects. The fluid miscibility leads to a non–zero divergence condition on the velocity field with the solution procedure also solving for mass fractions as opposed to fluid volume fractions. This chapter gives the details of the extension of the flow solver detailed in earlier chapters for miscible fluid flows and the implications of weak compressibility are discussed through several numerical experiments.

6.1 Handling miscible fluid flows

Immiscible fluid flows in the present work are studied using the VOF approach which solves the advection equation for volume fraction(s) Eq. (2.2). Miscible fluid flows do not have a sharp interface and in order to incorporate the mixing effects, we solve a convection–diffusion equation for the mass fraction (ϕ'), which in conservative form

reads,

$$\frac{\partial(\rho\phi')}{\partial t} + \nabla \cdot (\rho\phi'\mathbf{u}) = \frac{1}{ReSc}\nabla \cdot \rho\nabla\phi' \tag{6.1}$$

where $Sc = \dfrac{\mu_L}{\rho_L \mathcal{D}}$ is the Schmidt number and $\mathcal{D}$ is the binary diffusion coefficient. It is important to mention that we have chosen the lighter fluid for non–dimensionalisation (hence the subscript L) and that we only consider mixing due to molecular diffusion $\mathcal{D}$. Evidently, the right hand side of the Eq. (6.1), which is a non–zero quantity as opposed to the immiscible case, is responsible for mixing and the other sources like mixing due to chemical reaction or turbulence are ignored. Using the conservation of the species $\sum \phi_i' = 1$ i.e. $\phi_L' = \phi'$ and $\phi_H' = 1 - \phi'$, mixture density can be obtained as,

$$\frac{1}{\rho} = \phi' + \frac{(1-\phi')}{\rho_H/\rho_L} \tag{6.2}$$

Following [71], we compute the mixture viscosity as,

$$\mu = e^{(1-\phi')\ln(\frac{\mu_H}{\mu_L})} \tag{6.3}$$

It can be noticed that the viscosity is an exponential function of mass fraction, unlike the linear variation in the case of immiscible fluids. This is because viscosity does not evolve linearly at the interface due to diffusion. Therefore, in majority of the studies, the viscosity–mass fraction relationship is assumed to be exponential [71, 123] while the density–mass fraction relationship may be linear [71] or exponential [124]. Using the relations above and by using the continuity equation, Eq. (6.1) can be reduced to,

$$\frac{\partial\rho}{\partial t} + \mathbf{u}\cdot\nabla\rho = \frac{\rho}{ReSc}\nabla\cdot(\frac{1}{\rho}\nabla\rho) \tag{6.4}$$

The velocity divergence condition can be then derived as (see Section A.2 for details),

$$\nabla\cdot\mathbf{u} = -\frac{1}{ReSc}\nabla\cdot(\frac{1}{\rho}\nabla\rho) \tag{6.5}$$

We see from this equation that the velocity field is not divergence–free although the fluids are incompressible. We refer to such flows wherein weak compressibility effects exist but Mach numbers are very small as being quasi–incompressible [125]. The non–

zero divergence of the velocity field therefore modifies the pressure correction equation (Eq. (3.21)) in the fractional step algorithm,

$$\nabla \cdot \frac{\Delta t}{\rho^{n+1}} \nabla \mathcal{P} = \nabla \cdot \mathbf{u}^{\star} + \frac{1}{ReSc} \nabla \cdot (\frac{1}{\rho} \nabla \rho) \tag{6.6}$$

The quasi–incompressibility of the flow and the use of mass fractions instead of volume fractions, which lead to a convective–diffusive transport equation are the only amendments that are necessary to extend the numerical framework for immiscible flows in the miscible regime. It must be remarked that several researchers have chosen to model miscible flows as being fully incompressible despite Eq. (6.5) evidently indicating a non–zero divergence. We shall investigate the numerical implications of ignoring quasi–incompressibility, which is strictly possible only when $Sc \rightarrow \infty$, later in this chapter. It must be reiterated that our exploratory studies on miscible flows are presently limited to binary fluids and that the diffusion is assumed to be Fickian in our studies.

6.2 Discretisation of the convection–diffusion equation

The hybrid staggered/non-staggered framework stores the scalar quantities at cell centers and therefore the convection diffusion equation is discretised and integrated over the individual control cell (C) rather then combine control volume Ω. One can obtain the semi–discrete form of the Eq. (6.1),

$$\Omega_c \frac{d(\rho\phi')}{dt} + \sum_{f \in C} (\rho\phi')_f^{n+1} U_f^n \Delta s_f = \frac{1}{ReSc} \sum_{f \in C} \rho_f^{n+1} \frac{\delta \phi'}{\delta n}\Big|_f^n \Delta s_f \tag{6.7}$$

The temporal and convective term discretisations of this equation are same as that for the advection equation (see Section 2.1) and employ the second–order accurate three point backward differencing scheme and CUI scheme respectively. The diffusion term (on the right side of the equation) appears as a normal gradient for the mass fraction ($\frac{\delta \phi'}{\delta n}|_f$) which can be rewritten following Eq. (4.1). We treat the diffusion terms

implicitly and the fully discrete form of the mass fraction equation becomes,

$$\Omega_c \frac{3(\rho\phi')_c^{n+1} - 4(\rho\phi')_c^{n} + (\rho\phi')_c^{n-1}}{2\Delta t} + \sum_{f\in C}(\rho\phi')_f^{n+1} U_f^n \Delta s_f = \frac{1}{ReSc}\sum_{f\in C}\rho_f^{n+1}\left(\frac{\frac{(\rho\phi')_{c+1}^{n+1}}{\rho_{c+1}^{n+1}} - \frac{(\rho\phi')_c^{n+1}}{\rho_c^{n+1}}}{\Delta r}\right)\Delta s_f \qquad (6.8)$$

One can see from Eq. (6.8) that the diffusion terms are at the $(n+1)^{th}$ level, where subscript $(c+1)$ represents the neighbour cell. The resulting system of linear algebraic equations are solved using the same preconditioned Krylov solver as employed for the volume fraction advection equation with the help of LiS libraries [86].

6.3 Discretisation of the Poisson equation

The effect of quasi–incompressibility which gives a divergence constraint that is non–zero is numerically reflected in the Poisson equation for pressure correction as can be seen in Eq. (6.6). Unlike the fully incompressible immiscible fluid flows, the discrete pressure correction equation is modified by an additional term for miscible flows. The modified Poisson equation reads,

$$\frac{2}{3}\frac{\Delta t}{}\sum_{f\in C}\frac{1}{\rho_f^{n+1}}\frac{\delta\mathcal{P}}{\delta n}\Big|_f \Delta s_f = \sum_{f\in C} U_f^{\star}\,\Delta s_f + \frac{1}{ReSc}\sum_{f\in C}\frac{1}{\rho_f}\frac{\delta\rho}{\delta n}\Big|_f \Delta s_f \qquad (6.9)$$

The only difference one can observe as compared to a fully incompressible approach is the additional term which is a function of the normal density gradient $(\frac{\delta\rho}{\delta n}|_f)$. This term can be discretised similar to any of the diffusion terms following Eq. (4.1) and appears only a source term for the Poisson equation. The linear system resulting from the Poisson equation is solved in the usual fashion using SAAMG–preconditioned GMRES solver employing the LiS libraries [86].

6.4 Extending DIIBM to miscible flows

A major contribution of the present thesis is the diffuse interface immerse boundary framework for immiscible multiphase flows. This numerical methodology can be extended to handle solid objects in miscible flows and the salient details of the formulation are briefly summarised in Section A.3. As discussed earlier, the volume fraction transport is replaced by mass fraction transport and a variable coefficient Poisson equation with an additional source term need to be incorporated to account for miscibility. We also remark that although a consistent treatment of discrete transport of mass fraction and momentum equations is adopted, akin to immiscible flows, it is not mandatory in the miscible flow problems studied herein since the fluid density ratios are quite low and the physical diffusion which causes mixing would likely enhance the robustness of the numerical framework.

6.5 Results and Discussions

We devote this section to discuss the various test cases that we employ to assess the efficacy of the present flow solver to simulate miscible flows. Through the numerical experiments, we also show the implications of using quasi–incompressible and purely incompressible approaches and its effects on overall mixing efficiency. In addition, simulations are presented implementing DIIBM for a number of irregular geometries with complex mixing scenarios. We remark that, unlike the numerical test cases carried out in the previous chapters, the denser fluid may actually be the least viscous in miscible flows. This would only impact the definition of the “virtual" fluid for DIIBM and the definition of non–dimensional numbers are indeed based on the lighter fluid.

6.5.1 Lock exchange

The phenomenon of lock exchange typically occurs when a heavier fluid penetrates into lighter one. Numerous experimental and numerical investigations have been carried out to study this phenomenon and we choose to simulate the lock exchange problem to verify the accuracy of the quasi–incompressible formulation for practical applications.

Fluids are kept side by side in a 9×1 rectangular domain of grid resolution $\Delta x = \Delta y =$ 0.02, the left half portion is filled with the lighter fluid and the remaining half with the heavier fluid. No-slip boundary condition is provided to the all walls. Following the experiments conducted by [126], we have simulated two cases: the first is for the fresh water–sodium chloride system where the density difference is very small $\frac{\rho_H}{\rho_L}$ = 1.007 and the second for the relatively high density ratio $\frac{\rho_H}{\rho_L}$ = 1.46 case of fresh water–sodium iodide combination. The Reynolds number Re = 200942 and Froude number Fr = 1 for these studies are based on the fresh water properties.

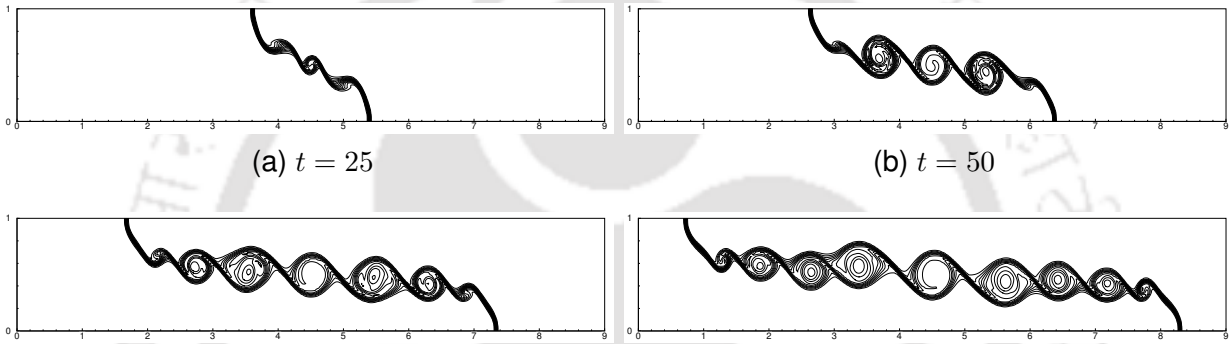

(a) $t = 25$ (b) $t = 50$

(c) $t = 75$ (d) $t = 100$

Figure 6.1: The time evolution of the density contours for $\frac{\rho_H}{\rho_L}$ = 1.007 fresh water sodium chloride system at t = (a) 25 (b) 50 (c) 75 and (d) 100, using quasi–incompressible formulation.

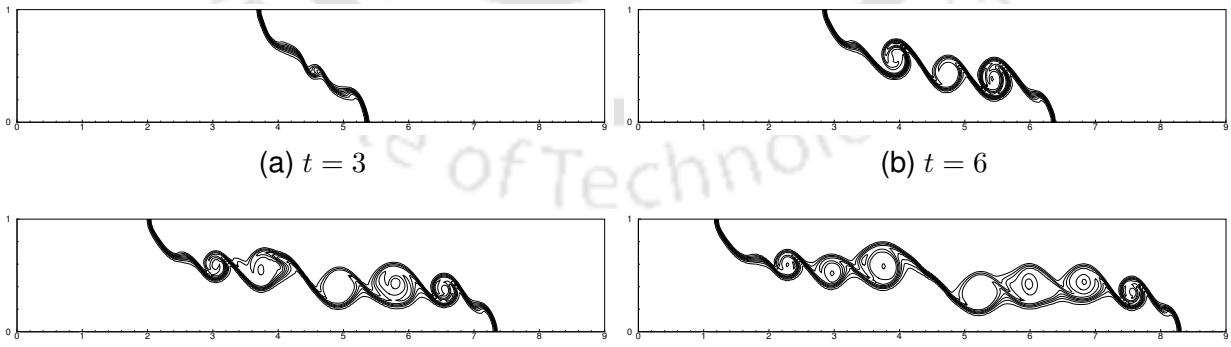

(a) $t = 3$ (b) $t = 6$

(c) $t = 9$ (d) $t = 12$

Figure 6.2: The time evolution of the density contours for $\frac{\rho_H}{\rho_L}$ = 1.46 fresh water sodium iodide system at t = (a) 3 (b) 6 (c) 9 and (d) 12, using quasi–incompressible formulation.

The contour plots of density for $\frac{\rho_H}{\rho_L}$ = 1.007 are shown in Figures 6.1(a) to 6.1(d). After the initial displacement, at t = 5 small roll–like structures are seen to originate near

the interface owing to the velocity shear across it. In the course of time, the strength and the number of the vortex increases and they eventually evolve into the Kelvin–Helmholtz instability which remains symmetric throughout the simulation. These observation are in agreement with the theoretical prediction for energy conserving waves and experimental findings of Lowe et al. [126]. On the other hand, the density contours for $\frac{\rho_H}{\rho_L}$ = 1.46 shown in Figures 6.2(a) to 6.2(d) exhibit an asymmetric behaviour in the later stages (t > 9). This is because the high density currents move faster than light currents and the asymmetric pattern is a consequence of the need to conserve the energy.

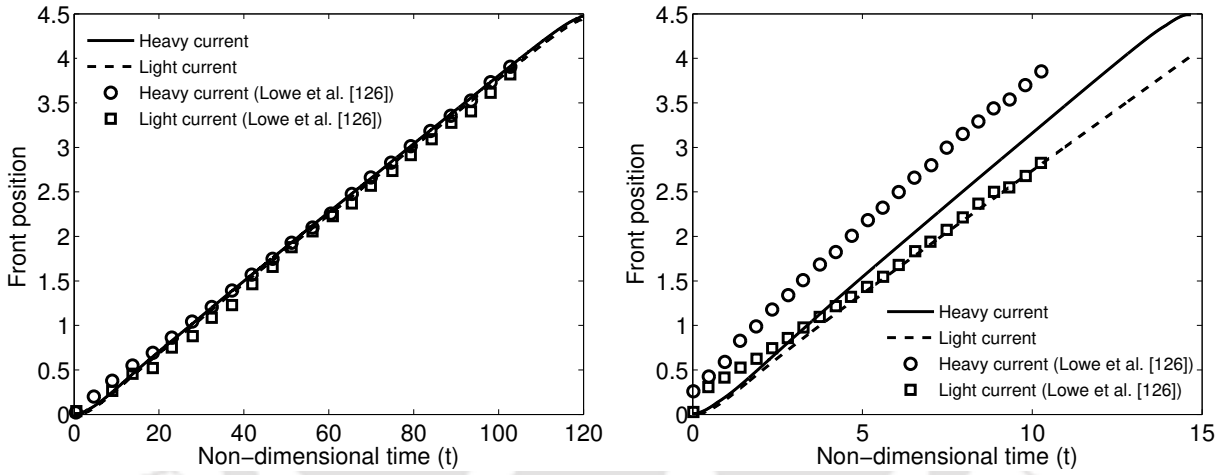

(a) $\frac{\rho_H}{\rho_L}$ =1.007 (b) $\frac{\rho_H}{\rho_L}$ =1.46

Figure 6.3: The history of the front position for (a) $\frac{\rho_H}{\rho_L}$ =1.007 and (b) $\frac{\rho_H}{\rho_L}$ =1.46.

The front position with time for both cases are plotted in Figures 6.3(a) and 6.3(b) and compared with the experimental measurements of Lowe et al. [126]. For $\frac{\rho_H}{\rho_L}$ = 1.007, displacement of the light and heavy currents are almost equal which reveals that the fronts move with the same velocity and thus remain symmetric. The mismatch of the heavy front position with [126], in case of $\frac{\rho_H}{\rho_L}$ = 1.46, can be attributed to deviations with experimental conditions. In the experiment, a gate that separates the fluids is removed slowly and heavy current starts moving before the gate is opened completely, unlike in simulations where the gate is completely removed at t = 0. The overall agreement for both cases are quite good which validates the present numerical approach for miscible flow computations.

6.5.2 Viscous fingering

We now analyse the problem of miscible displacement of a fluid by a less viscous fluid. The stability of the miscible fluid displacement in a pipe has been investigated by the several researchers [71, 72] in the past. The Schmidt number and Reynolds number are the critical parameters for the stability of such flows. In this test case we attempt to explore the ability of the numerical framework to predict the instabilities. The computational domain is a channel of cross section 40$\times$1 with a grid resolution $\Delta x = \Delta y =$ 0.02. We provide a parabolic velocity profile at the inlet and the Dirichlet boundary conditions are enforced at the outlet. All other boundaries are no-slip walls. Initially the whole domain is filled with a highly viscous fluid which is to be displaced by the less viscous fluid entering from the inlet. We use the viscosity ratio $\frac{\mu_H}{\mu_L}$ = 25 and both fluids are assumed to have same density for all the simulations.

The stability of this finger depends on the choice of Re and Sc for this problem. In this context, we have carried out the numerical experiments for three different Schmidt numbers (Sc = 1, 10, 100) while keeping the Reynolds number constant at Re = 500. The contour plots of viscosity are shown in Figures 6.4(a) to 6.4(c) at different time instants for the three cases. As the less viscous fluid enters the domain, it forms a finger–like shape with the maximum velocity at the centerline. For the case of low Schmidt number Sc = 1, mixing between the fluids is quite high due to greater diffusion and a stable but diffused interface is obtained, with the finger propagating in the channel with time. However, for the higher Schmidt numbers Sc = 10, 100, the diffusion is comparatively lower and instability develops as time proceeds at the front of the finger. The instability is more pronounced for the case of Schmidt number Sc = 100. These observations demonstrate that higher Schmidt numbers have an adverse effect on the flow stability. We have also perform a simulation for Re = 100 and Sc = 100 and the results for the time evolution of the finger are presented in Figure 6.5. Contrary to the previous case (Figure 6.4(c)), the interface remains stable throughout the course of simulation. The lower values of Re therefore introduce a stabilising effect and these numerical observation are consistent with the LBM simulations of Sahu et al. [71].

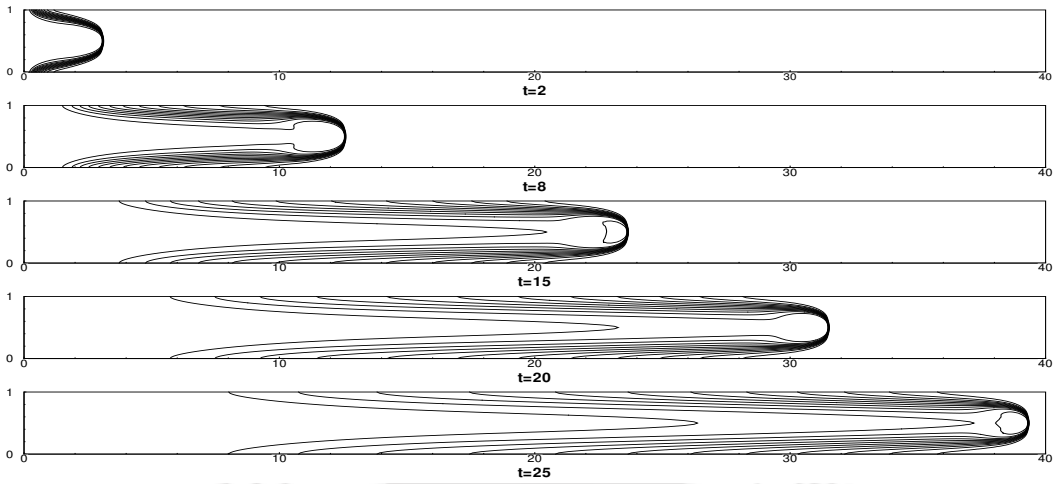

(a) Sc=1

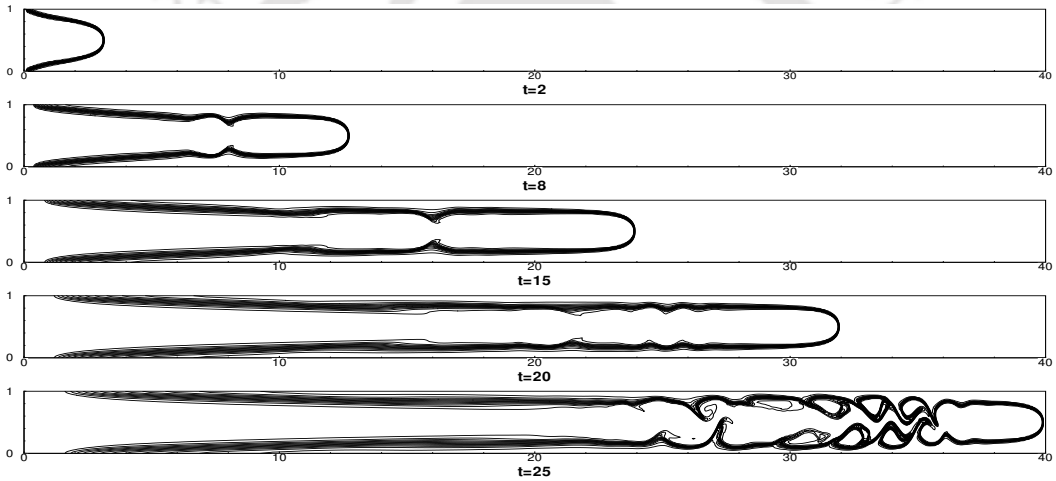

(b) Sc=10

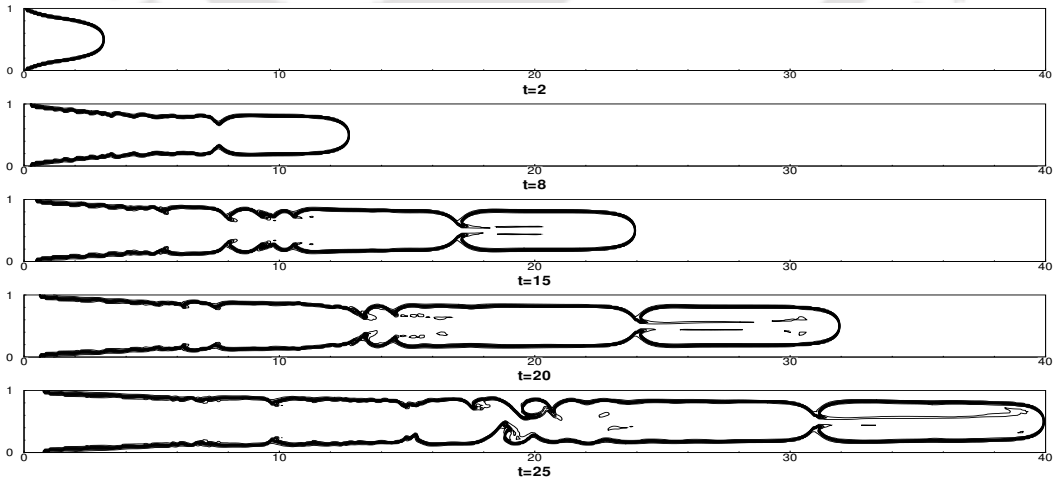

(c) Sc=100

Figure 6.4: Fingering instability of the viscosity contours for Sc = (a) 1 (b) 10 and (c) 100, using $Re = 500$, $\frac{\mu_H}{\mu_L} = 25$ and $\frac{\rho_H}{\rho_L} = 1$, by implementing quasi–incompressible formulation.

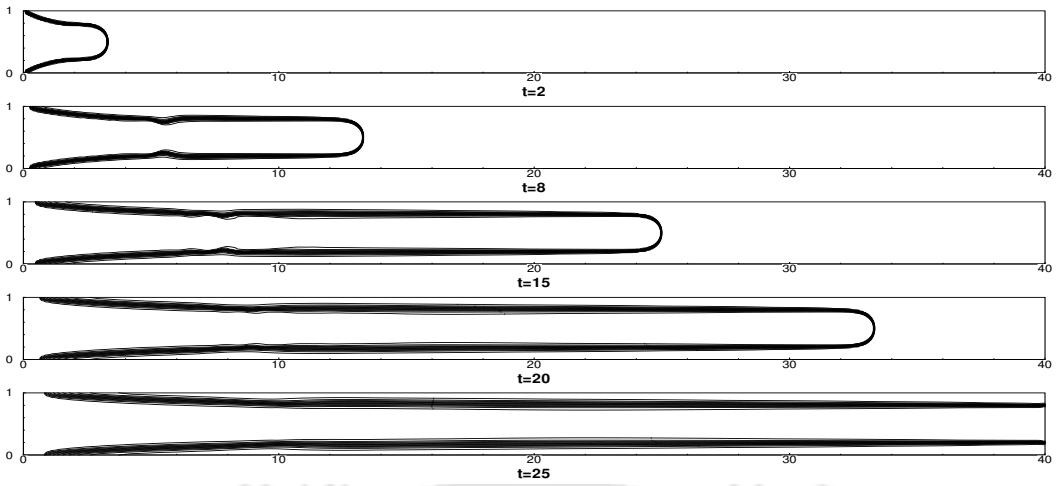

Figure 6.5: Fingering instability of the viscosity contour for $Re = 100$, $Sc = 100$, $\frac{\mu_H}{\mu_L} = 25$ and $\frac{\rho_H}{\rho_L} = 1$, using quasi–incompressible formulation.

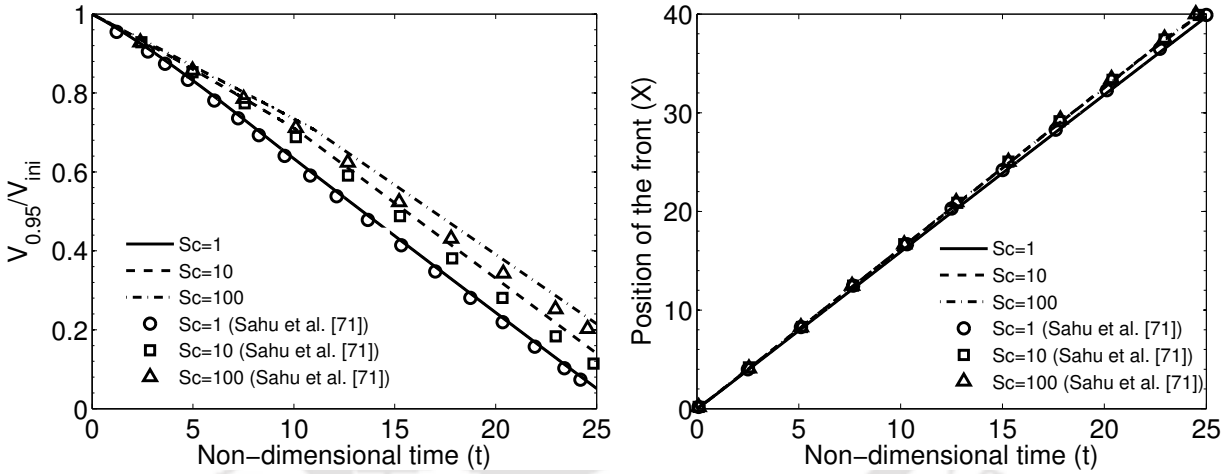

(a) Volume left (b) Finger tip position

Figure 6.6: The time history of (a) volume of high viscous fluid left in the channel and (b) position of the finger tip for $Re = 500$ and $\frac{\mu_H}{\mu_L}$= 25.

To present a quantitative analysis, in Figures 6.6(a) and 6.6(b), we show the position of the finger tip and the ratio of fluid volume left in the channel to the initial volume $\frac{V_{0.95}}{V_{ini}}$, where subscript 0.95 denotes the $\phi' \geq$0.95. The present results are compared with [71] and despite the difference in methodologies, a good agreement is observed between the results. Interestingly, the studies in [71] employ a zero divergence condition as opposed to the quasi–incompressible approach adopted in the present solver. The variation of maximum divergence in the domain with time is shown in Figure 6.7 for $Sc = 1$ and one can notice that the values are sufficiently small for this case. The

same is observed even for the higher Schmidt numbers, thereby justifying the choice of a purely incompressible approach in [71]. This is also supported by the fact that quasi-incompressibility effects vanish when the density ratio is unity, as in this case. While a quasi–incompressible approach is generic, it is not necessary in miscible flow cases where the density ratio is unity and possibly even for non-unit density ratios, if the values of velocity divergence are sufficiently close to zero.

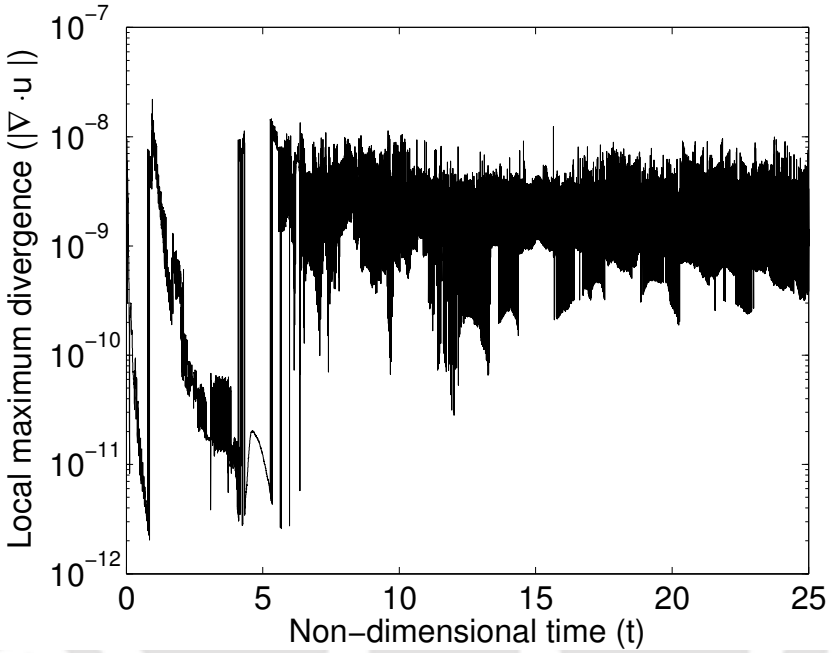

Figure 6.7: Local maximum divergence of in the computational domain for $Re = 500$, $Sc = 1$, $\frac{\mu_H}{\mu_L} = 25$ and $\frac{\rho_H}{\rho_L} = 1$, using quasi–incompressible formulation.

6.5.3 A passive micromixer

We have seen that velocity divergence could remain very small in some quasi–incompressible flows and the result would then be indistinguishable from those computed with a pure incompressible assumption. This may not be the case always, as we shall see for the case of a simple micromixer discussed in this section. In this test case, we simulate the mixing of two fluids in a simple passive micromixer at very low Re. Considering the low Re flows in such cases, one may expect the divergence of velocity to be significant according to the Eq. (6.5), especially for very large diffusion coefficients. The geometry the micromixer is shown in Figure 6.8, which is divided into rectangular elements with

resolution $\Delta x = \Delta y = 0.02$. To simulate the mixing process, we assume that water and ethanol enter from the inlets 1 and 2 respectively with uniform velocity while at the outlet, a zero pressure is prescribed. The rest of the walls are assigned no-slip condition. We use a density ratio $\frac{\rho_H}{\rho_L} = 1.267$ with the viscosity ratio $\frac{\mu_H}{\mu_L} = 0.75$ and Schmidt number $Sc = 1267$, based on the properties of ethanol and water [83].

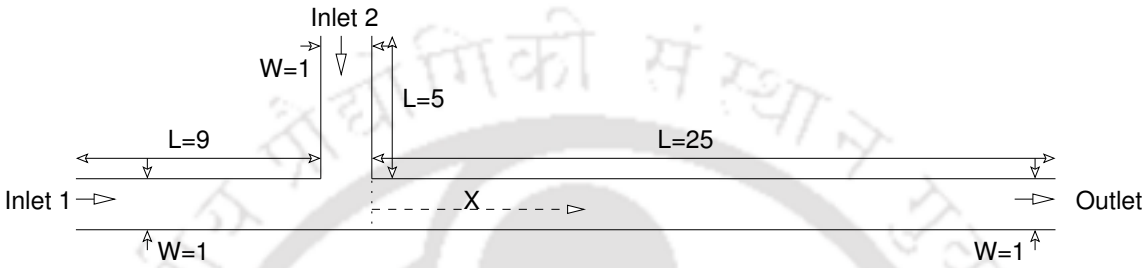

Figure 6.8: Geometry of the micromixer.

(a) $Re = 0.5$

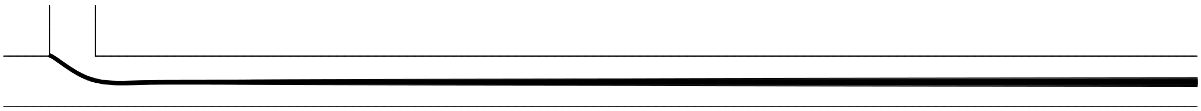

(b) $Re = 5$

Figure 6.9: The line contours of mass fraction for Re = (a) 0.5 and (b) 5, after steady state for ethanol water mixing of $\frac{\rho_H}{\rho_L} = 1.267$, $\frac{\mu_H}{\mu_L} = 0.75$ and $Sc = 1267$ using quasi–incompressible formulation.

We perform the simulations for two different Reynolds numbers, $Re = 0.5$ and 5 with a timestep of Δt = 0.001. The contours of mass fraction at steady state are depicted in Figures 6.9(a) and 6.9(b). The fluids first come in contact at the junction of the two inlets and start mixing. As the fluids move along the channel towards the exit, we observe that the mixing increases. The higher convection rate reduces the time for mixing and therefore it can be observed from the contour plots that there is lesser diffusion for Re = 5.

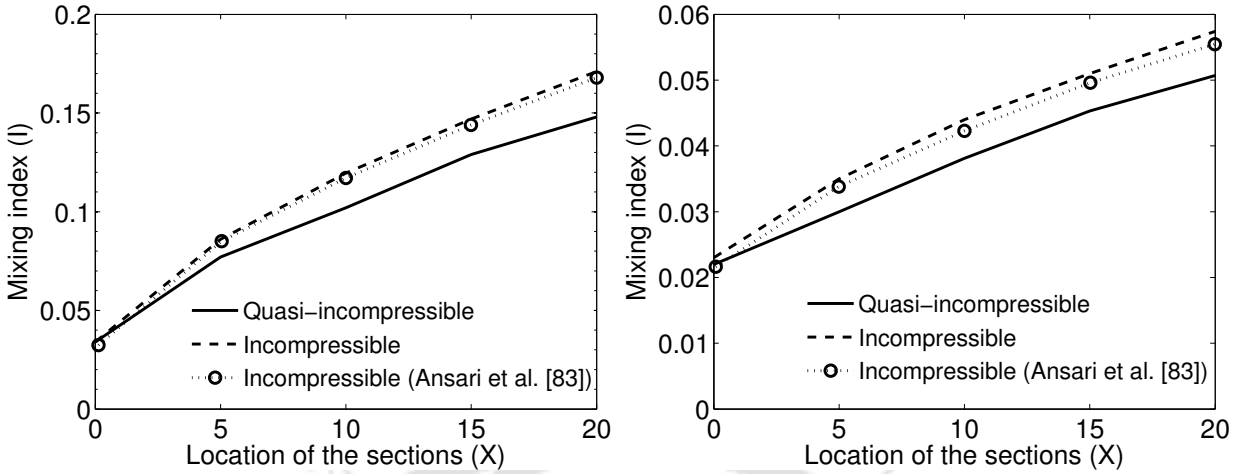

(a) $Re = 0.5$ (b) $Re = 5$

Figure 6.10: The mixing index (I) at different sections for ethanol water mixing of $\frac{\rho_H}{\rho_L} =$ 1.267, $\frac{\mu_H}{\mu_L} = 0.75$ and $Sc = 1267$ for Re = (a) 0.5 and (b) 5.

For a more in–depth analysis of the mixing performance, we calculate the mixing index as defined in [83] at the section X,

$$I = 1 - \sqrt{\frac{\sigma}{\sigma^2_{max}}} \tag{6.10}$$

where $\sigma = \sqrt{\frac{1}{N}\sum(\phi' - 0.5)^2}$ is the variance of the mass fraction in the direction perpendicular to the flow. The mixing index I at the different sections of the micromixer for $Re = 0.5$ and 5 are shown in Figures 6.10(a) and 6.10(b). We calculate the mixing index at five sections (X = 0, 5, 10, 15, 20) in the channel which increases gradually towards the outlet for both cases. However, and not surprisingly, for Re = 5 Figure 6.10(b) shows a lower mixing index at all the sections compared to $Re = 0.5$. A higher value of mixing index indicates better mixing and the passive micromixer has a better performance at the lower Re for the same Schmidt number. Towards a quantitative comparison, the present results are compared with the numerical predictions of Ansari et al. [83]. One can notice that the present results deviate from the numerical results in [83], with the present solver predicting a smaller mixing index at any streamwise location. To understand the differences, we also simulated the problem using a purely incompressible formulation. Our simulations with zero velocity divergence showed excellent agreement with Ansari's predictions, with the latter assuming purely incompressible flow as well.

The velocity divergence for the simulations with quasi–incompressibility are shown in Figure 6.11. A quick look reveals that the velocity divergence are appreciable and are larger for the lower Re case which is in contrast to our earlier findings in the previous subsection. This suggests that quasi–incompressibility could become significant in mixing simulations and ignoring this effect could lead to overpredictions of the mixing performance.

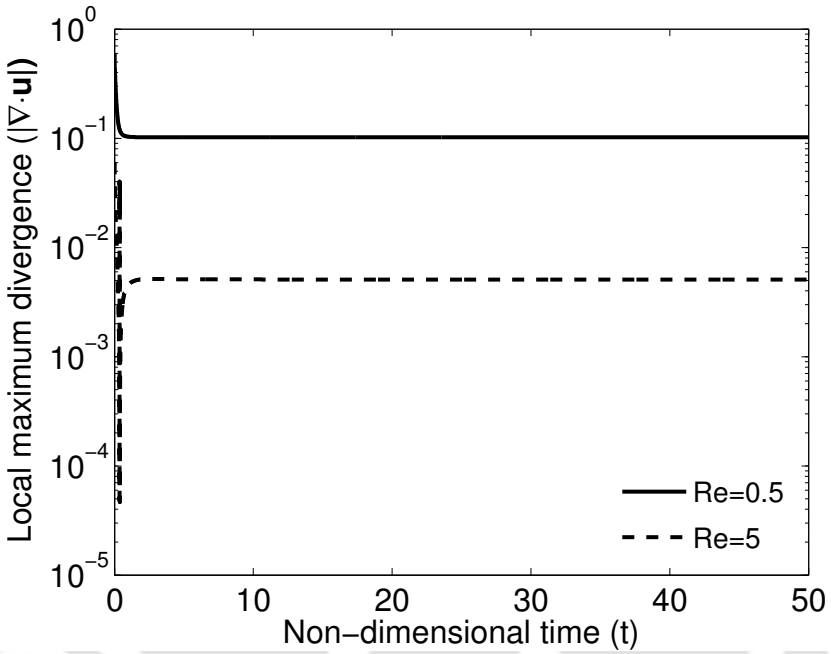

Figure 6.11: Local maximum divergence in the computational domain for $\frac{\rho_H}{\rho_L} = 1.267$, $\frac{\mu_H}{\mu_L} = 0.75$ and $Sc = 1267$ using quasi–incompressible formulation.

6.5.4 Fluid mixing in Y-type micromixer

Miscible fluid flows have been extensively studied in microchannels, where mixing of fluids is the primary objective. Fluid mixing in a microchannels is of interest in various microfluidic applications such as drug delivery systems and micro reactors. In such devices, mixing solely depends on the diffusion to a large extent. Longer the time for diffusion, higher is the efficiency of the micromixer. The performance of the micromixer can be enhanced by either using external sources or modifying the geometry of the micromixer. There have been studies in literature that have shown that the presence of one or more strategically placed obstacles can significantly increase the

mixing efficiency. Such passive micromixers usually irregular constrictions which can be analysed only using unstructured hybrid grids if conventional body–fitted solvers are used. However, we show that the cumbersome process of grid generation can be avoided by adopting the DIIBM approach for miscible flows, without compromising on the overall accuracy of the solution. The use of DIIBM to circumvent mesh generation and/or re–generation makes the approach attractive for micromixing applications, and in particular for deciding optimal configurations.

We study the mixing characteristics in a Y–type micromixer with a circular obstacle as shown in Figure 6.12. The fluid properties and simulation parameters are same as in the previous problem as also are the boundary conditions. We keep the same flow rate at both inlets and carry out simulations for Re = 0.157 as in [79].

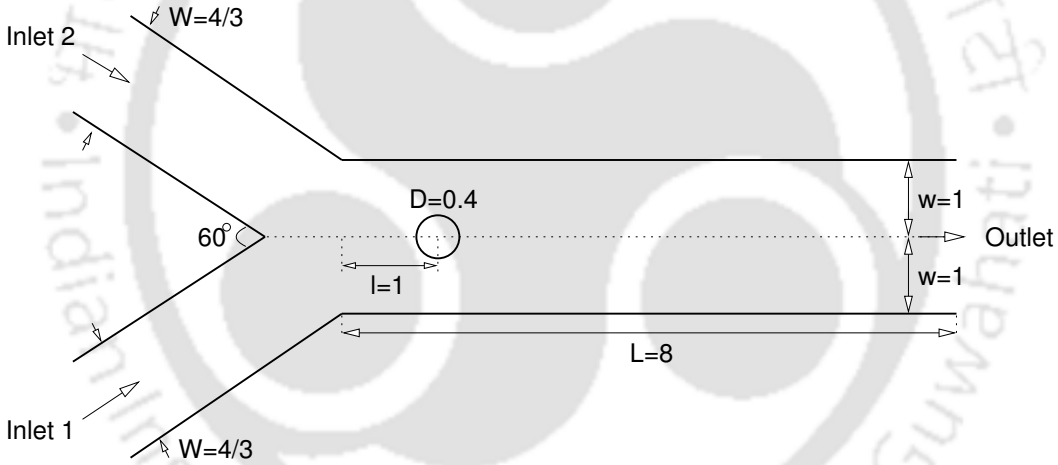

Figure 6.12: Geometry of the Y-type micromixer.

We first solve the problem using a body–fitted triangular mesh of 53786 elements, both employing purely incompressible as well as quasi–incompressible approaches. Mixing is quantified using the mixing efficiency at the outlet which has a width of $2W$ as,

$$\eta_{mix} = \left(1 - \frac{2}{W}\int_0^{2W} (\phi - 0.5)dy\right) \times 100 \tag{6.11}$$

The presence of an obstacle leads to enhanced mixing as can be seen from the data summarised in Table 6.1, although the increase in mixing efficiency is a lowly 2.5%. The quasi–incompressible results are seen to predict a marginally smaller efficiency when compared with the solutions using zero divergence condition, as was

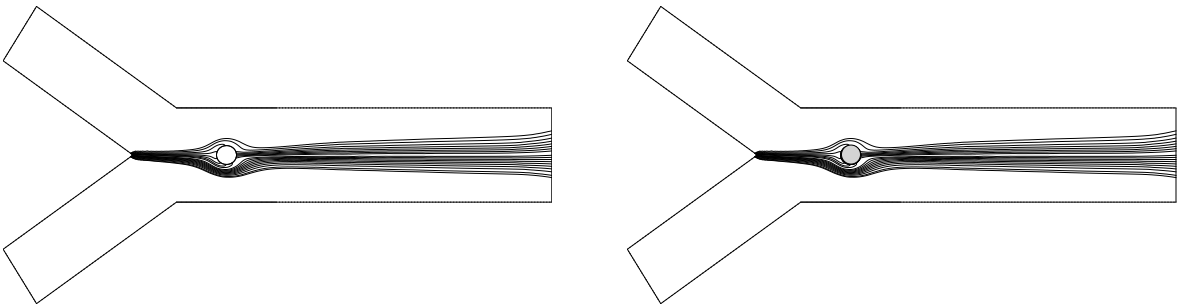

(a) Body–fitted

(b) DIIBM

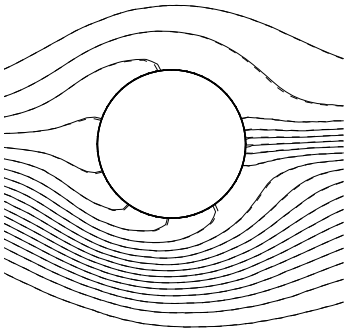

(c) Zoomed view showing mass fraction isocontours near the solid for body-fitted (solid line) and DIIBM (dashed line) cases

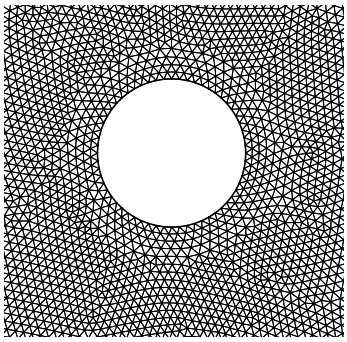

(d) Zoomed view of body fitted mesh near solid

Figure 6.13: The line contours of mass fraction for ethanol water mixing of $\frac{\rho_H}{\rho_L}$ = 1.267, $\frac{\mu_H}{\mu_L}$ = 0.75 and Sc = 1267 using incompressible formulation for (a) body–fitted (b) DIIBM methodologies (c) zoomed view of mass fraction isocontours and (d) zoomed view of mesh.

also found in the earlier study. We now attempt to reproduce these results and conclusions using the DIIBM approach, by immersing the circular obstacle in a triangulated background grid of 58652 elements, which is indeed having the same resolution as the body-fitted mesh employed earlier. This is a bit unusual, in that IB approaches are meant to work with Cartesian and even curvilinear meshes that are easy to generate and not unstructured triangular meshes. The generic nature of our flow solver that works on unstructured data can handle unstructured background grids with ease and we therefore proceed with the DIIBM simulations on the unstructured mesh. However, the solution to the mass fraction equation and more importantly, enforcing the Neumann boundary condition for mass fraction is not trivial in the DIIBM framework and

this has been discussed in some detail in Section A.3. The contours of mass fraction in Figure 6.13(b) from DIIBM are qualitatively identical to those in Figure 6.13(a) obtained with the body–fitted mesh. We also present the zoomed view near the solid body in Figure 6.13(c) which shows the line contours of mass fractions for both body fitted (solid lines) and DIIBM (dashed lines) cases. For sake of completeness, the zoomed view of the mesh in the vicinity of the cylinder is also shown in Figure 6.13(d). It can be seen from the contour plots that the solutions from both approaches are in good agreement with each other and that the isolines are orthogonal to the solid surface thereby satisfying the Neumann boundary condition. Table 6.1 also shows that the mixing efficiency predictions from DIIBM agree reasonably with those obtained with a conformal approach and also compare favourably with the computations in [79].

Table 6.1: Mixing efficiency of the Y micromixers.

Authors	Mixing efficiency (η_{mix})					
	Without obstacle		Body–fitted		DIIBM	
	Incom.	Quasi-incom.	Incom.	Quasi-incom.	Incom.	Quasi-incom.
Present	17.5	16.85	20.46	19.55	20.86	19.93
Wang et al. [79]	18	–	21	–	–	–

It is worth noting that most investigations in micromixers such as in [79, 83] employ a purely incompressible approach. This is likely because many studies in literature focus on comparing different designs and the relative performances are likely to be unaffected even if an incompressible approach is employed. Moreover, even if absolute mixing performance of micromixers were to be evaluated, the use of an incompressible formulation may be justified since it gives a conservative estimate, with the deviations from the quasi–incompressible approach not very significant as has been demonstrated in this numerical experiment.

6.5.5 Fluid mixing in T-type micromixer

As a final test of the efficacy of the miscible formulation in IB–FV framework and its utility for practical applications, we simulate the mixing of two fluids in the T microchannel.

Three different configurations, involving multiple obstacle arrangements are considered for the study. The first configuration is a plane channel as shown in Figure 6.14(a) while the other two consist respectively of inserts (Figure 6.15(a)) and grooves (Figure 6.16(a)). The channel is taken as the computational domain, which is discretised using a uniform Cartesian mesh of grid resolution $\Delta x = \Delta y = 0.02$. The inserts and grooves are treated as multiple solid bodies which are immersed into the domain and remain stationary.

In all three configurations, the fluids with mass fractions of 0 and 1 respectively enter through the two inlets, before mixing in the horizontal leg of the T–shaped micromixer. A constant velocity of unity is specified at both inlets and a fully–developed boundary condition is enforced at the outlet, with the domain initialised with a uniform mass fraction of unity. No–slip boundary condition are enforced on all boundaries and the two fluids are assumed to have equal densities and viscosities to facilitate comparison with the FEM simulations of Rasouli [82]. The Reynolds and Schmidt number characterising the simulation are chosen as 0.2 and 200 respectively and a constant timestep of Δt = 0.001 is used for the simulations in all three cases. The performance of the micromixer is evaluated by computing the mixing efficiency and analysing the mass fraction contours at steady state using the IB–FV solver. While different measures of mixing are possible, we define the mixing efficiency at the outlet consistent with the studies in [82] using Eq. (6.11).

One can see from Figure 6.14(a) that for the plane channel, which is the baseline case, the fluids meet at the center line and move towards the outlet, with molecular diffusion being the only source of mixing. The mass fraction distribution in the domain is shown in Figure 6.14(b) and Figure 6.17(a) shows the mass fraction profile at different streamline locations from the left wall, along the channel width. At X = 4, the profile is relatively more sharper indicating that the mixing occurs largely at the center of the channel. As we move downstream to the outlet (X= 8, 12) the diffusion increases causing the profiles to smear out considerably. The mass fraction profiles from the present approach are compared with the numerical results of Rasouli et al. [82], which show the

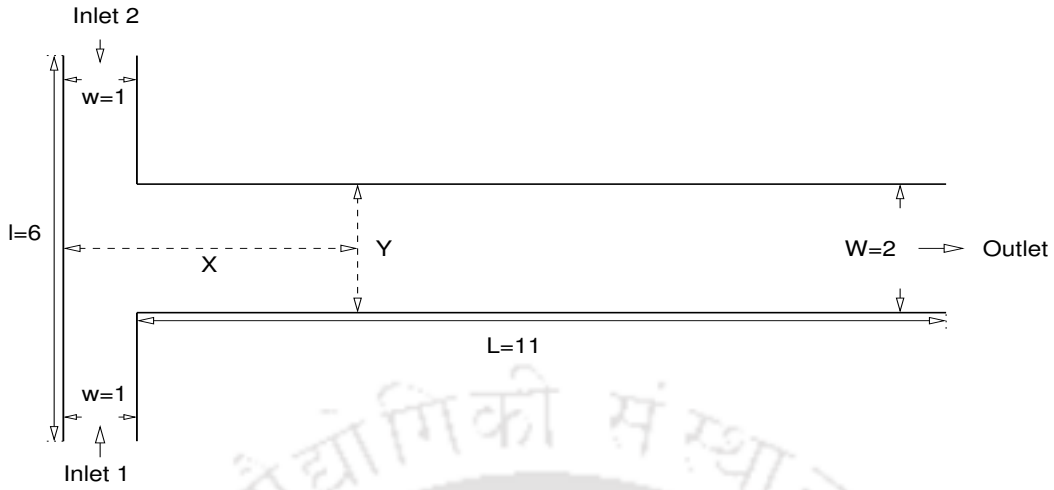

(a) Schematic geometry

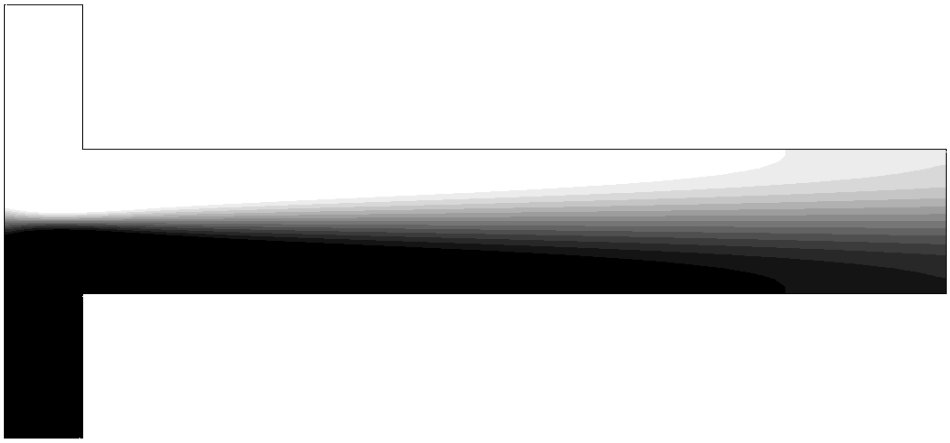

(b) Mass fraction contours

Figure 6.14: T–type micromixer showing (a) geometry and (b) mass fraction contours, for mixing of fluids of $\frac{\rho_H}{\rho_L}$ = 1, $\frac{\mu_H}{\mu_L}$ = 1, Sc = 200 and Re = 0.2 using incompressible formulation.

excellent agreement. It must be realised that there are no obstacles in this case and the IB–FV solver merely degenerates into a standard body–fitted FV solver in this case.

The mass fraction distribution when inserts are introduced is shown in Figure 6.15(b) while Figure 6.16(b) depicts the distribution of mass fraction when grooves are placed in the channel. Unlike the baseline case, one can easily observe an enhanced mixing with the modifications and these are reflected in the mass fraction profiles shown in Figures 6.17(b) and 6.17(c) as well. The mass fraction profiles appear to be more flattened, both in the case of inserts and grooves, as compared to the baseline case.

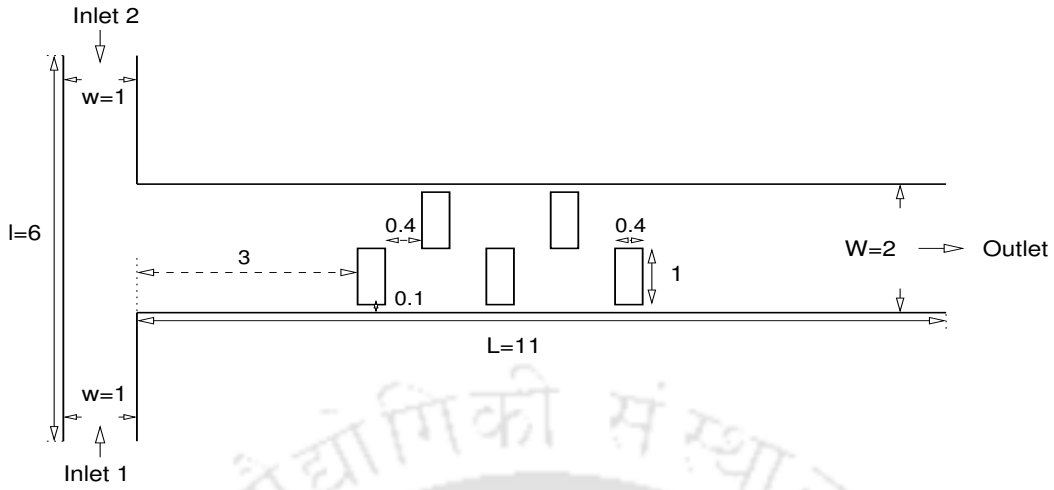

(a) Schematic geometry

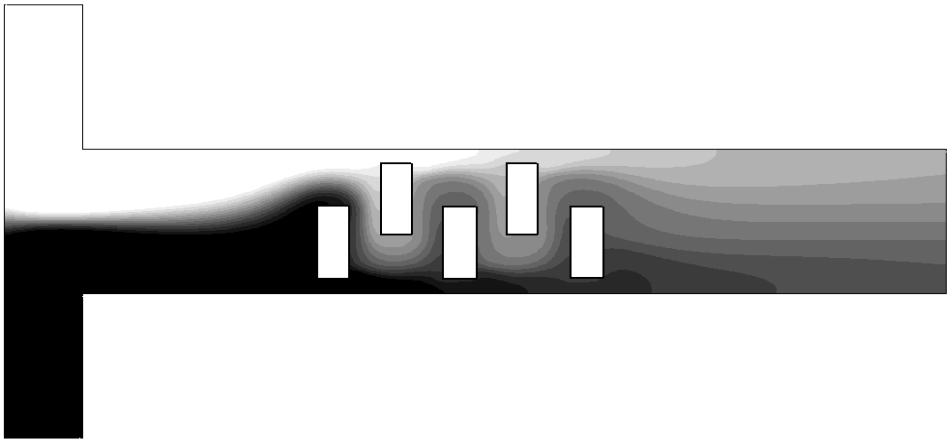

(b) Mass fraction contours

Figure 6.15: T–type micromixer with inserts showing (a) geometry and (b) mass fraction contours, for mixing of fluids of $\frac{\rho_H}{\rho_L}$ = 1, $\frac{\mu_H}{\mu_L}$ = 1, Sc = 200 and Re = 0.2 using incompressible formulation.

Moreover, the outlet mass fraction profiles appear to be more closer to the value of 0.5 (which denotes ideal and complete mixing) at the outlet for the T–channel with grooves which are interestingly asymmetric as well (see Figure 6.16(a)). The mass fraction profiles for the case of micromixer with inserts and grooves using the IB–FV approach show good agreement with those obtained using COMSOL in [82] and the mixing efficiencies for the three configurations, tabulated in Table 6.2, compare favourably with the predictions in [82] and are consistent with the computed mass fraction profiles. The improved mixing when obstacles such as inserts and grooves are introduced may be attributed to the significant transverse velocities in addition to physical diffusion (akin

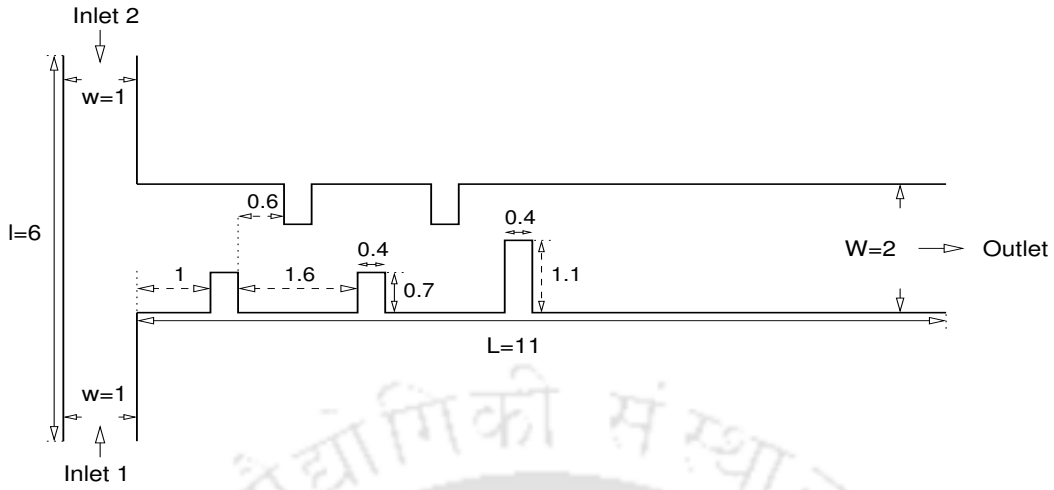

(a) Schematic geometry

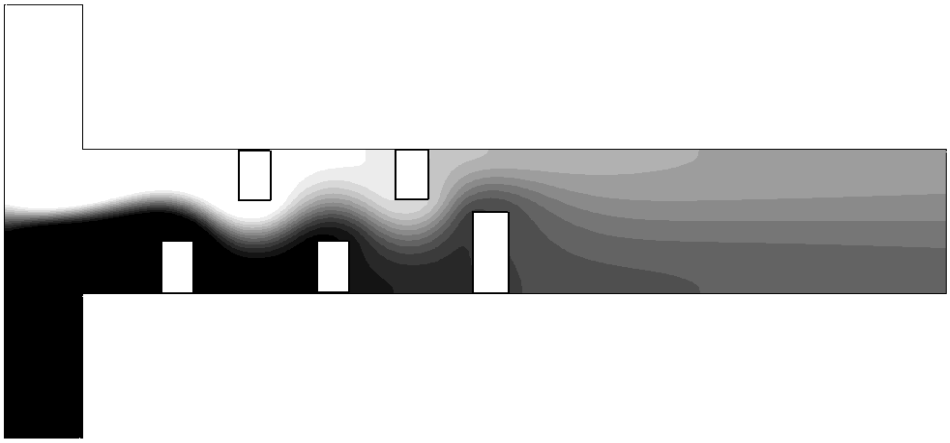

(b) Mass fraction contours

Figure 6.16: T–type micromixer with grooves showing (a) geometry and (b) mass fraction contours, for mixing of fluids of $\frac{\rho_H}{\rho_L}$ = 1, $\frac{\mu_H}{\mu_L}$ = 1, Sc = 200 and Re = 0.2 using incompressible formulation.

to the case of boundary layer growth) but these have not been dealt with in greater detail in this study. The highest mixing efficiency is observed for the configuration with grooves and its marginal increase over the configuration with inserts (by $\approx$ 4%) is likely due to the geometric asymmetry in the configuration. While the mechanisms enhancing the mixing for the micromixer configurations are interesting and need further investigations these are beyond the scope of the present work. Nevertheless, the study on fluid mixing in microchannels is an exposition of the ability of the approach to handle two–fluid miscible flows with multiple solid bodies with relative ease and high accuracy when compared with conformal mesh strategies. This numerical experiment

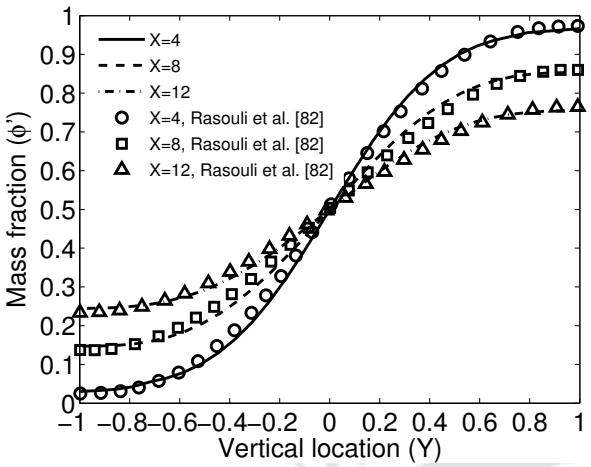

(a) Plane channel

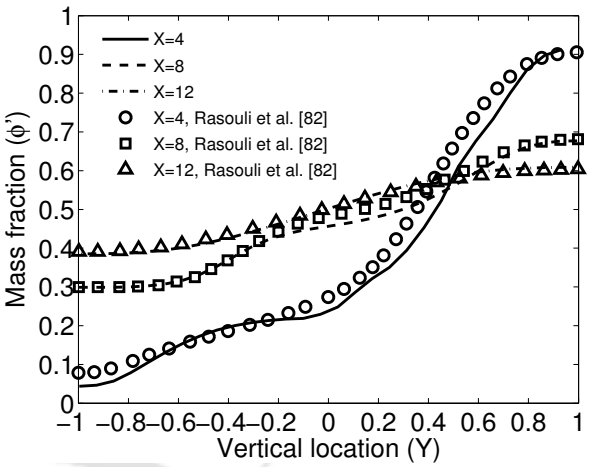

(b) Micromixer with inserts

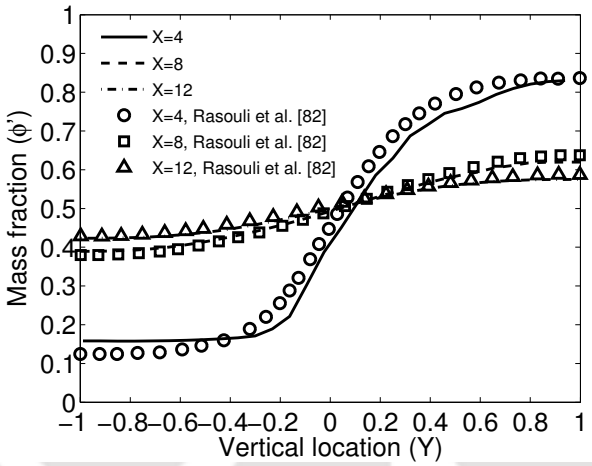

(c) Micromixer with grooves

Figure 6.17: Mass fraction profiles for (a) plane channel (b) with inserts and (c) with grooves, of different cross-sections at a distance X from the left wall, along the channel width Y.

provides ample evidence for researchers to adopt the proposed diffuse interface IB–FV solver for analysing micromixers with various modifications in a cost–effective manner without compromising on accuracy.

Table 6.2: Mixing efficiency of different T-type micromixers.

Authors	Mixing efficiency (η_{mix})		
	Plane channel	With–inserts	With–grooves
Present	63.40	85.12	88.86
Rasouli et al. [82]	61.48	84.39	88.41

CHAPTER 7

CONCLUSIONS AND FUTURE WORK

This chapter summarises the synthesis of key strategies implemented in the development of a multiphase/multi–fluid solver proposed in this thesis. We highlight the major contributions of the study, stress on the limitations and also provide the directions for future work.

7.1 Conclusions

Multiphase/multi–fluid flows which are immiscible require a sharp representation of the distinct interface(s) which led to the study of various interface capturing schemes available in the literature. Our first objective towards a numerical framework for multiphase flows resulted in a generic and unified framework for analysis and construction of interface capturing schemes. We used a volume–of–fluid approach with a single–fluid formalism for our studies and our earliest investigations centered on the convective schemes and their accuracy. Our observations and efforts towards fulfilling this objective are presented below.

1. Conventional interface capturing schemes are cast in an unified framework, where they may be interpreted as a combination of high resolution and compressive schemes, employing flux limiters. These limiters are generalised piecewise lim-

iters defined by a triad of values viz. κ, α and M, with the different choices resulting in different interface capturing schemes.

2. Principles governing the choice of the limiters were studied and guidelines for construction of interface capturing schemes were devised.

3. Existing schemes such as HRIC and CICSAM were analysed with the unified framework and their drawbacks/de–merits have been highlighted.

4. Two novel schemes called the M-Gamma and CUIBS, which are free of interface reconstruction, are proposed on the basis of the framework. These schemes are shown to be bounded and stable through studies on typical advection problems. These studies also demonstrated that the proposed schemes can preserve the sharpness of the interface both on structured and unstructured grids and their performance shows a weak dependence on the Courant number.

5. The CUIBS scheme is shown to outperform existing schemes and has the best performance among all schemes tested for typical advection tests in this thesis. We found that the method does not result in interface distortion which makes it a promising choice for interface capture in density and viscosity stratified multiphase flows.

The advection equation, which was the subject of study for the interface capturing schemes, was then coupled with the Navier–Stokes equations and numerical investigations of sloshing and Rayleigh–Taylor instability were performed to assess the accuracy of the scheme on different grid topologies. The Navier–Stokes equations are itself solved with a novel hybrid staggered/non–staggered approach whose development has been a collective effort. This approach has been adapted to multiphase flows in this thesis to deal with variable density flows. The key highlight of the approach is the use of overlapping control volumes for the solution of a normal momentum equation on cell faces while a variable coefficient Poisson equation enforces the continuity constraint. A segregated methodology using the incremental fractional step method is adopted as the solution methodology. The resulting finite volume flow solver, which combines the merits of both staggered and collocated meshes, was robust and accurate at low

density ratios but numerical instabilities were observed at high density contrasts.

Our second objective was therefore targeted at improving the robustness of the multiphase solver for interfacial flow computations with high density and viscosity ratios. In this thesis, we have now proposed a novel and generic algorithm to simulate multiphase flows with large density ratios and high shear without confronting issues of numerical instabilities. The key principles of this algorithm related to the understanding and implementation of discrete force balancing and consistency of discrete mass and momentum transport. We tested the algorithm rigorously on several multiphase flows of varying complexity that involve both gravity and surface tension dominated fluid flows. Our findings from the studies may be summarised as follows.

1. The hybrid staggered/non–staggered framework allows for a natural implementation of the balanced force framework. This framework ensures that competing forces in the Navier–Stokes equations are in discrete balance for steady–state cases. A lack of such discrete balance was shown to result in spurious solutions when interfacial and body forces were large.

2. Unlike previous studies, we have shown the similarity of operators during discretisation of force terms is not mandatory for a well–balanced framework. We have shown that body forces can be treated as volumetric terms, as opposed to recasting them as interfacial terms, and one can still achieve a near–perfect balance of forces on both structured and unstructured meshes. It is therefore not essential for both the pressure and body force terms to be expressed as gradients of scalars to effect a discrete balance of forces. This also means that one can employ either piezometric or hydrostatic pressures and still obtain very low spurious currents for gravity-dominated flows.

3. We have developed a consistent mass and momentum transport approach for treatment of multiphase flows with large density ratios. The fundamental idea of this approach is to use the same convective discretisation for transport of volume fractions (in VOF advection equation) and momentum (in the normal momentum equation). We have been able to perform simulations for density ratios as high as

10^9 using the consistent mass/momentum transport and highlight its importance for multiphase flows.

4. We also found that it is important to employ identical high resolution schemes in the consistent mass/momentum transport algorithm and that using dissimilar schemes of commensurate accuracies can lead to anomalous numerical solutions.

5. The studies also showed that an inconsistent formulation could work as well as a consistent formulation for some scenarios which could be characterised by a Reynolds number–like parameter Re^* remaining sufficiently small (typically less than 100).

The results of our numerical investigations demonstrated that the well–balanced algorithm results in acceptably low spurious currents while the consistent transport ensured that the numerical solutions remain physically consistent for large density and viscosity ratio flows, even at large times.

Since problems in multiphase flows, such as those encountered in free–surface flows, involve moving bodies, the multiphase flow solver was coupled with a novel diffuse interface immersed boundary method (DIIBM). The DIIBM in the present work treats solid–fluid interfaces analogous to the treatment of fluid–fluid interfaces in VOF method. The diffuse interface methodology in this thesis is unique in the respect that it assumes a “virtual" fluid to be filled within the solid(s) and a fully Eulerian approach is employed. Consequently, the motion of the solid is effected by solving a solid fraction advection equation and the advecting velocities are either known or obtained from Newton’s second law. The IB–FV solver described in this thesis, which formed the third objective, is shown to be a powerful numerical platform for multibody–multiphase flows using a spectrum of numerical experiments. The salient features of the flow solver and its utility for applications can be enumerated as follows.

1. The IB–FV solver discretely conserves mass, both locally and globally, and momentum even when the solid boundaries are non–aligned with the background grid.

2. The solver is shown to have a nominal second-order spatio-temporal accuracy and results in negligible spurious force oscillations without use of any special techniques.

3. The solver uses a fully Eulerian approach devoid of velocity and pressure interpolations which can be easily implemented into any standard finite volume solver with relative ease, even in three dimensions.

4. The simplicity of the flow solver and in particular the lack of sharp representation of the solid–fluid interface does not adversely affect the accuracy of the numerical solutions.

5. Applications to a wide variety of problems involving single phase and multiphase flows with one or more moving bodies show the versatility of the IB–FV solver. In particular, the flow solver is able to handle complex flow problems such as two–particle sedimentation in stratified environment and falling cylinders at air–water interfaces in a robust fashion while resolving the flow physics with acceptable accuracies. In particular, the IB–FV solver when employed for sedimentation in discretely stratified media uncovers the interesting and complex drafting–kissing–separation–kissing–tumbling phenomena.

As a final objective, the scope of the present multiphase/multi–fluid solver with DI-IBM has been stretched by extending it for problems involving miscible fluid flows. This was realised by replacing the volume fraction advection equation in VOF by its convective–diffusive counterpart that accounts for mixing. Our conclusions from exploratory studies on miscible flows, which consisted of binary fluids with Fickian diffusion are as follows.

1. Miscible flows theoretically lead to a non–zero velocity divergence, although it could be small in practice for some cases. Significant deviations from the zero divergence constraint can however be observed in mixing flows with very high diffusion coefficients.

2. The use of quasi–incompressibility which accounts for non–zero divergence does not have a significant impact on the numerical results in case of micromixer simu-

lations. We found that quasi–incompressibility led to marginally lesser predictions of mixing index/efficiency as compared to purely incompressible formulations, justifying the use of latter approach in research efforts reported in literature.

3. We demonstrated that the IB–FV solver was able to analyse different micromixer configurations circumventing the need for separate meshes without compromising on the solution accuracy. Predictions related to mixing performance from the present flow solver were in excellent agreement for different micromixers with previously published data, making it a promising alternative to more cumbersome conformal–mesh based approaches.

In a nutshell, this thesis attempts to develop a generic multiphase/multi–fluid solver that is capable of handling multiple immiscible fluids or binary miscible fluids interacting with multiple stationary/moving rigid solid(s) which can have a wide range of applications that include energy harvesting and micromixer design. The principal contributions of the work embodied in this thesis include a unified framework to understand and evolve interface capturing schemes, a novel approach for high density ratio two–phase flows with strong interfacial tension and body forces and a diffuse interface methodology for fluid–structure interactions with arbitrarily moving rigid bodies. The author is of the opinion that the proposed numerical framework, which has been implemented within an unstructured data finite volume framework encompasses all necessary requirements for an industry–standard solver for multiphase/multi–fluid flow applications. The spectrum of challenging problems, albeit two–dimensional and in the laminar regime, which can be tackled with the numerical framework is a testimony to the efficacy of the research contributions detailed in this thesis.

7.2 Directions for future research

The numerical framework described in this thesis is robust, generic and versatile but there are a few lacunae which need to be addressed in the future. We highlight some of the possible directions for future research that can further the exciting potential of the numerical framework in this thesis.

1. Adaptive mesh refinement: Despite the use of high resolution interface capturing schemes, the VOF methods inherently introduces a numerical diffusion that smears the interface. The use of a fully Eulerian approach with the IB–FV solver also means that the solid–fluid interface is equally diffused as well. The use of grid adaptation in selected regions, both in the vicinity of the body and those with prominent flow features, can help improve accuracy at lower computational costs in comparison to the use of uniformly very fine meshes. The use of solution adaptive refinement for unsteady flows, while important, is also a largely open problem.

2. Consistent vs Inconsistent transport: We have shown that while the consistent mass/momentum transport works for arbitrarily large density ratios, the inconsistent approach where mass and momentum are convected using dissimilar schemes works equally well for some but not all scenarios. While the present studies have shown that simulations of high density ratio flows can be influenced by several parameters including the (Re, Fr, We) triad, further investigation is warranted to better understand their specific influences. More specifically, a clearer picture of when inconsistent transport would fail needs to be brought out in future studies.

3. Handling Neumann and Robin boundary conditions: The proposed DIIBM inherently imposes the Dirichlet boundary condition on the solid surface and handling Neumann and Robin BCs are not straightforward in the present approach. It is therefore not possible to employ the DIIBM in this work for simulations involving inviscid flows or adiabatic boundary conditions. A deeper understanding of the approach and a way to overcome the limitation of handling only Dirichlet BCs is necessary for widening the scope of this IB method.

4. Flexible bodies: While the IB–FV solver in this work has been applied to a large number of rigid structure–fluid interactions, it would be interesting to extend the approach for flexible bodies such as shape–changing and morphing configurations such as those encountered with futuristic micro air vehicles.

5. Multiple miscible fluids: The present numerical framework may be extended to

interactions with multiple miscible fluids using the concept of effective diffusion coefficient. It would also interesting to analyse flows consisting of multiple miscible and immiscible fluid interactions.

6. Turbulent flows and parallelisation: Two aspects that require immediate attention in the context of problems discussed in this thesis are turbulent multiphase flows and three–dimensional computations. Realistic simulations of large–scale multiphase flows would involve turbulence, which is at best modelled (in view of present computing capabilities) and are inherently three–dimensional. Additionally, for problems which are dominated by surface tension, one must also suitably account for the contact angle boundary conditions at the solid-liquid-gas interfaces. In this direction, which should be in the immediate future, it is recommended that the solver be subject to parallelisation after incorporating a couple of URANS models for turbulent simulations. This would be beneficial in performing the first realistic simulations of complex flows such as wave impact on marine structures and primary jet atomisation using the proposed numerical framework.

APPENDIX A

A.1 Piezometric pressure formulation

We begin by substituting the piezometric pressure, $p = \acute{p} - \rho \mathbf{g} \cdot \mathbf{x}$ in Eq. (3.2) which gives,

$$\frac{\partial(\rho \mathbf{u})}{\partial t} + \nabla \cdot (\rho \mathbf{u}\mathbf{u}) = -\nabla(p + \rho \mathbf{g} \cdot \mathbf{x}) + \nabla \cdot (\ \mu(\nabla \mathbf{u} + \nabla \mathbf{u}^T)) + \rho \mathbf{g} + \mathbf{F_{st}} \tag{A.1}$$

Rearranging the first term in the right hand side of Eq. (A.1) gives,

$$\begin{aligned} \nabla(p + \rho \mathbf{g} \cdot \mathbf{x}) &= \nabla p + \nabla(\rho \mathbf{g} \cdot \mathbf{x}) \\ &= \nabla p + \mathbf{g} \cdot \mathbf{x} \nabla \rho + \rho \nabla(\mathbf{g} \cdot \mathbf{x}) \end{aligned} \tag{A.2}$$

The last term of the right hand side in Eq. (A.2) excluding ρ may be simplified as,

$$\begin{aligned} \nabla(\mathbf{g} \cdot \mathbf{x}) &= \frac{\partial(\mathbf{g} \cdot \mathbf{x})}{\partial x}\mathbf{i} + \frac{\partial(\mathbf{g} \cdot \mathbf{x})}{\partial y}\mathbf{j} \\ &= \frac{\partial(g_x x + g_y y)}{\partial x}\mathbf{i} + \frac{\partial(g_x x + g_y y)}{\partial y}\mathbf{j} \\ &= \frac{\partial(g_x x)}{\partial x}\mathbf{i} + \frac{\partial(g_y y)}{\partial x}\mathbf{i} + \frac{\partial(g_x x)}{\partial y}\mathbf{j} + \frac{\partial(g_y y)}{\partial y}\mathbf{j} \\ &= g_x \mathbf{i} + 0 + 0 + g_y \mathbf{j} \\ &= \mathbf{g} \end{aligned} \tag{A.3}$$

Combining Eqs. (A.2) and (A.3) and substituting into Eq. (A.1) gives,

$$\begin{aligned}\frac{\partial(\rho\mathbf{u})}{\partial t}+\nabla\cdot(\rho\mathbf{uu})&=-(\nabla p+\mathbf{g}\cdot\mathbf{x}\nabla\rho+\rho\mathbf{g})+\nabla\cdot(\ \mu(\nabla\mathbf{u}+\nabla\mathbf{u}^T))+\rho\mathbf{g}+\mathbf{F_{st}}\\ \frac{\partial(\rho\mathbf{u})}{\partial t}+\nabla\cdot(\rho\mathbf{uu})&=-\nabla p-\mathbf{g}\cdot\mathbf{x}\nabla\rho+\nabla\cdot(\ \mu(\nabla\mathbf{u}+\nabla\mathbf{u}^T))+\mathbf{F_{st}}\end{aligned}\tag{A.4}$$

A.2 Quasi-incompressible formulation for miscible flows

We begin with the convection–diffusion equation Eq. (6.1) for mass fraction,

$$\begin{aligned}\frac{\partial(\rho\phi')}{\partial t}+\nabla\cdot(\rho\phi'\mathbf{u})&=\frac{1}{ReSc}\nabla\cdot\rho\nabla\phi'\\ \rho\frac{\partial\phi'}{\partial t}+\underbrace{\phi'\frac{\partial\rho}{\partial t}+\phi'\nabla\cdot(\rho\mathbf{u})}_{\text{using }\frac{\partial\rho}{\partial t}+\nabla\cdot(\rho\mathbf{u})=0}+\rho\mathbf{u}\cdot\nabla\phi'&=\frac{1}{ReSc}\nabla\cdot\rho\nabla\phi'\\ \rho\frac{\partial\phi'}{\partial t}+\rho\mathbf{u}\cdot\nabla\phi'&=\frac{1}{ReSc}\nabla\cdot\rho\nabla\phi'\end{aligned}\tag{A.5}$$

From Eq. (6.2) the mass fraction may be rewritten in terms of density as,

$$\phi'=\frac{(r-\rho)}{\rho(r-1)}\qquad\text{where}\qquad r=\frac{\rho_H}{\rho_L}\tag{A.6}$$

Substituting the above expression into Eq. (A.5) and simplifying gives,

$$\frac{\partial\rho}{\partial t}+\mathbf{u}\cdot\nabla\rho=\frac{\rho}{ReSc}\nabla\cdot(\frac{1}{\rho}\nabla\rho)\tag{A.7}$$

The above equation may be rearranged and further simplified as,

$$\begin{aligned}\frac{\partial\rho}{\partial t}+\mathbf{u}\cdot\nabla\rho+\rho\nabla\cdot\mathbf{u}-\rho\nabla\cdot\mathbf{u}&=\frac{\rho}{ReSc}\nabla\cdot(\frac{1}{\rho}\nabla\rho)\\ \underbrace{\frac{\partial\rho}{\partial t}+\nabla\cdot(\rho\mathbf{u})}_{0}-\rho\nabla\cdot\mathbf{u}&=\frac{\rho}{ReSc}\nabla\cdot(\frac{1}{\rho}\nabla\rho)\\ \nabla\cdot\mathbf{u}&=-\frac{1}{ReSc}\nabla\cdot(\frac{1}{\rho}\nabla\rho)\end{aligned}\tag{A.8}$$

where the last step invokes mass conservation. The resulting velocity divergence is a non–zero quantity which is a function of Reynolds and Schmidt numbers.

A.3 Diffuse interface immersed boundary method for miscible flows

In this Appendix, we briefly discuss the handling of the mass fraction equation and implementation of the associated boundary condition within the proposed DIIBM framework. Recall that in case of immiscible binary flows with moving bodies, a “virtual" fluid was assumed inside the body. It must be however realised that the virtual fluid as well as the binary fluids involved were all immiscible with one another. However, in the present case, the two “real" fluids are assumed miscible with an associated binary diffusion coefficient. However, since the body is assumed to be rigid and impermeable, the “virtual" fluid should be immiscible with the “real" fluids. This can be achieved, in an indirect manner, thereby also effecting the Neumann boundary condition $\frac{\partial \phi'}{\partial n}$ = 0 at the solid surface. One can see that in regions devoid of the solid body, the mass fractions satisfy the dimensionless governing equation Eq. (A.9) which reads,

$$\frac{\partial(\rho\phi')}{\partial t} + \nabla \cdot (\rho\phi'\mathbf{u}) = \frac{1}{ReSc}\nabla \cdot \rho\nabla\phi' \tag{A.9}$$

However, as discussed before, the “virtual" fluid inside the solid should not mix with the “real" fluids. Therefore, the above equation is modified inside the solid, by considering that the body is stationary (as in the case of micromixers) and that the “virtual" fluid has a very small (dimensionless) diffusion coefficient given by $\frac{D_s}{D_f}$ (with the diffusion coefficient between the “real" fluids used as reference for non-dimensionalisation). The equation for conservation of mass fraction that the “virtual" fluid inside the body satisfies is,

$$\frac{\partial(\rho\phi')}{\partial t} = \frac{1}{ReSc}\nabla \cdot \left(\rho\frac{D_s}{D_f}\nabla\phi'\right) \tag{A.10}$$

It may be noted that, analogous to the immiscible case, we assume that the heavier of the two fluids is filled inside the solid. Moreover, we also assume that all the fluids in this case also mix with one another but have different diffusion coefficients. In the DIIBM framework, we solve an unified equation, akin to the normal momentum equation, which is obtained by a convex combination of the governing equations within the

fully fluid and fully solid domains. Thus, by combining Eqs. (A.9) and (A.10) using solid fraction φ we get,

$$(1-\varphi)\left[\frac{\partial(\rho\phi')}{\partial t}+\nabla\cdot(\rho\phi'\mathbf{u})-\frac{1}{ReSc}\nabla\cdot\rho\nabla\phi'\right]+\varphi\left[\frac{\partial(\rho\phi')}{\partial t}-\frac{1}{ReSc}\nabla\cdot\left(\rho\frac{D_s}{D_f}\nabla\phi'\right)\right]=0 \tag{A.11}$$

It is interesting to note that the Dirichlet boundary condition appearing in the unified normal momentum equation (see Eq. (5.4)) is replaced herein by a governing equation within the solid, with an aim to enforce the Neumann boundary condition. This is easily done by choosing a very small diffusion coefficient for the “virtual fluid–real fluid" interaction, so that the Neumann BC is weakly enforced in the DIIBM framework. We have employed $\frac{D_s}{D_f}=10^{-3}$ in the present study and the results shown in Sections 6.5.4 and 6.5.5 show that the Neumann boundary condition is indeed enforced correctly at the solid boundary. The rationale behind the choice of a small diffusion coefficient may be recognised easily by drawing an analogy with conjugate heat transfer - if the scalars were temperature instead of mass fraction and the mass diffusion coefficients were replaced by thermal diffusion coefficients, then a very low value of the ratio of solid-to-fluid diffusion would mean that there is no heat diffusion into the solid mimicking the adiabatic boundary condition. The unified equation Eq. (A.11) is a convection–diffusion equation which is discretised in a manner similar to other scalars. The resulting system of linear algebraic equations are solved using a preconditioned Krylov solver similar to the volume fraction equations, as discussed in Chapter 4.

REFERENCES

[1] A. Prosperetti, G. Tryggvason, Computational methods for multiphase flow, Cambridge university press, 2009.

[2] B. Ramaswamy, M. Kawahara, Lagrangian finite element analysis applied to viscous free surface fluid flow, International Journal for Numerical Methods in Fluids 7 (9) (1987) 953–984.

[3] S. O. Unverdi, G. Tryggvason, A front-tracking method for viscous, incompressible, multi-fluid flows, Journal of Computational Physics 100 (1) (1992) 25–37.

[4] S. Osher, J. A. Sethian, Fronts propagating with curvature-dependent speed: algorithms based on hamilton-jacobi formulations, Journal of Computational Physics 79 (1) (1988) 12–49.

[5] C. W. Hirt, B. D. Nichols, Volume of fluid (vof) method for the dynamics of free boundaries, Journal of Computational Physics 39 (1) (1981) 201–225.

[6] W. F. Noh, P. Woodward, Slic (simple line interface calculation), in: Proceedings of the Fifth International Conference on Numerical Methods in Fluid Dynamics June 28–July 2, 1976 Twente University, Enschede, Springer, 1976, pp. 330–340.

[7] D. L. Youngs, Time-dependent multi-material flow with large fluid distortion, Numerical Methods for Fluid Dynamics 24 (2) (1982) 273–285.

[8] S. Van der Pijl, A. Segal, C. Vuik, P. Wesseling, A mass-conserving level-set method for modelling of multi-phase flows, International Journal for Numerical Methods in Fluids 47 (4) (2005) 339–361.

[9] M. Sussman, E. G. Puckett, A coupled level set and volume-of-fluid method for computing 3d and axisymmetric incompressible two-phase flows, Journal of Computational Physics 162 (2) (2000) 301–337.

[10] T. Wang, H. Li, Y. Feng, D. Shi, A coupled volume-of-fluid and level set (voset) method on dynamically adaptive quadtree grids, International Journal of Heat and Mass Transfer 67 (2013) 70–73.

[11] P. R. Redapangu, S. Vanka, K. C. Sahu, Multiphase lattice boltzmann simulations of buoyancy-induced flow of two immiscible fluids with different viscosities, European Journal of Mechanics-B/Fluids 34 (2012) 105–114.

[12] J. Kim, A diffuse-interface model for axisymmetric immiscible two-phase flow, Applied Mathematics and Computation 160 (2) (2005) 589–606.

[13] J. J. Monaghan, Simulating free surface flows with sph, Journal of Computational Physics 110 (2) (1994) 399–406.

[14] S. Muzaferija, M. Peric, P. Sames, T. Schellin, A two-fluid navier-stokes solver to simulate water entry, in: Proceedings of the 22nd symposium on naval hydrodynamics, Washington, DC, 1998, pp. 277–289.

[15] O. Ubbink, R. Issa, A method for capturing sharp fluid interfaces on arbitrary meshes, Journal of Computational Physics 153 (1) (1999) 26–50.

[16] M. Darwish, F. Moukalled, Convective schemes for capturing interfaces of free-surface flows on unstructured grids, Numerical Heat Transfer, part B: Fundamentals 49 (1) (2006) 19–42.

[17] F. Moukalled, M. Darwish, Transient schemes for capturing interfaces of free-surface flows, Numerical Heat Transfer, Part B: Fundamentals 61 (3) (2012) 171–203.

[18] V. R. Gopala, B. G. van Wachem, Volume of fluid methods for immiscible-fluid and free-surface flows, Chemical Engineering Journal 141 (1) (2008) 204–221.

[19] H. Jasak, H. Weller, Interface tracking capabilities of the inter-gamma differencing scheme, 1995.

[20] D. K. Walters, N. M. Wolgemuth, A new interface-capturing discretization scheme for numerical solution of the volume fraction equation in two-phase flows, International Journal for Numerical Methods in Fluids 60 (8) (2009) 893–918.

[21] F. Xiao, Y. Honma, T. Kono, A simple algebraic interface capturing scheme using hyperbolic tangent function, International Journal for Numerical Methods in Fluids 48 (9) (2005) 1023–1040.

[22] Y.-Y. Tsui, S.-W. Lin, T.-T. Cheng, T.-C. Wu, Flux-blending schemes for interface capture in two-fluid flows, International Journal of Heat and Mass Transfer 52 (23) (2009) 5547–5556.

[23] J. Heyns, A. Malan, T. Harms, O. Oxtoby, Development of a compressive surface capturing formulation for modelling free-surface flow by using the volume-of-fluid approach, International Journal for Numerical Methods in Fluids 71 (6) (2013) 788–804.

[24] B. Lafaurie, C. Nardone, R. Scardovelli, S. Zaleski, G. Zanetti, Modelling merging and fragmentation in multiphase flows with surfer, Journal of Computational Physics 113 (1) (1994) 134–147.

[25] D. Gerlach, G. Tomar, G. Biswas, F. Durst, Comparison of volume-of-fluid methods for surface tension-dominant two-phase flows, International Journal of Heat and Mass Transfer 49 (3) (2006) 740–754.

[26] S. J. Cummins, M. M. Francois, D. B. Kothe, Estimating curvature from volume fractions, Computers & structures 83 (6) (2005) 425–434.

[27] S. Popinet, S. Zaleski, A front-tracking algorithm for accurate representation of surface tension, International Journal for Numerical Methods in Fluids 30 (6) (1999) 775–793.

[28] T. Abadie, J. Aubin, D. Legendre, On the combined effects of surface tension force calculation and interface advection on spurious currents within volume of fluid and level set frameworks, Journal of Computational Physics 297 (2015) 611–636.

[29] S. Popinet, An accurate adaptive solver for surface-tension-driven interfacial flows, Journal of Computational Physics 228 (16) (2009) 5838–5866.

[30] Z. Pan, J. A. Weibel, S. V. Garimella, Spurious current suppression in vof-csf simulation of slug flow through small channels, Numerical Heat Transfer, Part A: Applications 67 (1) (2015) 1–12.

[31] Y. Renardy, M. Renardy, Prost: a parabolic reconstruction of surface tension for the volume-of-fluid method, Journal of Computational Physics 183 (2) (2002) 400–421.

[32] M. M. Francois, S. J. Cummins, E. D. Dendy, D. B. Kothe, J. M. Sicilian, M. W. Williams, A balanced-force algorithm for continuous and sharp interfacial surface tension models within a volume tracking framework, Journal of Computational Physics 213 (1) (2006) 141–173.

[33] H. Montazeri, C. Ward, A balanced-force algorithm for two-phase flows, Journal of Computational Physics 257 (2014) 645–669.

[34] F. Denner, B. G. van Wachem, Fully-coupled balanced-force vof framework for arbitrary meshes with least-squares curvature evaluation from volume fractions, Numerical Heat Transfer, Part B: Fundamentals 65 (3) (2014) 218–255.

[35] S. Ghods, M. Herrmann, A consistent rescaled momentum transport method for simulating large density ratio incompressible multiphase flows using level set methods, Physica Scripta 2013 (T155) (2013) 014050.

[36] H. Montazeri, M. Bussmann, J. Mostaghimi, Accurate implementation of forcing terms for two-phase flows into simple algorithm, International Journal of Multiphase Flow 45 (2012) 40–52.

[37] J. Mencinger, I. Žun, On the finite volume discretization of discontinuous body force field on collocated grid: application to vof method, Journal of Computational Physics 221 (2) (2007) 524–538.

[38] M. Rudman, A volume-tracking method for incompressible multifluid flows with large density variations, International Journal for Numerical Methods in Fluids 28 (2) (1998) 357–378.

[39] O. Desjardins, V. Moureau, Methods for multiphase flows with high density ratio, Center for Turbulent Research, Summer Programm 2010 (2010) 313–322.

[40] M. Bussmann, D. B. Kothe, J. M. Sicilian, Modeling high density ratio incompressible interfacial flows, in: ASME 2002 Joint US-European Fluids Engineering Division Conference, American Society of Mechanical Engineers, 2002, pp. 707–713.

[41] M. Raessi, H. Pitsch, Consistent mass and momentum transport for simulating incompressible interfacial flows with large density ratios using the level set method, Computers & Fluids 63 (2012) 70–81.

[42] H. H. Hu, N. A. Patankar, M. Zhu, Direct numerical simulations of fluid–solid systems using the arbitrary lagrangian–eulerian technique, Journal of Computational Physics 169 (2) (2001) 427–462.

[43] W. D. Henshaw, A fourth-order accurate method for the incompressible navier-stokes equations on overlapping grids, Journal of Computational Physics 113 (1) (1994) 13–25.

[44] C. S. Peskin, Flow patterns around heart valves: a numerical method, Journal of Computational Physics 10 (2) (1972) 252–271.

[45] R. Mittal, G. Iaccarino, Immersed boundary methods, Annual Review of Fluid Mechanics 37 (2005) 239–261.

[46] Y.-H. Tseng, J. H. Ferziger, A ghost-cell immersed boundary method for flow in complex geometry, Journal of Computational Physics 192 (2) (2003) 593–623.

[47] P. Tucker, Z. Pan, A cartesian cut cell method for incompressible viscous flow, Applied Mathematical Modelling 24 (8) (2000) 591–606.

[48] I. Borazjani, L. Ge, F. Sotiropoulos, Curvilinear immersed boundary method for simulating fluid structure interaction with complex 3d rigid bodies, Journal of Computational physics 227 (16) (2008) 7587–7620.

[49] A. Gilmanov, F. Sotiropoulos, A hybrid cartesian/immersed boundary method for simulating flows with 3d, geometrically complex, moving bodies, Journal of Computational Physics 207 (2) (2005) 457–492.

[50] H. Luo, R. Mittal, X. Zheng, S. A. Bielamowicz, R. J. Walsh, J. K. Hahn, An immersed-boundary method for flow–structure interaction in biological systems with application to phonation, Journal of computational physics 227 (22) (2008) 9303–9332.

[51] I. Borazjani, L. Ge, T. Le, F. Sotiropoulos, A parallel overset-curvilinear-immersed boundary framework for simulating complex 3d incompressible flows, Computers & Fluids 77 (2013) 76–96.

[52] C. Escauriaza, F. Sotiropoulos, Lagrangian model of bed-load transport in turbulent junction flows, Journal of Fluid Mechanics 666 (2011) 36–76.

[53] A. Calderer, S. Kang, F. Sotiropoulos, Level set immersed boundary method for coupled simulation of air/water interaction with complex floating structures, Journal of Computational Physics 277 (2014) 201–227.

[54] R. Glowinski, T. Pan, T. Hesla, D. Joseph, J. Periaux, A fictitious domain approach to the direct numerical simulation of incompressible viscous flow past moving rigid bodies: application to particulate flow, Journal of Computational Physics 169 (2) (2001) 363–426.

[55] N. Sharma, N. A. Patankar, A fast computation technique for the direct numerical simulation of rigid particulate flows, Journal of Computational Physics 205 (2) (2005) 439–457.

[56] J. Blasco, M. C. Calzada, M. Marín, A fictitious domain, parallel numerical method for rigid particulate flows, Journal of Computational Physics 228 (20) (2009) 7596–7613.

[57] S. V. Apte, M. Martin, N. A. Patankar, A numerical method for fully resolved simulation (frs) of rigid particle–flow interactions in complex flows, Journal of Computational Physics 228 (8) (2009) 2712–2738.

[58] Q. Liu, O. V. Vasilyev, A brinkman penalization method for compressible flows in complex geometries, Journal of Computational Physics 227 (2) (2007) 946–966.

[59] Y. Bae, Y. J. Moon, Brinkman penalization method for computation of acoustic scattering from complex geometry,", in: 16th AIAA/CEAS Aeroacoustics Conference, 2010, p. 3939.

[60] B. Kadoch, D. Kolomenskiy, P. Angot, K. Schneider, A volume penalization method for incompressible flows and scalar advection–diffusion with moving obstacles, Journal of Computational Physics 231 (12) (2012) 4365–4383.

[61] Y. Nakayama, R. Yamamoto, Simulation method to resolve hydrodynamic interactions in colloidal dispersions, Physical Review E 71 (3) (2005) 036707.

[62] F. Xiao, A computational model for suspended large rigid bodies in 3d unsteady viscous flows, Journal of Computational Physics 155 (2) (1999) 348–379.

[63] D. Pan, An immersed boundary method for incompressible flows using volume of body function, International Journal for Numerical Methods in Fluids 50 (6) (2006) 733–750.

[64] A. De, A diffuse interface immersed boundary method for convective heat and fluid flow, International Journal of Heat and Mass Transfer 92 (2016) 957–969.

[65] H. Luo, H. Dai, P. J. F. de Sousa, B. Yin, On the numerical oscillation of the direct-forcing immersed-boundary method for moving boundaries, Computers & Fluids 56 (2012) 61–76.

[66] J. Yang, E. Balaras, An embedded-boundary formulation for large-eddy simulation of turbulent flows interacting with moving boundaries, Journal of Computational Physics 215 (1) (2006) 12–40.

[67] J. H. Seo, R. Mittal, A sharp-interface immersed boundary method with improved mass conservation and reduced spurious pressure oscillations, Journal of Computational Physics 230 (19) (2011) 7347–7363.

[68] I. Mirzaii, M. Passandideh-Fard, Modeling free surface flows in presence of an arbitrary moving object, International Journal of Multiphase Flow 39 (2012) 216–226.

[69] S. Kocabiyik, C. Bozkaya, Streamwise oscillations of a cylinder beneath a free surface: Free surface effects on fluid forces, Journal of Fluids and Structures 59 (2015) 394–405.

[70] A. Pathak, M. Raessi, A 3d, fully eulerian, vof-based solver to study the interaction between two fluids and moving rigid bodies using the fictitious domain method, Journal of Computational Physics 311 (2016) 87–113.

[71] K. Sahu, H. Ding, P. Valluri, O. Matar, Linear stability analysis and numerical simulation of miscible two-layer channel flow, Physics of Fluids 21 (4) (2009) 042104.

[72] B. T. Ranganathan, R. Govindarajan, Stabilization and destabilization of channel flow by location of viscosity-stratified fluid layer, Physics of Fluids 13 (1) (2001) 1–3.

[73] M. Mishra, A. De Wit, K. C. Sahu, Double diffusive effects on pressure-driven miscible displacement flows in a channel, Journal of Fluid Mechanics 712 (2012) 579–597.

[74] K. Bao, X. Wu, H. Zhang, E. Wu, Volume fraction based miscible and immiscible fluid animation, Computer Animation and Virtual Worlds 21 (3-4) (2010) 401–410.

[75] Y. Z. Liu, B. J. Kim, H. J. Sung, Two-fluid mixing in a microchannel, International Journal of Heat and Fluid Flow 25 (6) (2004) 986–995.

[76] C. Y. Lim, Y. C. Lam, Analysis on micro-mixing enhancement through a constriction under time periodic electroosmotic flow, Microfluidics and Nanofluidics 12 (1-4) (2012) 127–141.

[77] C.-C. Cho, C.-L. Chen, et al., Mixing enhancement in crisscross micromixer using aperiodic electrokinetic perturbing flows, International Journal of Heat and Mass Transfer 55 (11) (2012) 2926–2933.

[78] V. Rudyak, A. Minakov, Modeling and optimization of y-type micromixers, Micromachines 5 (4) (2014) 886–912.

[79] C. Wang, Y.-C. Hu, Mixing of liquids using obstacles in y-type microchannels, Tamkang Journal of Science and Engineering 13 (4) (2010) 385–394.

[80] C.-Y. Huang, S.-A. Wan, Y.-H. Hu, Oxygen and nitrogen gases mixing in t-type micromixers visualized and quantitatively characterized using pressure-sensitive paint, International Journal of Heat and Mass Transfer 111 (2017) 520–531.

[81] K. H. Kang, J. Park, I. S. Kang, K. Y. Huh, Initial growth of electrohydrodynamic instability of two-layered miscible fluids in t-shaped microchannels, International Journal of Heat and Mass Transfer 49 (23) (2006) 4577–4583.

[82] M. Rasouli, A. Abouei Mehrizi, A. Lashkaripour, Numerical study on low reynolds mixing oft-shaped micro-mixers with obstacles, Transport Phenomena in Nano and Micro Scales 3 (2) (2015) 68–76.

[83] M. Ansari, K.-Y. Kim, S. M. Kim, Numerical study of the effect on mixing of the position of fluid stream interfaces in a rectangular microchannel, Microsystem technologies 16 (10) (2010) 1757–1763.

[84] J. K. Patel, G. Natarajan, A generic framework for design of interface capturing schemes for multi-fluid flows, Computers & Fluids 106 (2015) 108–118.

[85] J. Blazek, Computational fluid dynamics: principles and applications, Vol. 1, Elsevier, 2001.

[86] Lis libraries (2013).
URL `http://www.ssisc.org/lis`

[87] P. Roe, Characteristic-based schemes for the euler equations, Annual Review of Fluid Mechanics 18 (1) (1986) 337–365.

[88] P. Gaskell, A. Lau, Curvature-compensated convective transport: Smart, a new boundedness-preserving transport algorithm, International Journal for Numerical Methods in Fluids 8 (6) (1988) 617–641.

[89] N. P. Waterson, H. Deconinck, Design principles for bounded higher-order convection schemes–a unified approach, Journal of Computational Physics 224 (1) (2007) 182–207.

[90] T. Wacławczyk, T. Koronowicz, Remarks on prediction of wave drag using vof method with interface capturing approach, Archives of Civil and Mechanical Engineering 8 (1) (2008) 5–14.

[91] T. Wacławczyk, T. Koronowicz, Comparison of cicsam and hric high-resolution schemes for interface capturing, Journal of Theoretical and Applied Mechanics 46 (2) (2008) 325–345.

[92] H. Jasak, H. Weller, A. Gosman, High resolution nvd differencing scheme for arbitrarily unstructured meshes, International Journal for Numerical Methods in Fluids 31 (2) (1999) 431–449.

[93] J. Brackbill, D. B. Kothe, C. Zemach, A continuum method for modeling surface tension, Journal of Computational Physics 100 (2) (1992) 335–354.

[94] O. Ubbink, Numerical prediction of two fluid systems with sharp interfaces, Ph.D. thesis, University of London PhD Thesis (1997).

[95] S. Balay, S. Abhyankar, M. Adams, J. Brown, P. Brune, K. Buschelman, V. Eijkhout, W. Gropp, D. Kaushik, M. Knepley, et al., Petsc users manual revision 3.5, Argonne National Laboratory (ANL).

[96] G. Natarajan, F. Sotiropoulos, Idec (k): A new velocity reconstruction algorithm on arbitrarily polygonal staggered meshes, Journal of Computational Physics 230 (17) (2011) 6583–6604.

[97] L. Ge, F. Sotiropoulos, A numerical method for solving the 3d unsteady incompressible navier–stokes equations in curvilinear domains with complex immersed boundaries, Journal of Computational Physics 225 (2) (2007) 1782–1809.

[98] T. Tezduyar, M. Behr, J. Liou, A new strategy for finite element computations involving moving boundaries and interfaces—the deforming-spatial-domain/space-time procedure: I. the concept and the preliminary numerical tests, Computer Methods in Applied Mechanics and Engineering 94 (3) (1992) 339–351.

[99] J.-L. Guermond, L. Quartapelle, A projection fem for variable density incompressible flows, Journal of Computational Physics 165 (1) (2000) 167–188.

[100] G. Tryggvason, Numerical simulations of the rayleigh-taylor instability, Journal of Computational Physics 75 (2) (1988) 253–282.

[101] Y. Wang, C. Shu, H. Huang, C. Teo, Multiphase lattice boltzmann flux solver for incompressible multiphase flows with large density ratio, Journal of Computational Physics 280 (2015) 404–423.

[102] H. G. Lee, J. Kim, Two-dimensional kelvin–helmholtz instabilities of multi-component fluids, European Journal of Mechanics-B/Fluids 49 (2015) 77–88.

[103] S.-R. Hysing, S. Turek, D. Kuzmin, N. Parolini, E. Burman, S. Ganesan, L. Tobiska, Quantitative benchmark computations of two-dimensional bubble dynamics, International Journal for Numerical Methods in Fluids 60 (11) (2009) 1259–1288.

[104] Q. Li, K. Luo, X. Li, Lattice boltzmann modeling of multiphase flows at large density ratio with an improved pseudopotential model, Physical Review E 87 (5) (2013) 053301.

[105] J. Martin, W. Moyce, Part iv. an experimental study of the collapse of liquid columns on a rigid horizontal plane, Philosophical Transactions of the Royal Society of London A: Mathematical, Physical and Engineering Sciences 244 (882) (1952) 312–324.

[106] O. Desjardins, H. Pitsch, A spectrally refined interface approach for simulating multiphase flows, Journal of Computational Physics 228 (5) (2009) 1658–1677.

[107] M. Basumatary, G. Natarajan, S. C. Mishra, Defect correction based velocity reconstruction for physically consistent simulations of non-newtonian flows on unstructured grids, Journal of Computational Physics 272 (2014) 227–244.

[108] K. Taira, T. Colonius, The immersed boundary method: a projection approach, Journal of Computational Physics 225 (2) (2007) 2118–2137.

[109] J.-I. Choi, R. C. Oberoi, J. R. Edwards, J. A. Rosati, An immersed boundary method for complex incompressible flows, Journal of Computational Physics 224 (2) (2007) 757–784.

[110] X. Zhang, S. Ni, G. He, A pressure-correction method and its applications on an unstructured chimera grid, Computers & Fluids 37 (8) (2008) 993–1010.

[111] R. Mittal, H. Dong, M. Bozkurttas, F. Najjar, A. Vargas, A. von Loebbecke, A versatile sharp interface immersed boundary method for incompressible flows with complex boundaries, Journal of Computational Physics 227 (10) (2008) 4825–4852.

[112] D. Russell, Z. J. Wang, A cartesian grid method for modeling multiple moving objects in 2d incompressible viscous flow, Journal of Computational Physics 191 (1) (2003) 177–205.

[113] I. Kroo, P. Kunz, Analysis and design of airfoils for use at ultra-low reynolds numbers, Fixed and Flapping Wing Aerodynamics for Micro Air Vehicle Applications, edited by TJ Mueller, Progress in Astronautics and Aeronautics, AIAA, Reston, VA (2001) 503517.

[114] H. Dütsch, F. Durst, S. Becker, H. Lienhart, Low-reynolds-number flow around an oscillating circular cylinder at low keulegan–carpenter numbers, Journal of Fluid Mechanics 360 (1998) 249–271.

[115] K. H. Jung, K.-A. Chang, H. J. Jo, Viscous effect on the roll motion of a rectangular structure, Journal of Engineering Mechanics 132 (2) (2006) 190–200.

[116] I. Campbell, P. Weynberg, Measurement of parameters affecting slamming. wolfson unit for marine technology and industrial aerodynamics univ. of southampton, Tech. rep., Report (1980).

[117] K. Kleefsman, G. Fekken, A. Veldman, B. Iwanowski, B. Buchner, A volume-of-fluid based simulation method for wave impact problems, Journal of Computational Physics 206 (1) (2005) 363–393.

[118] M. Greenhow, W.-M. Lin, Nonlinear-free surface effects: experiments and theory, Tech. rep., DTIC Document (1983).

[119] X. Zhu, O. M. Faltinsen, C. Hu, Water entry and exit of a horizontal circular cylinder, Journal of Offshore Mechanics and Arctic Engineering 129 (4) (2007) 253–264.

[120] H. Sun, O. M. Faltinsen, Water impact of horizontal circular cylinders and cylindrical shells, Applied Ocean Research 28 (5) (2006) 299–311.

[121] S. Di, W. Ge, Simulation of dynamic fluid–solid interactions with an improved direct-forcing immersed boundary method, Particuology 18 (2015) 22–34.

[122] A. Doostmohammadi, S. Dabiri, A. Ardekani, A numerical study of the dynamics of a particle settling at moderate reynolds numbers in a linearly stratified fluid, Journal of Fluid Mechanics 750 (2014) 5–32.

[123] B. Selvam, S. Merk, R. Govindarajan, E. Meiburg, Stability of miscible core–annular flows with viscosity stratification, Journal of Fluid Mechanics 592 (2007) 23–49.

[124] A. Rogerson, E. Meiburg, Numerical simulation of miscible displacement processes in porous media flows under gravity, Physics of Fluids A: Fluid Dynamics (1989-1993) 5 (11) (1993) 2644–2660.

[125] D. D. Joseph, R. Bai, K. Chen, Y. Y. Renardy, Core-annular flows, Annual Review of Fluid Mechanics 29 (1) (1997) 65–90.

[126] R. J. Lowe, J. W. Rottman, P. Linden, The non-boussinesq lock-exchange problem. part 1. theory and experiments, Journal of Fluid Mechanics 537 (2005) 101–124.

LIST OF PUBLICATIONS

Journals:

1. J.K. Patel, G. Natarajan, A generic framework for design of interface capturing schemes for multi-fluid flows, Computers & Fluids 106 (2015) 108–118.

2. J.K. Patel, G. Natarajan, A novel consistent and well–balanced algorithm for simulations of multiphase flows on unstructured grids, Journal of Computational Physics 350 (2017) 207–236.

3. J.K. Patel, G. Natarajan, Diffuse interface immersed boundary method for multi–fluid flows with arbitrarily moving rigid bodies, Journal of Computational Physics 360 (2018) 202–228.

Book Chapter:

1. J.K. Patel, G. Natarajan, Volume–of–solid immersed boundary method for free surface flows with arbitrary moving rigid bodies, Fluid Mechanics and Fluid Power–Contemporary Research, Springer India (2017) 1181–1192.

Conference Proceedings:

1. J.K. Patel, G. Natarajan, Volume–of–solid immersed boundary method for free surface flows with arbitrary moving rigid bodies, 5^{th} International Conference on Fluid Mechanics and Fluid Power, IIT Kanpur, India (2014).

2. J.K. Patel, G. Natarajan, Investigation of the consistent formulation for the simulation of the high density ratio multifluid flows, 6^{th} International Conference on Computational Mechanics and Simulation, IIT Bombay, Mumbai, India, June 27-July 1 (2016).